U.S. DEPARTMENT OF ENERGY | Energy Efficiency & Renewable Energy

Propulsion Materials

FY 2015 Annual Report

P. Davis, E. Owens, and J. Gibbs

December 2016

Energy Efficiency and Renewable Energy
Vehicle Technologies Office
Advanced Materials Technologies

(This page intentionally left blank)

Introduction

Propulsion Materials Research and Development: Enabling Materials Technologies to Meet Vehicle Technologies Office Goals

The Department of Energy's Vehicle Technologies Office (VTO) is pleased to introduce the *FY 2015 Annual Progress Report for the Propulsion Materials Research and Development Program.* Together with Department of Energy national laboratories and in partnership with universities and private industry across the United States, the Propulsion Materials Program continues to invest in research and development (R&D) that provide enabling materials technologies for fuel-efficient and environmentally friendly commercial and passenger vehicles.

This introduction summarizes the objectives and progress of the program in Fiscal Year 2015. The Propulsion Materials Program actively supports the energy security and reduction of greenhouse emissions goals of VTO by investigating and identifying the materials properties that are most essential for continued development of cost-effective, highly efficient, and environmentally friendly next-generation heavy and light-duty powertrains. The technical approaches available to enhance propulsion systems focus on improvements in both vehicle efficiency and fuel substitution, both of which must overcome the performance limitations of the materials currently in use. Propulsion Materials Program activities work with national laboratories, industry experts, and VTO powertrain systems (e.g., Advanced Combustion Engines [ACE], Advanced Power Electronics and Electrical Machines [APEEM], and fuels) teams to develop strategies that overcome materials limitations in future powertrain performance. The technical maturity of the portfolio of funded projects ranges from basic science to subsystem prototype validation.

Propulsion Materials Program activities are structured to serve as an enabling partner and supporter of hybrid and vehicle systems, energy storage, APEEM, ACE, and fuels and lubricants.

Projects within a Propulsion Materials Program activity address materials concerns that directly impact critical technology barriers within each of the above programs, including barriers that impact fuel efficiency, thermal management, emissions reduction, improved reliability, and reduced manufacturing costs. The program engages only the barriers that result from material property limitations and represent fundamental, high-risk materials issues.

Enabling Advanced Technologies

A Propulsion Materials Program activity focuses on key technical deficiencies in materials performance that limit the expanded capabilities of advanced combustion engines, electric-drive systems, and fuels and lubricants. It provides materials R&D expertise and advanced materials testing and development that support the goals of combustion, hybrid, and power electronics development. The program provides enabling materials support for combustion, hybrid, and power electronics development, including the following:

- Materials for high-efficiency combustion strategies such as homogenous-charge compression ignition
- Materials for 55% thermal efficiency for heavy-duty diesel engines
- Materials technologies for effective reduction of tailpipe emissions, including diesel particulate filters, low-temperature catalyst development, characterization and testing, and exhaust gas recirculation coolers
- Materials technologies for electric and hybrid-electric vehicles, including thermal management of advanced power electronics materials and reducing dependence on rare earth elements in electric motors
- Materials for alternate-fuels, including engine and exhaust aftertreatment materials compatibility and corrosion in biofuels
- Support for the Materials Genome Initiative by evaluating existing computational tools and identifying gaps necessary for seamless integration across multiple length scales. Projects in this portfolio are validating the performance of existing tools, identifying gaps, and developing a suite of new materials with improved properties for engine applications.

The program supports these core technology areas by providing materials expertise, testing capabilities, computational expertise, and technical solutions for materials problems. The component development, materials processing, and characterization that the program provides are enablers of the successful development of efficient, durable, and emissions-compliant engines.

Program Organization

The Propulsion Materials Program consists of the following five R&D projects, which support VTO propulsion technologies. Each project consists of several R&D agreements.

1. Materials for Electric and Hybrid Drive Systems

   Develop materials appropriate for automotive power electronics, electric motors, and other electric and hybrid system applications.

2. Materials for High-Efficiency Engines

   Develop materials for next-generation, high-efficiency engines and address anticipated issues with engine cylinder block, head, crankshafts, pistons, valves and valve train, fuel injectors, turbochargers, and exhaust gas recirculation systems.

3. Materials for Control of Exhaust Gases and Energy Recovery Systems

   Develop materials for exhaust aftertreatment and waste heat recovery applications.

4. Cast Alloys for Engines (group of competitively awarded industry-led projects)

   Develop a suite of new, high-performance, low-cost cast alloys using an integrated computational materials engineering approach, targeting lightweight aluminum alloys for light-duty engines, high-strength cast ferrous alloys for heavy-duty engines, and high-performance cast steel alloys for high-performance crank shafts.

5. Materials by Design (Application-Specific Materials Simulation, Characterization, and Synthesis)

   Adopt computational materials design, including an atomic-scale characterization protocol to develop advanced materials for NOx catalysts, cast engine components, and electric motors and providing a pathway to transition Basic Energy Science research to practical applications.

R&D projects are evaluated annually using strategic objectives. Activities are evaluated based on their relevance to VTO objectives, the supported team's (i.e., ACE, APEEM, and fuels) assessment of the work, and the strength of industrial support for the activity. In order to meet future efficiency improvement targets, new projects and areas of research will be identified by assessments of VTO stretch objectives and resultant demands for increased material performance.

Edward Owens
Team Leader, Advanced Materials Technologies
Vehicle Technologies Office
Energy Efficiency and Renewable Energy

Jerry L. Gibbs
Technology Manager
Vehicle Technologies Office
Energy Efficiency and Renewable Energy

List of Acronyms

ACE	advanced combustion engines
AFCT	aluminum-iron-chrome/titanium
AFM	aluminum-iron-manganese
Ag	silver
AMT	Advanced Materials for Transportation
ANL	Argonne National Laboratory
APEEM	Advanced Power Electronics and Electrical Machines
BTE	brake thermal efficiency
CAD	computer-aided design
CFD	computational fluid dynamic
CG	compact graphite
CGI	compacted graphite iron
Co	carbon monoxide
CRADA	Cooperative Research and Development Agreement
CSAM	c-mode scanning acoustic microscope
Cu	copper
DBC	direct bonding copper
DEF	diesel emissions fluid
DOC	diesel oxidation catalyst
DOE	U.S. Department of Energy
DPF	diesel particulate filters
EDS	energy dispersive x-ray spectroscopy

EGR	exhaust gas recirculation
EM	electric motors
Fe	iron
FEA	finite element analysis
FY	fiscal year
GHSV	gas hourly space velocity
HC	hydrocarbons
ICME	Integrated Computational Materials Engineering
IEA	International Energy Agency
IG	intermediate graphite
ISO	International Organization for Standards
LEAP	Local Electrode Atom Probe
MPB	morphotrophic phase boundaries
N_2O	nitrous oxide
NOx	nitrogen oxides
NREL	National Renewable Energy Laboratory
OD	oxygen-diffusion
ORNL	Oak Ridge National Laboratory
PCP	peak-cylinder-pressure
PEM	Power Electronic Module
PM	particulate matter
PNNL	Pacific Northwest National Laboratory
R&D	Research and Development
RS	rapid solidification

SCR	selective catalytic reduction
SEM	scanning electron microscopy
SG	spheroidal graphite
SLTNR	Sustained Low Temperature Nox Reduction
SMD	size mean diameter
TEM	transmission electron microscopy
TWC	three-way catalyst
VG	vermicular graphite
VTO	Vehicle Technology Office

Table of Contents

(This page intentionally left blank)

Project 18516 – Materials for Hybrid and Electric Drive Systems

Agreement 26461 – Enabling Materials for High-Temperature Power Electronics

Andrew A. Wereszczak,* Shirley B. Waters,* Max C. Modugno,† and Hsin Wang*
*Materials Science and Technology Division
†Electrical and Electronics Systems Research Division
Oak Ridge National Laboratory
P.O. Box 2008, MS 6068, Building 4515
Oak Ridge, TN 37831-6068
Phone: (865) 576-1169; fax: (865) 574-6098; e-mail: wereszczakaa@ornl.gov

DOE Technology Manager: Jerry L. Gibbs
Phone: (202) 586-1182; fax: (202) 586-1600; e-mail: jerry.gibbs@ee.doe.gov

ORNL Technical Advisor: J. Allen Haynes
Phone: (865) 576-2894; fax: (865) 574-4913; e-mail: haynesa@ornl.gov

Contractor: Oak Ridge National Laboratory, Oak Ridge, Tennessee
Prime Contract No.: DE-AC05-00OR22725

Objectives

- Pursue process improvements, identify geometrical limitations, and aid the maturation of 200°C-capable, sinterable silver interconnection technology for use in automotive power electronic devices.
- Improve thermal management and increase the high-temperature capability of automotive electric motors (EMs) through improved fundamental understanding of thermal transfer in these motors and evaluation of alterative, 200°C-capable materials that could be used as constituents in them

Approach

- Process sinterable-silver interconnects in a variety of ways to identify their strength limitation and potential fatigue limitation. Examine the roles of plating material and the paste deposition method.
- Measure the thermal response of custom-fabricated, copper-wound test coupons to study the effects of wire orientation and interstitial varnish.

Accomplishments

- Identified that commercially available sinterable silver has a cohesive shear strength of 40 to 50 MPa. The adjacent plating starts to de-adhere from the copper cladding on direct-bonded copper ceramic

substrates above 50 MPa.

- A simple method, or proof test, was identified to estimate the maximum (or potential maximum) area that can be fabricated for a sinterable silver system whereby delamination does not occur upon processing.
- A processing transfer method was developed for use with wet (or undried) sinterable silver paste; its function fulfills the same function as preform technology.
- The thermal conductivity of copper windings was measured to be highly anisotropic, with thermal conductivity parallel to the wire direction being approximately two orders of magnitude higher than when perpendicular to them.
- This project continues to benefit from synergistic collaborations with the National Renewable Energy Laboratory (NREL). These collaborations are led and guided by ORNL, with both the sinterable silver and EM research efforts.

Future Direction

- Compare the effects of pre-drying sinterable silver on achievable strength.
- Identify how much thermal conductivity increase can result in copper windings from use of thermally conductive alternatives to varnish.

Introduction

VTO's Electric Drive Technologies Program has placed emphasis on cost-reducing research targets, challenges, and areas. These include high-temperature components, packaging, and reliability for long-term transformation technologies and thermal management technologies to reduce volume and enhance thermal reliability. The technical goals of this project directly strike at that emphasis.

Power electronic modules (PEMs) and EMs are subjected to high service temperatures that require efficient and sustained thermal management; therefore, they can reliably perform during a 15-year lifetime. The achievement of increased reliability and temperature capability, with concomitant decreases in size, weight, and cost, will occur when any four (or combination thereof) of the following aspects are addressed in parallel:

- *PEMs – increase strain tolerance*. PEMs are comprised of many different material constituents, with each serving a specific electrical function. These dissimilar materials will impose residual strain on each other during service that can cause inter and intra-constituent mechanical failures (resulting in a loss of electrical function for the entire PEM) if those strains are sufficiently high. The strains are amplified as PEM service temperature increases. An increase in the inter-bonding strain tolerance, or strength, between constituents will improve overall PEM reliability.
- *PEMs – reduce imposed strain*. This is accomplished through improved thermal management of the constituents and simplifying the architectural design, including using more thermally conductive materials, where allowed, and reducing the complexity of the PEM's interior architecture to position the (Joule-heated) semiconductor closer to the heat sink. A reduction in the imposed strain, no matter the means, will improve overall PEM reliability.
- *PEMs and EMs – increase temperature capability*. As wide bandgap semiconductors are integrated more frequently into PEMs, the temperature capability of the rest of the PEM constituents must also increase because the temperature capability of the entire PEM is only as high as that of the lowest-temperature capable constituent. PEM constituents consist of polymers, metals, semiconductors, and ceramics; therefore, the consideration of higher-temperature capable polymers must occur to increase the temperature capability of the entire PEM. The higher temperature capability of material constituents

(e.g., the organics used in copper windings) in EMs will enable the EM to operate under harsher conditions, desirably increase its power density, and allow for pursuits of alternative designs that could increase EM efficiency.

– *PEMs and EMs – reduce or sustain cost.* This perhaps is the greatest challenge. However, careful and innovative materials science and engineering can accomplish reduced or sustained cost. Innovation can result via the use of unconventional, yet mature, materials that are used in other (i.e., non-electrical) applications.

A strategy for achieving improved reliability, smaller size, and higher-temperature capability of PEMs and EMs is best achieved through a marriage of electronic package engineering and materials science and engineering. This is accomplished through a collaboration of VTO's Propulsion Materials and Electric Drive Technologies Programs and the evaluation of materials, including new or modified materials, in context of the above four listed aspects. Collaboration with NREL is occurring and is led and guided by ORNL to take advantage of NREL's relevant thermal cycling test capabilities. Additionally, direct input from the USCAR Electrical and Electronic Technical Team directly contributes to this project's path or indirectly through the VTO Electric Drive Technologies Program.

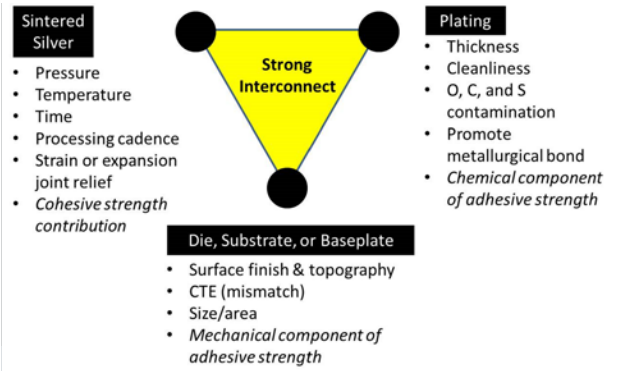

Figure 1: The strength and reliability of a sintered silver interconnect system is a function of many parameters.

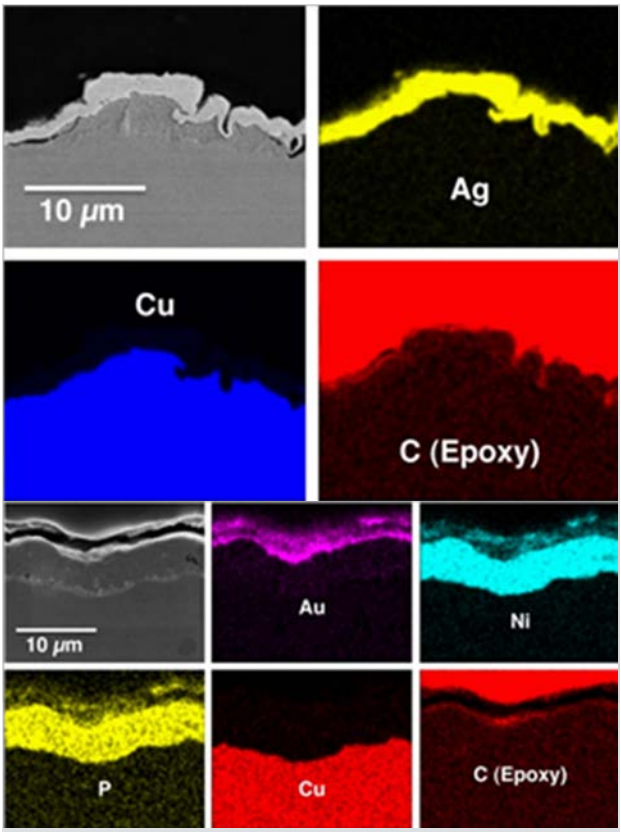

Figure 2: Elemental mapping of the polished cross-sections of the (top) silver-plating or the (bottom) gold-plating used on the DBC ceramic substrates. The sintered-silver interconnection bonds to these platings.

Two primary subtasks comprised the Fiscal Year (FY) 2015 effort. One was the processing and vetting of the high-temperature (i.e., 200°C-capable) silver sinter interconnection technology for PEMs. The other was the study of thermal transfer in EM copper windings, which is now seguing into the study of higher-temperature capable alternatives to interstitial varnishes for copper windings.

Results

200°C-Capable Power Electronic Modules Interconnects

The FY 2015 results are reflective of this project's pursuit of process improvements, its identification of geometrical limitations, and aiding the maturation of 200°C-capable, sinterable silver interconnection technology for use in automotive power electronic devices.

Numerous independent parameters can affect the bond strength and reliability of a sintered silver interconnect system (see Figure 1). The specific roles that the choices of plating material and paste deposition method have on those mechanical responses were a focus in FY 2015. Gold and silver platings were contrasted (see Figure 2) for images of their cross-sections. Additionally, any potential differences from the interconnect mechanical response caused by use of screen or stencil-printing of the wet paste was also examined.

Considerations of the plating material and printing method resulted in four test-set combinations. To enable their shear strength test comparisons, two square direct bonding copper (DBC) ceramic substrates, both having a size of 12.7 x 12.7 mm, were bonded with a commercially available sinterable silver paste to fabricate "DBC sandwiches." An illustration of them is shown in Figure 3.

Non-destructive imaging of their bonds (i.e., a "5-dice" pattern with a total bond area of 20 mm^2) was captured with the c-mode of a scanning acoustic microscope (CSAM) to judge the bonding efficacy prior to (destructive) shear testing. An example of a CSAM image of some test coupons in shown in Figure 4.

The shear strength of the fabricated DBC sandwich samples was measured using a shear tester (test setup shown in Figure 5). The strength data were regressed using a two-parameter Weibull distribution; 95% confidence ratio rings for them are shown in Figure 6. Failure analysis and further censoring is ongoing; however, the uncensored characteristic strengths were equivalent for the four test sets and a trend of a higher Weibull modulus (or less scatter) for the two stencil printed sets.

In addition to a shear strength measurement of the sintered silver interconnect, test coupons were fabricated to examine thermal cyclic reliability, with the latter involving a collaboration with NREL. These test coupons, referred to as "oreo cookie specimens"

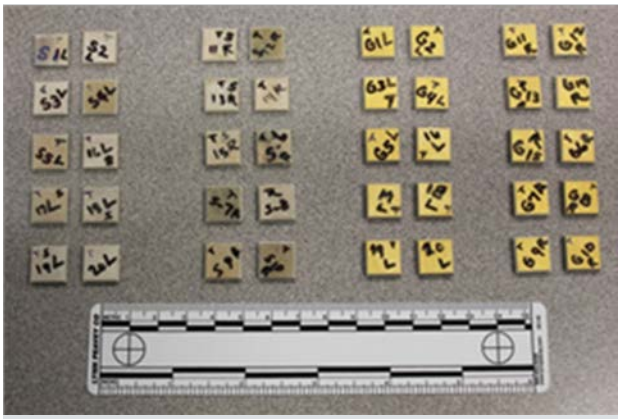

Figure 3: Examples of DBC ceramic substrates fabricated for shear strength measurements of sintered silver.

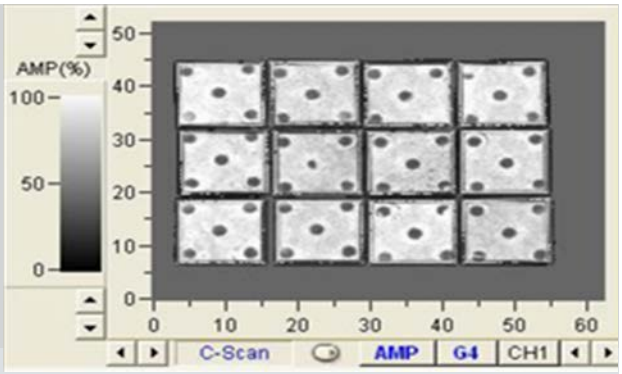

Figure 4: Example of a CSAM image of twelve DBC substrate sandwiches (12.7-mm x 12.7-mm squares,) with a "5-dice" interconnect printed pattern.

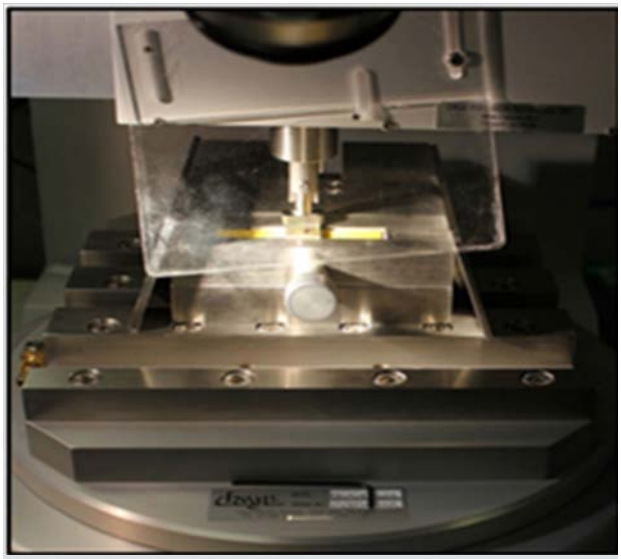

Figure 5: Image of the shea -test fixture and specimen setup.

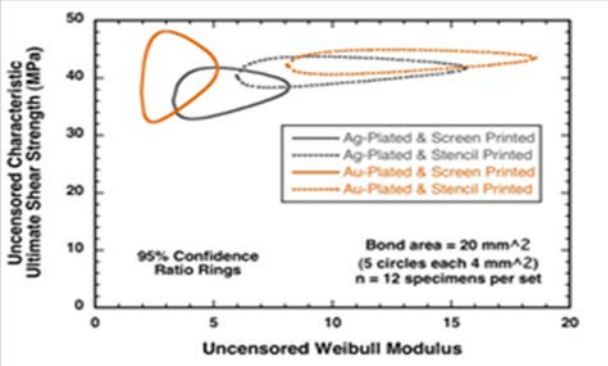

Figure 6: 95% two-parameter Weibull distribution confidence ratio rings of shear strength for four sintered silver sets.

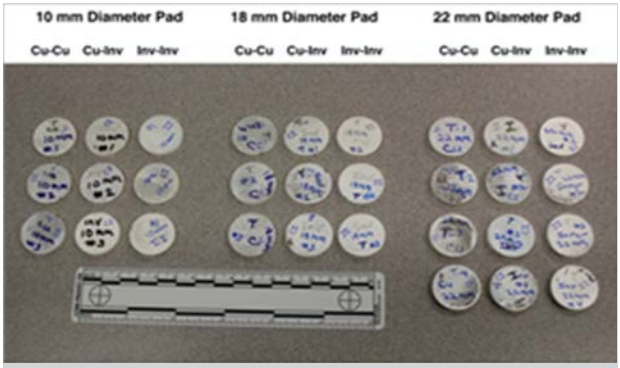

Figure 7: "Oreo-cookie" specimens, fabricated with either copper (Cu) or invar (Inv) 25-mm-diameter disks, bonded with circular pads of sintered silver with diameters of 10, 18, or 22-mm. All disks were silver plated.

(see Figure 7), purposely vary the imposed residual stress in a sintered silver interconnection. That variation was produced using two different metals (i.e., copper or invar disks having a 25-mm diameter and 2-mm thickness) having different coefficients of thermal expansion (i.e., 17 x 10^{-6}/°C for copper, about 3 x 10^{-6}/°C for invar, and 20 x 10^{-6}/°C for silver) and different sintered silver printed pad diameters (i.e., 10, 18, or 22 mm). Samples were sintered at 250°C using a commercially available sinterable silver paste.

Thermal cycling testing is continuing into early FY 2016; however, an observed response immediately after sinter processing with these processed oreo-cooking samples indicates that a potential maximum bond size may be identifiable for a sintered silver interconnect system (as described in Figure 1). This response is illustrated in Figure 8. For some copper-invar combinations, CSAM imaging showed that delamination of the larger sintered silver bond diameters occurred upon cool-down from the 250°C sintering. These results are now undergoing further interpretation to identify the maximum bond area that can be used for a given sintered silver interconnect system, so that delamination does not occur. These results will be featured and discussed in a to-be-written journal article jointly written by ORNL and NREL.

Lastly, during the various sinterable silver processing efforts in FY 2015, a processing transfer method was developed for use with wet (or undried) sinterable silver paste. The rationale for the paste was that it provided a function equivalent to what solder-based preform technology does. Test coupons were fabricated using this method and the measured shear strength of its interconnect was equivalent to the shear strengths

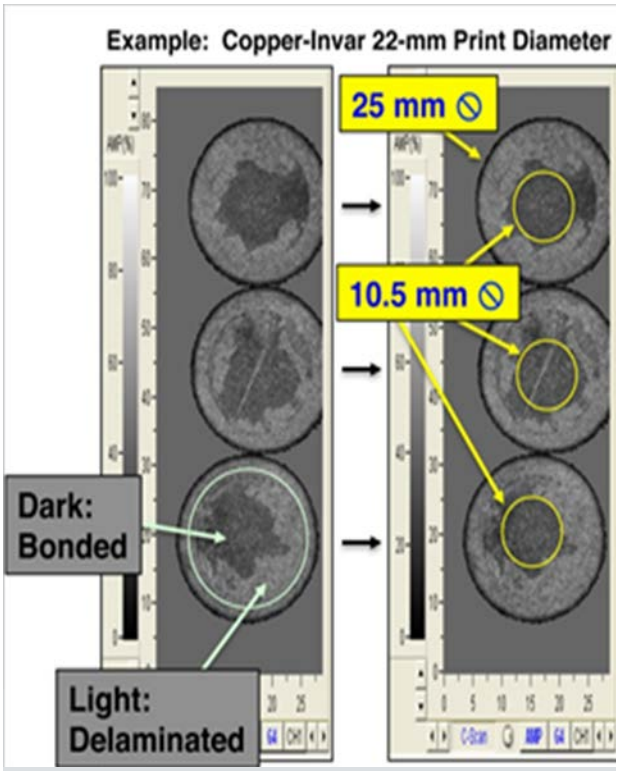

Figure 8: The residual stresses from the coefficients of thermal expansion mismatches and 250°C sintering would sometimes initiate delamination upon cool-down to room temperature. The significance and size of those sustained bonded areas continue to undergo interpretation.

produced with conventionally deposited sintered silver (illustrated in Figure 6). An invention disclosure was submitted and discussion will occur in early FY 2016 with an established manufacturer who may be interested in licensing its procedure. With this method, sinterable silver interconnects can be deposited onto non-planar or small surfaces (i.e., not relegated to direct screen or stencil printing onto a planar target surface).

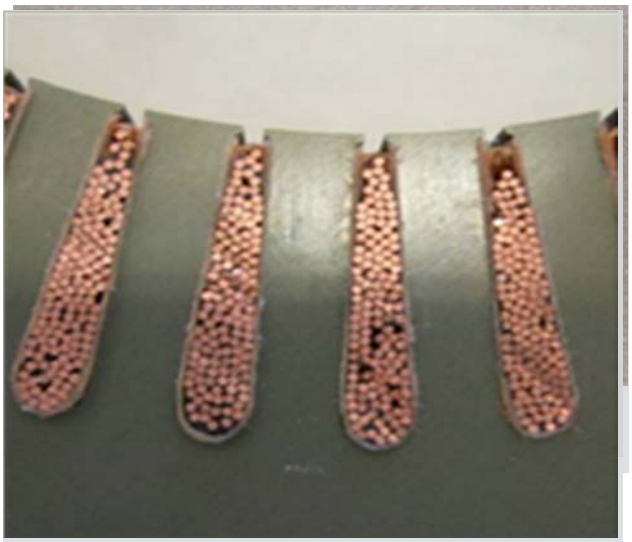

Figure 9: Sectioned copper wires in EM slot liners (photo from Sato et al. SAE International, 2011-01-0350.

Thermal Characterization of Electric Motor Copper Winding

Minimizing the service temperature in EM's copper windings in slot liners will promote greater efficiency and enable overall size and weight reductions. An image of these wires in the EM slot liners is shown in Figure 9. Two ways to ultimately achieve temperature minimization are to use more thermally conductive materials in EMs and to improve the understanding of the anisotropic thermal transfer within those copper windings. New potting and molding compounds that have better thermal transfer characteristics and higher-temperature capability are attractive candidates for this purpose, provided they are cost-competitive with currently used materials and do not introduce performance compromises. Greater understanding of the thermal transfer characteristics starts with the fundamental study and measurement of the directional thermal transfer in copper windings used in EMs.

Figure 10: Fabricated copper-wire coupons that underwent sectioning to fabricate specimens for thermal response (i.e., thermal conductivity and diffusivity) measurements.

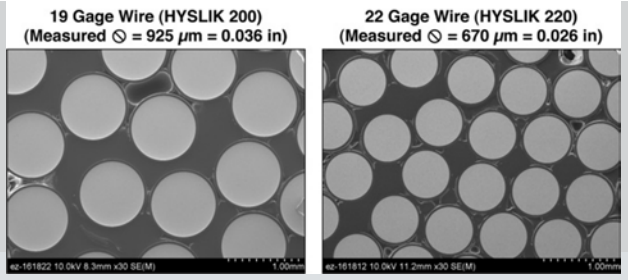

Figure 11: Cross-sections of the two wire diameters used in the fabricated coupons.

ORNL conceived of, coordinated, and continues to lead (into FY 2016) a collaboration with NREL to better understand the directional thermal response of packed copper wires. The effort included examination of valid measurements of thermal diffusivity and thermal conductivity as a function of wire orientation. Six cubes of copper windings (nominally 50 mm on a side) were fabricated at ORNL using conventional varnish with custom-fabricated molds (Figure 10). Three were fabricated with 19-gage wire (925-µm diameter) and three with 22-gage wire (670-µm diameter). Polished cross-sections of these copper wires are shown in Figure 11.

Three thermal response test methods are being used among ORNL and NREL to measure either thermal

conductivity or thermal diffusivity; those efforts are continuing into early FY 2016. However, results from one of those test methods at ORNL (i.e., laser flash diffusivity; with specimens shown in Figure 12) has conclusively and quantitatively showed that thermal conductivity in the direction parallel to the copper wires was more than two orders of magnitude higher than thermal conductivity perpendicular to the wires. The combination of varnish, interstitial voids, and wire coatings all combined to comprise thermal transfer perpendicular to the wires. Results from the three test methods, once all available, will be featured and discussed in a to-be-written journal article jointly written by ORNL and NREL.

Conclusions

We determined that commercially available sinterable silver has a cohesive shear strength of 40 to 50 MPa. The adjacent plating starts to de-adhere from the copper cladding on direct-bonded copper ceramic substrates under higher stress. Therefore, benefits from efforts to further increase the cohesive shear strength of sintered silver will only be realized if the concomitant adhesive strength of the metal platings used with sintered silver technology are also increased.

A simple method (i.e., essentially a processing proof test) was identified to estimate the maximum (or potential maximum) area that can be fabricated for a sinterable silver system where delamination does not occur from the act of sinter-processing itself. This is relevant to bonding large areas with sintered silver (e.g., bonding large die onto substrates or bonding substrates to heat sinks or base plates).

A processing transfer method was developed for use with wet (or undried) sinterable silver paste; the paste's function fulfills the same function as preform technology used with solders. This method increases the versatility of using sinterable silver paste because it allows the paste to be deposited onto non-planar or small surfaces, whose action may not be possible with conventional screen or stencil printing.

The thermal conductivity of copper windings was measured to be highly anisotropic, with thermal conductivity parallel to the wire direction being approximately two orders of magnitude higher than when perpendicular to them. This large anisotropy is a consequence of the poor thermal transfer characteristics of the varnish and voids located in the interstices between the packed copper wires and numerous interfaces. Understanding of this anisotropy is useful to the pursuit of improved thermal transfer in a direction perpendicular to the copper wire packing.

This project continues to benefit from synergistic collaborations with NREL that are led and guided by ORNL, with both the sinterable silver and EM research efforts.

Publications

Wereszczak, A., Z. Liang, M. K. Ferber, and L. D. Marlino, 2014, "Uniqueness and Challenges of Sintered Silver as a Bonded Interface Material," *Journal of Microelectronics and Electronic Packaging* 11: 158-165.

Wereszczak, A. A., S. B. Waters, and W. Carty, 2015, *Transfer Method for Printed Sinterable Paste Having Nonaqueous Solvent*, Invention Disclosure Number 201503508, DOE S-138, 140, April 04, 2015.

Wereszczak, A. A. and W. Carty, 2015, *Drying Method for Sinterable Paste Used for Bonded Joints*, Invention Disclosure Number 201503507, DOE S-138, 139, April 03, 2015.

Wereszczak, A. A. and V. Grosu, 2015, *Bonding Strategy for Large Area Metal-Cladded Ceramic Substrate*, U.S. Patent Application P027090-PTUS-RRM, February 24, 2015.

Project 18518 – Materials for High-Efficiency Engines

Agreement 17257 – Materials for Advanced Turbocharger Designs

Philip J. Maziasz
Oak Ridge National Laboratory
Materials Science and Technology Division
P.O. Box 2008, MS 6115
Oak Ridge, TN 37831-6115
Phone: (865) 574-5082; fax: (865) 574-7659; e-mail: maziaszpj@ornl.gov

DOE Technology Manager: Jerry L. Gibbs
Phone: (202) 586-1182; fax: (202) 586-1600; e-mail: jerry.gibbs@ee.doe.gov

ORNL Technical Advisor: J. Allen Haynes
Phone: (865) 576-2894; fax: (865) 574-4913; e-mail: haynesa@ornl.gov

Contractor: Oak Ridge National Laboratory, Oak Ridge, Tennessee
Prime Contract No.: DE-AC05-00OR22725

Objectives

- Cast CF8C-Plus steel is adequate for turbocharger housings for diesel engines (i.e., 750 to 800°C), but improved alloys must be developed for automotive turbocharger housings for gasoline engines that will experience temperatures up to 950°C.
- Cast CN12-Plus stainless steels have a higher temperature capability and strength at 800 to 1000°C and, with 25% Cr, have better oxidation resistance and provide a baseline for improved performance.
- The objective is to develop Al-modified CN12-Plus alloys with improved oxidation resistance at 950°C and above without sacrificing strength.

Approach

- Use a microstructural design approach that was used to develop CF8C-Plus for developing improved alloys with capability at 950°C and above.
- Conduct testing at ORNL above 800°C and approach Ford for input on turbocharger housing and exhaust manifold needs for light-duty vehicle applications.

Accomplishments

- Two heats of cast CN-12 Plus steel (i.e., standard and CuW modified) were obtained from Stainless Foundry and Engineering this year. Tensile, creep, and oxidation specimens are being machined for testing.

- Several small heats of Al-modified CN12-Plus steels were melted at ORNL and found to be fully austenitic with acceptable chemistries. Several larger heats of one of the alloys were made for mechanical properties testing.
- Severe oxidation testing of the preliminary Al-modified CN12-Plus alloys at 1000°C in air with 1-hour cycles after 200 hours showed positive behavior and were better than the HK30Nb and HP40Nb alloys, which both contain 25% Cr.

Future Direction

- Work with Ford to establish alloy performance and critical testing needs for turbocharger housing and exhaust manifold applications for gasoline engine applications for light-duty vehicles.

Introduction

Automotive exhaust components are expected to experience metal temperatures of 950°C or higher in the near future; therefore, turbocharger housings and exhaust manifolds will require affordable cast materials that can operate at such temperatures. In FY 2015, ORNL undertook a new project to address these issues after discussions with Ford. ORNL began to investigate the properties of CN12-Plus (a cast austenitic stainless steel developed over a decade ago with Caterpillar with 25% Cr and 0.8 C+N) for strength and oxidation resistance at 800 to 950°C. ORNL also began development of an Al-modified version of CN12-Plus steel for more oxidation resistance at high temperatures without sacrificing strength. These new steels are expected to have better performance at 800 to 950°C than CF8C-Plus steel, which previously has been studied extensively.

Results

CN12-Plus for Automotive Gasoline Engine Exhaust Component Applications

This new project follows several years of efforts for exhaust components for advanced diesel engine applications that emphasized cast CF8C-Plus austenitic stainless steel for applications that were in the 750 to 800°C temperature range, with durability requirements of at least 1 million highway miles. This new project focuses on turbochargers; exhaust manifolds for next generation automotive gasoline engines must withstand much higher temperatures than for diesel engine applications, with maximum metal temperatures $\geq$950°C and a durability of several hundred thousand miles. The need for more oxidation resistance and creep strength at 950°C and above created the opportunity to consider the cast CN12-Plus austenitic stainless steel also developed by ORNL and Caterpillar in 1999 through 2002 in the same project that developed the CF8C-Plus steel.

CN12 was a cast steel with a high sulfur level to provide the brittle MnS phase for enhanced machinability that was developed in an earlier project involving Ford, Caterpillar, and ORNL. CN12-Plus was developed by adding more Mn, eliminating the S, and adjusting the other elements to provide a stable austenitic parent phase strengthened by carbides and nitrides. CN12-Plus was patented in 2007 (U.S. Patent 7,255,755); creep-rupture data at 850°C/110 MPa showed its improvement relative to the standard CN12 steel. CN12-Plus has 25Cr/16Ni, and has more tensile and creep strength than CF8C-Plus steel because it has C+N=0.8 instead of 0.35 to 0.40 found in the latter. CN12-Plus should be stronger than HK30Nb and HP40Nb, both of which have 0.3C and 0.4C and no N, respectively, and will cost less as well.

CN12-Plus heats of steel were ordered from Stainless Foundry and Engineering late in 2014 and keel bars were

delivered to ORNL for testing in 2015. Two 300-lb heats were melted: one with the standard composition and one with 3W and 3Cu added. Both heats were easily controlled and cast in the foundry (a fluidity spiral from the standard CN12-Plus heat is shown in Figure 1). The metal fluidity of the CN12-Plus is similar to that of the CF8C-Plus steel and a good indicator of excellent castability for casting exhaust components with complex shapes. The as-cast microstructure of the standard CN12-Plus steel is shown in Figure 2. The mixture of Nb carbides and nitrides, as well as Cr carbides, is expected to boost the strength of the CN12-Plus steel relative to the CF8C-Plus steel in the 900 to 1000^{o}C range.

As with CF8C-Plus, CN12-Plus steel is used in the as-cast condition without any additional heat treatment, thus further moderating the cost.

Al-Modified CN12-Plus Steel Development, Creep, and Oxidation Testing for Automotive Gasoline Engine Exhaust Applications

This year, an effort began at ORNL to develop Al-modified cast stainless alloys based on the general CN12-Plus-type base composition for increased oxidation resistance in the 800 to 1000^{o}C temperature range for automotive exhaust component applications. Approximately, 3.5 to 4.0 wt. % Al was added to a base composition of CN12-Plus, adjusted to maintain a 100% austenitic (i.e., non-magnetic) matrix phase. Five modified alloys were made as 0.25-lb small rectangular ingots for chemistry verification and magnetic property, microstructure, and oxidation testing (PJM-Al1 through PJM-Al5), and then one of the alloys was selected to make several larger (i.e., 1-lb) rectangular ingots for mechanical properties testing (PJM-Al2). The backscattered electron scanning electron microscopy (SEM) image of the as-cast microstructure of PJM-Al3 is shown in Figure 3 and it is similar to that observed for the CN12-Plus steel in Figure 2.

Figure 1: A fluidity spiral of CN12-Plus steel poured at Stainless Foundry and Engineering with the same superheat used to cast keel bars for mechanical properties testing. The multiple loops indicate good metal fluidity.

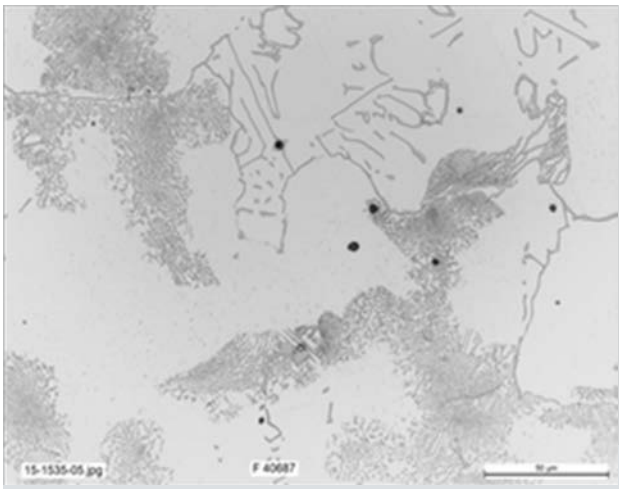

Figure 2: Optical metallography, showing the as-cast microstructure of standard CN12-Plus steel, with mixtures of carbides and nitrides along the interdendritic boundaries.

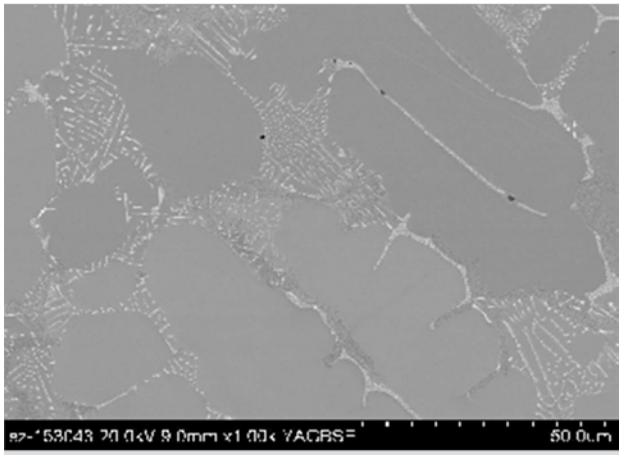

Figure 3. Backscattered electron SEM of as-cast microstructure of Al-modified CN12-Plus alloy (PJM-Al3) showing a mixture of carbides and other phase along the interdendritic boundaries.

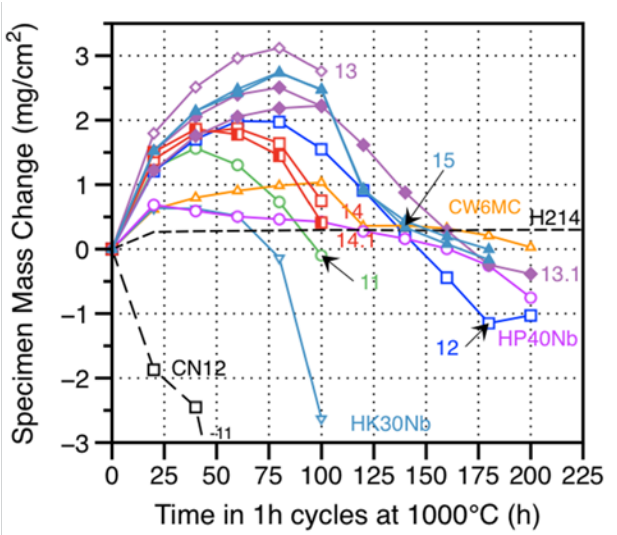

Figure 4: Plot of mass change versus time for oxidation testing in air at 1000°C and a 1-hou cycle time for various cast stainless steels, alloys, and nickel-based alloys. Alloys include standard CN12 steel, the Al-modified CN12-Plus alloys (11-15), HK^{30}Nb (^{25}Cr/^{20}Ni) alloy, HP^{40}Nb (^{25}Cr/^{35}Ni) alloy, and CW6MC nickel-based alloy (cast version of alloy 625) with ^{21}Cr, and H214, a nickel-based aluminia former. The Al-modified alloys show better oxidation resistance than the chromia-forming alloys, but the results are only out to 200 hours.

The small heats of Al-modified cast stainless alloys made this year were non-magnetic, indicating a fully austenitic parent matrix phase. Verification chemistries indicated that the alloys were consistent with their target compositions. Accelerated oxidation testing at 1000°C in air with 1-hour cycling was conducted to simulate automotive stop and start operation. The results of the oxidation testing at 1000°C are shown in Figure4. The new Al-modified cast alloys show relatively good oxidation resistance compared to the chromia-forming alloys; however, these accelerated results are only to 200 hours. Longer-term testing at the actual target temperature (i.e., 950°C) will be needed to verify adequate behavior. An optical metallographic cross-section microstructure of a corrosion coupon of PJM-Al2 is shown in Figure 5; this figure shows evidence of moderate internal oxidation to form oxides or nitrides beneath the surface.

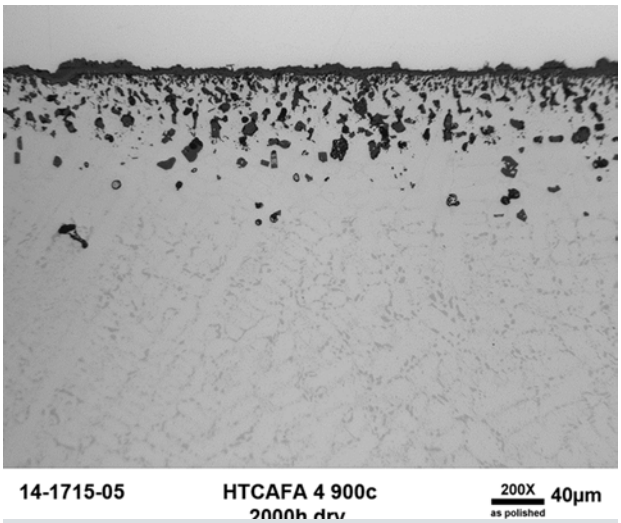

Figure 5. Cross-section metallographic microstructure of PJM-Al2 alloy after oxidation in dry air for 200 hours at 1000°C for 1-hour cycles. The microstructure shows internal oxides or nitrides beneath the oxide scale at the surface.

Mechanical testing of the PJM-Al2 alloy was done, with tensile tests at room temperature and 1000°C and creep-rupture tests at 1000 and 1050°C at stresses of 25 and 10 MPa, respectively. The Al-modified cast alloy had a moderate increase in strength compared to CF8C-Plus cast steel at room temperature (YS of 53 ksi compared to 42 to 45 ksi), but had similar yield strength at 1000°C (YS of 14 ksi) and similar creep-rupture lives at 1000 and 1050°C (118 and 470 hours,

respectively). The combination of oxidation resistance and high-temperature strength of the new Al-modified CN12 alloys is promising so far and warrants consideration for scaling up the size of the heats.

Finally, contact was made with Ford Motor Company earlier this year to discuss results and progress on cast austenitic stainless steels capable of performance at 950^{o}C; there was an agreement that it would be mutually beneficial to interact on this work in the future.

Conclusions

1. Keel bars for mechanical properties and oxidation testing of CN12-Plus and CN12-Plus CuW were ordered and obtained from Stainless Foundry and Engineering at ORNL this year; mechanical properties specimens are currently being machined from these bars.
2. The cast CN12-Plus steel showed good metal fluidity for solidification spiral tests conducted at the foundry. The microstructure showed considerable precipitation of carbide and nitride phases in the as-cast structure, consistent with the high levels of C and N in the alloys.

Laboratory heats of new Al-modified CN12-Plus alloys with 3.5 to 4 wt. % Al were developed at ORNL this year. The best compositions are non-magnetic, indicating a fully austenitic matrix parent phase. Severe short-term oxidation testing at an accelerated temperature of 1000^{o}C shows relatively good behavior of the new alloys compared to similar chromia-forming steels (such as CF8C-Plus). Creep and tensile testing at 1000^{o}C indicates the Al-modified alloys have strength comparable to CF8C-Plus steel.

Project 18518 – Materials for High-Efficiency Engines

Agreement 18571 – Materials Issues Associated with Exhaust Gas Recirculation Systems

M. J. Lance
Ceramic Science and Technology Group
Oak Ridge National Laboratory
P.O. Box 2008, MS 6068, Building 4515
Oak Ridge, TN 37831-6068
Phone: (865) 241-4536; fax: (865) 574-6098; e-mail: lancem@ornl.gov

DOE Technology Manager: Jerry L. Gibbs
Phone: (202) 586-1182; fax: (202) 586-1600; e-mail: jerry.gibbs@ee.doe.gov

ORNL Technical Advisor: J. Allen Haynes
Phone: (865) 576-2894; fax: (865) 574-4913; e-mail: haynesa@ornl.gov

Contractor: Oak Ridge National Laboratory, Oak Ridge, Tennessee
Prime Contract No.: DE-AC05-00OR22725

Objectives

- Provide information to industry about fouling deposit properties to enable improved models and potential design improvements to reduce fouling and its impact on the performance of exhaust gas recirculation (EGR) coolers.
- Develop a protocol for refreshing the EGR cooler during use or during service.

Approach

- Assemble EGR engineers from member companies of the Diesel Crosscut Team to serve as an advisory board for this project.
- Determine novel cooler geometries that will promote deposit removal.

Accomplishments

- Determined the effect of substrate temperature on the deposit thickness after fouling under different operating conditions using epoxy-mounted, cross-sectioned samples.
- Using structured-light optical profilometry, the effect of cooler geometry on deposit thickness was measured and found to contradict current theoretical fouling models.

Future Direction

- Complete analysis of deposit thickness data on all 45 samples (15 conditions and three locations).

– Collaborate with EGR team members to model the effect of shear forces on EGR cooler fouling.

– Measure deposit strength using instrumented indentation and shear testing.

Introduction

High-pressure EGR is the primary nitrous oxide (NO_x) reduction technology used by the diesel industry. Exhaust gas is directed through a heat exchanger (or EGR cooler), where it is cooled before being directed back into the engine intake. Inclusion of exhaust in the incoming charge reduces the combustion temperature and oxygen content, thereby reducing the oxidation of N_2. The EGR stream also contains particulate matter (PM) and hydrocarbons (HC), which, when directed through the EGR cooler, form deposits through thermophoresis and condensation, respectively. Under some combustion and EGR cooler conditions, high concentrations of HCs in the exhaust gas may accelerate the rate of deposition, causing plugging of the EGR cooler channels. These conditions may occur, for example, during regeneration of diesel particulate filters. As EGR utilization continues to be expanded to new operating regimes, EGR fractions are likely to increase and the coolant temperature to decrease, exacerbating fouling.

At the start of this project, a team consisting of engineers responsible for EGR systems was assembled from nine diesel engine manufacturers: Caterpillar, Cummins, Detroit Diesel, Ford, GM, John Deere, Navistar, DAF Trucks, and Volvo/Mack; and one heat exchanger supplier: Modine. They were asked what is the biggest problem facing EGR cooling systems? The clear winner was fouling. Over the course of this project, the EGR team has been notified of generated results and has contributed coolers for forensic analysis of fouling deposits. To date, studies of EGR fouling have focused mainly on the cause of stabilized effectiveness loss, whereby low HC deposits form but rapidly reach a plateau in thickness on flat substrate tubes [1-4] despite the fact that all EGR coolers are not flat but contain turbulators designed to enhance heat transfer. Previous work on this project has found that the presence of turbulation structures significantly alters the local surface topology of EGR deposits found in field-tested coolers [5, 6], with signs of shear removal occurring on regions where the exhaust gas is impinging on the cooler substrate (e.g., on the leading edge of the sine wave of a cooler fin). This suggests there is potential to design a better cooler geometry that would promote deposit removal by shear forces while still maintaining high heat transfer.

In order to better understand the role that cooler geometry plays in deposit formation and removal, 21 tube-in-shell EGR coolers, with a sinusoidal wave geometry, were fouled by John Deere using a five-factor, three-level design-of-experiments with the following variables:

– EGR flow rate

– EGR inlet gas temperature

– Soot (PM) level (i.e., smoke)

– HC concentration

– Coolant temperature.

Samples were extracted and the deposit thickness measured using two novel imaging methods that will be described in the following sections.

Results

Epoxy-Mounted Cross-Sections

A 9-liter engine and ultra-low sulfur diesel fuel were used to form the cooler deposits at John Deere. Coolers were run until the effectiveness stabilized (typically 40 to 70 hours). They were cooled down to room temperature and then run for an additional few hours in order to measure the change in effectiveness (i.e., refreshment) due to shut down. A single tube from the center of each cooler was extracted and divided into 3/4-in. segments using a band saw. The band saw was used without coolant and cutting was performed at a slow rate to minimize damage to the deposit. Three of the 3/4-in. long segments were taken from within 2 in. of the inlet and the outlet and from approximately the middle of the tube. Samples were then immersed in epoxy that contained a fluorescent dye that greatly enhances the contrast between the deposit and the epoxy. Images were collected using a Keyence VHX-200 digital microscope, with an illumination source from the side.

Figure 1A shows a representative image collected from an epoxy-mounted sample. The flow direction is into the plane of the image. The internal structure contained two heat transfer surfaces: the primary surface, which is the outer oblong tube that is in direct contact with the coolant, and the secondary surface, which is the inner 20 fins that are in contact with the primary surface through weld points. This geometry will cause the primary heat transfer surface to be at the coolant temperature at all times; however, the secondary heat transfer surface (i.e., fins) will have to transfer the heat from the gas along the thin fin wall to the primary heat transfer surface and then into the coolant.

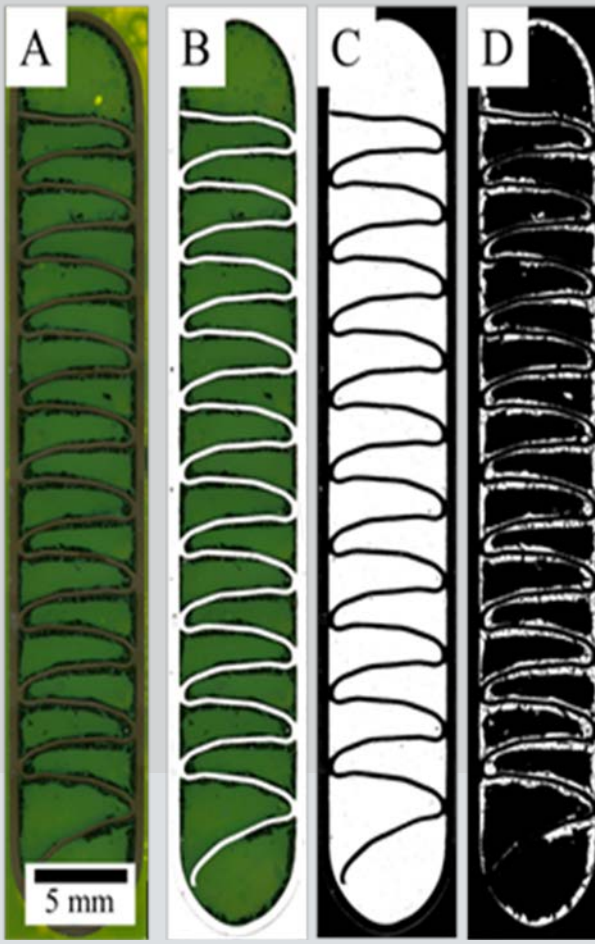

Figure 1: Image of an epoxy-mounted EGR cooler section with the exhaust flow into the figure (A); the metal is removed (B); the total area of the empty space is measured (C); and the deposit area (D).

Using the image processing software, ImageJ, the images were thresholded to highlight just the parts of the image where there was no metal (Figure 1B), where the gas flowed (Figure 1C), and where the deposit is (Figure 1D). Using these images, the percentage of the EGR tube that contained deposit was directly measured. Of the five variables tested, the HC content and the soot (i.e., smoke) correlated positively with the percentage of the tube filled with deposit and the EGR inlet gas temperature correlated negatively. As was discussed in previous work on these samples [6], a higher EGR gas temperature may be promoting deposit removal near the inlet; however, it is not clear from which of the two heat transfer surfaces the deposit is being removed.

In order to determine the amount of the deposit on the fins and on the outer shell, the total deposit thickness was summed along the long axis of the tube cross-section

in Figure 1. An example of this is shown in Figure 2 for two different EGR inlet temperatures. The far left and far right sides of Figure 2 correspond to the deposit that formed on the primary heat transfer surface (i.e., outer tube) and the region in the middle corresponds to the deposit formed on the secondary heat transfer surface (i.e., fins). The EGR inlet gas temperature had a strong effect on the amount of deposit on the fins, with higher temperatures reducing deposition on the fins.

The deposit thickness from the outer 10% from both sides of Figure 2 was designated deposit that had formed on the outer tube and the inner 80% was designated deposit formed on the fins. From this, the percentage of the deposit formed on the fins was measured; it was found that only the HC content (Figure 3A) and the EGR inlet gas temperature

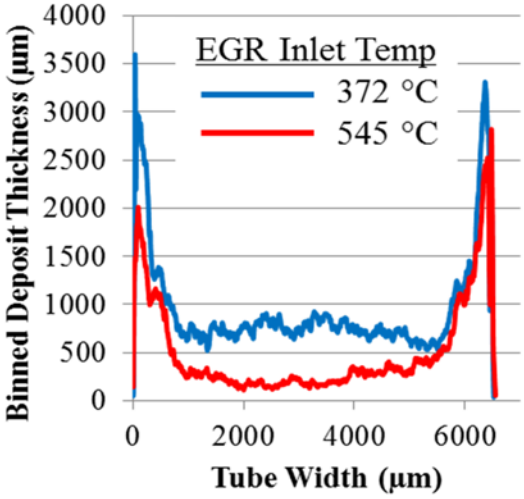

Figure 2: Binned total deposit thickness versus tube width for two samples run with significantly different inlet gas temperatures.

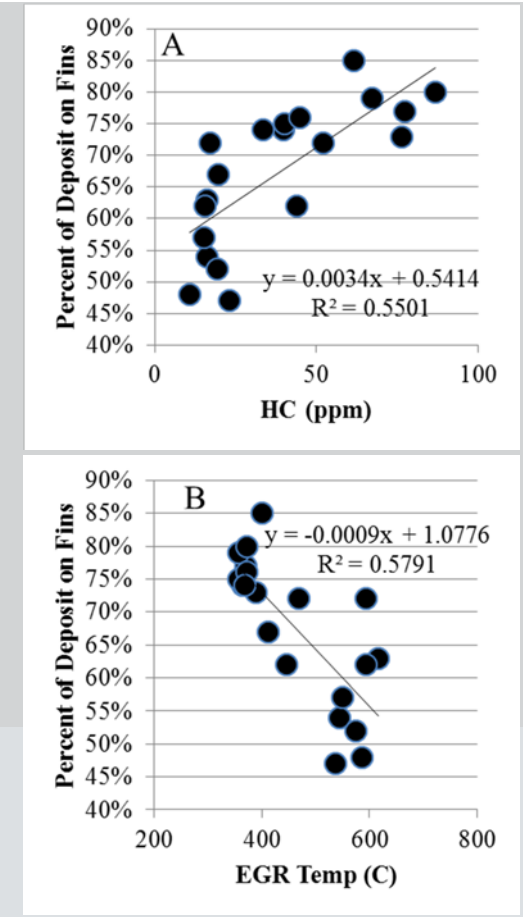

Figure 3: The percentage of the deposit that formed on the fins versus the HC content (A) and the EGR inlet temperature (B).

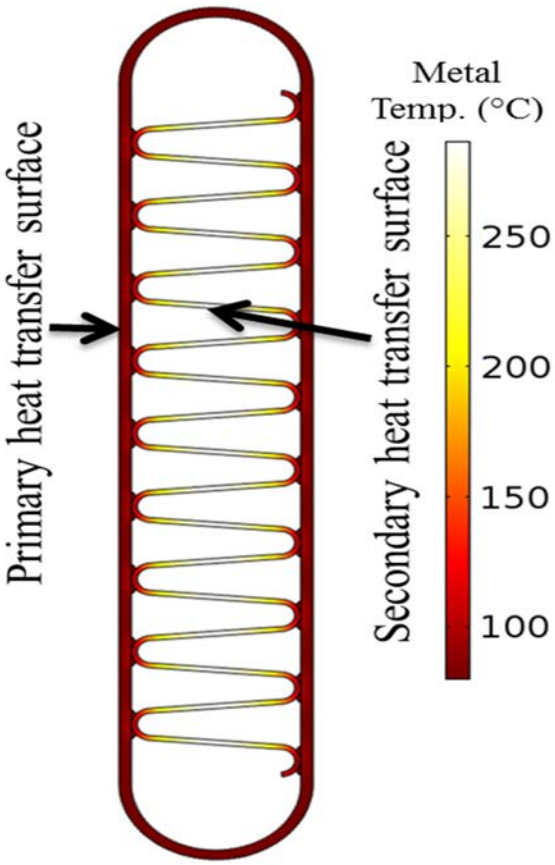

Figure 4: Simulation of the substrate temperature with an inlet gas temperature of 550°C and a coolant temperature of 90°C.

(Figure 3B) showed strong correlations. It is speculated that higher hydrocarbon promotes deposit formation by making the metal fin stickier for PM to attach.

Conversely, high inlet gas temperatures increase the metal temperature, thereby reducing thermophoresis. This can be observed in Figure 4, which shows a map of the substrate temperature, assuming an inlet gas temperature of 550°C and a coolant temperature of 90°C. This model shows that the fins in the center are hotter (up to 300°C) than the outer surface, which is in contact with the coolant.

Structured-Light Optical Profilometry

A line running parallel to the exhaust flow was milled on both sides of each segment, leaving behind a notch that was approximately 2-mils thick. The samples were carefully broken open along this notch, revealing the inner fin surfaces of one channel. A Keyence VR-3000 microscope was used to collect three-dimensional images of the deposit surface. This microscope uses structured light to illuminate the surface and then calculates surface height to an approximate 1-µm resolution. Surface height is measured before and after the deposit is removed (Figure 5) and subtracting these two maps results in a map of the deposit thickness.

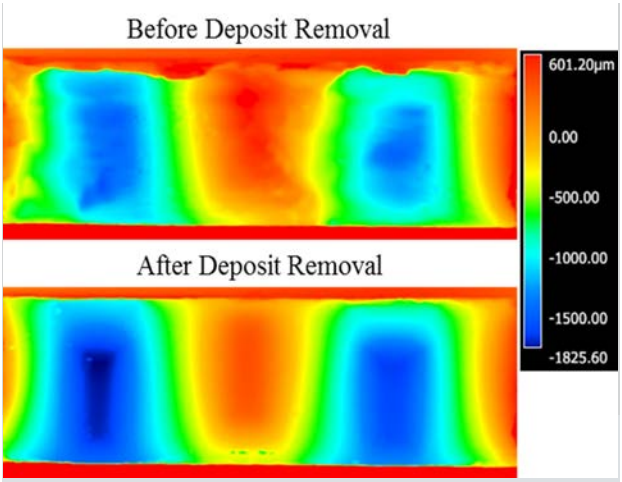

Figure 5: Surface height maps of a single fin before the deposit has been removed (top) and after (bottom).

Figure 6 shows the thickness measurements from 45 different samples compared to computational fluid dynamic (CFD) modelling performed by Modine [7]. The deposit is the thinnest on the upstream side of the wave and the thickest is on the downstream side, whereas the CFD model predicted the thickest deposit upstream from the peak of the fin. This shows that our measurements contradicted the CFD model because the thickest deposit occurred downstream from the peak. The highest heat transfer occurs at the upstream side of the peak, where the boundary layer is the thinnest. The CFD model also predicted that the thin boundary layer will result in the most deposition. Our results significantly alter this model of fouling and show the importance of shear forces and their interaction with cooler geometry for controlling the deposit thickness and the impact of fouling on EGR performance. This suggests that there may be ways to optimize the geometry of the EGR cooler in order to promote shear removal of the deposit.

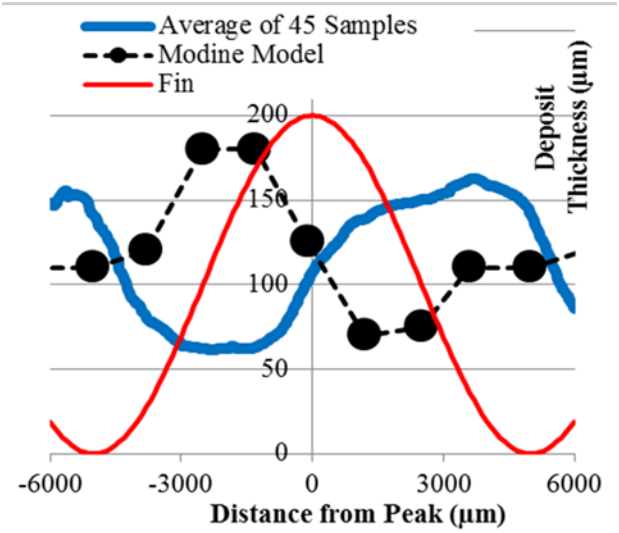

Figure 6: The average deposit thickness measured along the sinusoidal fin compared to CFD modeling. The flow direction is left to right.

Milestones

Milestone	Completion Date
Deposit thickness will be measured on two modine tubes (one a production geometry and the other an experimental geometry) as a function of location.	December 2014
Measure deposit density changes caused by temperature and water condensation under controlled conditions.	March 2015
Deposit thickness will be measured on cross-sectioned samples generated by John Deere at various engine set points.	June 2015
The annual report will be submitted.	November 2015

Conclusions

Two new experimental approaches for measuring deposit thickness were established.

Temperature of the secondary heat transfer surface (i.e., fins) may be substantially higher than the coolant temperature.

High inlet temperatures increase the temperature of the fins well above the coolant temperature, thereby reducing the temperature gradient, which is the driving force for thermophoresis.

Hydrocarbon condensation may act as glue, promoting deposit formation on the finned surfaces.

Deposit thickness measurements contradicted CFD modeling; this illustrates the central importance of shear forces and cooler geometry in EGR fouling.

References

Lepperhoff, G. and M. Houben, 1993, "Mechanisms of Deposit Formation in Internal Combustion Engines and Heat Exchangers," SAE Technical Paper 931032, doi:10.4271/931032.

Sluder, C. S., J. Storey, M. J. Lance, and T. Barone, 2013, "Removal of EGR Cooler Deposit Material by Flow-Induced Shear," *SAE Int. J. Engines* 6(2): 999-1008, doi:10.4271/2013-01-1292.

Abarham, M., P. Zamankhan, J. W. Hoard, D. Styles et al., 2013, "CFD analysis of particle transport in axi-symmetric tube flows under the influence of thermophoretic force," *International Journal of Heat and Mass Transfer* 61:94-105, doi:10.1016/j.ijheatmasstransfer.2013.01.071.

Warey, A., D. Long, S. Balestrino, P. Szymkowicz et al., 2013, "Visualization and Analysis of Condensation in Exhaust Gas Recirculation Coolers," 2013-01-05402013, doi:10.4271/2013-01-0540.

Lance, M. J., S. Sluder, S. Lewis, and J. Storey, 2010, "Characterization of Field-Aged EGR Cooler Deposits," *SAE Int. J. Engines* 3(2):126-136, doi:10.4271/2010-01-2091.

Lance, M. J., J. Storey, C. S. Sluder, H. Meyer III et al., 2013, "Microstructural Analysis of Deposits on Heavy-Duty EGR Coolers," SAE Technical Paper 2013-01-1288, doi:10.4271/2013-01-1288.

Nagendra, K., D. K. Tafti, A. K. and Viswanathan, 2011, "Modeling of soot deposition in wavy-fin exhaust gas recirculator coolers," *International Journal of Heat and Mass Transfer* 54(7-8): 1671-1681, doi:10.1016/j.ijheatmasstransfer.2010.10.033.

Publications and Presentations

Lance, M. J., H. Bilheux, J.-C. Bilheux, S. Voisin et al., 2014, "Neutron Tomography of Exhaust Gas Recirculation Cooler Deposits," SAE Technical Paper 2014-01-0628, doi:10.4271/2014-01-0628.

Lance, M. J., J. Storey, S. Lewis, and C. S. Sluder, 2014, "Analysis of Lacquer Deposits and Plugging Found in Field-Tested EGR Coolers," SAE Technical Paper 2014-01-0629, doi:10.4271/2014-01-0629.

Sluder, C. S., J. M. E. Storey, and M. J. Lance, 2014, "Effectiveness Stabilization and Plugging in EGR Cooler Fouling," SAE Technical Paper 2014-01-0640, doi:10.4271/2014-01-0640.

Lance, M. J., 2015, "Materials Issues Associated with EGR Systems," U.S. DOE Vehicle Technologies Office 2015 Annual Merit Review and Peer Evaluation Meeting, Washington D.C., June 10, 2015.

Project 18518 – Materials for High-Efficiency Engines

Agreement 23425a – Lightweight Heavy-Duty Engines (CRADA with Cummins Inc.)

G. Muralidharan, Allen Haynes, Hsin Wang, Wallace Porter
Oak Ridge National Laboratory
Materials Science and Technology Division
1 Bethel Valley Road
P.O. Box 2008, MS 6068, Building 4515
Oak Ridge, TN 37934
Phone: (865) 574-4281; fax: (865) 574-4357; e-mail: muralidhargn@ornl.gov

DOE Technology Manager: Jerry L. Gibbs
Phone: (202) 586-1182; fax: (202) 586-1600; e-mail: jerry.gibbs@ee.doe.gov

ORNL Technical Advisor: J. Allen Haynes
Phone: (865) 576-2894; fax: (865) 574-4913; e-mail: haynesa@ornl.gov

Contractor: Oak Ridge National Laboratory, Oak Ridge, Tennessee
Prime Contract No.: DE-AC05-00OR22725

Objectives

- The primary focus of this project is to develop/identify alternate materials for heavy-duty diesel engine exhaust manifolds and pistons that would enable improvements in the high-temperature capabilities of these components and facilitate improvements in break thermal efficiency (BTE) and power density.

Approach

- Evaluation of component design, materials, and manufacturing process for selected components with impact on engine BTE
- Evaluation of alternate materials, materials testing, and component design modification
- Prototype component fabrication and testing
- Wear testing of engine materials and coatings, including those related to pistons (reported in a separate task report, immediately following this report).

Accomplishments

- First prototype exhaust manifolds have been fabricated using new alloy- CF8C+
- Thermal properties of coatings have been measured.

Future Direction

- Performance of prototype exhaust manifold will be evaluated using engine testing
- Evaluate thermal-physical properties and reliability of new multi-material, substrate-coating combinations for pistons.

Introduction

This project with Cummins supports development of next generation heavy-duty diesel engines that can achieve a 50% or better BTE. The fuel efficiency roadmap for the 50% BTE engine considers six main areas for efficiency improvement in the baseline engine, several of which involve making more efficient use of thermal energy (i.e., heat) in the engine. Increased operating temperatures and improved thermal management are expected to enable significant increases in ***power density***, thus resulting in greater power output for the same sized engine or engine downsizing (or light weighting) for the same power output. However, it is becoming apparent that several key components will be exposed to temperatures beyond the capabilities of current engine and exhaust materials, requiring availability of the next generation of high-temperature materials to allow the engine to reach the efficiency, commercially viable durability, and emission targets. Because of different combinations of property requirements, new materials' technologies specific to the targeted engine components are needed to enable operation in the higher-temperature environment.

A detailed analysis of the development of the high-efficiency engine being envisioned by Cummins showed that a higher-temperature capability in the exhaust system has significant impact on technologies that improve BTE by waste heat recovery from exhaust gases. In addition, an increase in the temperature capability of piston materials also had a positive influence on the efficiency of the next generation diesel engines. Because current materials (i.e., high silicon molybdenum cast irons in exhaust manifolds and 4140 steel in pistons) are already operating near the limits of their temperature and strength capabilities, it has been determined that new materials with the right combination of properties are required for these components.

Replacement of current materials with materials having a higher strength and oxidation resistance at higher temperature also allows redesign of components to have thinner walls for the same stress levels, thus facilitating light-weighting and increased power density. It is anticipated that critical technologies (such as waste heat recovery) will not only demand the availability of improved materials to achieve the efficiency targets for the SuperTruck Program in short-term engine efficiency measurements, but will continue to drive development of advanced materials that would enable manufacture of a durable, commercially viable, high-thermal efficiency engine. Table 1 shows the key properties that were initially identified by the team to be of interest for the two components. These properties will be used for initial screening of new materials for this application and to define the initial test matrix.

Table 1. Components down selected and the critical materials properties of interest.

Component	Critical Material Properties of Interest
Exhaust Manifold	Constrained thermal fatigue strength, elevated temperature strength, high-temperature fatigue strength, creep strength, oxidation resistance, thermal expansion coefficient, specific heat, density, elastic modulus, thermal conductivity, microstructural stability at high temperatures, and the ability to be cast into complex shapes.
Piston	Constrained thermal fatigue strength, high-temperature strength, high-temperature fatigue strength, thermal conductivity, density, specific heat, and oxidation resistance.

Results

Exhaust Manifolds

Several new classes of materials were identified as alternatives to the high silicon molybdenum cast irons currently used in exhaust manifolds, including the following three major classes of materials:

– D5S-austenitic nodular cast iron

– Cast austenitic stainless steels (chromia-forming)

– Alumina-forming, cast austenitic stainless steels.

Table 2 shows some example candidates of cast austenitic stainless steels being considered for this application. The “ORNL” in parenthesis shows that a particular class of alloy was developed at ORNL.

Table 2. Compositions of cast austenitic stainless steel being evaluated for application in exhaust manifolds

Alloy	Type of Alloy	Fe	Cr	Ni	Mn	Mo	Nb	W	Si	C	Remarks
High Silicon Molybdenum Cast Iron	Nodular ferritic cast iron	Bal.			0.3	0.6			4.0	3.45	Baseline alloys
D5S	Nodular austenitic cast iron	Bal.	2	35	0.5				5	1.9	High-performance cast iron
Cast CF8C+ (ORNL)	Cast austenitic	Bal.	19	12.5	4.0	0.3	0.8	0	0.5	0.1	0.25N
TMA®4705 (ORNL) Typical	Cast austenitic	Bal.	26	23.5	0.6	0.47	0.35	0.28	1.33	0.6	Centrifugal casting data only
TMA®6301 (ORNL) Typical	Cast austenitic	Bal.	24	34.2	1.0	0.02	0.41	0.35	1.22	0.43	Centrifugal casting data only
Cast AFA (ORNL) Typical	Alumina-forming cast austenitic	Bal.	14	25	2	2	1	1	1	0.45	Vacuum casting data only, Al 3.5 C:0.2-0.5

Two major properties were considered key for prolonged exhaust manifold life: (1) resistance to constrained thermal fatigue and (2) oxidation resistance. Because an initial evaluation of their potential to perform adequately in an exhaust manifold application, constrained thermal fatigue tests and oxidation resistance were evaluated for the baseline high silicon molybdenum cast iron and other candidate alloys, including D5S, Cast CF8C+, TMA®4705, and TMA®6301. In addition, thermo-physical properties (such as thermal conductivity, thermal expansion coefficients, and elastic moduli) were evaluated for selected candidate alloys for incorporation into finite element models. Constrained thermal fatigue testing, oxidation testing, and cost factors were used to down select CF8C+ as the alloy for prototype exhaust manifold fabrication. Figure 1 shows an image of several sets of a two-piece exhaust manifold that were investment cast from stainless alloy CF8C-Plus and are currently being machined prior to engine testing on a marine engine platform at Cummins (which imposes more severe conditions than those of an on-road engine cycle).

Figure 1: Several pieces of a two-piece exhaust manifold have been cast from stainless alloy CF8C-Plus and are being machined in preparation for engine testing at Cummins.

Piston Materials

In previous work, decreasing the piston thermal conductivity was shown to increase the BTE by up to 1.3%. One method of decreasing the thermal conductivity of pistons is to coat the piston faces with a low thermal conductivity metallic alloy. In FY 2013, it was demonstrated that a 4140 steel substrate could be coated with a low-thermal conductivity coating. A 25% decrease in thermal diffusivity of the composite was observed at room temperature using an Alloy 625 coating on a 4140 substrate, with the effect of coating decreasing gradually with increasing temperature.

Figure 2 shows the thermal diffusivities of a free-standing (i.e., sprayed on graphite and removed), multi-layered, graded thermal barrier coating as a function of temperature and increased layering. Note that the thermal diffusivity has decreased to less than 25% with addition of increasing layers to the base coating (i.e., coating G versus coating J). It should be noted that additional layers were designed to have much lower thermal conductivities than the base layer. Effects of depositing these coatings on metallic substrates and the effects of cyclic oxidation testing at 600 and 800°C are now being evaluated. Figure 2 also shows a substantial change in thermal diffusivities after heating the coatings to a temperature of 800°C. Experiments show that such changes can be eliminated during further testing by annealing at 800°C.

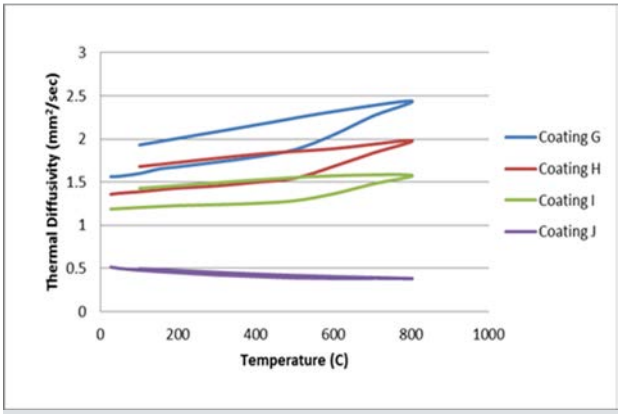

Figure 2: Effects of temperature on the thermal diffusivities of a free-standing multi-layered film with incremental layering.

Conclusions

Prototype exhaust manifolds have been fabricated using CF8C+ and will be engine tested.

The properties of free-standing, new, multi-layered composite coatings have been measured and shown to have significantly lower thermal diffusivities with an increasing number of layers. The effect of depositing these multi-layered coatings on a metallic matrix is currently being evaluated.

A task from this CRADA, evaluating wear of piston materials in a lightweight engine, is presented in the report on Agreement 23425b.

Project 18518 – Materials for High-Efficiency Engines

Agreement 23425b – Investigating and Addressing Wear in a Lightweight Diesel Engine

Jun Qu[1], Austin H. Shaw[1], Roger D. England[2], and Chinpei Wang[2]
[1]Oak Ridge National Laboratory
Materials Science and Technology Division
P.O. Box 2008, MS 6068, Building 4515
Oak Ridge, TN 37934
[2]Cummins, Inc., Technical Center

DOE Technology Manager: Jerry L. Gibbs
Phone: (202) 586-1182; fax: (202) 586-1600; e-mail: jerry.gibbs@ee.doe.gov

ORNL Technical Advisor: J. Allen Haynes
Phone: (865) 576-2894; fax: (865) 574-4913; e-mail: haynesa@ornl.gov

Contractor: Oak Ridge National Laboratory, Oak Ridge, Tennessee
Prime Contract No.: DE-AC05-00OR22725

Objectives

- To address the increasing peak-cylinder-pressure (PCP) and reduce parasitic frictional energy loss in heavy-duty diesel engines.
- This is a new FY 2015 task under the Lightweight Heavy-Duty Engines CRADA with Cummins; the remainder of which is described in the report for Agreement 23425a.

Approach

- Applying advanced surface engineering and/or lightweight alloys to critical engine-bearing components, such as piston skirt, crankshaft, connecting rod pin, and bushing.

Accomplishments

- It was discovered, to the surprise of all involved, that a production Grafal coating on a diesel piston skirt consistently increases the piston wear rate by 2 to 4 times in five different diesel engine oils.
- Results suggest that Ti-6Al-4V pistons may not survive without a proper surface treatment, but they perform well with ORNL-developed oxygen-diffusion (OD) case hardening.

Future Direction

- Investigate the friction and wear behavior of Cummins piston skirt coatings and their compatibility with conventional and new PC-11 (a and b) diesel engine oils.

– Continue studying the OD-Ti piston to identify the optimal OD treatment condition.

Introduction

Advanced coatings and lightweight materials are being investigated for heavy-duty diesel engines to address the increasing PCP and decreasing engine oil viscosity. Cummins has applied anti-friction/anti-wear coatings (such as graphite and magnesium phosphate on production components) and plans to extend to more components with other advanced coatings (such as diamond-like-carbon, CrN, and MoN). In addition, the feasibility of using titanium as a piston material is being investigated from a tribological perspective because titanium is prone to scuffing.

Results

Materials and Experimental

Production diesel engine piston and cylinder liners were supplied by Cummins (shown in Figure 1 [left]). The piston skirt surface came with a Grafal coating, which is a polymer-based system containing graphite particles. Samples were machined out of the piston and liner for tribological bench testing. Tests were conducted on a Plint TE-77 reciprocating sliding tribometer (shown in Figure 1 [right]).

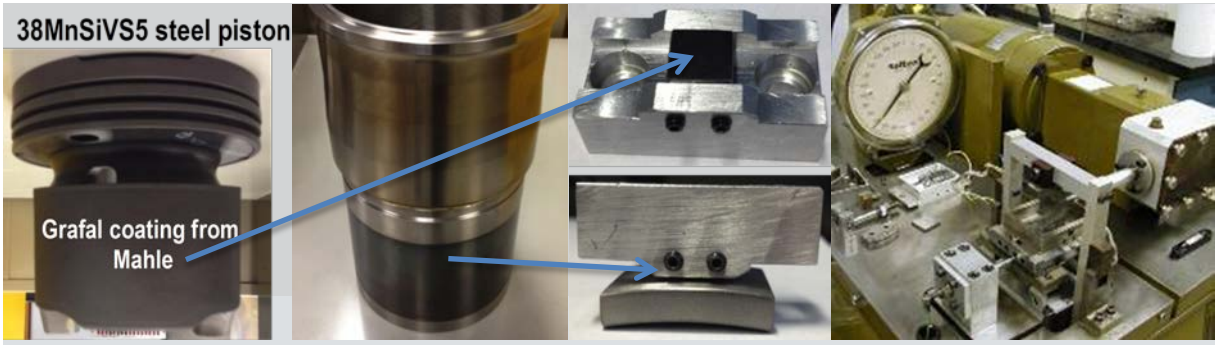

Figure 1: Production diesel engine piston, cylinder liner, and bench tribological testing of samples cut off a piston and liner. Test parameters: 240 N, 10 Hz with 10-mm stroke at 23, 100, and 150°C.

Based on contact mechanics analysis, the Hertzian contact stresses of the piston liner contact in an actual engine and bench tribo-tests are compared in Table 1. Because of the limited load capacity of the tribometer (i.e., 240 N), the cross piston skirt on the cylinder back surface (i.e., coating polished off) was selected to allow accelerated wear tests. The point contact also avoids the potential problem of misalignment.

Table 1. Hertzian contact stresses of the piston-liner contact in an actual engine and bench tribo-tests.

	Normal Load	Hertzian Contact Stress (MPa)	
In engine: piston skirt on cylinder liner (conformal contact)	0 to 25k	62.3 (maximum)	48.8 (mean)
Bench: piston skirt on cylinder liner (conformal contact)	240	13.4 (maximum)	10.5 (mean)
Bench: cross piston skirt on cylinder back (point contact)	240	398 (maximum)	265 (mean)

Wear Issue of Grafal Coating

A polymer-based piston skirt coating (i.e., Grafal) currently is used in commercial heavy-duty diesel engines for

reduction of friction, noise, and scuffing. However, this study discovered that the Grafal coating may actually increase wear loss, which is an unexpected result. Reciprocating sliding bench tests were performed on samples cut from a pair of actual diesel engine piston skirts and cylinder liners. Tests were conducted under boundary lubrication at 100°C in API CJ-4 (SAE 15W-40) and in candidate PC-11 (SAE 10W-30, 5W-30, and 5W-20) diesel engine oils. Results showed that although this polymer-graphite coating reduced the friction coefficient by about 10%, it consistently increased the wear rate of the steel piston substrate by two to four times in all of the oils tested. Results are summarized in Figures 2 and 3.

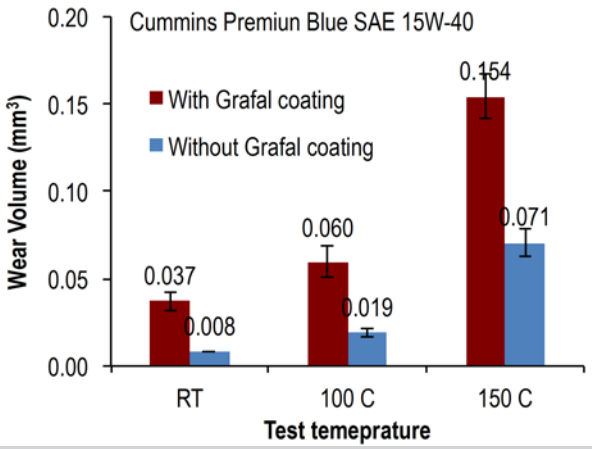

Figure 2: Wear volumes of steel piston skirt samples with and without the Grafal coating tested in Cummins Premium Blue SAE 15W-40 at various temperatures. The wear volumes on the piston samples with the Grafal coating were much higher than those of the piston samples after Grafal was polished off.

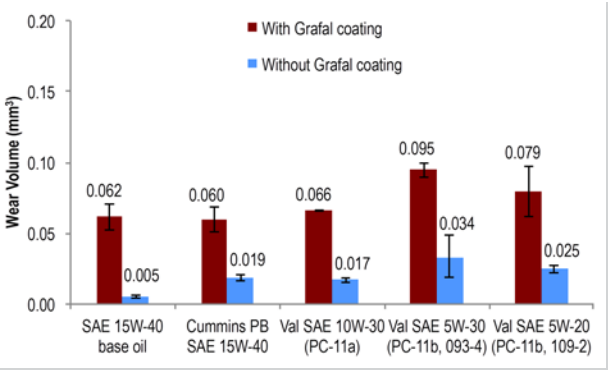

Figure 3: Wear volumes of steel piston skirt samples with and without Grafal coatings tested at 100°C in various oils. The wear volumes on the piston samples with the Grafal coating were much higher than those of the piston samples after Grafal was polished off.

Multiple hypotheses are proposed for this polymer-coating-induced high wear rate; the leading one is that wear debris from the polymer coating is adhesive in nature and traps the abrasive metallic wear debris at the interface to cause three-body abrasive wear. Characterization of the wear surface and debris analysis are planned to explore wear mechanisms.

Titanium Piston and Oxygen Diffusion Treatment

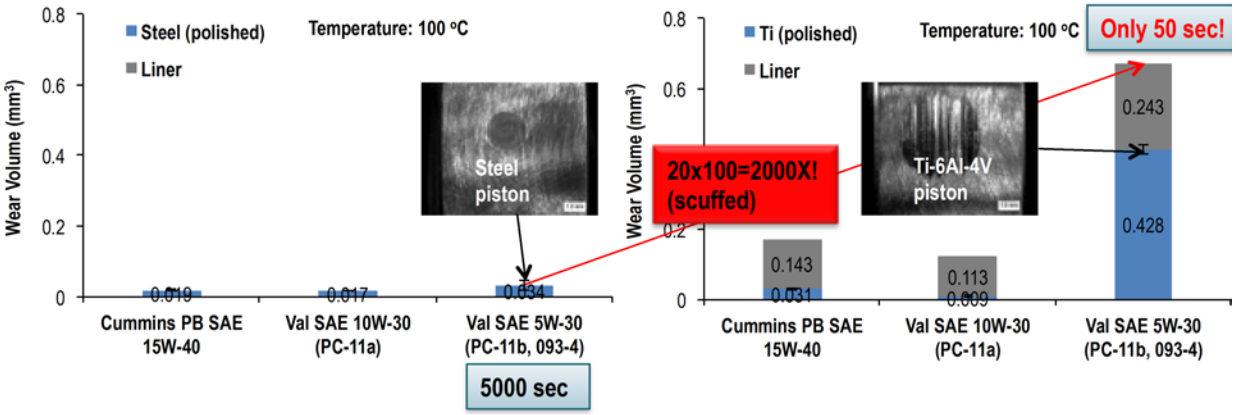

Figure 4: Wear volumes of steel and titanium samples tested at 100°C in various oils. Results suggest that the Ti-6Al-4V piston may substantially increase wear on the cast iron liner in all engine oils and would have a high risk of scuffing in a new PC-11b low-viscosity engine oil.

This study investigated the feasibility of using titanium as a piston material from a tribological perspective, because titanium is known to be prone to scuffing. In piston skirt-cylinder liner sliding bench tests, untreated Ti-6Al-4V piston samples showed localized scuffing surface damage in API CJ-4 (SAE 15W-40) and PC-11a (10W-30) diesel engine oils, but had major scuffing failure in PC-11b (5W-30) engine oil with significant material loss (i.e., a wear rate 2,000 times higher than a steel piston) (shown in Figure 4).Oxygen diffusion case hardening [J. Qu et al., 2009, *Scripta Materialia* 60: 886] was applied to the titanium samples at three different temperatures: 650, 750, and 850°C. Figure 5 shows the cross-sectional hardness profiles of the treated Ti-6Al-4V samples. It clearly shows that the higher temperature increases the depth of oxygen penetration. In addition to higher surface hardness, the OD treatment is known to enable the zinc dialkyldithiophosphates oil additive to form an anti-wear tribofilm on the titanium surface to reduce friction and wear. Additional advantages of OD treatment over other coatings or surface treatments include low cost and easy to apply with little part size and geometry restriction.

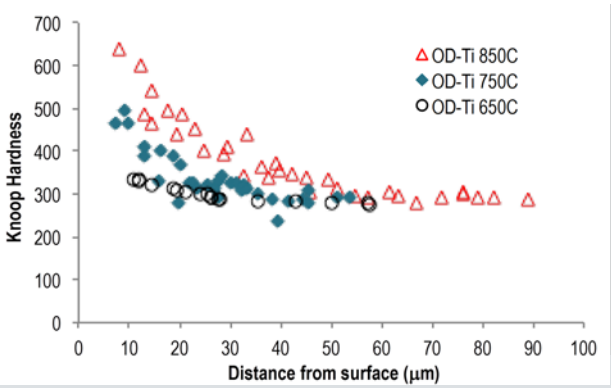

Figure 5: Cross-sectional hardness depth profile of OD-treated Ti-6Al-4V samples showing significantly increased surface hardness.

The OD-treated titanium samples exhibited excellent wear performance in both the conventional SAE 15W-40 and the new PC-11b low-viscosity engine oils (shown in Figure 6).

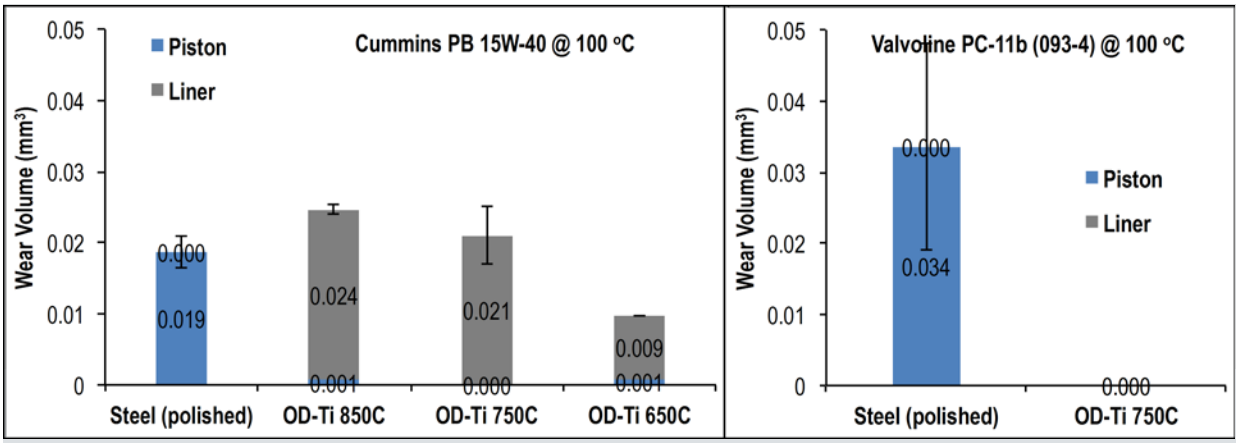

Figure 6: Wear volumes of steel and OD-treated Ti-6Al-4V samples tested at 100°C in various oils. Results suggest that OD-Ti possesses higher wear resistance than steel in the new PC-11b engine oil.

Conclusions

The production Grafal piston skirt coating was surprisingly found to cause increased piston wear in both conventional and new diesel engine oils. Investigation is ongoing to understand the wear mechanism. The friction and wear behavior of other Cummins candidate piston skirt coatings and their compatibility with diesel engine oils will be studied. Initial results suggest that an untreated Ti-6Al-4V piston may not survive in the new PC-11b low-viscosity diesel engine oil, but could perform well when treated with oxygen-diffusion. We will

continue studying the feasibility of OD-Ti diesel pistons.

Publications

Qu, J., A. H. Shaw, R. D. England, and C. Wang, 2016, "Effect of Anti-Friction Polymer Piston Skirt Coating on Wear Resistance in CJ-4 and PC-11 Diesel Engine Oils," to be presented at the *SAE 2016 World Congress*, April 12-14, 2016, Detroit, MI.

Qu, J., A. H. Shaw, R. D. England, and C. Wang, 2016, "Tribological Feasibility Study of Oxygen-Diffusion Case-Hardened Titanium Diesel Piston in CJ-4 and PC-11 Engine Oils," to be presented at the *STLE 71st Annual Meeting*, May 15-19, 2016, Las Vegas, NV.

Project 18518 – Materials for High-Efficiency Engines

Agreement 24034 – High Temperature Aluminum Alloys

Stan G. Pitman
Energy Materials Group
Pacific Northwest National Laboratory
P.O. Box 999, MS K2-03
Richland, WA 99352
Phone: (509) 371-6746; fax: (509) 375-4448; e-mail: stan.pitman@pnnl.gov

Howard Savage
Cummins, Inc.
Phone: (812) 377-5998; e-mail: howard.savage@cummins.com

DOE Technology Manager: Jerry L. Gibbs
Phone: (202) 586-1182; fax: (202) 586-1600; e-mail: jerry.gibbs@ee.doe.gov

Field Technical Manager: Yuri Hovanksi
Phone: (509) 395-3940; fax: (509)375-4448; e-mail: yuri.hovanski@pnnl.gov

Contractor: Pacific Northwest National Laboratory, Richland, Washington
Prime Contract No.: DE-AC05-76RL01830

Aluminum alloys that possess strengths approaching 300 MPa at 300°C have been produced in small quantities by numerous mechanical attrition methods. Although mechanical attrition can produce unique combinations of properties, mechanical attrition processing approaches have not been able to meet the requirements for low-cost, high-volume production. The purpose of this project is to demonstrate that mechanical attrition-type alloys can be produced with adequate high-temperature mechanical properties through development of a low-cost, high-volume, rapid solidification (RS) production process.

Mechanical attrition aluminum alloys with strengths approaching 300 MPa at 300°C have been produced by adding alloying elements with very low solubility and that form intermetallic dispersions (e.g., Fe, Ti, Cr, Mn, and Zr) in the aluminum matrix. Milling cycles can require hundreds of hours to adequately homogenize the alloy, which produces a large amount of oxide, limiting production and ductility, respectively. In the past, Pacific Northwest National Laboratory (PNNL) has worked with melt-spinning methods to produce alloys by RS using a process that produces a low surface area particulate (i.e., flake).

The RS flake can be consolidated by elevated temperature extrusion. This project intends to use the RS flake/extrusion process to produce an aluminum alloy with increased elevated temperature strength that can be used in diesel engine service environments up to 300°C.

Approach

High-Strength and High-Temperature Aluminum Alloy Development

Evaluate the feasibility of producing Al-Fe high-temperature alloys by two different RS methods: (1) melt spinning of flake and (2) rotating cup processing of powder particles. The two methods are known to have solidification rates that differ by several orders of magnitude, with the RS flake estimated at 10^7 degrees per second cooling rate and the rotating cup particle process at 10^4 degrees per second. The rotating cup RS method was being evaluated in spite of the lower solidification rate, because it is established as one of the high-volume RS processes and because the shot particulate has some advantages in handling and consolidation.

This evaluation has been completed and will be discussed in a subsequent section of this report. The primary objectives of this work focus on the following:

- Production of rapidly solidified alloy compositions using the PNNL pilot flake system. The PNNL flake melt spinning machine can produce limited quantities of experimental alloys in the form of rapidly solidified flake. The following subtasks were initiated after producing aluminum flake feedstock by melt spinning:
  - A comprehensive technology review of prior high-temperature and high-strength aluminum alloy development, including alloys developed by Allied Signal and academic institutions
  - Selection of three alloy compositions: two similar to the early Allied Signal Al-Fe-X compositions and the third the Al3Fe2Cr2Ti previously developed by mechanical attrition.

In addition to the primary objectives of this work, project milestones were identified as follows:

- Consolidate flake materials via extrusion using laboratory-scale extrusion tooling at PNNL. Rapidly solidified flake will be consolidated using the canning and indirect extrusion process previously developed by PNNL.
- Measure elevated temperature mechanical properties and compare to baseline materials. Elevated temperature tensile tests of sample materials will be conducted to establish temperature-strength behavior for the materials.
- Produce larger quantities of flake via Transmet (under subcontract to PNNL) using the production melt spinning system. The downselected alloy composition(s) will be made into master alloy feedstock and provided to Transmet for melt spinning into rapidly solidified feedstock. Quantities of several hundred pounds are anticipated, depending on the alloy systems selected.
- Consolidate the production flake by degassing, canning, and hot isostatic pressing, followed by extrusion. Larger billet diameters will be used and processing will simulate anticipated full-scale production methods.
- Test full-scale components using the appropriate test system at Cummins, Inc. Cummins, Inc. will select components that will benefit from the high-temperature aluminum properties and process the materials supplied by PNNL into full-scale test components.
- Perform engine testing at Cummins, Inc. if component test is successful. Established rig-testing will be conducted to establish performance and mass reduction benefits.

The primary deliverables from the project focused on the following:

- Development and production of high-temperature aluminum alloys by RS.

– Demonstration of successful scale-up of RS processing.

– Characterization of the RS alloys and baseline materials for room and elevated temperature strength.

Results and Discussion

Work on this project began in May 2011, conducted under a Cooperative Research and Development Agreement (CRADA) between Cummins, Inc. and PNNL. This effort has focused on identification of candidate aluminum alloy systems that can provide higher strengths (250-300 MPa) at elevated temperatures of approximately 300^{o}C. Highlights from the duration for the project are shown as well as additional studies performed this fiscal year.

A series of five alloy compositions were evaluated along with two different consolidation and extrusion processes. All alloys contain iron (Fe) as a key alloy addition along with smaller additions of silicon, Ti-Cr-V, and manganese. With the exception of silicon, alloy additions were chosen for their low solubility in aluminum and ability to form stable second-phase particles. Evaluated alloy compositions are listed in Table 1.

The first two alloys contain Si and V, while the aluminum-iron-chrome/titanium (AFCT) alloy contains a lower level of Fe, combined with higher weight percentages of Cr and Ti. The aluminum-iron-manganese (AFM) alloy was developed at PNNL in earlier work.

Table 1. Initial high-temperature, high-strength aluminum alloys.

Alloy Designation	Fe	Si	V	Cr	Ti	Mn
Al-12Fe	12.4	2.3	1.2			
Al-8.5Fe	8.5	1.7	1.3			
AFCT	6.0			3.4	3.2	
AFM-11	11.4	1.8	1.6			0.9
AFM-13	13.2	2.6	.50			0.9

The first three alloys have been previously produced in small quantities and tensile tested at a range of temperatures. Tensile strengths for these alloys at 300°C have been reported in the 250 to 300 MPa range, which is close to or meeting the property goals. Tensile test results of these materials were carried out at room and elevated temperature and are shown in Table 2.

Table 2. Room and elevated temperature tensile test results for candidate high-temperature extruded aluminum alloys.

Alloy Designation	Extrusion Temperature (°C)	Elastic Modulus (GPa)	Elastic Modulus (GPa) 300°C	Tensile Yield Strength (MPa)	Tensile Yield Strength (MPa) 300°C	Ultimate Tensile Strength (MPa)	Failure Strain (%)	Failure Strain (%) 300°C
Al-8.5Fe - EB	450	83.5	74.5	345.0	210.9	390.4	19.1	25.1
Al-8.5Fe - EB	500	84.2	76.6	331.2	208.2	389.4	18.0	21.7
Al-8.5Fe - HP	500	86.9	71.8	338.1	204.2	384.9	18.3	18.4
AFCT - HP	500	95.9	80.7	400.2	226.7	448.6	12.2	18.8
AFM-11-HP	500	96.0	91.1	427.8	256.8	493.6	7.2	17.0

EB = vacuum electron beam welded can without hot press; HP = vacuum hot pressed billet. Failure strains were measured using an extensometer. Notes: Yield strength and ultimate strength are the same at the 300°C test temperature. Extension at failure calculated from gage section measurements.

The processing steps that were selected for this project include: (1) induction melting to produce suitable feedstock alloys (of the approximate compositions found in Table 1), (2) analysis of actual compositions and melting characteristics, (3) induction re-melting of the alloys, and (4) production of RS material for subsequent processing.

Following production of the RS precursor material, a second focus of the project was development of laboratory-scale extrusion tooling to be used in consolidation and production of wrought extruded rod. Extruded rod from precursor material was then utilized to produce tensile specimens for room and elevated temperature (i.e., 300°C) tensile testing. Figure 1 shows an example of the melt spinning equipment, successfully produced RS flake material, and the consolidated and extruded rod material.

(a) (b) (c)

Figure 1: (a) Picture of the PNNL flake melt spinning machine with the front chamber removed. (b) Typical RS flake product produced with the melt spinning equipment. (c) Photograph of the canned RS flake billet (top) and the extruded rod.

Two processing approaches were developed for preparing the RS flake material for extrusion. The first approach involved cold (i.e., room temperature) pressing of the RS flake into an aluminum can, followed by weld-sealing the can under vacuum conditions. The sealed can was heated and extruded to the rod product using a 19:1 extrusion ratio. In the second approach, the canned flake was placed in a vacuum hot press at 450°C and pressed to pre-consolidate the RS flake to approximately 90% theoretical density. The canned and consolidated billet

was then extruded into the rod using the same 19:1 extrusion ratio. Figure 1 also shows an example of the canned billet (i.e., 50-mm diameter) and the resulting extruded rod (11.4-mm diameter).

Following extrusion of the RS flake materials, the extruded rods were cut into lengths and machined into round American Society for Testing and Materials subsized tensile specimens with a gage length of 25 mm and a gage diameter of 6.4 mm. Approximately 150 mm of the nose and tail of the extrusion were discarded to minimize non-uniform material. Machined tensile specimens were then tested at room temperature and at an elevated temperature of 300°C. A minimum of three tests were conducted at each temperature. Results of the tensile tests for the various aluminum alloys and heat-treated conditions are shown in Table 2.

The goal of this project was to approach a tensile strength of 300 MPa at a 300°C test temperature. As shown in Table 2, the AFM-11 alloy comes closest to meeting that goal. Based on initial results for the candidate alloys, further processing of the AFCT and AFM-11 alloys was initiated. These alloys were chosen because they showed the most pronounced increase in the measured elastic modulus of the tested materials. Initial characterization showed that all compositions exhibited refined grain size (i.e., less than 5µm), along with an extensive distribution of sub-micron secondary phase particles. Both the AL-8.5Fe and the AFM alloy have areas of larger, less dense secondary particles, indicating some phase growth during processing. Figure 2 shows low magnification micrographs of these three extruded aluminum alloys.

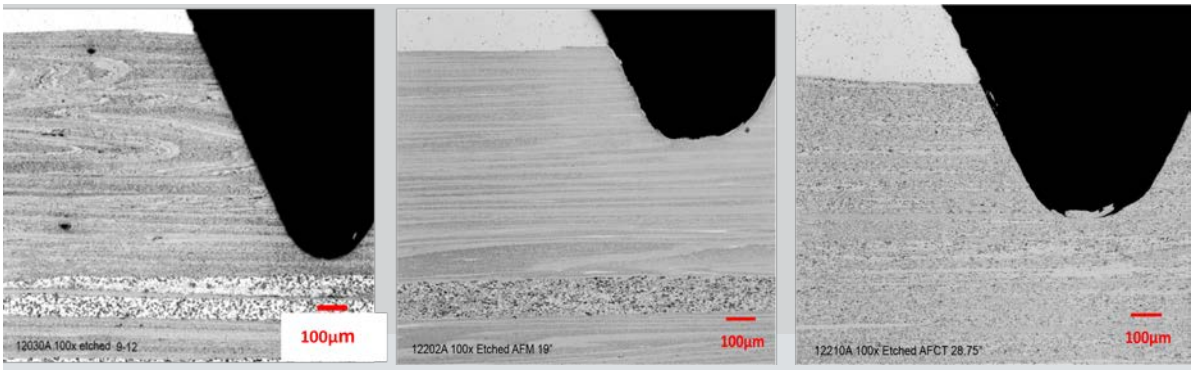

Figure 2: Low-magnification micrographs of extruded aluminum alloys (left) AL-8.5Fe, (center) AFM-11, and (right) AFCT. Specimens are from the thread ends of actual tensile specimens as indicated by the black thread contour. The white upper material is the 6061 aluminum can used for extrusion.

In addition to the elevated temperature strength goal, high-temperature (i.e., 300°C) fatigue life is an important material property for heavy-duty engine applications. To meet these project goals, two different processing techniques (i.e., melt spinning and rotating cup processing) were tested for their ability to elevate mechanical properties beyond that of the extruded values (Table 2). RS techniques are well known for their ability to improve mechanical properties such as wear resistance, thermal expansion, and high-temperature strength of microcrystalline aluminum. All of these are ideal properties for applications such as engine components

Discussion of Melt Spinning Relative to Rotating Cup Processing for Processing of Al-Fe High-Temperature Alloys

Processing of Al-Fe series high-temperature alloys was conducted by two different RS methods: melt spinning of flake and rotating cup processing of powder particles. The two methods are known to have solidification rates that differ by several orders of magnitude. Two high-temperature aluminum alloys (i.e., AFCT and AFM-11)

were processed by melt spinning and subsequently consolidated into billets and extruded to make a round rod product, as described previously.

The same two alloys were then processed by Transmet Corporation (Columbus, Ohio) using their rotating cup RS shot process. PNNL supplied induction-melted ingots of the two alloy compositions to Transmet, who then processed them into RS shot samples. After receiving the shot samples and performing optical metallography of the materials, the shot-processed alloys were canned, cold compacted, and consolidated using the same vacuum hot press parameters. Several consolidated billets were then extruded using the same temperatures and extrusion parameters utilized for the RS flake materials. As with the RS flake extrusions, a minimum of three tensile specimens were then tested at room temperature and 300°C to measure tensile properties of the RS shot materials. Tensile test results are summarized in Table 3.

Table 3. Tensile test results for extruded RS flake and rotating cup shot material alloys AFCT and AFM-11.

Alloy Designation	Test Temperature (°C)	Yield Strength (MPa)	Ultimate Tensile Strength (MPa)	Failure Strain (%)
AFCT flake	Room	400.2	448.6	12.2
AFCT shot	Room	169.0	215.3	4.9
AFM-11 flake	Room	427.8	493.6	7.2
AFM-11 shot	Room	287.0	411.2	1.8
AFCT flake	300°C	(1)	226.7	18.8
AFCT shot	300°C	(1)	91.8	2.9
AFM-11 flake	300°C	(1)	256.8	17.0
AFM-11 shot	300°C	(1)	185.6	5.8

Tensile test results show that the flake material has significantly higher tensile strengths when compared to the extruded shot material. The extruded flake materials also display relatively high elongations to failure, which would indicate good consolidation during extrusion and a stable, refined microstructure.

Because tensile data and optical microscopy indicated the AFM-11 alloy was the ideal candidate for optimization, detailed characterization of the flake and shot material of this alloy was conducted at various stages during processing.

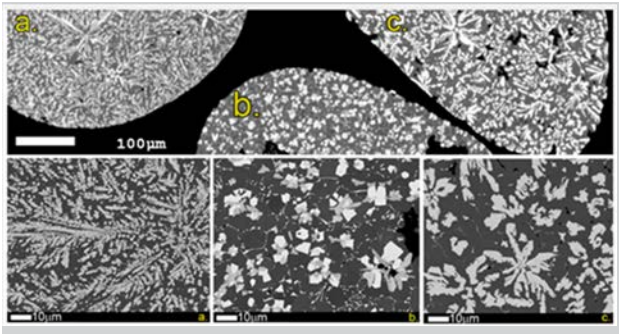

Figure 3: Microstructural features seen in the room temperature rotating cup processed shot material: (a) dendrites, (b) angular precipitates of two different compositions (possibly primary phases), and (c) rosettes.

Characterization of Rapid Solidification Shot Precursor

In the ‘as-solidified’ state, significant structural differences were observed between the rapidly solidified shot and flake material. This variation was expected due to the significant cooling rate differences between the two production methods. Both the melt spinning and rotating cup processing generated materials with a wide array of microstructures, differing primarily in length scale. As an example, secondary dendritic branching in the flake material was on the order of 0.10 to 0.25µm, whereas branching in the shot material was 0.5 to 1.0 µm. As seen in Figure 3, the shape of shot is similar to a water droplet with elongation in the direction of the centrifugal force. The larger microstructural features of the shot material can be easily understood due to the comparatively slower cooling rates associated with this processing method over the melt spinning technique.

Energy dispersive x-ray spectroscopy (EDS) data were collected from each of the different shot material morphologies. The matrix phase was identified to consist primarily of aluminum. Dispersed between the rosette structures in Figure 1c are areas of weak backscatter contrast that correspond to silicon enrichment. The composition of these regions is approximately 70 wt. % Al and 30 wt.% Si, identified by local area analysis of the EDS spectra.

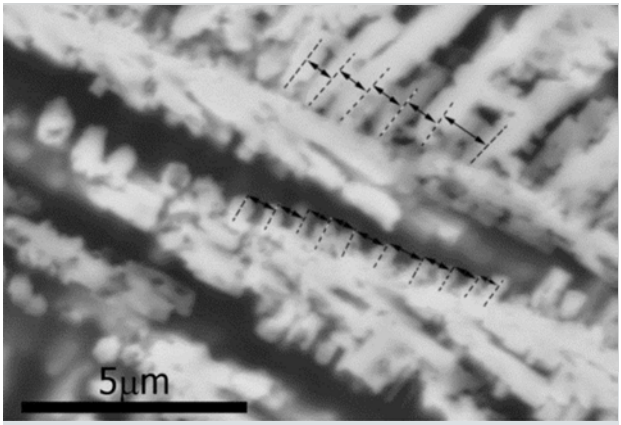

Figure 4: Electron backscatter image showing dendritic phase formed in the RS shot material. Secondary dendrite arm spacing is indicated.

Figure 4 shows secondary dendrite arm spacing that was measured and used to calculate an average spacing of 0.72µm ± 0.2µm. While the exact calculation of the cooling rate is dependent on diffusion coefficients and alloy composition, an approximation of the cooling rate for aluminum alloys based on dendritic arm spacing was shown in the work of Dobatkin et al. and indicates the cooling rate for the shot material is likely in the range 10^4-10^6 K/s

Characterization of Rapid Solidification Flake Precursor

A micrograph of the cross-section of an Al-Fe RS flake is shown in Figure 5. Nanocrystalline regions are present near the wheel side of the flake. The thickness of these nanocrystalline regions is variable and can be attributed to large thermal gradients and the surface variation (i.e., knurled pattern) on the spinning copper wheel.

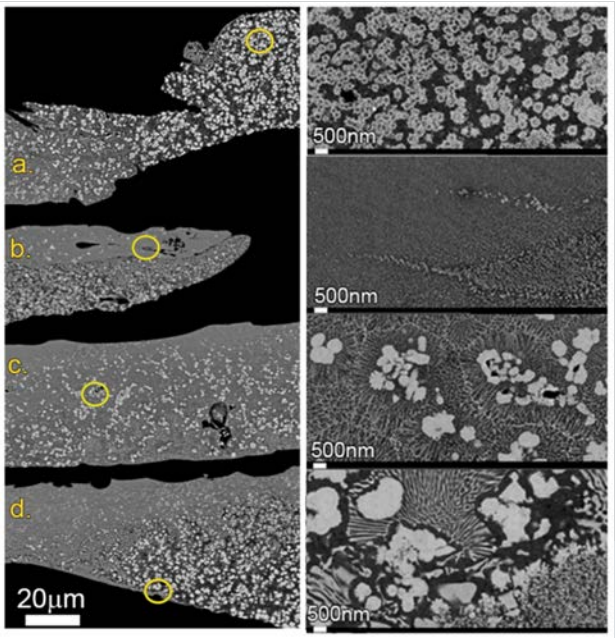

Figure 5: Microstructural variance in the room temperature flake material: (a) rings, (b) amorphous/nanocrystalline regions, (c) dendritic-cellular network, and (d) lamella/eutectic phase.

Aside from the nanocrystalline area, additional bright phases were also visible (Figure 5). EDS results indicated that these phases were iron rich. The visible increase of the formation of bright phases away from the wheel side of the flake is indicative of diffusion-

controlled growth and a cooling rate gradient through the thickness of the flake. Several other unique dispersed phases were identified in the AFM-11 material when viewed at elevated magnification, including ring structures, dendritic cellular networks, and eutectic/lamellar structures.

The distinct phase morphologies observed in the room temperature flake material were compared with variations seen in the shot material. Two key differences exist between the flake and shot microstructures: (1) the nanocrystalline or amorphous layer is not present in the shot material, and (2) the length scale of phases in the shot material is much larger than that of the flake.

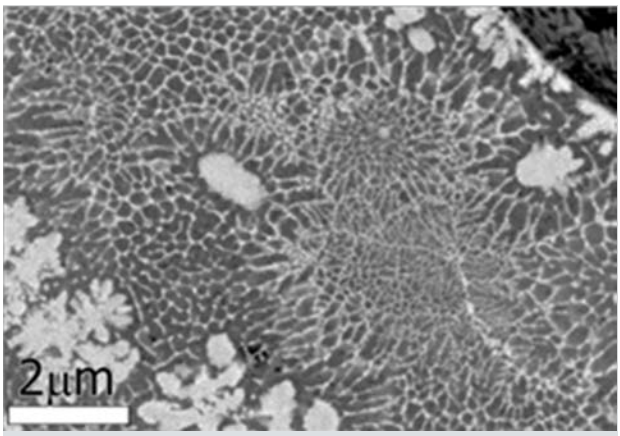

Figure 6: Low kV electron backscatter image showing dendritic phase formed in the RS flake material. Secondary dendrite arm spacing was measured and found to be 0.21 ± 0.06 μm.

The secondary dendrite arm spacing of the flake material was measured from several areas within Figure 6 and was found to be 0.21 ± 0.06 μm. This secondary dendrite arm spacing is indicative of a cooling rate between 10^7 to 10^9 K/s for the flake material, which is significantly faster than the dendrite morphology created using rotating cup atomization.

Mechanical Evaluation of Consolidated and Extruded Flake and Shot Material at Room and Elevated Temperature

Tensile test results of the consolidated and extruded rapidly solidified material are shown in Table 4. The failure extension is a measure of the crosshead displacement at failure. All values shown are the average of three tests performed for each condition. As expected, the more refined microstructure of the flake material resulted in dramatic increases in both the yield and ultimate tensile strength when compared to the shot material. The yield strength of the extruded flake material was in excess of 275 MPa at 300°C. Room temperature tests of the extruded flake material exhibited a 544.2-MPa yield strength. An additional processing condition (i.e., a forging step following the initial consolidation and extrusion) was also tested to evaluate thermal stability at temperatures significantly above 300°C.

Table 4. Tensile results summary of AFM-11 flake and shot material.

Alloy Designation	Condition	Test Temperature (°C)	Yield Strength (MPa)	Ultimate Tensile Strength (MPa)	Failure Extension (%)
AFM-11 shot	Extruded	Room	287.0	411.2	1.8
AFM-11 shot	Extruded	300°C	185.6	185.6	5.8
AFM-11 flake	Extruded	Room	544.2	544.2	3.6
AFM-11 flake	Extruded	300°C	278.4	298.0	6.1
AFM-11 flake	Extruded + Forged	Room	351.3	360.7	2.7
AFM-11 flake	Extruded + Forged	300°C	200.0	202.7	2.1

Engineering stress versus strain plots were generated to illustrate the effects of temperature and forging on the higher-strength flake material (see Figure 7). The plotted data show a representative stress versus strain curve for each condition. Elevated temperature testing and an additional forging step during processing resulted in lower yield strength. The added forging step also resulted in lower ductility at high temperature.

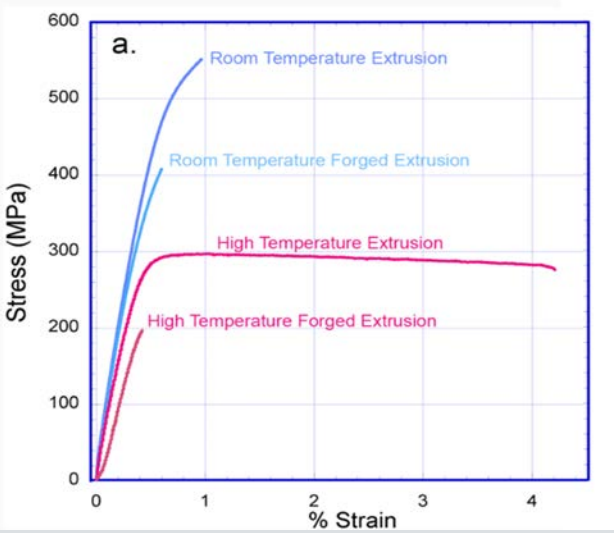

Figure 7: Engineering stress versus strain plot for the RS aluminum flake material.

Across all samples, it is evident the 300°C test temperature resulted in a reduction in material strength. Strength reduction at elevated temperature is anticipated because dislocation climb and glide become active deformation mechanisms in high-temperature regimes. As a result, the generally observed trend should be a decrease in strength and an increase in ductility during high-temperature testing. In the case of the extruded material, this expected trend is clearly visible. The strain to failure is significantly larger in the high-temperature extrusion compared to the room temperature extrusion. Deviation from the expected trend (i.e., depressed ductility at high temperature) was seen in the forged extrusions. Experimental data shown for the high-temperature forged extrusion are typical of all the tests on that material. Ductility did not increase during high-temperature testing in specimens that underwent the added forging step. This lack of increased ductility was identified as microstructural coarsening, which was observed in the forged specimens (see Figure 8).

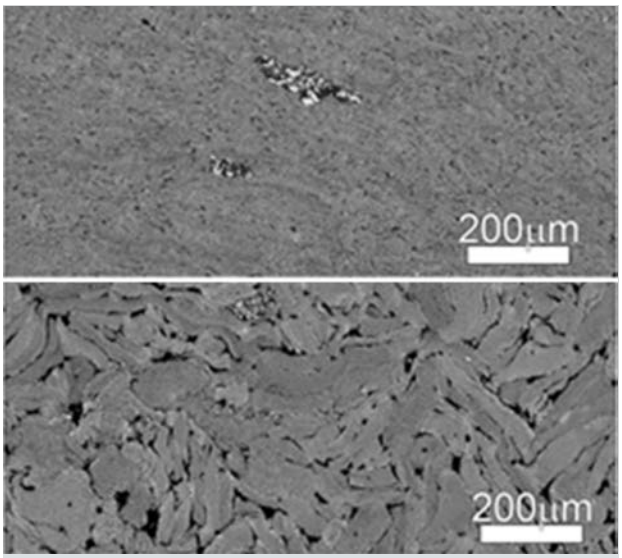

Figure 8: Polished cross-sections showing microstructural coarsening of high-temperature forged extrusions (bottom) compared to extruded material (top).

Additional forged extrusions, performed at a lower temperature (i.e., 450°C) were tested in contrast to the initial 480°C forging in an attempt to reduce microstructural coarsening. These extrusions also exhibited lower ultimate tensile strengths than the non-forged material. Ultimate tensile strength was measured at 328 ±14.2MPa at room temperature and 248.6 ±17 MPa at 300°C.

Technology Transfer and Conclusions

By participating in this CRADA, Cummins, Inc. will benefit by applying new technology to improve the high-temperature performance and life of engine combustion components, air-handling systems, and emission-control components. In addition, Cummins, Inc. benefits by coupling its own engineering production experience and know-how with scientific expertise and technical capabilities of PNNL staff and U.S. Department of Energy

(DOE) laboratories to solve relevant problems that benefit industry and achieve DOE fuel economy goals.

This project has evaluated potential high-temperature, high-strength aluminum alloy systems that can be produced by RS and subsequently processed via extrusion. A group of five candidate alloys were selected for processing and characterization. Feedstock melting methods were developed, which resulted in production of the AFM-11 alloy that has a tensile strength exceeding the target value of 250 MPa. Work has focused on developing a more detailed understanding of the microstructural evolution of the AFM-11 alloy during processing and to identify potential scale-up issues. One potential issue (i.e., additional forging following extrusion) was shown to result in microstructural degradation.

Project 18518 – Materials for High-Efficiency Engines

Agreement 26190 – High Temperature Materials for High Efficiency Engines

G. Muralidharan and B. Pint
Materials Science and Technology Division
Oak Ridge National Laboratory
1 Bethel Valley Road
Oak Ridge, TN 378313
Phone: (865) 574-4281; fax: (865) 574-4357; e-mail: muralidhargn@ornl.gov

DOE Technology Manager: Jerry L. Gibbs
Phone: (202) 586-1182; fax: (202) 586-1600; e-mail: jerry.gibbs@ee.doe.gov

ORNL Technical Advisor: J. Allen Haynes
Phone: (865) 576-2894; fax: (865) 574-4913; e-mail: haynesa@ornl.gov

Contractor: Oak Ridge National Laboratory, Oak Ridge, Tennessee
Prime Contract No.: DE-AC05-00OR22725

Objectives

- Identify and catalog the materials property requirements for exhaust valves in next generation high-efficiency engines.
- Evaluate mechanical properties and oxidation resistance of leading existing nickel-based alloy candidates and alternate materials with the capability to operate at 950ºC.
- Adopt Integrated Computational Materials Engineering (ICME)-based techniques to develop alternate lower-cost nickel-based alloys for exhaust valve applications at temperatures up to 950ºC.

Approach

- Mechanical property requirements for operation at 950ºC will be defined and the microstructure required to achieve these properties will be identified.
- Oxidation tests will be performed to understand composition effects on oxidation behavior and establish the limits of critical elements.
- A synergistic computational modeling and experimental evaluation approach followed in the design of new alloys for exhaust valve applications up to 870ºC in a previous project will be refined and used to identify promising compositions for service at 950ºC.
- Trial heats of new compositions will be prepared, properties measured, and compositions refined in an iterative manner.

Accomplishments

- New alloys with better high-temperature strength than Alloy 751 at 950°C have been designed.
- Two patent applications have been filed.
- The feasibility of transferring technology to industry has been demonstrated.

Future Direction

- Evaluate alloying element additions and strategies to improve high-temperature oxidation resistance.

Introduction

Improving the engine efficiencies of passenger and commercial vehicles is a major goal of VTO and propulsion materials play a significant role in achieving this objective. One of the important strategies for achieving the goals of improving engine thermal efficiency is by advancing technologies that increase engine combustion efficiency such as lean-burn operation (high-efficiency clean combustion), high levels of exhaust gas recirculation, turbocharging, variable valve actuation, and/or variable compression ratios. One of the barriers to achieving increased efficiency is the need to simultaneously reduce pollutant formation, which is achievable through high-efficiency combustion technologies. One potential method to achieving improved engine efficiency while reducing emissions is through retaining more heat in the exhaust gas.

Strategies for retaining more heat in the exhaust naturally result in increased exhaust gas temperatures, thus increasing the operational temperature requirements of components in the exhaust gas path, particularly exhaust valves. It has been projected that exhaust gas temperatures would increase from a current value of 760ºC to values of at least 870ºC and very likely reaching as high as 1000ºC in the long-term. Availability of materials with adequate high-temperature mechanical properties and oxidation resistance to enable the projected engine operating parameters without exceeding the cost constraints is a barrier to adoption of new high-efficiency technologies. The objective of this project is to address the needs of cost-effective materials for exhaust valves for operation up to 950ºC.

A recently concluded project successfully addressed development of new lower cost alloys for use in exhaust valves at temperatures up to 870ºC through a "materials-by-design" approach. "Materials-by-design" is a concept that encompasses a collection of materials-related techniques, including modeling, correlation, and materials modification. The premise behind materials-by-design is that mechanical properties are correlated to microstructure and phase chemistry. The phase composition and microstructure can be achieved through thermodynamic equilibrium or through non-equilibrium techniques such as quenching, rapid casting solidification, or mechanical working. These characteristics can then be correlated to desired mechanical properties through computational equilibrium thermodynamics or through a variety of correlation techniques.

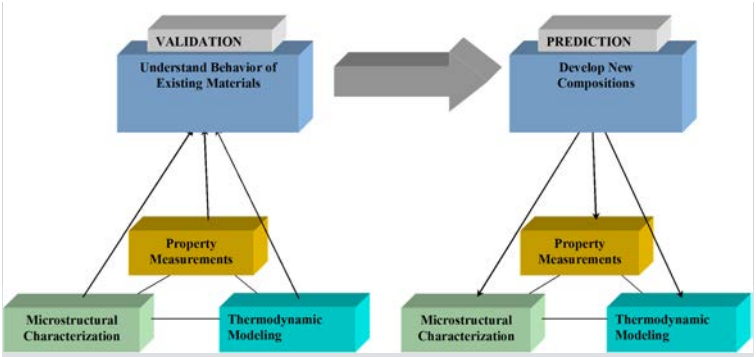

Figure 1: Overall approach for materials-by-design.

The correlations allow untested compositions or treatments to be computationally modeled; therefore, the desired trends can be rapidly established. Small heats of targeted materials can be processed to confirm the modeled properties and to broaden the correlation database. Figure 1 captures the concepts in this approach.

Exhaust valves currently used at temperatures up to about 760ºC are fabricated using nickel-based alloys (such as Alloy 751). Other higher-performance nickel-based alloys primarily developed for aerospace applications have the potential to operate at temperatures of 950ºC with desired strength and oxidation resistance; however, they may be expensive for automotive applications or very difficult to form. Therefore, new alloys with appropriate strength, oxidation resistance, and formability may have to be specifically developed for the operating characteristics and lifetime expectations for automotive valves.

In an earlier study on automotive valves for performance at 870ºC, a "materials-by-design" approach consisting of synergistic computational and experimental aspects was used to develop cost-effective nickel-based alloys for use at this temperature. High-temperature fatigue strength was identified as a critical factor in determining the performance of these alloys in the valve application. An understanding of the strengthening mechanisms in existing commercial alloys was required to use the computational modeling approach for developing materials with improved properties and lower cost. A range of nickel-based alloys with potentially varying weight fractions (or volume fractions) of γ' were identified in efforts to correlate the fatigue properties with the microstructure of the alloys. The selection of nine commercial nickel-based alloys included Alloy 751, Waspaloy, Udimet 520, and Udimet 720. The Ni+Co contents ranged from 66 to 76 wt. %. To obtain initial information on the microstructures of these alloys at equilibrium, thermodynamic calculations were carried out.

Comparison of the calculation results showed that all alloys have a matrix of γ with the major strengthening phase as γ'. One or more carbide phases (such as $M_{23}C_6$, MC, and M_7C_3) may also be present in different alloys. The primary difference between the microstructures of the various alloys was the weight percent of the γ' phase at a given temperature and the highest temperature at which the γ' phase is stable in the different alloys. Because the size of the strengthening precipitates is also critical, it was anticipated that the coarsening kinetics of this phase would also be influential in the long-term performance of the alloys in this application.

Using the microstructures of these alloys as a guide, computational thermodynamics was used to design new alloys with a microstructure similar to the commercial alloys in an effort to obtain materials with desirable properties. In contrast to the commercially available alloys with Ni+Co contents greater than 66 wt%, the Ni+Co content in these newly identified candidate alloys was lower than 50 wt.% (nickel being replaced with other elements such as iron) with the potential to achieve comparable properties. The lower nickel content implies that the alloys would be of lower cost with the potential to achieve targeted fatigue life.

Based on the results of this computational alloy design process, small batches of the new lower-nickel candidate alloys were cast. The alloys were then homogenized and rolled at high temperatures. Small tensile specimens were machined from these alloys and tensile tests were conducted in-situ at 870^{o}C. Based on the results of the tensile tests, several of the candidate alloys from the newly developed suite of promising compositions with Ni+Co contents lower than 50 wt% were down-selected for the preparation of larger-sized heats. These were cast under inert gas cover and then mechanically processed into plates for further machining. High-temperature fatigue tests were performed on the down-selected alloys. New alloys with fatigue lives of 100 million cycles at stresses of 25 to 30 Ksi at 870^{o}C were identified and two invention disclosure have been filed.

The purpose of this project is to extend this successful approach to the identification/development of materials for exhaust valves that could operate at temperatures up to 950ºC. In addition to high-temperature mechanical properties (i.e., creep and fatigue), oxidation resistance is expected to play a role in determining the lifetime of exhaust valves at higher temperatures and will be considered in the identification/development of new materials for exhaust valves. As part of this project, the required materials properties will be identified, baseline material properties will be evaluated, and the development of new materials will be targeted to achieve required properties at low cost. Initial work will be focused on nickel-based alloys; however, if properties and cost targets cannot be met, intermetallics will be considered as an alternate option.

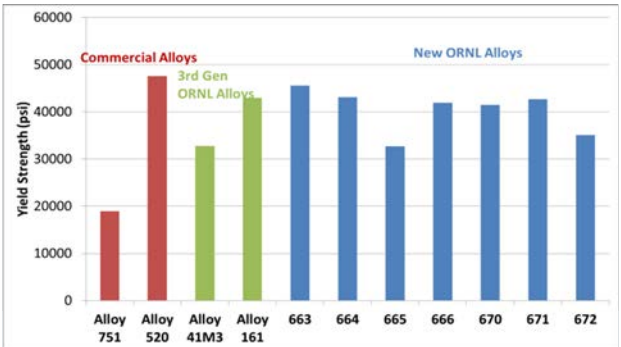

Figure 2: Yield strength of commercial Alloys 751, 520, and ORNL developmental alloys at 950°C.

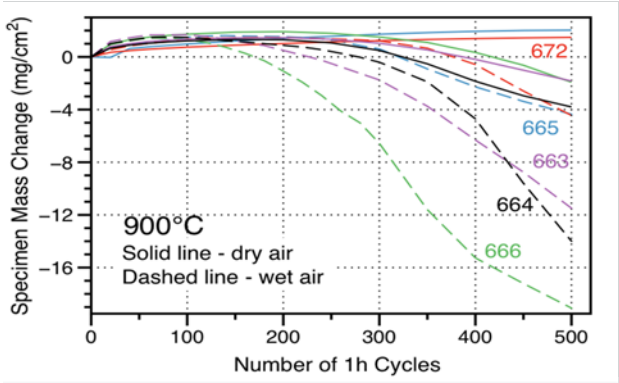

Figure 3: Specific mass change (i.e., mass change/unit area) at 900°C measured and compared in several new developmental alloys in air and an in air+10% water vapor environment.

Results

In an effort to understand the mechanical properties and oxidation resistance of candidate nickel-based alloys, high-temperature tensile testing and oxidation testing was performed on newly developed nickel-based alloys. Figure 2 shows the yield strength at 950°C of several Ni-Fe-based alloys. Note that the yield strengths of the ORNL alloys are much better than Alloy 751 and are almost comparable to that of Alloy 520 at 950°C.

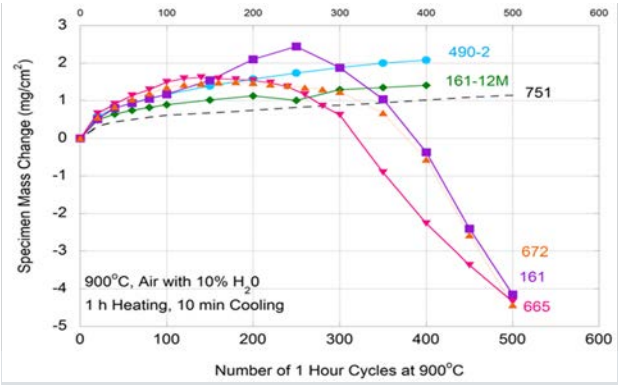

Figure 4: Comparison of the oxidation behavior of new alloys designed for improved oxidation resistance with that of previous generations of ORNL alloys.

Figure 3 shows the specific mass change for the laboratory-scale developmental alloys (from Figure 2) at 900°C in air and an air + 10% water vapor environment. It can be observed from Figures 2 and 3 that the alloys that show higher strength typically show lower oxidation resistance at 900°C. This is related to the alloying element additions required to increase the strengthening phase fractions. Thus, there is an increasing need to determine alloying strategies that improve strength without jeopardizing oxidation resistance. Figure 3 also illustrates the detrimental effect of water vapor (present in the combustion exhaust stream) on oxidation resistance of these chromia-forming alloys, with the effect most evident in Alloys 672 and 665.

Figure 4 shows the effect of alloying elements on improving the oxidation performance of Alloys 490-2 and

161-12M specifically designed to improve oxidation resistance. Note that their oxidation behavior has been significantly improved over Alloys 672, 161, and 665. Further work is ongoing to understand the high-temperature mechanical behavior of these alloys.

Figure 5 shows a comparison of the yield strengths of two ORNL alloy compositions fabricated by Carpenter Technologies with that of Alloy 751 at 870°C. Note that the new alloys have improved yield strength over Alloy 751, but they can be obtained at much lower cost due to reduced Ni and Co. Two patent applications have been filed on these newly developed ORNL alloys.

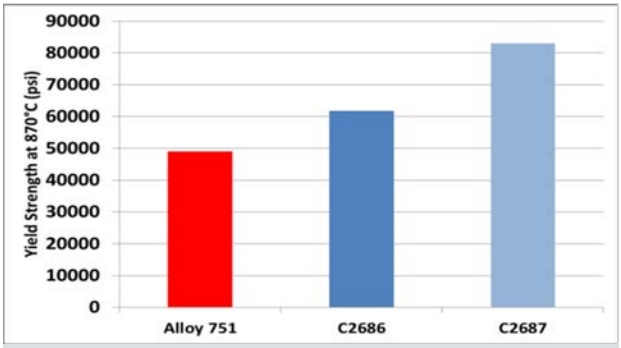

Figure 5: Yield strengths of two ORNL alloys fabricated in a commercial-scale batch by Carpenter Technologies (C2686 and C2687) compared with that of Alloy 751.

Conclusions

Development of exhaust valve materials for use at temperatures up to 950°C requires balancing oxidation resistance with high-temperature mechanical properties. New alloys with yield strengths greater than that of Alloy 751 and approaching that of Alloy 520 at 950°C have been designed. Initial results showed that the oxidation performance of this class of lower-nickel, higher-strength alloys need improvement. A new generation of alloys with improved oxidation resistance has been designed and fabricated at the laboratory scale. Further efforts to balance oxidation resistance with high-temperature mechanical properties are in progress. Initial experiments with two ORNL-developed alloy compositions show the feasibility of achieving desired properties in industrial-scale alloys of composition similar to those of alloys fabricated in laboratory scale.

Project 18519 – Materials for Exhaust and Energy Recovery

Agreement 10461 – Durability of Diesel Particulate Filters (CRADA with Cummins Inc.)

Thomas R. Watkins, Amit Shyam, and Ryan Cooper
Oak Ridge National Laboratory
P.O. Box 2008, MS 6064
Oak Ridge, TN 37831-6064
Phone: (865) 387-6472; fax: (865) 574-3940; e-mail: watkinstr@ornl.gov

Randall J. Stafford
Cummins, Inc.
1900 McKinley Avenue, MC 50183
Columbus, IN 47201
Phone: (812) 377-3279; fax: (812) 377-7050; e-mail: randy.j.safford@cummins.com

DOE Technology Manager: Jerry L. Gibbs
Phone: (202) 586-1182; fax: (202) 586-1600; e-mail: jerry.gibbs@ee.doe.gov

ORNL Technical Advisor: J. Allen Haynes
Phone: (865) 576-2894; fax: (865) 574-4913; e-mail: haynesa@ornl.gov

Contractor: Oak Ridge National Laboratory, Oak Ridge, Tennessee
Prime Contract No.: DE-AC05-00OR22725

Objectives

- To identify and implement test techniques for characterizing the physical and mechanical properties of ceramic substrates used as diesel particulate filters (DPFs)
- To identify the mechanisms responsible for progressive thermo-mechanical degradation and resultant fracture of DPFs
- To develop analyses and provide data for simulation tools for predicting the long-term reliability and durability for DPFs under engine operating conditions.

Approach

- Application of advanced characterization techniques to DPF ceramic substrates.
- Refinement of DPF service lifetime prediction models based on characterization of filter materials.

Accomplishments

- Determined the origin/mechanism of increased fracture toughness with temperature observed in the silicon-carbide-based DPF material.
- Initiated model development and new testing methodologies for fracture toughness/fracture energy of DPF honeycomb structures.
- Initiated studies on the effects of machining on the mechanical properties of cordierite DPFs.

Future Direction

- Conduct fracture toughness measurements on a cordierite honeycomb structure.
- Initiate a study of fracture toughness anisotropy on a cordierite honeycomb structure.

Introduction

The Environmental Protection Agency regulates the emissions of NO_x and PM from diesel engines. Stringent regulation on PM went into effect in 2007. There are many technologies designed to reduce emissions from diesel engines; prominent among the technologies for PM control are DPFs. A DPF often is a ceramic device that collects particulate matter in the exhaust stream. The high-temperature nature of the ceramic withstands the heat of the exhaust and allows heating to break down (or oxidize) the particles inside. DPFs reduce emissions of PM, hydrocarbons, and CO by 60 to 90%.

Most DPFs consist of a ceramic honeycomb with hundreds of cell passages partitioned by walls (Figure 1). Each cell passage has a square cell opening at one end and a plug at the other end; therefore, the cell passages are alternately closed at each end. The so-called checkerboard plugging structure forces the exhaust gases through the porous, thin ceramic honeycomb walls. When the gases carrying the PM flow through the fine pores of the walls, the PM is filtered out. High porosity values, in the range of 40 to 70%, heighten filtration efficiency to more than 90% and reduce gas-flow resistance (i.e., back pressure) for better engine performance.

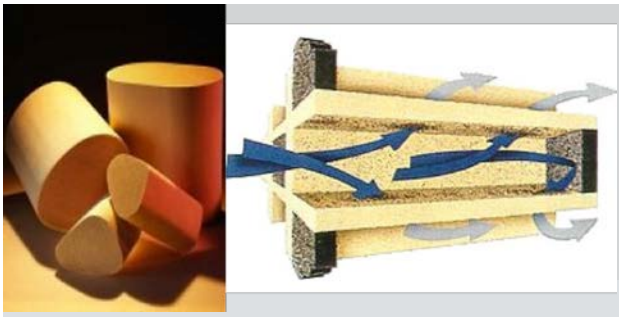

Figure 1: (top) Image of cordierite-based DPFs; (bottom) schematic of exhaust flow through a DPF.

The process of diesel PM collection is continuous while the engine is operating. The particles are collected on the ceramic walls and, as a result, the back pressure of the system increases. The back pressure is reduced by oxidizing the trapped PM, aided by a catalytic reaction using exhaust gas heat at 400°C or more, into CO_2 and water vapor. This process, called regeneration, results in a cleaner filter. The regeneration process is dependent on exhaust temperature, oxygen, NO_x content, time, and PM levels.

The key to successful application of DPFs is to reliably regenerate the filter (e.g., to oxidize/remove the PM the filter continues to trap or collect). Traditionally, combustion of soot is done in an oxygen atmosphere (i.e., air). In air, the soot will oxidize at about 500°C and up. However, this is not a typical operating temperature for a diesel engine exhaust stream. Therefore, to oxidize soot in air, an active system (i.e., one that increases the

temperature of the exhaust using some external heat source) is required. However, if an active system is not carefully controlled, or if too much PM collects on the filter walls, the filters can experience an "uncontrolled regeneration," wherein the temperature increases to 600°C or more, resulting in damage to the filter element.

The objectives of this project are to identify and implement test techniques to characterize the physical and mechanical properties of ceramic substrates used as DPFs, to understand the mechanisms responsible for the progressive thermo-mechanical degradation and resultant fracture of DPFs, and to develop analyses and provide data for simulation tools for predicting the long-term reliability and durability for DPFs under engine operating conditions, particularly through the regeneration cycle.

Goals, Barriers, Relevance, and Integration[1]

This work is in the study area of VTO's Propulsion Materials Program and addresses the goal of: "By 2015, develop materials that reduce the fuel economy penalty of particle filter regeneration by at least 25% relative to the 2008 baseline." This project addresses three of the barriers associated with propulsion materials: (1) changing internal combustion engine combustion regimes, (2) long lead times for materials commercialization, and (3) cost. It also addresses four barriers within advanced combustion engine, R&D-combustion, and emission control R&D: (1) lack of cost-effective emission control, (2) lack of modeling capability for combustion and emission control, (3) durability, and (4) cost. This project is relevant to the goal and barriers because the thrust is to characterize the material properties and improve the durability and lifetime prediction, resulting in the lowest overall cost, while preventing emission release in service. This is achieved by understanding the relationships of the material properties for the filter substrates by characterizing the porosity, strength, elastic modulus, thermal expansion, and so forth leading to improved regeneration strategies and fuel efficiency. This work supports clean diesel, which increases acceptance by the public. Larger acceptance, in turn, results in larger percentages of conversion to diesel, with the resulting reduction in petroleum usage/dependency on foreign oil.[2,3] This project is integrated within VTO because DPF substrate materials are used in both DPF and catalyst systems and because it utilizes many of the characterization tools acquired and formerly maintained by the High-Temperature Materials Laboratory Program.

Approach

The design process for making DPFs that are durable and reliable includes a complex materials property optimization and selection process.[4] For example, the porosity of DPFs, which allows the removal of PM from the exhaust gas stream, has a deleterious effect on their mechanical and fracture strength. However, a higher porosity decreases the engine back pressure and increases efficiency of the diesel engine. Designing mechanically reliable DPFs is important because these components will experience demanding thermos-mechanical conditions during service. These include, for example, thermal shock resulting from rapid heating/cooling and thermal stresses that arise from temperature gradients.

Techniques for assessing the elastic and fracture properties of virgin or unexposed DPF substrates have been identified, implemented, and reported earlier.[5] Test techniques were applied to rank the suitability of common candidate substrates for application in DPFs. The developed test techniques were applied to characterize DPFs returned from field service. The material properties responsible for thermal shock resistance and mechanical property degradation in the various stages of the bathtub curve were determined. These properties include thermal expansion, thermal conductivity, heat capacity, density, porosity, elastic properties, strength, fracture

toughness, and environmentally assisted crack growth at ambient and elevated temperatures in air and in relevant environments.

The information generated has, in turn, been input into predictive models. These service life predictions are based on a combination of experimentally determined strength data, stress analyses of the component using a finite-element analysis, and selection of appropriate failure criteria. The durability (i.e., service life) of the component can also be predicted using this framework by considering the elastic behavior as a function of load.

Results

Work was discontinued on a fourth alternate substrate material (i.e., a zeolite) because this material is no longer a viable alternative. Limited strength and single-edge notched beam fracture toughness testing was completed before cessation, but will not be reported here. This milestone was replaced with one related to earlier work on the in situ fracture toughness of the silicon-carbide–based material, which showed an increase in toughness with in situ testing temperature.[5] The mechanism for this increase needs to be determined and was speculated to be related to the softening of free silicon.

Transmission electron microscope (TEM) and SEM studies were conducted to observe evidence of plastic deformation in the form of dislocations and relative grain displacements, respectively. Figure 2 displays dislocations that are present near the fracture surface of a double torsion sample that was tested at 900°C. These dislocations provide some evidence that the observed increasing toughening behavior as a function of testing temperature was due to plastic deformation occurring within the silicon nodules.

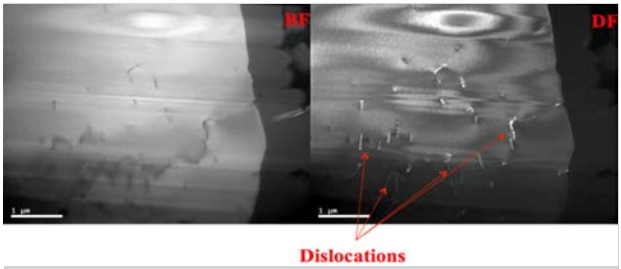

Figure 2: Bright field and dark field images of a region of free silicon within a silicon-carbide sample that was tested at 900°C to measure fracture toughness. The selected region is near the fracture surface.

SEM, coupled with static deformation studies, was conducted in order to observe relative grain movement. These relative grain movements were not observed, leading to the conclusion that most of the increase in toughness is related to the oxide layer or crust that forms with time at temperature in ambient atmosphere.[5] The oxidation forms a SiO_2 layer, which seals, fills, alters, and/or joins cracks and rounds pores present in the as-received silicon-carbide DPF components, thus resulting in the increase in fracture strength/fracture toughness measured previously.[5]

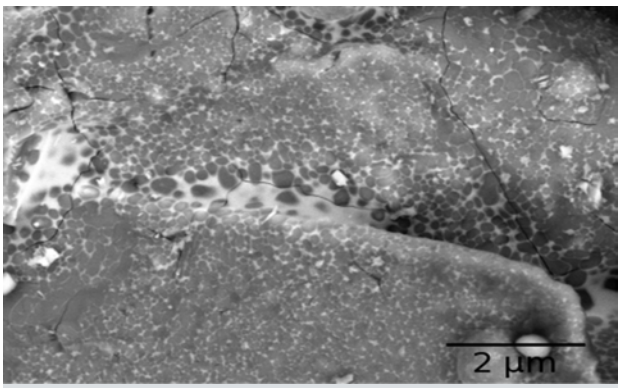

Figure 3: SEM images showing micro-cracks in an as-received sample.

Figure 3 shows micro-cracks not observed before. The distribution of these small micro-cracks is much narrower than the distributions observed in the cordierite and aluminum-titanate based materials. This is an important finding because it explains the small, but present, inelastic behavior observed previously.[6]

Prior work has shown that sample preparation for

double torsion fracture toughness testing is quite exacting and non-trivial. In an effort to make the sample preparation easier for the community and to begin testing samples that are closer to the actual application, the fracture behavior of structures began. The single-edge notch beam sample geometry is being considered in various orientations (see Figure 4). Sample size calculations have been done, indicating that for these geometries, the samples would need to be quite large[7] (about 1 or 3 m in length, depending on cell size) in order to assure pure mode I loading (i.e., opening mode).

Because the cell structure leads to orthotropic elastic constants, this anisotropy leads to changes in the stress intensity at the crack tip. The 0/90 orientations (depicted in Figure 4) experience a decrease in stress intensity compared to an isotropic material. This decrease in stress intensity requires a longer initial crack length to ensure the loading is in the linear elastic fracture mechanics regime. A smaller crack length leads to strength-controlled fracture.[8] The anisotropic stress intensity factors were calculated for the three orientations shown in Figure 4 and three orientations where the cells are rotated by 45 degrees (not shown). These results repeat the results of Quintana-Alonso et al.[8] and extend the same to the five orientations in question. Because continuous filter stock is not available in greater than 0.3-m sizes, sample sizes will be smaller and the R-curve affect will need to be considered.

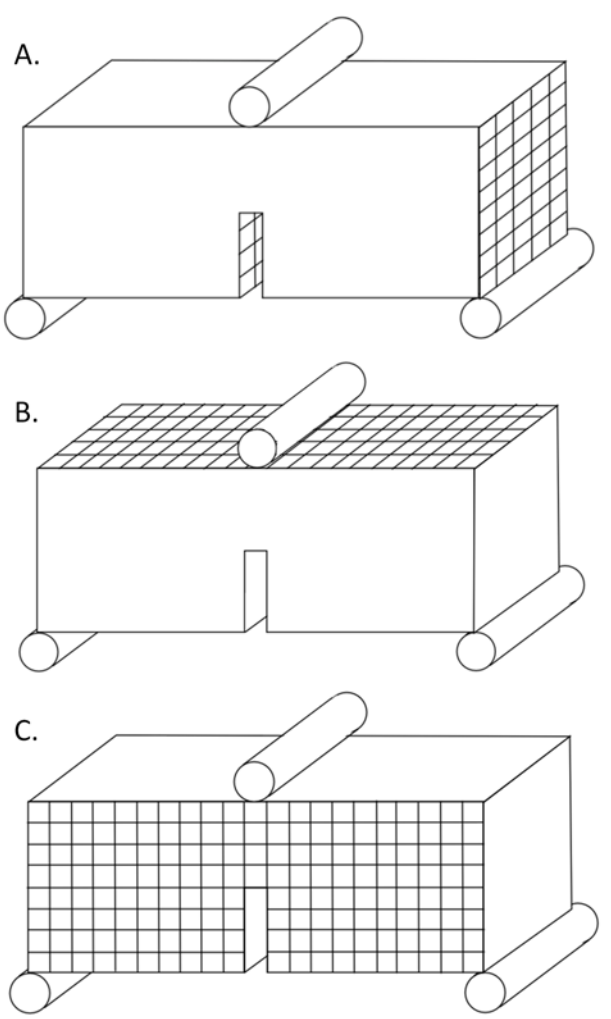

Figure 4: The “0/90” orientation with the notch plane (a) perpendicular to the channels, (b) parallel to vertical channels, and (c) parallel to horizontal channels.

As indicated earlier, careful sample preparation prior to testing is required to assure measurement of the material properties and not artifacts introduced during machining. The effects of machining on the mechanical properties of cordierite DPFs is being investigated, wherein three microstructural features are considered as sample thickness is reduced: (1) variations in the porosity, (2) reduction in the minimum solid area (i.e., a measure of the connected material over the cross-section), and (3) changes in the micro-crack density. We machined cordierite specimens to different thicknesses and characterized the tensile properties. The results revealed that specimen preparation reduces the Young’s modulus. Results from x-ray CT scans do not reveal drastic changes in the minimum solid area or porosity. This indicates that decreasing the sample thickness via grinding leads to a higher micro-crack density.

Summary

The increase in fracture toughness with increasing temperature observed in the silicon-carbide-based material is

mostly due to the strengthening effect of the oxide layer formed at high temperature that alters, seals, or joins the pre-existing cracks. Analyses of the fracture mechanics of DPF structures has begun in an effort to provide another measure of the fracture toughness from test samples that are easier to fabricate and closer to the actual product. Research on the prior test samples carefully machined from the walls of the honeycomb structure shows that although machining debris accumulates in pores, it does not have a significant impact on the properties of the contiguous portion of the sample. Further, the bulk porosity does not seem to change significantly with decreasing wall thickness. Therefore, machining must introduce additional micro-cracks into the machining damaged layers and, as the thickness of those layers becomes significant with respect to the total sample thickness, the impact of this increase is measureable in the Young's modulus.

Presentations

Cooper, R. C., A. Pandey, A. Shyam, T. R. Watkins, R. Parten, E. Lara-Curzio, G. Bruno, Z. Ladouceur, and R. Stafford, 2015, "Nonlinear and Anisotropic Mechanical Response of Porous Microcracked Ceramics," presented at *TMS 2015, 144th Annual Meeting and Exhibition*, March 17, 2015, Orlando, FL.

Cooper, R. C., A Pandey, A. Shyam., T. R. Watkins, R. Parten, E. Lara-Curzio, G. Bruno, Z. Ladouceur, and R. Stafford, 2015, "The effect of Machining on the Mechanical Properties of Porous Microcracked Cordierite," presented at the *39th International Conference and Expo on Advanced Ceramics and Composites*, January 27, 2015, Daytona Beach, FL.

References

"Multi-Year Program Plan 2011-2015," Vehicle Technologies Program, U.S. Department of Energy, Energy Efficiency and Renewable Energy, December 2010, pp. 2.3-4; 2.5-7, 8. (http://www1.eere.energy.gov/vehiclesandfuels/resources/fcvt_plans_roadmaps.html).

Hansen, S., 2013, "U.S. Clean Diesel Auto Sales Increase 41% in August 2013, Hybrid Sales Jump 38%," *Diesel Technology Forum*, http://www.dieselforum.org/index.cfm?objectid=4FD0F215-1A56-11E3-95AC000C296BA163, September 11, 2013.

Ulrich, L., "Fossil-Fuel Mileage Champ," New York Times, http://www.nytimes.com/2013/07/21/automobiles/autoreviews/fossil-fuel-mileage-champ.html?_r=0&pagewanted=all, July 19, 2013.

Adler, J., 2005, "Ceramic Diesel Particulate Filters," *International Journal of Applied Ceramic Technology* 2(6): 429-39.

"Propulsion Materials Annual Progress Reports," Vehicle Technologies Program, U.S. Department of Energy, Energy Efficiency and Renewable Energy, Office of Vehicle Technologies: www.ornl.gov/sci/propulsionmaterials/Reports.html; http://energy.gov/sites/prod/files/2014/03/f8/2012_propulsion_materials.pdf; http://energy.gov/sites/prod/files/2014/06/f16/2013_Progress_Report_for_Propulsion_Materials.pdf; http://energy.gov/sites/prod/files/2015/07/f25/FY2014_APR_PropulsionMaterials_R%26D_FINAL.pdf.

Pandey, A., A. Shyam, T. R. Watkins, E. Lara-Curzio, R. J. Stafford, and K. J. Hemker, 2014, "The Uniaxial Tensile Response of Porous and Microcracked Ceramic Materials," *Journal of American Ceramics Society* 97(3): 899–906.

Drugan, W. J., 2015, "Fracture Analysis of Thin-Walled Ceramic Catalysts and DPFs," private communication, March 25, 2015.

Quintana-Alonso, I. et al., 2007, "The fracture toughness of a cordierite square lattice," *Acta Materiala* 55(12): 2538–2564.

Project 18519 – Materials for Exhaust and Energy Recovery

Agreement 26462 – International Energy Agency (IEA IA-AMT) Characterization Methods

Hsin Wang
Materials Science and Technology Division
Oak Ridge National Laboratory
1 Bethel Valley Road
Oak Ridge, TN 37831
Phone (865) 576-5074; fax: (865) 574-3940; e-mail: wangh2@ornl.gov

DOE Technology Manager: Jerry L. Gibbs
Phone: (202) 586-1182; fax: (202) 586-1600; e-mail: jerry.gibbs@ee.doe.gov

ORNL Technical Advisor: J. Allen Haynes
Phone: (865) 576-2894; fax: (865) 574-4913; e-mail: haynesa@ornl.gov

Contractor: Oak Ridge National Laboratory, Oak Ridge, Tennessee
Prime Contract No.: DE-AC05-00OR22725

Objectives

Thermoelectric materials capture waste heat from engine operations and can contribute significantly to the energy efficiency of cars and trucks. Creation of a standard test procedure, coupled with standard reference materials issued by national laboratories, will pave the way for rapid high-efficiency thermoelectric materials and devices. The main objectives of this project are as follows:

- Lead a thermoelectric materials annex for International Energy Agency Advanced Materials for Transportation (IEA-AMT), with a focus on evaluating transport properties measurement methods and developing standard testing procedures to evaluate the figure of merit, ZT.
- Develop measurement standards of bulk thermoelectric materials and devices for vehicle waste heat recovery application in the temperature range of 300 to 800K.

Approach

- After initial round-robin studies on state-of-the-art bismuth telluride materials, the study is focusing on bulk thermoelectrics for vehicle waste heat recovery application in the temperature range of 300 to 800K. At the device level, energy conversion devices need to be evaluated for conversion efficiency. The lack of standard testing methods and procedures requires an international study. These are important steps to bringing advanced materials from research laboratories to scaled-up vehicle applications.

Accomplishments

- Third international round-robin of n-type half-heusler material was completed with 12 laboratories in six IEA-AMT member countries. The results were published in the *Journal of Electronic Materials*.
- International survey of thermoelectric module efficiency testing method was completed and published.
- The annex results were reported to the biannual IEA-AMT executive committee in Saarbrucken, Germany (December 2014) and Hamilton, Ontario, Canada (June 2015).

Future Direction

- Expanding the IEA-AMT results into International Standards Organization (ISO) standards
- Organize international round-robin testing on the efficiency of thermoelectric modules.

Introduction

Thermal management is critical to the efficiency of internal combustion engines. Depending on engine designs, up to 65% of energy is lost through the engine cooling and exhaust systems. Thermoelectric materials are ideal as all solid-state devices for thermal-to-electric energy conversion. For cost-effective engine waste heat recovery in vehicles, a much higher-efficiency material is needed. Current literature contains many thermoelectric materials with much higher efficiency; however, clear verifications of those claims are confounded by a wide variation in measurement techniques. Creation of a standard test procedure, coupled with standard reference materials issued by national laboratories, will pave the way for rapid development of high-efficiency thermoelectric materials.

The IEA-AMT thermoelectric annex is focusing on measurements standardization. After initial round-robin studies on state-of-the-art bismuth telluride materials, the study is focusing on bulk thermoelectrics for vehicle waste heat recovery application in the temperature range of 300 to 800K. In addition to bulk materials, the IEA-AMT annex is also going to evaluate measurement reliability of low-dimensional materials. At the device level, energy conversion devices need to be evaluated for conversion efficiency. The lack of standard testing methods and procedures requires international study. These steps are important to bring advanced materials from research laboratories up to scaled-up vehicle applications.

Task 1: International Round-Robin of High-Temperature Bulk Thermoelectric

Complete reporting to IEA on third international round-robin testing. Publish the results to promote standardization of transport property measurements. Explore the possibility of developing the IEA procedures into an ISO standard.

Task 2: Survey of Low-Dimensional Thermoelectric Materials Characterization

The IEA annex will organize an international study to evaluate the reliability of transport properties of low-dimensional materials. Past studies on thin film and nano-wire thermoelectrics will be reviewed and evaluated on measurement technique and data analysis. The potential of low-dimensional materials in applications and materials development will be accessed.

Task 3: Efficiency Testing of Energy Conversion Devices

The IEA-AMT Annex VIII will start a new task for conducting a study of the current state-of-the-art methods for determining energy conversion efficiency of thermoelectric devices for vehicle applications. Intentional collaboration will be coordinated by ORNL to assess the efficiency testing system in each participating laboratory and to publish the results in literature. This is a new IEA-AMT effort to evaluate and standardize efficiency testing methods for advanced vehicle energy conversion materials.

Results

FY 2015 efforts are summarized in the following subsection.

Third International Round-Robin Study

An international round-robin test of n-type half heusler material was conducted among 11 laboratories in six countries. The tests were completed in FY 2015 and the results have been published in the Journal of Electronic Materials.[1] The mains results are shown in Figures 1 through 4.

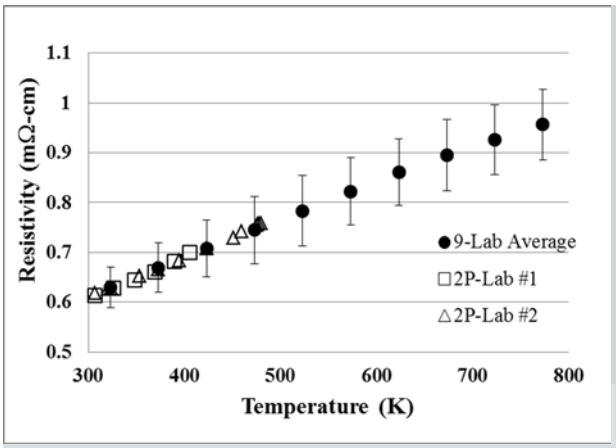

Figure 1: Electrical resistivity results of 11 laboratories, interlaboratory uncertainty ±6.5 to ±7.4%.

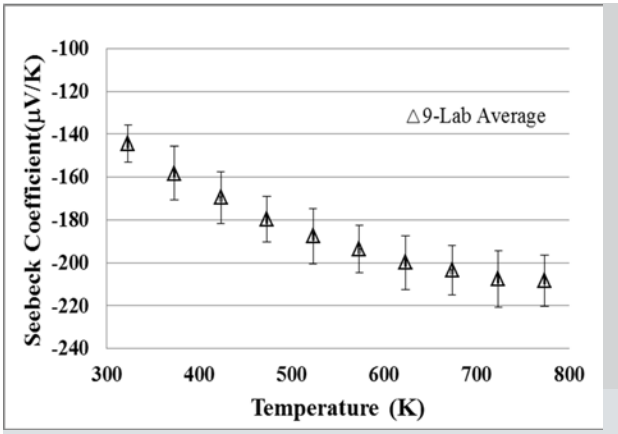

Figure 2: Seebeck coefficient results of nine laboratories using four-point methods, interlaboratory uncertainty ±5.7 to ±7.9%.

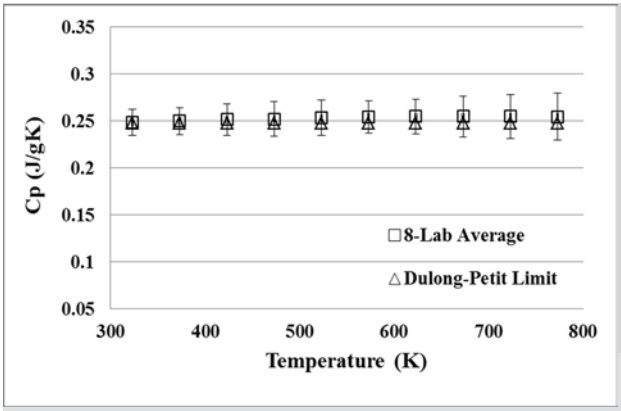

Figure 3: Specific heat results of eight laboratories, interlaboratory uncertainty ±5.6to ±10.0%.

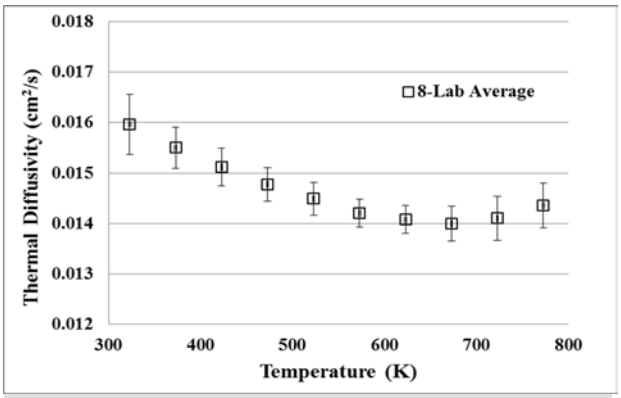

Figure 4: Thermal diffusivity results of 11 laboratories, inter laboratory uncertainty ±1.9 to ±3.7%.

Figure 5 shows that the figure of merit, ZT, was calculated using the equation for $ZT = s^2T/\rho k$, in which s is the Seebeck coefficient, ρ is the electrical resistivity, T is temperature in Kelvin, and k is thermal conductivity. Thermal conductivity, k, is calculated using $k = \alpha DC_p$, where α is thermal diffusivity, D is density, and C_p is specific heat. A total of six measurements are needed to determine ZT. Each input carries uncertainty, the error propagation rules must be used, and final uncertainties for ZT are ±11.6 to ±16.4%.

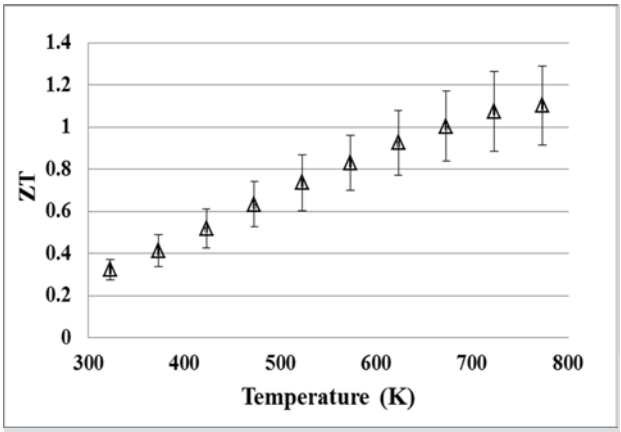

Figure 5: Figure of merit, ZT, of the study, interlaboratory uncertainty ±11.6 to ±16.4%.

Low-Dimensional Thermoelectrics

An international survey of low-dimensional thermoelectric measurements was conducted. Measurement experts in this area have been consulted, including Professor David Cahill from the University of Illinois, Professor Ali Shakouri from Purdue University, Professor Li Shi from the University of Texas at Austin, and Dr. Jae Yong Song from KRISS in Korea. Several review articles published by the consulted experts were used as references on measurements of low-dimensional thermoelectric materials. The summary was reported to the IEA-AMT executive committee. Based on the study results, an internal round-robin study on low-dimensional materials was not recommended due to the lack of actual applications and the difficulties of testing the same specimens for each measurement. An independent IEA-AMT report may be issued on this topic.

International Module Testing Survey

An international survey of thermoelectric module efficiency testing has been conducted and published.[2] This survey was done in preparation for the international round-robin testing of thermoelectric modules.

International Round-Robin Testing of Thermoelectric Modules

International round-robin testing of thermoelectric module has been planned and was started at the end of FY 2015. The initial participants are from five IEA-AMT countries: USA, Canada, Germany, United Kingdom, and China. Two commercially available bismuth telluride modules from Marlow Industries have been selected (Figure 6).

Figure 6: Thermoelectric modules selected for international round-robin testing.

Thermoelectric Materials Testing and Validation

Thermoelectric materials testing and validation measurements have been conducted at ORNL in collaboration with the University of Tennessee and the University of South Florida.[3-5]

References

Wang, H., S. Bai, L. Chen, A. Cuenat, G. Joshi, H. Kleinke, J. König, H.-W. Lee, J. Martin, M.-W. Oh, W. D. Porter, Z. Ren, J. Salvador, J. Sharp, P. Taylor, A. J. Thompson, and Y. C. Tseng, 2015, "International Round-Robin Study on Thermoelectric Transport Properties of n-type Half-Heusler from 300 K to 773 K," *Journal of Electronic Materials*, DOI: 10.1007/s11664-015-4006-z.

Wang, H., R. McCarty, J. R. Salvador, A. Yamamoto, and J. Konig, 2014, "Determination of Thermoelectric Module Efficiency – A Survey," *Journal of Electronic Materials* 43(6): 2274–2286.

Dong, Y., B. Eckert, H. Wang, X. Zeng, T. M. Tritt, and G. S. Nolas, 2015, "Synthesis, Crystal Structure, and Transport Properties of Cu2.2Zn0.8SnSe4-xTex," *Dalton Transactions* 44: 9014–9019.

Hu, D., Q. Liu, J. Tisdale, T. Lei, J. Pei, H. Wang, A. Urbas, and B. Hu, 2015, "Seebeck Effects in n-Type and p-Type Polymers Driven Simultaneously by Surface Polarization and Entropy Differences Based on Conductor/Polymer/Conductor Thin-Film Devices," *ACS Nano* 9(5): 5208–5213.

Wei, K., L. Beauchemin, H. Wang, W. D. Porter, J. Martin, and G. S. Nolas, 2015, "Enhanced Thermoelectric Properties for Cu2ZnSnSe4 with Ga-doping," *Journal of Alloys and Compounds* 650: 844–847.

Project 18519 – Materials for Exhaust and Energy Recovery

Agreement 26463 – Biofuel Impact on Aftertreatment Devices

M. J. Lance and T. J. Toops*
Ceramic Science and Technology Group
Oak Ridge National Laboratory
P.O. Box 2008, MS 6068, Building 4515
Oak Ridge, TN 37831
Phone: (865) 241-4536; fax: (865) 574-6098; e-mail: lancem@ornl.gov
*Fuels, Engines, and Emissions Research Center, ORNL

DOE Technology Manager: Jerry L. Gibbs
Phone: (202) 586-1182; fax: (202) 586-1600; e-mail: jerry.gibbs@ee.doe.gov

ORNL Technical Advisor: J. Allen Haynes
Phone: (865) 576-2894; fax: (865) 574-4913; e-mail: haynesa@ornl.gov

Contractor: Oak Ridge National Laboratory, Oak Ridge, Tennessee
Prime Contract No.: DE-AC05-00OR22725

Objectives

- Characterize selective catalytic reduction (SCR), diesel oxidation catalyst (DOC), and DPF devices following exposure to elevated levels of metal contaminants present in biodiesel to identify the deactivation and degradation mechanisms that may occur in emissions control devices operated with biodiesel fuel.

Approach

- Use state-of-the-art characterization tools within the High-Temperature Materials Laboratory to analyze the degradation mechanisms occurring in the emissions control devices that had underwent accelerated aging in biodiesel received from our collaboration with Cummins, NREL, the Manufacturers of Emission Controls Association, and the National Biodiesel Board.
- Establish accelerated aging methodology using an ORNL stationary diesel generator.

Accomplishments

- It was determined that sodium (Na) cannot be directly linked to a significant decline in the catalytic activity of emissions control devices.
- Na will increase ash levels in the DPF and should be a major consideration when setting biodiesel impurity standards.

– A stationary generator can mimic degradation mechanisms observed in full-scale engine tests.

Future Direction

– Analysis of heavy-duty and light-duty emissions control devices aged with 20 vol% biodiesel (B20) + 14 ppm sodium and potassium (K) will continue with scanning TEM.

– Targeted studies of metal impurity poisoning of emissions control devices will be conducted with a stationary generator.

Introduction

To enable renewable fuels to displace petroleum, it is critical their compatibility with emissions control devices is evaluated. Biodiesel fuel is known to contain elevated alkaline (i.e., Na and K) metal levels left over from the processing methods of these fuels. These metallic fuel contaminants are converted to oxides, sulfates, hydroxides, or carbonates in the combustion process to form an inorganic ash that can be deposited onto the exhaust emissions control devices found in modern diesel engines. Alkali metals are well known poisons for catalysts and have been shown to negatively impact the mechanical properties of ceramic substrates.[1] Furthermore, alkali metal hydroxides (such as Na and K) are volatilized in the presence of steam; therefore, they can penetrate the catalyst washcoat or substrate.

We are collaborating with Cummins, NREL, the Manufacturers of Emission Controls Association, and the National Biodiesel Board to characterize accelerated biodiesel-aged specimens. The first phase of this research focused on the effect of Na, K, and calcium (Ca) on heavy-duty catalyst parts referenced to a system that has aged with un-doped ultra-low sulfur diesel.[1] The aged system did not meet the 0.2-g/bhp-hr NO_x emission standard. However, the results could not be attributed to metal exposure because no Na was observed on the catalyst. In addition, the thermal shock resistance of the cordierite DPF declined 69% following simulated aging to 425,000 miles. Phase 2 focused on the effect of Na, K, and Ca on light-duty exhaust systems and the determination of an acceptable acceleration level.[2] Phase 3, discussed below, returns to a heavy-duty system in order to determine if lower metal limits are needed based on issues seen in Phase 1. Using a testing protocol developed at Cummins, full production exhaust systems were aged at NREL with biodiesel fuel doped with 14 ppm of Na in order to determine if there will be increased degradation of the emissions control devices when operated with B20 compared to ultra-low sulfur diesel. Samples were characterized using tools and techniques (such as SEM, EDS, electron probe microanalysis, x-ray fluorescence, x-ray diffraction, Raman spectroscopy, and thermogravimetry) at the High-Temperature Materials Laboratory at ORNL.

Long-term, low-cost testing of materials in real diesel engine exhaust was established through a previous annual operating plan at the Fuels, Engines, and Emissions Research Center using a stationary diesel generator (i.e., genset). This genset can be run unattended overnight with different fuels, enabling low-cost testing without the use of an entire test-cell and full-scale diesel engine. Accelerated aging with Na doping of biodiesel fuel was conducted using this genset in order to further specify the effect of metal impurities on emission control device performance.

The expected benefit of this project is to identify the poisoning mechanisms of alkali metals by tracking local chemical changes in the washcoat or substrate using high-resolution probes (both electron and photon). With this information, we will be able to make recommendations to industry regarding the fuel composition and operating conditions necessary to ensure the same lifetime of emission control devices operated with B20 that

they currently have with ultra-low sulfur diesel.

Results

Aging of a full-production exhaust system from a Cummins ISL was conducted at NREL to 435,000 miles simulated in 1,000 hours using B20 + 14 ppm Na. Aging was conducted on the Cat C9 test stand. The emissions control devices were positioned with the DOC at the front, followed by DPF and the SCR system. The heating cycle is shown in Figure 1. The Cummins ISL tailpipe NO_x emissions increased from 0.25 to 0.40 g/hp-hour over the course of the test, which exceeded the Environmental Protection Agency standard of 0.33 g/hp-hour. A hot-start FTP was used to assess the aftertreatment component contributions to the degradation of the system by systematically swapping aged for de-greened components. It was discovered that aging impacts all component catalysts at similar levels. In order to identify the failure cause of each component, samples were studied using tools within the High-Temperature Materials Laboratory. The results are presented in the following subsections.

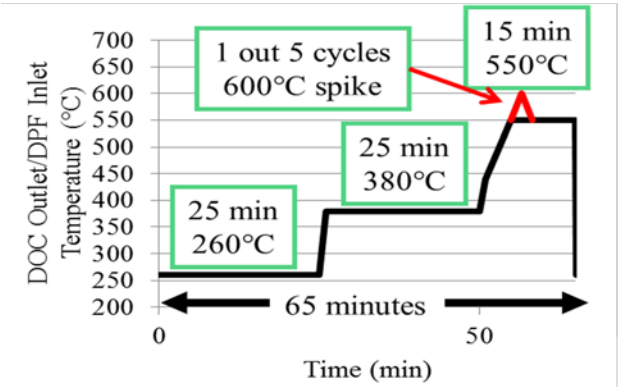

Figure 1: Heating cycle used to age the aftertreatment devices.

Diesel Oxidation Catalyst

Elemental maps were collected on cross-sections of the DOC after 1,000 hours of aging and are shown in Figure 2. Na was found across the washcoat thickness along the entire DOC length at roughly the same concentration. P was present only near the surface and decreased in concentration down the DOC length. Therefore, the degradation may be related to buildup and stabilization of contaminants from either Na in the biodiesel or lube-oil metals (P).

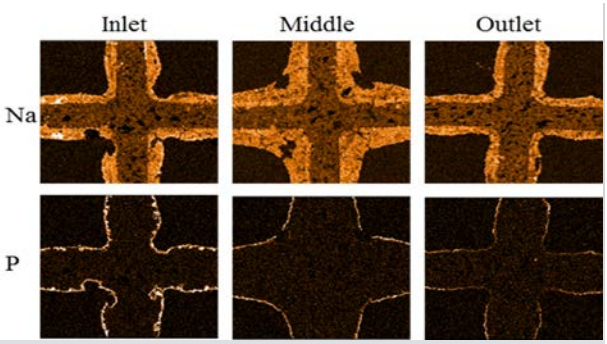

Figure 2: Maps of Na (top) and P (bottom) after aging from 1 cm from the inlet, the middle, and 1 cm from the outlet.

In order to understand which element was causing the DOC degradation, Cummins applied five washing protocols to five separate micro-cores extracted from the front face of the aged DOC. The five protocols were, in order: (1) high-temperature oxidation to remove the hydrocarbon and water, (2) a desulfation step to remove sulfur, (3) water washing to remove soluble species such as Na, (4) a second desulfation, and (5) an acid wash to remove phosphorus. A performance evaluation was conducted following each treatment. Washed samples were sent to ORNL, where they were analyzed using electron probe microanalysis (results are shown in Figure 3). Na was removed

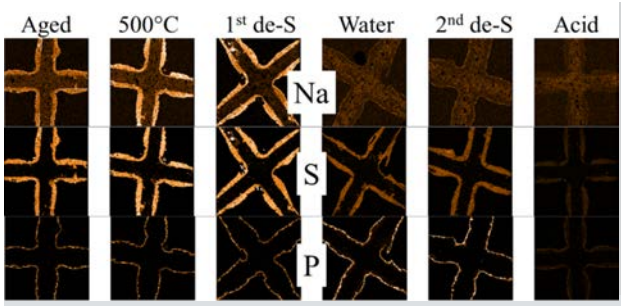

Figure 3: Electron probe microanalysis maps of the treated cores showing the distributions of Na (top), S (middle) and P (bottom).

following the water washing step (i.e., fourth column in Figure 3); however, there was only a 5% improvement in the NO to NO_2 conversion following this treatment step. Acid washing removed significant amounts of P (sixth column) and led to a 26% improvement of NO oxidation. This indicates that engine oil phosphorus was the primary source of deactivation, not Na.

Diesel Particulate Filter

Figure 4 shows the DPF washcoat from the fresh and aged samples. The bright spots in the aged washcoat are Pt particles that have sintered due to high temperatures during testing. This sintering, and the subsequent loss of surface area, was not caused by the presence of Na. Nevertheless, the DPF filled with 857 g (45 g/L) of ash during aging, with 79% due to Na in the B20 fuel. This corresponds to 20% more ash over the full useful life coming from the maximum specified American Society for Testing and Materials limit for Na in biodiesel. Most biodiesel is well below this limit; therefore, this represents the worst case scenario for biodiesel-produced ash loading in a DPF.

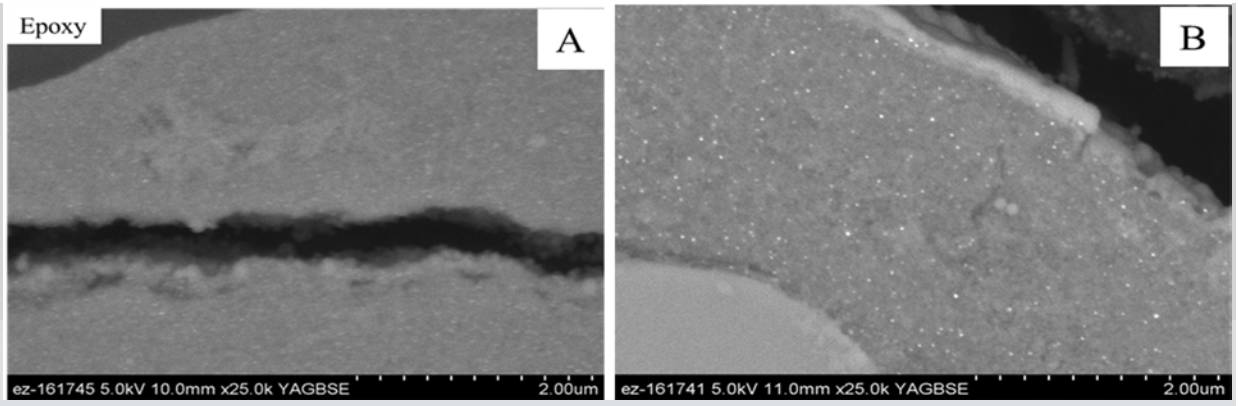

Figure 4: SEM images of the DPF washcoat from the fresh sample (A) and the aged sample (B).

The chemical integrity of the DPF was also assessed by mapping the Na in the fresh and aged cordierite (Figure 5). There was no evidence of Na diffusion into the cordierite DPF, which is not surprising given the low regeneration temperature used here (550°C).

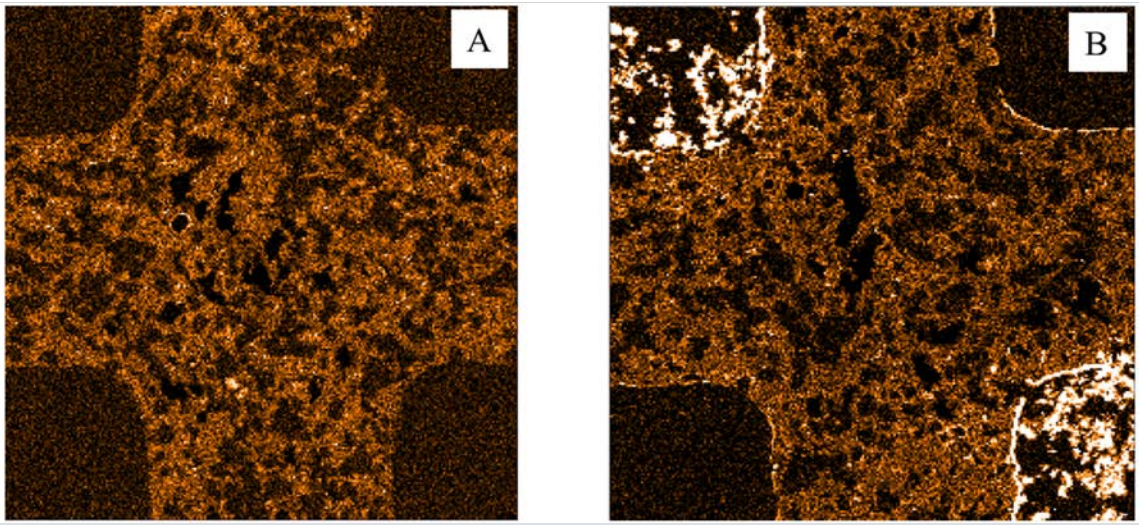

Figure 5: Na elemental maps on the fresh DPF (A) and the aged DPF (B).

The fresh and aged DPF bricks were sliced into 6-mm thick tiles for fracture strength testing. The DPF strength increased 19% following aging (Figure 6). It is speculated that the increase was due to ash in the aged sample imparting some mechanical strength to the cordierite. There was also no change in the coefficient of thermal expansion following aging. This shows that under these conditions, no degradation of the thermal shock resistance of the DPF occurs due to the presence of Na in biodiesel.

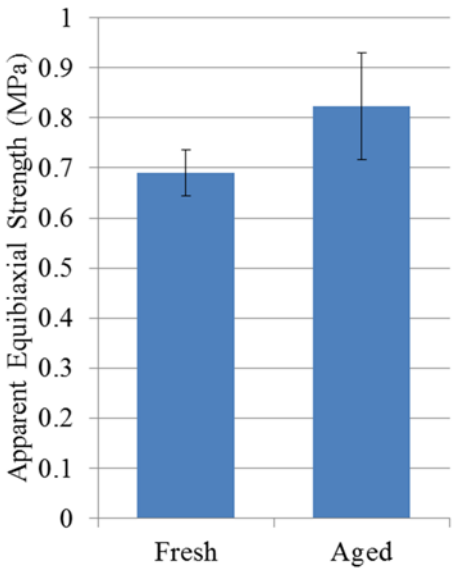

Figure 6: Apparent equibiaxial flexure strength for the fresh and aged DPFs.

Selective Catalytic Reduction

The composition of the SCR washcoat was measured using inductively coupled plasma mass spectrometry, the results of which are shown in Table 1. Both the fresh washcoat and the fresh cordierite substrate contained some Na, which is an impurity in cordierite. This made it difficult to say if the Na increased following aging, because the small increase found in Table 1 may be due to cordierite debris contaminating the SCR washcoat during sample collection. In any case, such a low level of Na is not anticipated to degrade the functionality of the SCR. This low Na level shows that the DOC and DPF shield the SCR from Na. Bench reactor testing performed at Cummins revealed the signatures consistent with Pt contamination of the SCR, which may have happened from vapor migration from the DPF during an atypical thermal event. Therefore, degradation of the SCR was unrelated to the Na dopant in the B20 fuel.

Table 1. Inductively coupled plasma mass spectrometry measurements of the Na composition of the SCR washcoat before and after aging.

Sample	Na (µg/g)
Fresh SCR Washcoat	309
Fresh Cordierite	444
Aged SCR Washcoat	486

Stationary Generator

A Northern Lights 9-kW stationary generator is installed at the Fuels, Engines, and Emissions Research Center and was operated with an Na-doped B20 under the same conditions

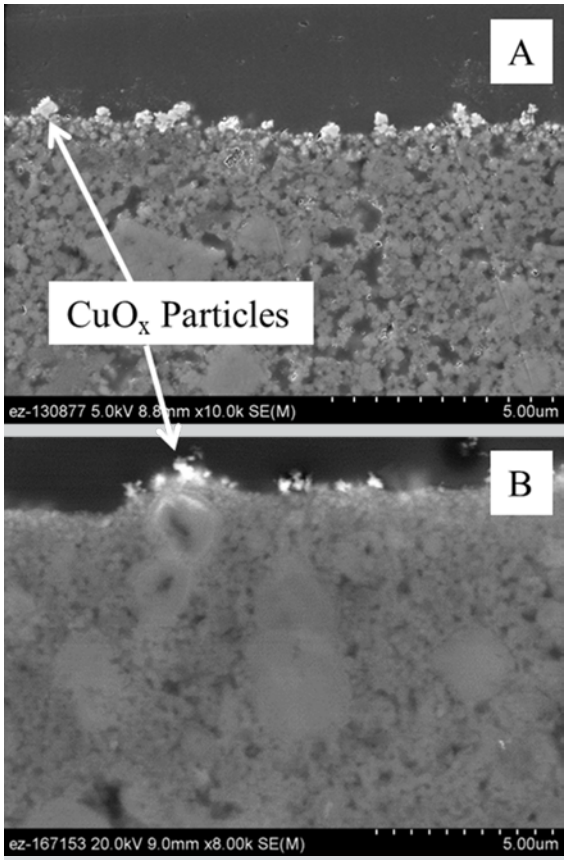

Figure 7: SCR surface following aging with a full-scale engine (A) and a stationary generator (B).

that were tested during Phase 2 of this project.[3] Figure 7 shows that the SCR aged with the stationary generator exhibited the same degradation mechanism observed following aging with the full-scale engine; copper was replaced by Na in the zeolite structure and migrated to the SCR washcoat surface in the form of CuO_x particles. This shows that the stationary generator can be used to simulate aging with doped fuels at a far lower cost than with an engine test.

Milestones

Milestone	Completion Date
Conduct electron probe microanalysis maps on cross-sectioned samples to identify the location of Na, P, Ca, Zn, and S elements in both SCR and DOC cores following accelerated aging at NREL.	December 2014
Identify deactivation mechanisms in heavy-duty SCR and DOC samples aged with Na-doped fuel provided by NREL.	March 2015
Mimic conditions and dopant levels used at NREL using genset at ORNL	June 2014
Submit annual report	November 2015

Conclusions

The objective of this work was to understand the impact of Na metal contaminants in biodiesel fuel on a heavy-duty aftertreatment system (DOC+DPF+SCR).

For DOC, laboratory diagnostics suggest that the Na contamination is not a key factor in the degradation of NO oxidation.

The increase in ash content could shorten the DPF maintenance interval to an unacceptable level. The decline of catalytic function of the DPF during aging was due to either increased ash accumulation, P inhibition, or the observed PGM sintering.

Results suggest that when the SCR is downstream of a DPF, there is little or no Na contamination of the SCR. The observed SCR activity loss is consistent with low levels of Pt contamination.

The stationary generator can be used for accelerated aging tests at much lower cost compared to engine testing.

References

Williams, A. et al., 2011, “Impact of Biodiesel Impurities on the Performance and Durability of DOC, DPF and SCR Technologies,” *SAE International Journal of Fuels Lubr*. 4(1): 110-124.

Williams, A. et al., 2013, “Impact of Fuel Metal Impurities on the Durability of a Light-Duty Diesel Aftertreatment System,” *SAE International*.

Williams, A. et al., 2014, "Effect of Accelerated Aging Rate on the Capture of Fuel-Borne Metal Impurities by Emissions Control Devices," *SAE International Journal of Fuels Lubr.* 7(2).

Publications and Presentations

Williams, A., R. McCormick, M. Lance, C. Xie et al., 2014, "Effect of Accelerated Aging Rate on the Capture of Fuel-Borne Metal Impurities by Emissions Control Devices," *SAE International Journal of Fuels Lubr.* 7(2), doi:10.4271/2014-01-1500.

McCormick, R., T. J. Toops, and M. J. Lance, 2014, "Impact of Metal Impurities on Catalyst Durability," *Biodiesel Technical Workshop*, October 29, 2014.

Lance, M. J., T. J. Toops, C. Xie, W. Brookshear, R. McCormick, A. Ragatz, R. Ancimer, H. An, and L. Rogoski, 2015, "Impact of Metal Impurities in Biodiesel on Catalyst Durability," *24th North American Catalysis Society Meeting (NAM)*, Pittsburgh, Pennsylvania, June 17, 2015.

Project 18865 – Application-Specific Materials Simulation, Characterization, and Synthesis

Agreement 9105 – Characterization of Catalyst Microstructures

Dr. Lawrence F. Allard
Materials Science and Technology Division
Oak Ridge National Laboratory
1 Bethel Valley Road
Oak Ridge, TN 37831
Phone (865) 607-1144; fax: (865)576-5413; e-mail: allardLFjr@ornl.gov

DOE Technology Manager: Jerry L. Gibbs
Phone: (202) 586-1182; fax: (202) 586-1600; e-mail: jerry.gibbs@ee.doe.gov

ORNL Technical Advisor: J. Allen Haynes
Phone: (865) 576-2894; fax: (865) 574-4913; e-mail: haynesa@ornl.gov

Contractor: Oak Ridge National Laboratory, Oak Ridge, Tennessee
Prime Contract No.: DE-AC05-00OR22725

Objectives

- Provide unique catalyst characterization capabilities to help meet mandated emissions reduction targets for automotive and diesel engines.
- Primary focus is atomic-level aberration-corrected electron microscope coupled with both in-situ and ex-situ gas reaction capabilities.
- Support strong collaborations with several external and internal colleagues in expanded atomic-level studies to accelerate development of a broad base of understanding of the efficacy of single-atom catalysis, which is the holy grail of catalytic science.

Approach

- Partner with Protochips Co. to expand capabilities for in-situ reaction studies with a unique gas-cell reactor system for the aberration-corrected electron microscope. Utilize the capabilities of the now-commercial system (called Atmosphere 200^{TM}, formerly "Gen 4" while in development) for reaction studies with several collaborators.
- Expand collaboration with the University of New Mexico colleagues (Datye group) to characterize regenerability of atomically dispersed Pd on γ-alumina for low-T exhaust treatment catalysis; correlate in-situ gas-cell experiment with the University of New Mexico ex-situ work to verify utility of gas cell for reliable experimental data.

– Continue collaboration with the University of Michigan and ORNL colleagues to develop new gas-cell capabilities (e.g. capability for water vapor experiments and gas mixing capabilities in the commercial manifold).

Accomplishments

– An extensive suite of calibration experiments with Protochips Inc. to permit accurate control of temperature in the gas cell was successful in determining that temperature versus resistance of the heater membrane yielded a gas composition and temperature-independent control method.

– Work with the University of New Mexico has showed the addition of LaOx to the γ-alumina support helps stabilize the dispersion of single Pd atoms, which leads to low-temperature (i.e., 40°C) onset of catalytic activity in CO oxidation reactions. A paper on this work was published in *Nature Communications*.

Future Direction

– Continue studies with leading collaborators in the broad thrust areas of "regenerable" and "single-atom" catalysts.

Introduction

Work has continued during FY 2015 with the use of the fully functional ORNL "Gen 4" version of the now commercial Protochips Atmosphere 200™ gas-cell in-situ reactor system on several ongoing catalyst projects with both local and external collaborators. In one thrust area, with Professor Abhaya Datye's group at the University of New Mexico, we have extended the study of regenerable Pd/La-doped alumina to a series of bimetallic Pt-Pd/La-doped alumina to determine the fundamental mechanisms of the control of stability and regenerability by Pd in the system. This study is being correlated to concurrent ex-situ reaction studies to better understand the efficacy of the gas cell in producing reliable "real-life" results.

The second major thrust area for our work continues to be studies of single-atom catalysts, with several colleagues, most notably, Dr. Chaitanya Narula at ORNL and Professors Maria Flytzani-Stephanopoulos of Tufts and Abhaya Datye of University of New Mexico. With regard to continuing development of in-situ gas cell capabilities, we have partnered with Dr. George Graham in Professor Xiaoqing Pan's group at the University of Michigan to develop the technique of doing water vapor experiments in gas reactions and with Dr. Melanie Debusk at the ORNL National Transportation Research Center on techniques for gas mixing internal to the Protochips gas manifold. This report will highlight an example of the results from the research in the three thrust areas.

Results

Pd/Alumina Regenerable Catalysts

Work on the Pd/alumina (i.e., lanthana-stabilized alumina) catalyst system specifically related to diesel oxidation catalysts led to a webinar hosted by *Materials Today* where Professor Datye discussed the need for in-situ studies to understand the action mechanisms of complex catalytic processes related to the combustion of methane in exhaust emissions. The full story can be found at:
http://www.materialstoday.com/characterization/webinars/catalyst-behavior-at-operational-

temperatures/. Figures 1 through 4 summarize some of the results. Figure 1 shows a typical La-alumina aggregate with Pd particles ideally dispersed so that a number of particles are positioned at the edge of the aggregate (particles b-g) and can be followed in sequential oxidation runs. The figure gives the oxidation conditions and the final reduction experimental conditions. Figure 2 shows Particle B first as-prepared, with the cell at vacuum and 200°C (Panel a), then after oxidation in 130 Torr O_2 for 10 minutes at 300°C (Panel b) and at 500°C (Panel c). The particle is fully metallic Pd at 200°C, is partially oxidized after 300°C treatment, and is nearly fully oxidized (with a significant change in volume) after 500°C treatment. Figure 3 compares the aggregate after an oxidation treatment at 1000°C, where no Pd particles remained. It was surmised that the PdO had become fully dispersed on the support at 1000°C; therefore, the sample was run in a reducing environment (H_2/Ar gas) at 300°C to re-grow the residual Pd into new particles. Figure 4 shows an interesting result where no Pd particles were observed to grow, but the alumina support appeared to become "decorated" with individual heavy atoms that were thought to likely be Pd. However, EDS analysis after removing the heater from the gas cell showed no Pd remaining on the aggregate or on the local SiN support membrane of the heater device. X-ray photoelectron spectroscopy run on the bottom SiN window of the cell showed a clear Pd signal, suggesting that all of the Pd evaporated during the high-temperature treatment and deposited on the opposing window surface.

The EDS spectrum also contained a significant La signal, equivalent to the level of La seen in the original material, suggesting that the decorating atoms were actually La species coming out of the lattice to collect on ledges, defects, and boundaries on the alumina. This also shows the outstanding ability of the gas cell to permit full atomic level imaging even under conditions of high pressure and temperature.

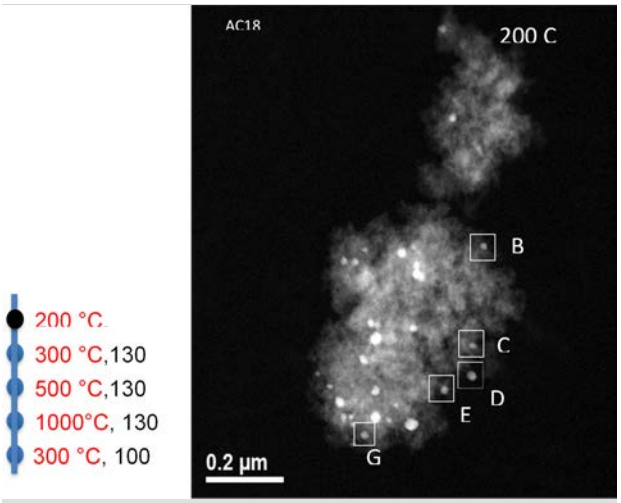

Figure 1: Alumina aggregate with "good" distribution of Pd nanoparticles (i.e. particles at the edge of the aggregate with minimal alumina support below the particle).

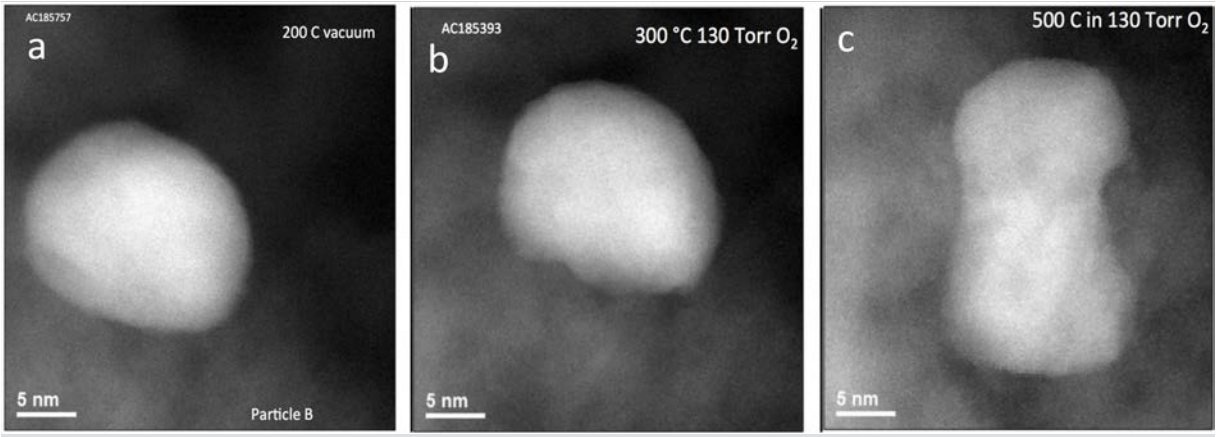

Figure 2: Pd particle B in the aggregate of Figure 1 (a) as-prepared and at 200°C in vacuum in the cell; (b) after oxidation at 300°C and 130 Torr O_2; and (c) after further oxidation at 500°C and 130 Torr.

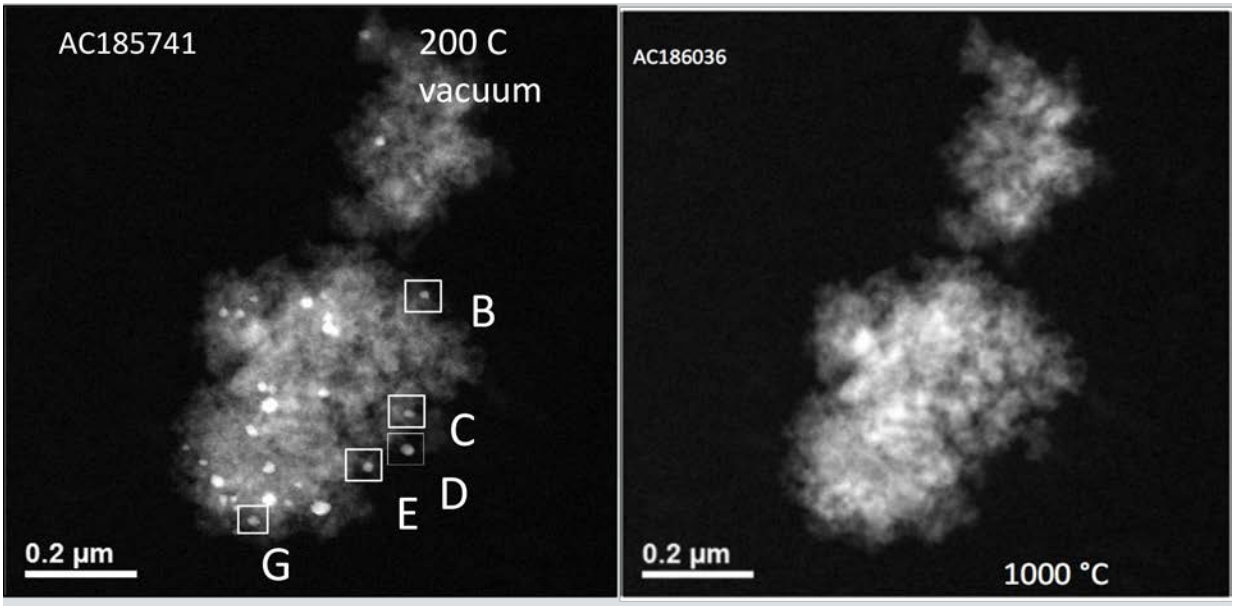

Figure 3: Before and after views of the initial alumina aggregate. After 1000°C oxidation, all Pd is apparently gone, because discrete Pd nanoparticles are no longer evident.

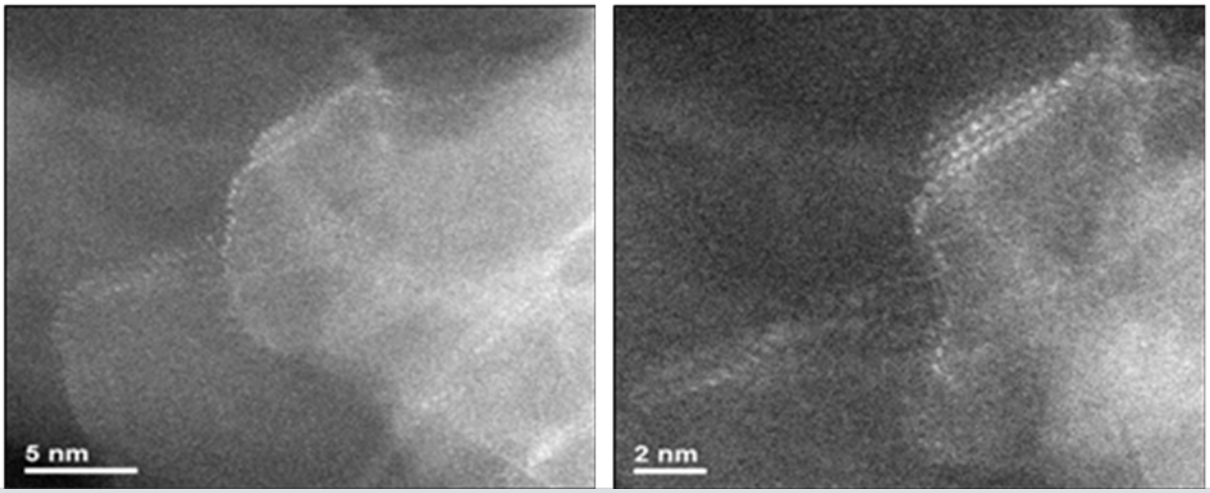

Figure 4: Medium (a) and high (b) magnification images of the same area of alumina aggregate, showing decoration of surfaces, ledges, and defects by a heavy metal species, most likely La from the alumina lattice.

Single-Atom Catalysis Studies

While it is long known that different types of support oxides have different capabilities to anchor metals and, thus, tailor the catalytic behavior, it is not always clear whether the support is a mere carrier of the active metal site itself and not participating directly in the reaction pathway. We reported in JACS[2] that catalytically similar single-atom-centric Pt sites are formed by binding to sodium ions through –O ligands, the ensemble being equally effective on supports as diverse as TiO_2, L-zeolites, and mesoporous silica MCM-41. Loading of 0.5 wt% Pt on all these supports preserves the Pt in atomic dispersion as Pt(II); the Pt-$O(OH)_x$- species catalyzes

the water-gas shift reaction from about 120 to 400°C. Because the effect of support is "indiGas0rect," these findings pave the way for use of a variety of earth-abundant supports as carriers of atomically dispersed platinum for application to catalytic fuel-gas processing. Figure 5 shows single-atom dispersions of Pt-Na species on TiO_2, KLTL (an L-zeolite) and mesoporous silica ((Si)MCM41), in Figures 5a, 5b, and 5c, respectively.

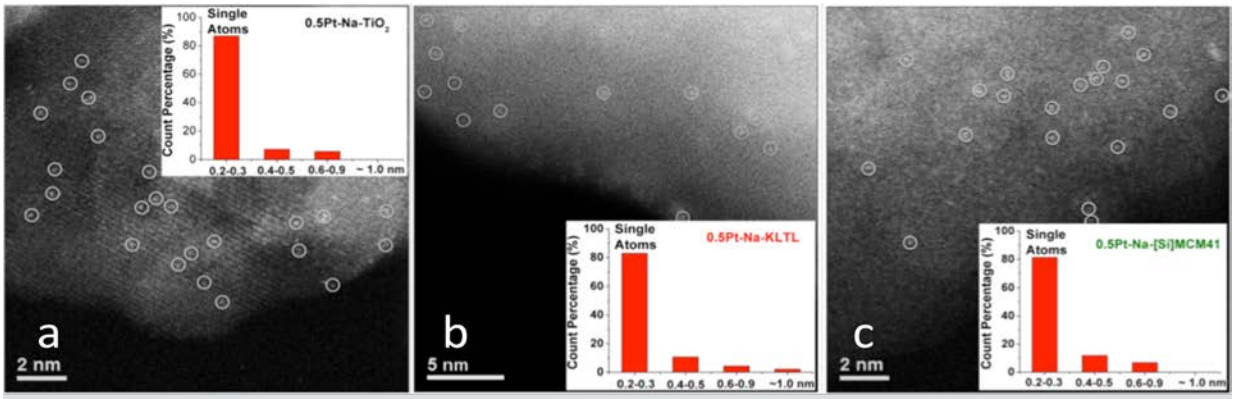

Figure 5: Single-atom Pt-Na species dispersed on (a) TiO_2, (b) KLTL zeolite, and (c) mesoporous silica MCM41 supports at the 0.5% Pt loading level.

Gas-Cell Reaction Developments: Water Vapor

It has long been of great interest to not only perform standard reactions (such as oxidation and reduction in the gas-cell system), but also to run reactions with gas compositions that more accurately simulate real life or bench-top reactor conditions. These often include introduction of water vapor into the gas stream; water is maintained in the vapor phase at concentrations above those that occur naturally, which is about a 2% level at room temperature and atmospheric pressure (i.e., about 17 Torr partial pressure). This is done by heating the reaction lines to an appropriate temperature above room temperature, using e.g. heating tape. However, this solution is not amenable to the Protochips gas-reactor holder, which has capillaries inside the specimen rod that allow flow through the gas cell in the tip of the holder. There is no way to keep this part of the reaction path at an elevated temperature and also maintain the stability of the rod against drift that degrades the imaging performance required for atomic-level studies. The solution to this problem has been to recognize that as long as the total pressure of H_2O vapor is not above 17 Torr, the water will remain in the vapor phase; therefore, higher partial pressures in a gas stream can be obtained by lowering the overall pressure of the gas supplied from the chosen experimental tank in the gas manifold. For example, gas at 170 Torr total pressure can contain 17 Torr of H_2O vapor for a partial pressure of 10% H_2O vapor; the total pressure of 170 Torr is considered by the catalytic chemists as reasonable for comparing to bench-top reactor experiments, given the extremely tiny amount of catalyst material that is typically present in the gas cell for the electron microscopy experiments.

Tests were conducted at the University of Michigan, using the H_2O vapor supplied by the system shown in Figure 6. Here a glass flask with a glass-to-metal seal that connects to the gas manifold was charged with water (by soaking cotton gauze contained in the small projection seen in the figure). The flask was pumped to a pressure of 17 Torr, as measured by a capacitance manometer (i.e., Baratron gage), and used to supply vapor to the experimental tank in the manifold. Initial tests confirmed that water vapor could be introduced into the gas cell with no apparent condensation. Further work is underway to set up a simpler and more permanent water supply system on both the University of Michigan gas manifold and the ORNL gas manifold.

Future Work

Work has continued during FY 2015 with use of the fully functional ORNL Gen 4 version of the now commercial Protochips Atmosphere 200^{TM} gas-cell in-situ reactor system on several ongoing catalyst projects with both local and external collaborators. In one thrust area, with Professor Abhaya Datye's group at the University of New Mexico, we have extended the study of regenerable Pd/La-doped alumina to a series of bimetallic Pt-Pd/La-doped alumina to determine the fundamental mechanisms of the control of stability and regenerability by Pd in the system. This study is being correlated to concurrent ex-situ reaction studies to better understand the efficacy of the gas cell in producing reliable real-life results.

In order to validate the gas-cell experiments, the purpose of the initial Pt and Pd heating experiments was to correlate the behavior in the gas cell of well-defined Pd and Pt particles on the LaAlOx support with the behavior of similar material when run under equivalent reaction conditions in an ex-situ reactor system. Essentially, we have used the emission of Pt and Pd from automotive look-alike catalysts to "calibrate" the cell. When those experiments have been completed and a paper prepared, we will study the role of Pd on Pt, with the question "does it slow emission in proportion to its concentration (e.g. a simple dilution) or is the mechanism more involved? Is there a thin film of PdO formed that impedes the emission of Pt from the bimetallic?" Those results will naturally lead to a study of the role of the support to determine how the support modifies the emission of the PGM atoms from the metal phase.

The single-atom catalysis work with Tufts and others has demonstrated how reaction mechanisms involving single metal atoms/cations transcend support structure and composition as long as the metal atom-centered active site is allowed to form in a stable manner. Continuing atomic-level microscopy studies will involve materials synthesized by novel methods and will correlate to the stability of atomically dispersed catalysts in various reaction environments, including, but not limited to, the water-gas shift reaction (better three-way catalyst [TWC] designs, methanol steam reforming with 100% hydrogen selectivity, and selective hydrogenation reactions. Our studies will continue to lead to novel catalyst design concepts aimed at more efficient and sustainable processes, particularly in the realm of single-atom catalytic materials.

Conclusions

Having integrated the full commercial version of the Protochips gas-cell system into our catalyst characterization program, including the advanced computer control capabilities provided by the automated valves and gages in the gas-handling manifold, our research efforts utilizing in-situ reaction techniques is now ramping up. Similarly, the collaborative efforts with several high-level research groups in the realm of single atom catalysis studies (that our program helped pioneer with the 2011 *Nature Chemistry* publication showing the first direct correlation between single Pt species on Fe_2O_3 imaged with the aberration-corrected JEOL 2200FS scanning TEM/TEM instrument) have gained momentum and shown great promise for ultimately achieving large gains in catalyst performance with a concomitant large decrease in the use of expensive catalytic metals.

Publications, Presentations, and Visits

Yang, M., S. Li, Y. Wang, J. A. Herron, Y. Xu, L. F. Allard, S. Lee, J. Huang, M. Mavrikakis, and M. Flytzani-Stephanopoulos, 2014, "Catalytically active Au-O(OH)$_x$- species stabilized by alkali ions on zeolites

and mesoporous oxides," *Science* 346(6216): 1498-1501, DOI: 10.1126/science.1260526.

Yang, M., J. Liu, S. Lee, B. Zugic, J. Huang, L. F. Allard, and M. Flytzani-Stephanopoulos, 2015, "A Common Single-Site Pt(II)-O9OH) – Species Stabilized by Sodium on 'Active' and 'inert' Supports Catalyzes the Water-Gas Shift Reaction," *Journal of American Chemistry Society* 137(10): 3470–3473, DOI: 10.1021/ja513292k.

Howe, J. Y., L. F. Allard, W. C. Bigelow, H. Demers, and S. H. Overbury, 2014, "Understanding catalyst behavior during *in-situ* heating through simultaneous secondary and transmitted electron imaging," *Nanoscale Research Letters* 9: 614.

Moses-DeBusk, M., L. F. Allard, D. A. Blom, and C. K. Narula, 2015, "Oxidation-Induced Structural Changes in Sub-Nanometer Platinum Supported on Alumina," *ChemCatChem*, article first published online Volume 7, DOI: 10.1002/cctc.201500267.

Narula, C. K., L. F. Allard, G. M. Stocks, and M. Moses-DeBusk, 2014, "Remarkable NO oxidation on single supported platinum atoms," *Nature Scientific Reports* 4: 7238, DOI:10.1038/srep07238.

Wang, C., G. Garbarino, L. F. Allard, F. Wilson, G. Busca, and M. Flytzani-Stephanopoulos, 2015, "Low-Temperature Dehydrogenation of Ethanol on Atomically Dispersed Gold Supported on $ZnZrO_x$," *JACS*, in press September 2015.

Lucci, F. R., J. Liu, M. D. Marcinkowski, M. Yang, L. F. Allard, M. Flytzani-Stephanopoulos, and E. C. H. Sykes, 2015, "Selective hydrogenation of butadiene by Pt/Cu at the single atom limit," *Nature Communications*, published online October 9, 2015.

Narula, C. K., L. F. Allard, G. M. Stocks, and M. M. DeBusk, 2015, "CO and NO Interaction with Pd Atoms on θ-Al_2O_3 (010) Surface," in revision for *Journal of the American Chemical Society*, September 2015.

Kwak, J. H., R. Dagle, G. C. Tustin, J. R. Zoeller, L. F. Allard, and Y. Wang, 2014, "Molecular Active Sites in Heterogeneous Ir–La/C-Catalyzed Carbonylation of Methanol to Acetates," *Journal of Physics Chemistry Letters* 5(3): 566–572, DOI: 10.1021/jz402728e.

June 29 and 30, 2015 Dr. Larry Allard visited Professor Xiaoqing Pan's group at the University of Michigan to work with Dr. George Graham and graduate student Shuyi Zhang on development of capability for water vapor introduction into the in-situ gas-cell reactor holder and on capability to do electron energy loss spectroscopy in gas cell experiments.

July 9 and 10, 2015, Dr. Larry Allard visited Professor David Bell, Director of the Central Microscopy Facility at Harvard University, for discussion of new microscopy technologies. Also visited Tufts University to sit on the PhD Committee of Ming Yang, student of collaborator Professor Maria Flytzani-Stephanopoulos.

Invited Talks

Appalachian Region EM Society Fall Meeting, "In-situ (S)TEM Gas-Reaction Studies: Then and Now,"

Knoxville, Tennessee, October 22, 2014.

Texas Society for Microscopy 50th Anniversary Meeting: Presented Plenary talk, "In-situ Gas Reaction Electron Microscopy: A 50-year Perspective," Austin, Texas, February 23, 2015.

University of Texas-San Antonio, Department of Physics and Astronomy Seminar: "In-situ Gas Reaction Electron Microscopy: Then and Now," San Antonio, Texas, March 6, 2015.

Tufts University, Department of Chemical Engineering Seminar, "Controlled In-situ Gas Reaction Studies of Catalysts at High Temperature and Pressure with Atomic Resolution," Medford, Massachusetts, July 9, 2015.

R&D 100 Award Finalists

Dr. Larry Allard is a "Supporting Developer" with the Protochips Inc. team for the Protochips "Atmosphere 200" environmental gas cell system that was recently chosen as a finalist for a 2015 R&D 100 Award. Winners will be announced at the November R&D 100 Awards and Technology Conference in Las Vegas. This newly commercialized technology is a result of the 9-year collaboration between Protochips and ORNL, via Dr. Allard's Energy Efficiency and Renewable Energy catalyst characterization research project.

Materials Today Webinar

Datye, A. K., L. F. Allard, and J. Damiano, "Understanding Commercial Catalyst Behavior at Operational Temperatures and Pressures via High Resolution In-situ Microscopy," http://www.materialstoday.com/characterization/webinars/catalyst-behavior-at-operational-temperatures/ hosted by Materials Today (greater than 340 participants) on July 15, 2015.

Project 18865 – Application-Specific Materials Simulation, Characterization, and Synthesis

Agreement 26391 (Task 1) – ICME Tools for Powertrain Materials Development: Catalyst Materials

Chaitanya K. Narula
Materials Science and Technology Division
Oak Ridge National Laboratory
P.O. Box 2008, MS 6133, Building 4500S
Oak Ridge, TN 37831
Phone: (865) 574-8445; e-mail: narulack@ornl.gov

DOE Technology Manager: Jerry L. Gibbs
Phone: (202) 586-1182; fax: (202) 586-1600; e-mail: jerry.gibbs@ee.doe.gov

ORNL Technical Advisor: J. Allen Haynes
Phone: (865) 576-2894; fax: (865) 574-4913; e-mail: haynesa@ornl.gov

Contractor: Oak Ridge National Laboratory, Oak Ridge, Tennessee
Prime Contract No.: DE-AC05-00OR22725

Objectives

- The objective of this work is to search for durable emission treatment catalysts, including lean NO_x traps, TWC, oxidation catalyst, and SCR from a protocol based on an integrated approach between computational modeling and experimental development, design, and testing of new catalyst materials to rapidly identify the key physiochemical parameters necessary for improving the catalytic efficiency of these materials.

Approach

- Theoretical and experimental studies of Pt and Pd clusters and atoms supported on alumina and metal-exchanged zeolites. Interaction of CO, NO_x, and HC with Pt clusters supported on alumina and NO_x reduction on zeolites.
- Theoretical and experimental studies of understanding non-structural changes in catalyst under operating conditions and correlating the changes to performance.

Accomplishments

- We have shown that single-supported Pt and Pd atoms are highly active for CO oxidation, but only single-supported Pt atoms catalyze NO oxidation.
- Theoretical studies suggest CO and NO oxidation on single atoms is possible through a modified Langmuir-Hinshelwood scheme without involving the alumina supports.

- It is known that Pd stabilizes Pt toward sintering. Our experimental studies show agglomeration and sintering of Pt-Pd core-shell structure occurring via a reverse mitosis-type mechanism, leading to merging of core and shell.
- We have found that impregnation synthesized CuMn-ZSM-5 is a low-temperature NO_x reduction catalyst.

Future Direction

- Guided by our results, we plan to synthesize and evaluate low-temperature CO and NO oxidation catalysts for systems such as TWC and oxidation catalyst for diesel.
- Low-temperature NO_x catalyst that is effective even under standard NO_x reduction catalyst.
- Scale up and preparation for engine testing of heterobimetallic catalyst as a low-temperature NO_x reduction catalyst for diesel engines.

Introduction

This research focuses on an integrated approach between computational modeling and experimental development, design, and testing of new catalyst materials that we believe will rapidly identify the key physiochemical parameters necessary for improving the catalytic efficiency of these materials at low temperatures.

The development of new catalytic materials is still dominated by trial and error methods, even though the experimental and theoretical bases for their characterization have improved dramatically in recent years. Although it has been successful, the empirical development of catalytic materials is time consuming and expensive and brings no guarantees of success. Part of the difficulty is that most catalytic materials are highly non-uniform and complex and most characterization methods provide only average structural data. Now, with improved capabilities for synthesis of nearly uniform catalysts, which offer the prospects of high selectivity combined with state-of-the science characterization methods, we have a compelling opportunity to markedly accelerate the advancement of catalysis science and technology.

Recent advances in high-performance computing enables more realistic first-principles simulations of a large ensemble of atoms, including the local environment of a catalyst site in heterogeneous catalysis. These types of simulations, when combined with microscopic and spectroscopic characterization of catalysts, can lead to a much deeper understanding of the reaction chemistry that is difficult to decipher from experimental work alone.

We have been developing a protocol to systematically find the optimum catalyst that combines the power of theory and experiments for the atomistic design of catalytically active sites and can translate the fundamental insights gained directly to a complete catalyst system that can be technically deployed. Although it is beyond doubt computationally challenging, the study of surface, nanometer-sized, metal clusters is accomplished by state-of-the-art, density-functional-based, electronic-structure techniques. These techniques provide accurate energetics, force, and electronic information. We examine “computationally complex but experimentally simple” systems by both theoretical models and experimental work to forecast improvements to obtain optimum catalyst systems. Then, new catalysts are synthesized and evaluated for emission treatment. The results from FY 2015 are presented in the following sections.

Results

CO and NO Oxidation on Single-Supported Pt and Pd

Previously, we have shown that single-supported Pt atoms are highly effective CO oxidation[1] and NO oxidation[2] catalysts. A recent publication[3] suggested that single γ-alumina-supported Pd atoms can catalyze CO oxidation at low temperature. The proposed mechanism attributed this activity to a Langmuir-Hinshelwood type pathway, where CO adsorbs on Pd and reacts with oxygen on alumina. Thus, alumina acts as oxygen storage materials for CO oxidation.

We synthesized θ-alumina supported Pd materials by an impregnation method. The loading of 0.2% and 2% Pd results in Pd single atoms, rafts, and nanoparticles. The 0.2%-Pd-loaded sample redistributes Pd over alumina as monodisperse single Pd atoms after sintering at 700^{o}C (Figure 1, left). The samples labeled Pd_s-θ-alumina are monodisperse single Pd atoms with 0.2% Pd loading; Pd-θ-alumina contain rafts and nanoparticles with 2% Pd loading. The CO oxidation experiments were carried out at a fixed flow mixture of CO, oxygen, and helium at a constant hourly space velocity (i.e., constant weight of catalyst). CO oxidation on Pd_s-θ-alumina and Pd-θ-alumina initiates at about 104°C and 94°C, respectively, at a gas hourly space velocity (GHSV) of 51.4k h^{-1}. Pds/θ-alumina exhibits primarily large particles with a few single atoms after CO oxidation runs (Figure 1, right). Pd/θ-alumina also exhibits primarily large particles and even rafts become undefined particles.

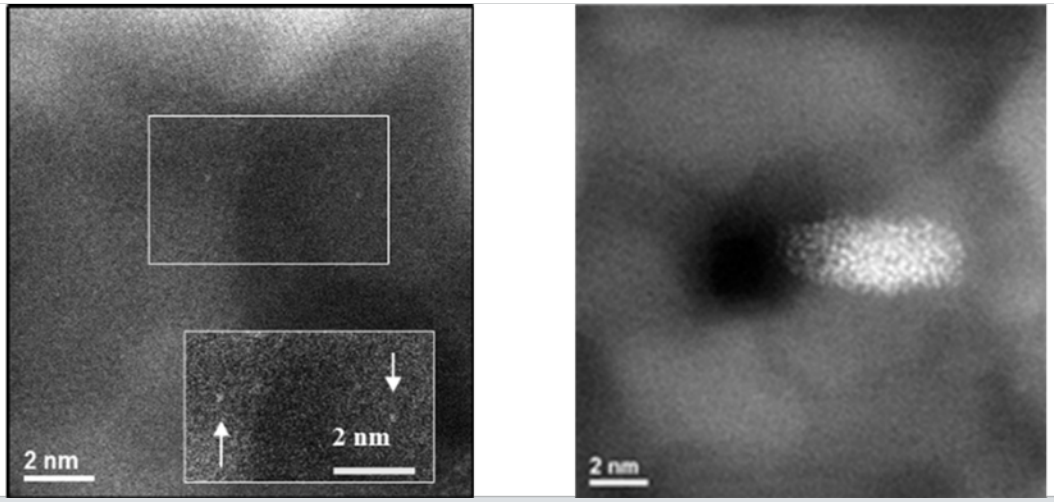

Figure 1: Images of fresh (left) and post-CO oxidation experiment (right) samples of Pd-θ-alumina.

While Pd/θ-alumina shows NO oxidation activity under both 50 ppm NO + 1% O_2 and 500 ppm NO + 5% O_2 (Figure 3) at a GHSV of 51.4 k h^{-1} conditions, the Pds/θ-alumina did not show detectable NO oxidation.

Thus, our work confirms low-temperature CO oxidation by θ-alumina supported-single Pd atoms, but showed no NO oxidation activity (Figure 2).

Our theoretical modeling shows that the proposed

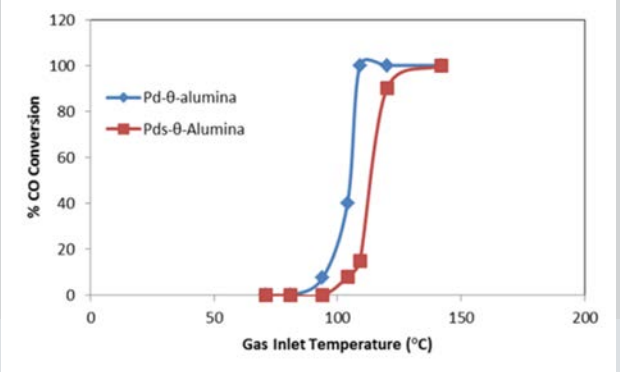

Figure 2: CO oxidation on Pds-alumina and Pd-alumina.

mechanism is incorrect and CO oxidation occurs without alumina involvement. This also explains a lack of NO oxidation on θ-alumina supported single Pd atoms.

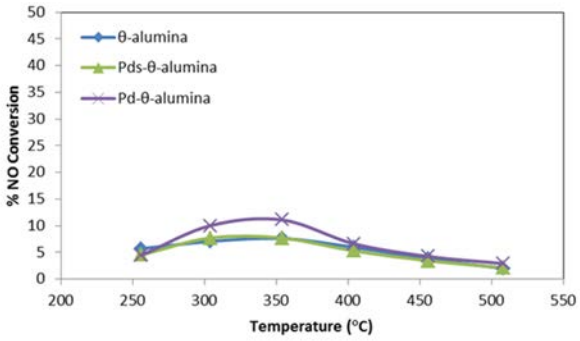

Figure 3: NO oxidation on Pds-alumina and Pd-alumina.

Pt-Pd/Alumina System

We have previously shown that pre-formed Pt-Pd nanoclusters with a Pt-Pd ratio of 3:1, 1:1, and 1:3 supported on γ-alumina are hydrothermally more stable than Pt/γ-alumina in the 500 to 900°C range and do not form extra large clusters of 300 to 400 nm commonly observed upon hydrothermal aging of Pt/γ-alumina. The study of hydrothermally aged core-shell Pt-Pd nanoparticles by Aberration Corrected Electron Microscopy shows two Pt-Pd core - shell particles in the process of coalescing after hydrothermal aging at 500°C [Figure 4].

We propose a new pathway that suggests the core-shell Pd-Pt particles first grow by merging cores and shells of individual particles under hydrothermal aging and, subsequently, form Pd-Pt alloys at very high temperatures.[4]

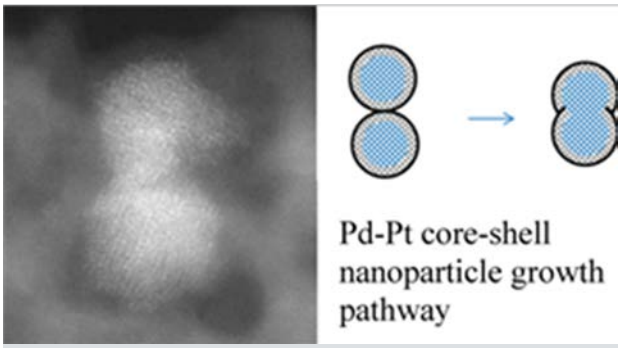

Figure 4: Pd-Pt core shell particles in the process of merging.

Heterobimetallic Zeolite Catalysts

We have previously shown that CuMn-ZSM-5 is a more effective catalyst than Cu-ZSM-5 at low temperatures under both on-road and off-road conditions and under fast and standard SCR conditions (Figure 5). We find that hydrothermal aging results in loss of benefits of Mn incorporation in CuMn-ZSM-5.

As noted previously, a comparison of NOx reduction under off-road conditions of NH_3-SCR (i.e., GHSV of 50K h^{-1}) shows that CuMn-ZSM-5 has higher NO_x conversion activity at 150°C compared to Cu-ZSM-5; however, there is no significant difference above 200°C (Figure 6).

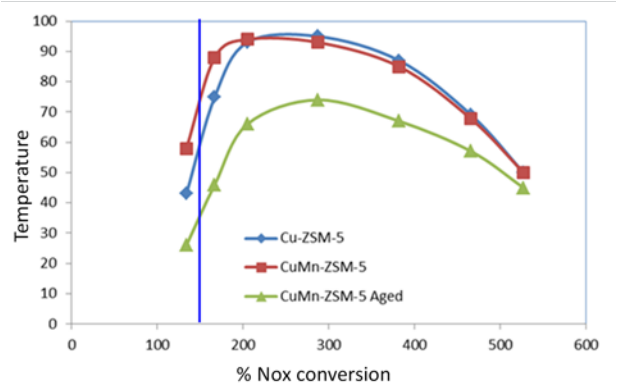

Figure 5: A comparison of CuMn-ZSM-5 with Cu-ZSM-5.

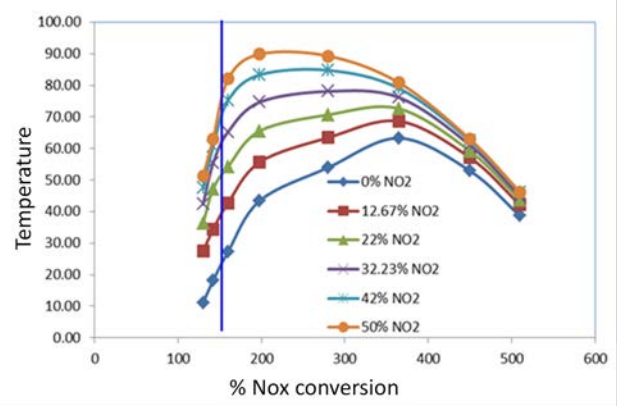

Figure 6: The impact of NO_2 on NO_x conversion under off-road conditions.

The impact of NO_2 on NO_x conversion under off-road conditions (Figure 2, middle) shows NO_2 has a dramatic impact on NO_x conversion. For example, about 82% of NO_x is reduced when NO and NO_2 are present in an equal ratio, but drop to about 28% when there is no NO_2. Even a small amount of NO_2 (i.e., 12.67%) increases the NOx conversion to 43% at 160°C.

Conclusions

Our previous work showed that single-supported Pt atoms are excellent CO oxidation catalysts. Our theoretical modeling work predicted that single-supported Pt atoms will also be able to catalyze NO, which is contradictory to conventional wisdom that reduction in Pt size leads to reduction in NO oxidation. Our experimental work confirmed that single -supported Pt atoms are as good as fully formed Pt particles for NO oxidation. This is an excellent example of the "catalyst by design" approach and work that has been published in N*ature's Scientific Reports*. At the same time, we found that an incorrect theoretical model (i.e., the model reported by Datye et al. 2014 for CO oxidation) for CO oxidation on single-supported Pd atoms incorrectly predicted facile NO oxidation on single supported Pd atoms. Our experiments showed that single-supported Pd atoms exhibit no NO oxidation activity. We found the correct model is a variation of Langmuir-Hinshelwood pathway, does not involve alumina, and is commensurate with experimental observations of facile CO oxidation, but not NO oxidation.

We also published our experimental results, showing a new growth pathway for core-shell Pd-Pt nanoparticles. These core-shell particles first grow by merging to form larger nano-particles that retain core-shell structure and finally transform to alloy structure.

Finally, we showed that CuMn-ZSM-5, prepared by impregnation method, is a better NOx reduction catalyst than Cu-ZSM-5 for both standard and fast SCR conditions.

Publications

Narula, C. K. and X. Yang, 2015, "Hydrothermally stable, low-temperature NOx reduction NH_3-SCR catalyst," U.S. Patent 8,987,162, March 24, 2015.

Narula, C. K. and X. Yang, 2015, "Zeolite-based SCR catalysts and their use in diesel engine emission treatment," U.S. Patent 8,987,161, March 24, 2015.

Narula, C. K., X. Yang, C. Li, A. Lupini, and S. J. Pennycook, 2015, "A Pathway for the Growth of Core-Shell Pt-Pd Nanoparticles," *Journal Physics Chemistry C* 119: 25114.

Narula, C. K. and M. M. DeBusk, 2015, "Catalysis on single supported atoms," in *Catalysis by Materials with Well-Defined Structures*, Ed. Z. Wu and S. H. Overbury, Elsevier, New York, pp 263.

Narula, C. K., L. F. Allard, G. M. Stocks, and M. M. DeBusk, 2014, "Remarkable NO oxidation on single supported platinum atoms," *Scientific Reports* 4: 7238.

Narula, C. K. and X. Yang, 2015, "Hydrothermally stable, low-temperature NOx reduction NH_3-SCR catalyst," U.S. Patent Application 20150238946, March 19, 2015.

Narula, C. K. and X. Yang, "Zeolite-based SCR catalysts and their use in diesel engine emission treatment," U.S. Patent Application 20150238944, March 19, 2015.

Narula, C. K., 2015, "NO Oxidation on Supported Single Pt Atoms," *North American Catalysis Society Meeting (NAM24)*, Pittsburgh, June 14 through 19, 2015.

Narula, C. K., L. F. Allard, G. M. Stocks, and M. M. DeBusk, 2015, "Catalysis on single supported atom catalysis," *American Chemical Society Meeting*, Boston, Massachusetts, August 10 through 13, 2015.

References

Narula, C. K. et al., 2013, *Journal of American Chemical Society* 135: 12634.

Narula, C. K. et al., 2014, *Scientific Reports* 4: 7238.

Datye et al., 2014, *Nature Communications*.

Narula, C. K., X. Yang, C. Li, A. Lupini, and S. J. Pennycook, 2015, "A Pathway for the Growth of Core-Shell Pt-Pd Nanoparticles," *Journal Physics Chemistry C* 119: 25114.

Project 18865 – Application-Specific Materials Simulation, Characterization, and Synthesis

Agreement 26391 (Task 2) – Applied ICME: Materials Needs for Ultra-High Efficiency Heavy-Duty Engine Operation

Charles E. A. Finne
Fuels, Engines, and Emissions Research Center
Energy and Transportation Science Division
2360 Cherahala Boulevard
Knoxville, TN 37932
Phone: (865) 946-1243; fax: (865) 946-1398; e-mail: finneyc@ornl.gov

DOE Technology Manager: Jerry L. Gibbs
Phone: (202) 586-1182; fax: (202) 586-1600; e-mail: jerry.gibbs@ee.doe.gov

ORNL Technical Advisor: J. Allen Haynes
Phone: (865) 576-2894; fax: (865) 574-4913; e-mail: haynesa@ornl.gov

Contractor: Oak Ridge National Laboratory, Oak Ridge, Tennessee
Prime Contract No.: DE-AC05-00OR22725

Objectives

- Study the effects of operating heavy-duty internal combustion engines at higher PCP to increase engine thermodynamic efficiency.
- Evaluate performance of currently available materials at current and projected future PCP conditions.
- Identify properties requirements of powertrain materials suitable to withstand a lifetime of operation at the elevated temperatures and pressures in future higher-efficiency heavy-duty engines.

Approach

- Use a three-dimensional finite element analysis (FEA) model of a modern 15L diesel engine that is provided by an original equipment manufacturer.
- Use computational simulations to estimate combustion intensity and heat transfer using computational fluid dynamics software and evaluate the thermo-mechanical effects on materials using finite element modeling software.
- Focus on the following three conditions: 190 bar (1 bar = 10^5 Pa) (current baseline), 225 bar (current stretch), and 300 bar (projected future) PCP.

- Measure relevant properties at a range of temperatures for an intermediate-grade material for use in models.
- Evaluate materials stresses and design safety factors with current materials and engine design, with a focus on the cylinder head, valve faces, liner, and piston.
- Use steady-state conditions cycling between pressure extrema to estimate fatigue life.

Accomplishments

- Tuned the engine combustion model to match loads, using constant boundary temperatures and gauged parametric sensitivities.
- Prepared engine combustion model for variable energy transfer mechanisms and boundary temperatures.
- Measured certain materials properties at a range of temperatures for compacted graphite iron (CGI)-450 samples.

Future Direction

- Evaluate and complete engine combustion simulations with high-fidelity temperature and heat flux treatment.
- Complete materials properties measurements for CGI-450 for use in stress and fatigue models.
- Identify properties needed for prospective materials to be suitable for future production environments.
- Develop simultaneous simulations of combustion and finite-element modeling.
- Extend these to light-duty engine applications.

Introduction

Heavy-duty internal combustion engines for the transportation sector are operating at increasingly high PCPs to achieve required increases in brake thermal efficiency to improve fuel economy. Current operating ranges are 75 to 190 bar PCP, and it is projected that the next decade or so could see over 250 bar and up to 300 bar PCP. The current generation of materials (such as gray cast iron) is not adequate for the projected higher pressures and temperatures of future higher-efficiency engines. Although candidate replacement materials (such as CGI) are being developed and evaluated for use in intermediate applications, a robust understanding of near-cylinder stresses and the materials properties necessary to enable desired engine efficiency and power densities of future HD engines is lacking.

Numerical simulations offer insight into the cylinder environment at such elevated pressures and temperatures and can help identify design needs and changes more rapidly than can be identified experimentally. The current practice of simulation can achieve low or high-dimensional modeling of the combustion environment or the cylinder/engine structure. However, a fully coupled, high-dimensional CFD-FEA simulation of combustion, heat transfer, and consequential material temperatures and stresses is a fundamental development need

Part of this limitation is the time and level of detail required to set up simulations. For FEA particularly, a proper meshing of complex geometries for a high-fidelity calculation of material stresses with conjugate heat transfer can be very labor intensive. However, with simplifications, a sufficient first-order estimate of future required materials properties can be gauged with simulations. This project is employing an incremental process

for this problem, starting with use of CFD results as inputs to FEA simulations and leading to fully coupled co-simulations.

Results

This year work focused on two areas: (1) acquisition and experimental characterization of materials properties for engine-grade CGI-450 samples and (2) simulation studies of engine combustion for better input to FEA simulations.

Materials properties for a candidate intermediate cast iron alloy, CGI-450, are not readily available at elevated temperatures up to 600 to 800°C; this lack of data limits the accuracy of the materials stress and fatigue modeling. Using materials specimens provided by an engine manufacturer, ORNL has begun measuring critical materials properties for CGI-450 over a range of temperatures from room temperature up to 600 to 800°C.

The following properties for at least one set of specimens were measured over a relevant temperature range:

- Thermal conductivity (see Figure 1)
- Thermal diffusivity
- Coefficient of thermal expansion
- Specific heats.

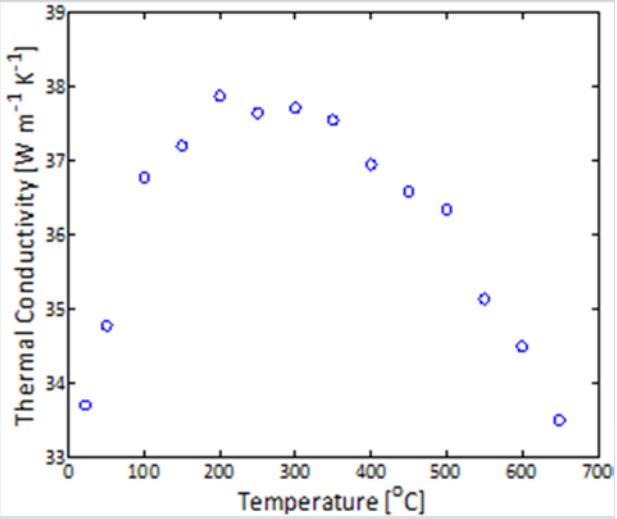

Figure 1: Measured mean thermal conductivity of one sample of CGI-450 as a function of temperature.

Additionally, material critical temperatures were measured, tensile tests were initiated, and samples for short-term creep tests were fabricated.

ORNL will complete measurements using multiple specimen sets for statistical reliability, verify and reduce data, and publish a report for public use within the next year. This valuable data resource will aid researchers and designers working to increase heavy-duty transportation engine fuel efficiency over the coming decades to meet the nation's needs and mitigate climate impact. Additionally, these properties data will be used in the current study to evaluate future engine performance.

Engine combustion modeling activities using CFD simulations included the following:

- Matching loads (indicated work output) at PCP target conditions using static boundary temperatures.
- Exploring sensitivities of combustion performance output to simulation parameters to help gauge uncertainties in predicted performance.
- Preparation of the simulation platform for dynamic boundary conditions and advanced energy-transport modes.

The computational study has focused on an interior cylinder of an in-line 6-cylinder 15-L 2013 production engine, with boundary conditions at the centerlines of neighboring cylinders. Figure 2 shows the overall

computational domain and the domain used by the CFD simulations, which include the cylinder and piston, valves, and intake and exhaust manifolds. The CFD domain will expand with calculation of conjugate heat transfer.

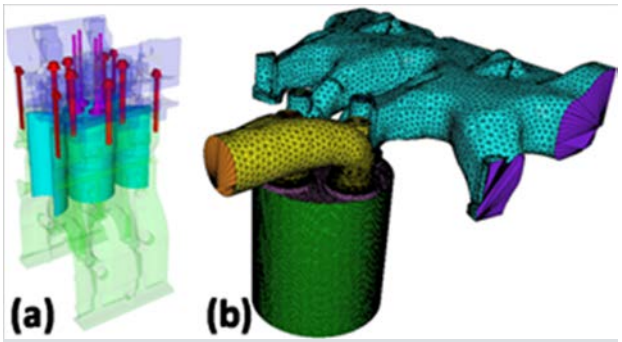

Figure 2: Overall computational domain (a) and CFD computational domain (b).

Part of the effort in matching loads involved employing advanced sampling methods, similar to design of experiments, to minimize the number of simulations required. This technique will accelerate future condition-matching efforts.

Combustion simulations rely on estimation of dozens of parameters used in various physical-process sub-models and on certain boundary conditions such as surface temperatures, which often cannot be measured experimentally over space and time and must be set at an estimated constant value. In-cylinder surface temperatures affect calculated heat fluxes from the cylinder surfaces, which in turn affect materials performance. Therefore, understanding the effect of estimation uncertainties in various parameters is important for assigning confidence to simulation predictions.

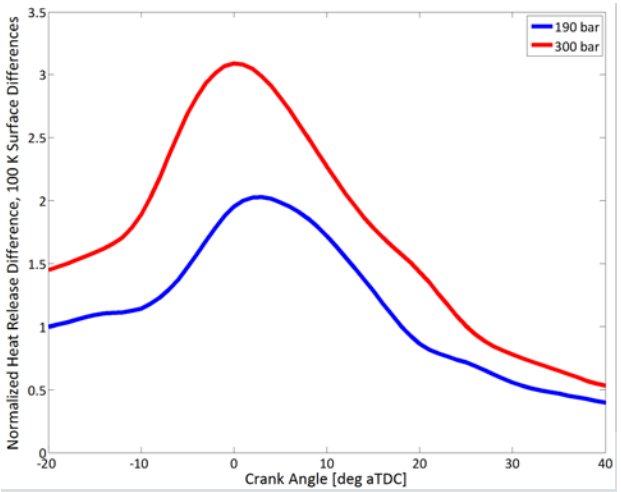

Figure 3: Difference in heat transfer across cylinder boundaries for a 100K difference in surface temperatures calculated at two PCP conditions.

A series of parametric variations was simulated at two PCP conditions (i.e., 190 and 300 bar). As an example, the effect of surface temperatures ±50K from the baseline condition during the combustion phase of the engine cycle is shown in Figure 3, with significant calculated heat transfers across the cylinder surfaces. Because estimating surface temperatures is very difficult, especially at high PCP conditions not fully explored experimentally, the use of conjugate heat transfer is desired.

To this end, the engine simulation platform has been adapted for conjugate heat transfer simulations for early next FY and for exploration of the effects of radiative heat transport. These methods will increase the accuracy of the inputs to the FEA modeling simulations that will be performed next fiscal year.

Conclusions

To produce the best estimates of materials properties and requirements of projected future operating conditions, accurate data inputs are needed. This year's activities began the process of filling gaps in openly available materials properties for a candidate advanced engine alloy, as well as provide estimates of thermal loads for conditions that have not been measured experimentally.

Project 18865 – Application-Specific Materials Simulation, Characterization, and Synthesis

Agreement 26391 (Task 3) – Applied ICME: Piezoelectric Materials

David S. Parker
Materials Science and Technology Division
Oak Ridge National Laboratory
P.O. Box 2008, MS 6056, Building 4100
Oak Ridge, TN 37831-6056
Phone: (865) 574-7128; fax: (865) 574-7659; e-mail: parkerds@ornl.gov

DOE Technology Manager: Jerry L. Gibbs
Phone: (202) 586-1182; fax: (202) 586-1600; e-mail: jerry.gibbs@ee.doe.gov

ORNL Technical Advisor: J. Allen Haynes
Phone: (865) 576-2894; fax: (865) 574-4913; e-mail: haynesa@ornl.gov

Contractor: Oak Ridge National Laboratory, Oak Ridge, Tennessee
Prime Contract No.: DE-AC05-00OR22725

Objectives

- Employ an ICME approach that encompasses close feedback between theory and experiment to meet the need for higher-performance piezoelectric materials. These would be used as actuators in the high-performance fuel injectors necessary to meet future DOE fuel efficiency targets.

Approach

- Perform first principles calculations of the structure and properties of perovskite oxides related to $Pb(Zr,Ti)O_3$ (PZT), along with synthesis and characterization of perovskite oxides with feedback between theory and experiment to optimize properties.

Accomplishments

- Theoretically found that oxide $(PbZr_{0.5}Ti_{0.5}O_3)_{0.75}(BiZn_{0.5}Ti_{0.5}O_3)_{0.25}$ is near a morphotrophic phase boundary with lattice distortion of c/a=1.08, which is substantially larger than the c/a value of PZT of approximately 1.022.
- Theoretically calculated the ferroelectric polarization of $(PbZr_{0.5}Ti_{0.5}O_3)_{0.75}(BiZn_{0.5}Ti_{0.5}O_3)_{0.25}$ and found it to be 0.94 C/m^2, which is significantly larger than the 0.81 C/m^2 value calculated for PZT using the same methods.
- Determined atomic displacement patterns of $(PbZr_{0.5}Ti_{0.5}O_3)_{0.75}(BiZn_{0.5}Ti_{0.5}O_3)_{0.25}$, finding larger cation displacements than in PZT.

– Sample synthesis of $(PbZr_{0.5}Ti_{0.5}O_3)_{0.9}(BiZn_{0.5}Ti_{0.5}O_3)_{0.1}$ and $(PbZr_{0.5}Ti_{0.5}O_3)_{0.9}(BiZn_{0.5}Zr_{0.5}O_3)_{0.1}$ completed. Predicted tetragonality of former compound confirmed.

– A technical report describing all of the above findings was completed and submitted to *Physical Review B.*

Future Direction

– Continue application of ICME approach to meet needs for improved piezoelectric materials.

– Identification and optimization of advanced piezoelectric materials.

Introduction

Improved fuel injection control is necessary in order to achieve DOE targets for fuel economy (such as those in the SuperTruck program[1]). These targets typically require advanced combustion techniques in order to achieve excellent fuel economy without sacrificing the control of criteria pollutants such as hydrocarbons, carbon monoxide, and nitrogen oxides. An example of these techniques is the use of high-performance fuel injectors, which typically use piezoelectric actuators (see Figure 1) such as $PbZr_{0.5}Ti_{0.5}O_3$ (PZT). Piezoelectrics are used for actuation because they change their length extremely rapidly upon application of an electric field. Because the electric field can be applied over very short time scales, this rapid motion allows precise control over the fuel injection process. However, PZT is not sufficiently high performance for the high-performance engines under current development. In particular, its tetragonality (a key measure of the distortion producible by electric fields) is only approximately 1.022,[2] limiting its performance; its ferroelectric polarization[3] at approximately 0.81 C/m^2 is not sufficiently large. Therefore, we seek a compound with similar characteristics to PZT but larger tetragonality and ferroelectric polarization.

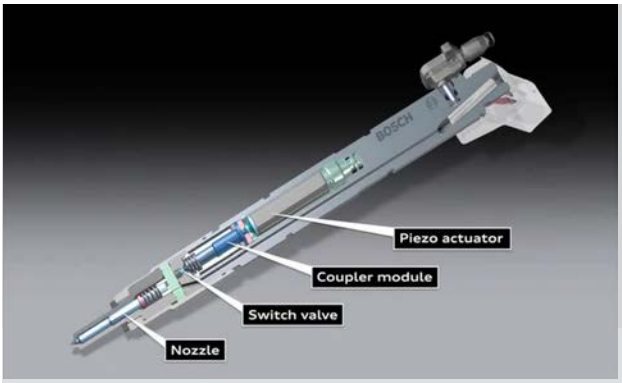

Figure 1: A piezoelectric-actuated fuel injector (image courtesy of Audi Technology Portal).

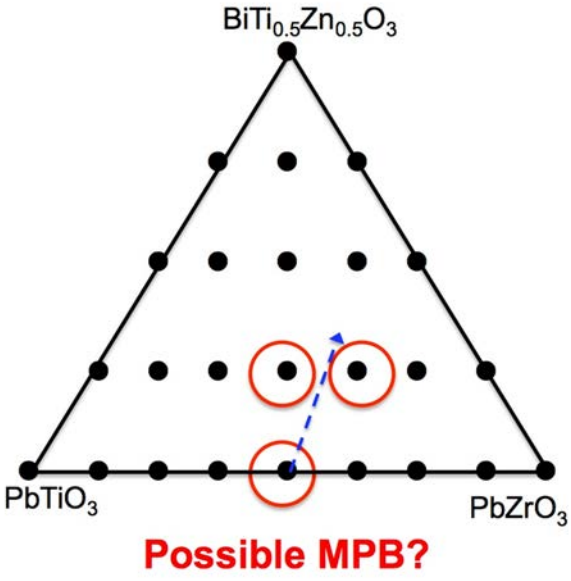

Figure 2: A ternary diagram of the compositions studied theoretically and experimentally, with the potential morphotrophic phase boundary indicated.

Piezoelectrics (such as PZT) are typically found near morphotrophic phase boundaries (MPB)[4] in a ferroelectric system, where the crystalline structure of a compound changes abruptly as a function of chemical composition. For example, the PZT system shows such a boundary very near the 50:50 mixture of Zr and Ti. As might be expected, the sensitivity of the

structure to the exact chemical composition near an MPB leads to a great enhancement of piezoelectric properties for materials near this point. However, finding an MPB experimentally is difficult and time consuming, because there is no way to know at what composition an MPB, if present, might emerge.

Therefore, we adopt a theoretical approach, based on the first principles density functional theory, combined with experimental synthesis and study. By studying the energies, atomic displacements (relative to symmetric "centered" positions), and ferroelectric polarizations of both tetragonal and rhombohedral structures (the usual structures on opposite sides of an MPB), we can estimate the potential piezoelectric performance of a material and assess its nearness to an MPB. We are studying the compositions depicted in Figure 2, with an eye toward a possible MPB as indicated in the figure. We summarize our theoretical and experimental results in the following section.

Results

In Table 1, we present the main result of our theoretical work. We calculated a total ferroelectric polarization of 0.94 C/m^2 for the alloy $(PbZr_{0.5}Ti_{0.5}O_3)_{0.75}(BiZn_{0.5}Ti_{0.5}O_3)_{0.25}$ (PZT-BZnT), which was substantially larger than the value of 0.81 C/m^2 that we calculated for the PZT alloy itself. This means that, as desired, PZT-BZnT will tend to be a higher performance alloy than PZT itself and could (upon experimental synthesis and optimization) become a candidate for usage in actuators for high-performance fuel injectors. These calculations also determine the c/a ratio of this compound to be 1.08, which is significantly larger than both the experimental value for PZT of 1.022 and our theoretical value for PZT of 1.06 [5]. Both the larger ferroelectric polarization and increased c/a ratio are characteristic of higher piezoelectric performance.

In Figure 3, we present a second important result of our theoretical work. We present the optimized displacement patterns (relative to the "symmetric" positions) of the atoms for the two alloys depicted in the second row of Figure 2 (i.e., red circles). These are $(PbZr_{0.5}Ti_{0.5}O_3)_{0.75}(BiZn_{0.5}Ti_{0.5}O_3)_{0.25}$ (PZT-BZnT) and $(PbZr_{0.5}Ti_{0.5}O_3)_{0.75}(BiZn_{0.5}Zr_{0.5}O_3)_{0.25}$, or PZT-PZnZr. Note that these two alloys differ only in the substitution of one Zr for one Ti, which is a change of only one atom per 40-atom cell. Despite this small change, the displacement patterns for the two alloys are completely different. In the top plot, the PZT-BZnT alloys show clear indications of tetragonality, with the largest displacements for all atoms being in the *c*-axis direction. However, for the PZT-BZnZr alloy in the bottom plot, it is the planar (i.e., *a* and *b*-axis) displacements that are largest, with the *c*-axis displacements an order of magnitude smaller, indicative of a monoclinic or perhaps rhombohedral phase. This is strong evidence for the existence of an

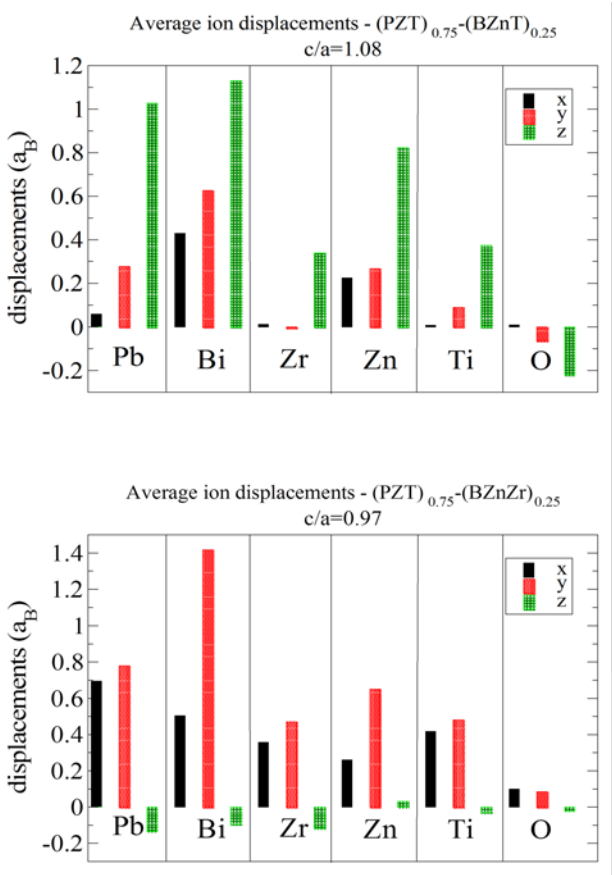

Figure 3: The optimized displacement patterns of the PZT-BZnT and PZT-BZnZr alloys.

MPB, because we observe a substantial change in crystal symmetry despite a very small change in chemical composition. Note that our calculations find a similar change in the crystalline symmetry of PZT between the two optimized structures for this material, as observed in experiment.

We have also performed experimental synthesis work on the two alloys described above: $(PZT)_{0.9}(BZnT)_{0.1}$ and $(PZT)_{0.9}(BZnZr)_{0.1}$. The lower concentrations (i.e., at 10% percent) of BZnT and BZnZr in these alloys were chosen to facilitate sample synthesis; we intend to study higher concentrations in FY 2016. We depict the x-ray diffractometer patterns of these alloys in Figure 4.

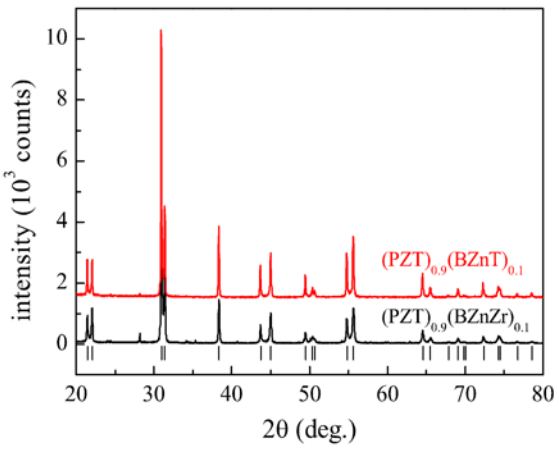

Figure 4. Measured x-ray diffraction patterns from the PZT-BZnT and PZT-BZnZr alloys.

Both alloys formed with a larger c/a ratio, approximately 1.028, than the PZT experimental c/a ratio of 1.022. This is consistent with the larger c/a ratios relative to PZT that we observed in our theoretical calculations. The PZT-BZnT alloy formed in a tetragonal state, consistent with our predictions in the top panel of Figure 3. While the PZT-BZnZr alloy also formed in a tetragonal state, this was after multiple synthesis firings at 1000°C. The initial synthesis efforts found a mixture of tetragonal and rhombohedral phases. This is suggestive of the desired MPB that we have found theoretically.

Conclusions

In Table 1, we present the main results of our theoretical work. We calculated a total ferroelectric polarization of 0.94 C/m^2 for the alloy $(PbZr_{0.5}Ti_{0.5}O_3)_{0.75}(BiZn_{0.5}Ti_{0.5}O_3)_{0.25}$ (PZT-BZnT), which is substantially larger than the value of 0.81 C/m^2 that we calculate for the PZT alloy itself. This means that, as desired, PZT-BZnT will tend to be a higher performance alloy than PZT itself and could (upon experimental synthesis and optimization) become a candidate for usage in actuators for high-performance fuel injectors. These calculations also determine the c/a ratio of this compound to be 1.08, which is significantly larger than both the experimental value for PZT of 1.022 and our theoretical value for PZT of 1.06.[5] Both the larger ferroelectric polarization and increased c/a ratio are characteristic of likely higher piezoelectric performance.

We have theoretically and experimentally studied alloys of PZT with $BiZn_{0.5}Ti_{0.5}O_3$ (BZnT) and $BiZn_{0.5}Zr_{0.5}O_3$ (BZnZr). First principles calculations of a $(PZT)_{0.75}(BZnT)_{0.25}$ alloy found a tetragonal ground state and a ferroelectric polarization of 0.94 C/m^2, which was significantly larger than the PZT value of 0.81 C/m^2 that was calculated using the same methods. In addition, we found evidence for an MPB near this composition and we found a substantially different ground state (rhombohedral or monoclinic) for a $(PZT)_{0.75}(BZnZr)_{0.25}$ alloy differing only slightly in composition. Experimental work (Michael A. McGuire) demonstrated the feasibility of sample synthesis in this system. In addition, we find some experimental evidence for the MPB, with a tetragonal symmetry found for $(PZT)_{0.9}(BZnT)_{0.1}$ and the initial sample synthesis for $(PZT)_{0.9}(BZnZr)_{0.1}$ finding a mixture of rhombohedral and tetragonal phases, suggestive of the MPB. A technical report summarizing these findings has been submitted for publication.

References

DOE SuperTruck Program Benefits Analysis, TA Engineering, December 2012, available at http://www.transportation.anl.gov/pdfs/TA/903.PDF.

Frantti, J., J. Lappalainen, S. Eriksson, V. Lantto, S. Nishio, M. Kakihana, S. Ivanov, and H. Rundlöf, "Neutron diffraction studies of Pb (Zr_xTi_{1-x})O_3 ceramics," *Japanese Journal of Applied Physics* 39**:** 5697.

Sághi-Szabó, G., R. E. Cohen, and H. Krakauer, 1999, "First-principles study of piezoelectricity in tetragonal $PbTiO_3$ and $PbZr_{1/2}Ti_{1/2}O_{3,}$" *Physical Review B* 59: 12771.

Cooper, V. R., A. S. Henry, S. M. Takagi, and D. J. Singh, 2011, "First principles prediction of a morphotropic phase boundary in the Bi ($Zn_{1/2}Ti_{1/2}$)O_3-($Bi_{1/2}Sr_{1/2}$)($Zn_{1/2}Nb_{1/2}$)O_3 alloy," *Applied Physics Letters* 98: 122903.

Ghita, M., M. Fornari, D. J. Singh, and S. V. Halilov, 2005, "Interplay between A-site and B-site driven instabilities in perovskites." *Physical Review B* 72: 054114.

Parker, D. S., M. A. McGuire, and D. J. Singh, 2015, "Enhanced ferroelectric polarization and potential morphotrophic phase boundary in PZT-based alloys," submitted to *Physical Review B*, September 2015.

Project 18865 – Application-Specific Materials Simulation, Characterization, and Synthesis

Agreement 26391 (Task 4) - Applied ICME for New Propulsion Materials: Permanent Magnets

Michael A. McGuire
Materials Science and Technology Division
Oak Ridge National Laboratory
P.O. Box 2008, MS 6056, Building 4100
Oak Ridge, TN 37831-6056
Phone: (865) 574-5496; fax: (865) 576-5023; e-mail: mcguirema@ornl.gov

DOE Technology Manager: Jerry L. Gibbs
Phone: (202) 586-1182; fax: (202) 586-1600; e-mail: jerry.gibbs@ee.doe.gov

ORNL Technical Advisor: J. Allen Haynes
Phone: (865) 576-2894; fax: (865) 574-4913; e-mail: haynesa@ornl.gov

Contractor: Oak Ridge National Laboratory, Oak Ridge, Tennessee
Prime Contract No.: DE-AC05-00OR22725

Objectives

- Identify and characterize new permanent magnet materials that do not contain rare earth elements.
- Develop an understanding of the magnetic properties of candidate materials through a closely coupled experiment and theory to direct work toward improved permanent magnet properties.

Approach

- Synthesize and characterize magnetic properties of rare-earth-free ferromagnetic materials that have potential for permanent magnet applications and are relevant to hybrid and electric drive systems.
- Use results of first-principles calculations of magnetic properties to guide chemical modification for performance enhancements.
- Examine tetragonal $Fe_3(Si/Ge/Sn)$ and $Fe_5(Si/P)B_2$ compounds as potential permanent magnet materials.
- Understand thermal evolution of microstructural and magnetic properties of $Hf_2Co_{11}B$ permanent magnet alloys.

Accomplishments

- Published six technical reports in peer-reviewed scientific literature.
- Demonstrated experimental control over magnetic anisotropy in Fe_3Ge and Fe_3Sn using strategies

predicted by theoretical calculations.

- Confirmed the importance of far-from-equilibrium processing in development of permanent magnetic properties of $Hf_2Co_{11}B$ alloys.
- Determined effects of Mn and Co substitution on the magnetization and anisotropy of Fe_5PB_2 and Fe_5SiB_2.
- Identified new high-temperature ferromagnet composed of Fe, Si, and B.

Future Direction

- Optimization studies of magnetic anisotropy in Fe_3Si-Fe_3Ge-Fe_3Sn-based ferromagnets using chemical substitutions for iron.
- Characterize newly discovered ferromagnet in the Fe-Si-B system.

Introduction

In the Vehicles Technology Multi-Year Program Plan, the propulsion materials activity has identified a limited domestic supply of materials required for advanced vehicle technology, among them rare-earth elements, as a key barrier to enabling expanded capabilities of electric drive systems. Currently, no alternative materials do not contain rare earth elements and are competitive with $Nd_2Fe_{14}B$-based permanent magnets. The availability of permanent magnets composed of lower-cost elements with a more stable supply would enable significant progress toward the VTO cost targets for electric and hybrid drive systems.

The "strength" of a permanent magnet can be characterized by the amount of energy that is stored in the magnetic field and is available to do work. This is quantified by the maximum product of the magnetic induction (B), in the presence of a demagnetizing field (H) written as $BH_{max.}$ Large values of BH_{max} are possible in materials with a large magnetic moment that persists upon removal of the magnetizing field (i.e., remnant magnetization or remanence), and a large field required to reverse the direction of that moment (coercive field or coercivity). These are extrinsic properties strongly dependent on microstructure.

The strongest $Nd_2Fe_{14}B$-based magnets have energy products near 50 MGOe, remanence near 15 kG, and coercivity near 11 kOe at room temperature. The best $Nd_2Fe_{14}B$-based magnets designed to operate near 180°C and have, at room temperature, energy products near 40 MGOe, remanence near 13 kG, and coercivity near 25 kOe. These extrinsic properties can be seen as a benchmarks against which candidate materials can be compared. However, because cost is a significant concern, a new technologically important magnet material does not need necessarily meet or exceed these values of energy product, remanence, and coercivity. Recently, Coey has proposed the idea of "gap" magnets, which fill the role of balancing cost with performance. Based on this analysis, magnets with $BH_{max} \approx$ 38, 25, and 12 MGOe would be impactful if their cost is less than 100, 50, and 10 $/kg, respectively.

Intrinsic physical properties place some limitations on the ultimate magnet performance, including saturation magnetization (M_S), the anisotropy field (H_A), and the Curie temperature (T_C). These are the properties of interest in studies of new compounds as candidate permanent magnet materials. As a reference, the intrinsic properties of $Nd_2Fe_{14}B$ include an anisotropy field of about 73 kOe, a saturation magnetization of about 16 kG, and a Curie temperature of 310°C. In general, good candidate materials should have saturation magnetization exceeding 10 kG and anisotropy fields exceeding 10 kOe. Importantly, the anisotropy must be uniaxial,

meaning there is a single preferred direction for the magnetic moments and opposed to planar. Many of these properties can be calculated from first principles once the crystal structure of the material is determined. In addition, these properties are often very sensitive to composition; therefore, chemical substitutions can be used to tune the magnetic performance in both theoretical and experimental studies.

Developing substitutes for $Nd_2Fe_{14}B$-based permanent magnets is a daunting but important materials challenge that will require a long-term research effort. This effort must include advancements in performance and understanding of known rare earth-free permanent magnets, as well as identification and development of new magnet materials. The objective of this task is to examine materials identified through both simple chemical design criteria and first principles density functional theory calculations as potential permanent magnets relevant for use in electric and hybrid drive systems.

Results

Accomplishments from FY 2015 related to several ferromagnetic material systems are highlighted here; full details of the work are found in the publications listed in the reference section. The following subsections highlight the results from theory-guided efforts to manipulate the magnetic anisotropy of Fe_3Ge and Fe_3Sn,[1,2] experimental and computational studies of the intrinsic magnetic properties and effects of compositional tuning of Fe_5SiB_2 and Fe_5PB_2,[3] and an investigation of the microstructural and magnetic evolution of amorphous $Hf_2Co_{11}B$ alloys on crystallization and thermal annealing.[4] Work on the $Fe_3(Ge/Sn)$ and $Fe_5(P/Si)B_2$ systems was done in collaboration with the Critical Materials Institute, an Energy Innovation Hub funded by DOE, Energy Efficiency and Renewable Energy, and the Advanced Manufacturing Office. Work on MnBi[5] and $BaFe_{12}O_{19}$[6] were in collaboration with DOE, Basic Energy Sciences, and the Materials Sciences and Engineering Division.

Magnetic Anisotropy of Fe_3X, X = Ge, Sn

These studies[1,2] were motivated by literature reports that suggest good permanent magnet performance may be attainable in these compounds.

Fe3Sn had been reported to be a uniaxial ferromagnet with a large moment and high TC. However, first principles calculations conducted as part of the present study indicated planar anisotropy was favored; this was confirmed by experimental measurements of magnetization along different crystallographic directions. Thus, Fe3Sn was found to be unsuitable for permanent magnet applications. Because the magnetization and Curie temperature were favorable, calculations were performed to investigate the possibility of inducing uniaxial anisotropy by chemical substitutions. Substitution of Sb for Sn at a level of 25% was predicted to switch the magnetism to uniaxial. Experimental efforts confirmed this were unsuccessful due to low solubility of Sb in the material. However, for low Sb doping, the planar anisotropy was reduced, confirming the trend predicted by theory.

Fe3Ge has the same hexagonal crystal structure as Fe3Sn, with a similarly high curie temperature, magnetization, and planar anisotropy at room temperature. Uniaxial anisotropy is reported at higher temperature (i.e., from about 110°C up to the curie temperature of about 350°C). In this task, we considered alloying in Fe3Ge as a means to extend the uniaxial behavior to room temperature. First principles calculations suggested this could be achieved by Si substitution for Ge. Unlike Fe3Ge, Fe3Si is cubic; therefore, the solubility of Si in Fe3Ge is limited. It was found that about 10% Si favors uniaxial anisotropy, extending the temperature range over which it is observed by about 35°C and bringing the transition from planar to uniaxial down to near room temperature (40°C). The change in the anisotropy transition temperature, curie temperature, and temperature ranges over which uniaxial behavior is observed are summarized in Figure 1.

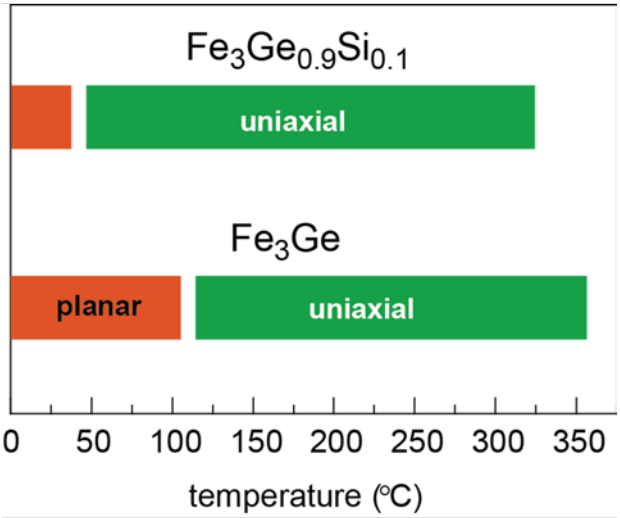

Figure 1: Temperature ranges over which uniaxial (i.e., green, desirable) and planar (i.e., orange, undesirable) magnetic anisotropy is observed.

Alternative synthesis or processing strategies, including co-doping with other elements, may enable higher concentrations of Sb in Fe_3Sn and Si in Fe_3Ge. If so, this should produce promising permanent magnet materials.

Intrinsic Properties and Alloying in Fe_5PB_2 and Fe_5SiB_2

Fe_5PB_2 and Fe_5SiB_2 are known uniaxial ferromagnets containing earth abundant elements, but no systematic study of their crystallography, magnetic properties, and alloying behaviors has been reported. The effects of Co and Mn substitution were investigated using both experiment and theory.[3]

Table 1. Properties of Fe5(P/Si)B_2-based ferromagnets.

	Unit Cell Volume (Å^3)	M_{Sat} 300K (T)	Curie Temperature (°C)
Fe_5PB_2	311.7	1.09	367
Fe_4CoPB_2	307.9	0.87	242
Fe_4MnPB_2	313.3	1.00	377
Fe_5SiB_2	318.5	1.21	511
Fe_4CoSiB_2	314.4	0.961	402
Fe_4MnSiB_2	321.2	1.17	497

Magnetization and diffraction measurements show all six compounds to be uniaxial ferromagnets at room temperature, with stronger anisotropy in the phosphides than the silicides. Experimental results, including unit cell volume, saturation magnetization, and T_C for the six compounds examined in this study are summarized in Table 1. Cobalt substitution reduces T_C by more than 100°C and reduces M_{sat} by about 20%. Manganese has a

much smaller effect on both properties. This indicates that Co is non-magnetic and Mn is ferromagnetic in these structures. Results of the calculations of magnetic anisotropy and magnetic moment agree well with measured values. During the course of this work, a new Fe-Si-B-based ferromagnet was discovered and will be the subject of further investigation.

Evolution of Microstructural and Magnetic Properties of $Hf_2Co_{11}B$ Alloys

A series of systematic annealing studies[4] were performed on amorphous $Hf_2Co_{11}B$ magnet alloys. Findings include rapid acceleration of the microstructural evolution caused by the application of a magnetic field during annealing and close ties between the observed microstructure and resulting magnetic properties (Figure 2). The best properties occur with a high concentration of small $HfCo_7$-type precipitates. Figure 2 shows higher coercivity in the fine grained microstructure.

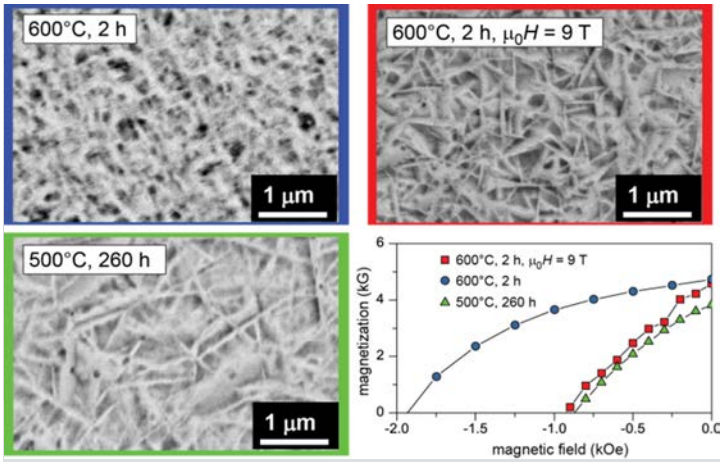

Figure 2: Scanning electron micrographs and corresponding demagnetization curves for $Hf_2Co_{11}B$ ribbons after annealing at the indicated conditions.

None of the post-annealing treatments of the amorphous precursor material produced coercivity as high as that found previously in under-quenched melt-spun ribbons of this material. This indicates that non-equilibrium conditions are key to evolving optimized microstructures in this complex permanent magnet alloy.

Conclusions

It is expected that increasing the Sb content in Fe_3Sn or Si content in Fe_3Ge will produce a promising uniaxial magnet material.

A new ferromagnet composed of Fe, Si, and B was discovered and will be the subject of future study.

Far from equilibrium, processing produces the best magnetic properties in $Hf_2Co_{11}B$ alloys.

References

Sales, B. C., B. Saparov, M. A. McGuire, D. J. Singh, and D.S. Parker, 2014, "Ferromagnetism of Fe_3Sn and Alloys," *Scientific Reports* 4: 7024.

Shanavas, K. V., M. A. McGuire, and D. S. Parker, 2015, "Electronic and Magnetic Properties of Si Substituted Fe_3Ge," *Journal of Applied Physics* 118: 123902.

McGuire, M. A. and D. S. Parker, 2015, "Magnetic and structural properties of ferromagnetic Fe_5PB_2 and Fe_5SiB_2 and effects of Co and Mn substitutions," *Journal of Applied Physics* 118: 163903.

McGuire, M. A. and O. Rios, 2015, "Evolution of magnetic properties and microstructure of $Hf_2Co_{11}B$ alloys," *Journal of Applied Physics* 117: 053912.

McGuire, M. A., H. Cao, B. C. Chakoumakos, and B. C. Sales, 2014, "Symmetry-lowering lattice distortion at the spin reorientation in MnBi single crystals," *Physical Review B* 90: 174425.

Cao, H. B., Z. Y. Zhao, M. Lee, E. S. Choi, M. A. McGuire, B. C. Sales, H. D. Zhou, J.-Q. Yan, and D. G. Mandrus, 2015, "High pressure floating zone growth and structural properties of ferrimagnetic quantum paraelectric $BaFe_{12}O_{19,}$" *APL Materials* 3: 062512.

Project 21656 – Development of High-Strength Crankshafts

Agreement 27387 – ANL: Development of High-Performance Crankshafts

Dileep Singh (coworkers: J. Hryn and C. Chuang)
Energy Systems Division
Argonne National Laboratory
9700 S. Cass Avenue
Argonne, IL 60439
Phone (630) 252-5009; fax: (630) 252-2785; e-mail: dsingh@anl.gov

DOE Technology Manager: Jerry L. Gibbs
Phone (202) 586-1182; fax: (202) 586-1600; e-mail: jerry.gibbs@ee.doe.gov

ANL Technical Advisor: John Hryn
Phone (630) 252-5894; fax: (630) 252-5132; e-mail: jhryn@anl.gov

Contractor: Argonne National Laboratory, Argonne, Illinois
Prime Contract No.: DE-FOA-0000793

Objectives

- Develop cast steel alloys and processing techniques that are tailored for high-performance crankshafts and achieve target as-cast properties of 800-MPa ultimate tensile strength and 615 MPa yield strength as a replacement for expensive forgings.
- Develop cast materials that can achieve sufficient local fatigue properties to satisfy the durability requirements in today's high-performance gasoline and diesel engine applications, which currently use forged crankshafts.
- The stiffness, ductility, and high-cycle fatigue properties of the newly developed alloy will be over other traditional cast crankshaft material choices.
- As part of the project team, Argonne National Laboratory (ANL) will utilize various advanced material characterization capabilities provided by the Advanced Photon Source to determine internal casting quality of the samples and conduct innovative in-situ measurements of phase evolutions and damage nucleation during heating and cooling under various loading conditions. The goal is to better understand the chemistry-structure-process relationships.

Approach

- Use high-energy tomography to assess the basic casting quality, including size and distribution of porosity and inclusion of casting samples. Absorption and/or phase contrast micro-tomography will be used in conjunction with metallography to understand the three-dimensional structure (e.g., shape, cell size, and interconnectivity) of the internal defects.

– Use in-situ high-energy x-ray diffraction to study phase evolution for new compositions being developed; correlate this to the mechanical performance of alloys. The experiments will involve heating the samples to a high temperature (i.e., 1200 to 1300 °C) in a ceramic mold and monitoring the phases developed as the sample is cooled down at cooling rates similar to those in actual castings.

– Mechanical testing equipment available at the beam line will be utilized to conduct in-situ mechanical property characterizations up to a temperature of 350°C.

Accomplishments

– Developed apparatus for an in-situ high-temperature imaging experiment. The system allows the in-situ characterization of phase formation and dendrite growth during the alloy solidification process.

– Conducted an in-situ phase evolution experiment to validate the system and successfully demonstrate the in-situ phase characterization capabilities using high-energy imaging techniques.

Future Direction

– Utilize a developed three-dimensional diffraction and imaging technique to evaluate the microstructure-process condition relationship of casting alloys.

Introduction

The demand for smaller and lower weight engines with improved efficiency to reduce fuel consumption, emissions, and costs for vehicle use, while maintaining or even increasing engine performance, has been increasing rapidly in recent years. Increasing engine power and efficiency requires higher operating cylinder pressures, resulting in increased loads on the crankshaft. For high-performance engines, the loads on the crankshaft are too high for today's cast materials and are required to be produced from more expensive forgings. Material and process developments are required for design and production of high-performance cast crankshafts that meet strength and other functional requirements in order to produce a high-efficiency engine that is both lightweight and cost-effective.

The objective of this project is to develop cast steel alloys and processing techniques that are tailored for high-performance crankshafts and achieve target as-cast properties of 800 MPa ultimate tensile strength and 615 MPa yield strength as a replacement for expensive forgings. Even more challenging, the cast material must achieve sufficient local fatigue properties to satisfy the durability requirements in today's high-performance gasoline and diesel engine applications that currently use forged crankshafts.

The project team will focus on cast steel alloys and processes to take advantage of the higher stiffness, ductility, and high-cycle fatigue properties over other traditional cast crankshaft material choices. The team will tailor the alloy design and develop innovative processing methods to produce clean steel castings with refined microstructures and required soundness and hardenability. Utilizing the casting process and the stiffness advantage of steel will allow the weight reduction potential to be maximized without sacrificing performance. The technology developed should be able to produce high-performance crankshafts at no more than 110% of the cost of current production low-performance cast units.

As part of the project team, ANL will utilize the Advanced Photon Source to quantify casting quality and conduct innovative in-situ measurements of phase evolutions and damage nucleation during thermal and mechanical loading conditions to better understand the chemistry-structure-process relationships.

For the first year of the project, ANL focused on three-dimensional tomography of casting quality and structure. In this task, x-ray tomography will be used to assess the basic casting quality of casting samples, including size and distribution of porosity and inclusions. Absorption and/or phase contrast micro-tomography will be used in conjunction with metallography to understand the three-dimensional structure (e.g., shape, cell size, and interconnectivity) of the internal defects. Understanding the three-dimensional features of the microstructure (such as grain size and phase distribution) will also be of interest.

In the second year of the project, ANL designed built and validated the high-temperature apparatus for the in-situ phase evolution studies. The objective of this part was to study phase evolution for the new compositions being developed by high-energy x-ray diffraction and/or imaging techniques and correlate the micro-structure of the alloy to the process parameters and mechanical performance of the alloys. A typical experiment will involve heating the samples to their liquid state (i.e., high temperature 1200 to1400 °C) in a ceramic mold and monitor the phases developed as the sample is cooled down (at rates similar to the actual castings process). The technique allows capturing phase evolution by using high-energy x-rays in the bulk as a function of time. Formation of precipitates (i.e., size, distributions, and locations) and voids can be followed as the sample is cooled down. Information generated will be critical in the alloy development and optimization of the controlled cooling process to achieve the required structures.

Results

In the past year, ANL's effort focused on development of an experimental apparatus for the in-situ phase evaluation studies. The primary activities included: (1) design and build a high-temperature environmental chamber to heat, hold, and cool the sample in a controlled manner, which allows in-situ phase evolution studies and (2) conduct the in-situ melting experiment at the Advanced Photon Source in ANL to validate the prototype test system.

High-Temperature Environmental Cell

To observe phase formation in real-time during the solidification process, one needs to melt the sample and cool it with a varied cooling rate. A sample holder has to be able to hold the sample at both liquid and solid state without reacting with the material; the design needs to allow the synchrotron x-ray to go in and out of sample for structure visualization. During this phase of the project, we utilized cast iron from a related project as a model material for testing because alloys compositions for the cast crankshaft are being developed.

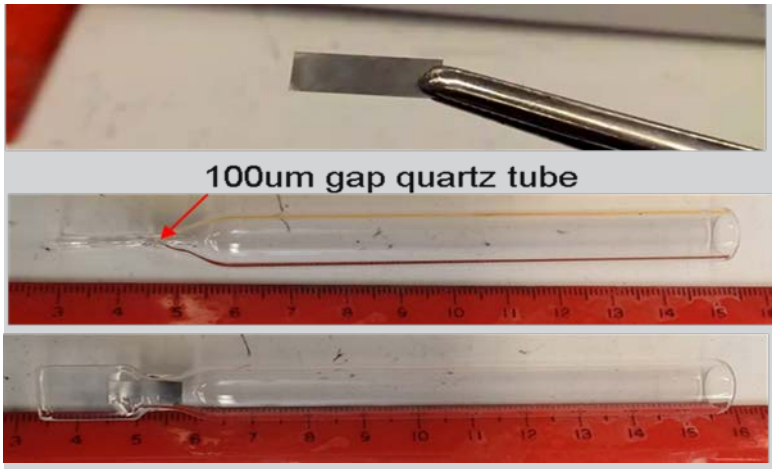

Figure 1: (Top) Geometry of the sample is a 5 x 12 x 0.1-mm sheet prepared by electric discharge machining and mechanical polishing. (Middle) The cell is made of quartz. A 100-um wide (inner dimension) and 8 x 12-mm rectangular container that hosts the thin sheet is attached to the tube. (Bottom) A sample is placed inside the cell.

From previous studies, we have learned that the size of graphite particles in cast

iron are in the range of 10 to 100 µm. In order to observe the individual graphite particles, a special sample cell was designed to avoid over-lapping of images of particles in the x-ray incident direction. With this design, one can observe the nucleation and growth of individual solid phases during solidification. The cell has an 8-mm x 12-mm x 0.12-mm rectangular chamber, which is attached to a ½in. diameter tube (Figure 1). The sample was polished to a thin sheet with a thickness of 80 to 100 µm in order to fit into the sample chamber at the bottom of the tube.

The overall x-ray radiography setup is shown in Figure 2. An RF suscepter was added to the system as a sleeve to cover the thin-rectangular chamber. It was used to improve the temperature uniformity and heating efficiency of the sample cell. A 4-mm diameter window was made on the susceptor for an x-ray to pass through. An additional quartz tube was used to contain the whole system and provides a controlled atmosphere (either filled with argon or under vacuum). The main purpose of the second tube is to avoid the degradation of the susceptor at an elevated temperature. The whole dual tube cell was placed inside a multi-turn induction coil for the experiment.

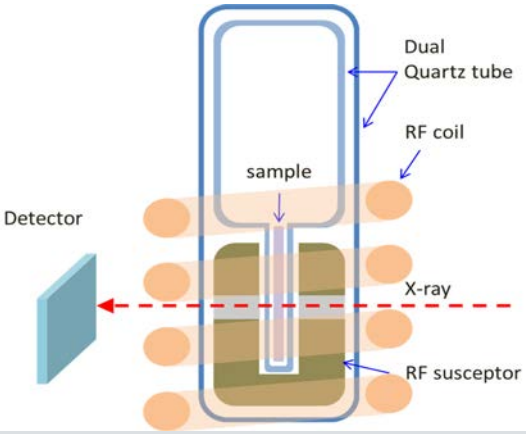

Figure 2: Schematic diagram of an x-ray imaging (radiography) system.

High-energy x-ray was incident from one side of the sample and a two-dimensional area detector was placed at the down-stream position to record the radiography images of the sample. The induction heating system was selected to minimize the thermal load to the environment and provide a wide range of heating and cooling rates.

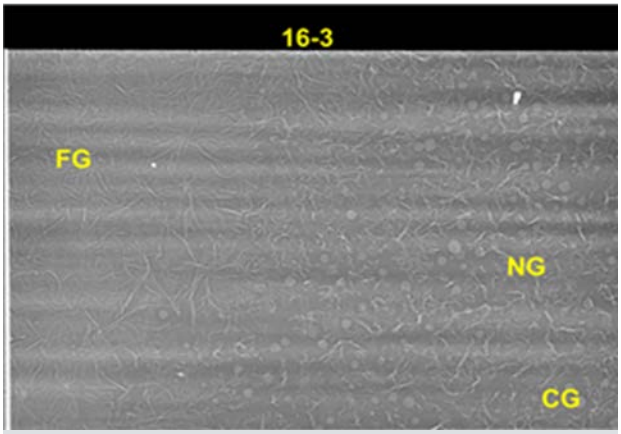

Figure 3: Radiography image of the sample before melting. The sample consists of flake graphite (FG), nodular graphite (NG), and compact graphite (CG)

A selected cast iron sample was used to validate the system. The sample is a high CE, high sulfur, high Mg, low-post inoculant level, zero Al addition cast iron. The design of the process condition is to have a compact graphite iron with moderate nodularity. A typical radiography image of the sample in the as-polished condition is shown in Figure 3. The image showed that the sample contains flake graphite in addition to the expected nodular graphite and compact graphite.

In-Situ Phase Evolution Experiment

The in-situ melting experiment was conducted at Sector 1 of the Advanced Photon Source to validate the system. The sample was placed inside the cell and heated by induction coil until it melted. The whole process was monitored by radiography images. After the sample was melted, the x-ray image detector was moved around to locate the boundary of the heating zone. Once the liquid/solid interface was located, the specimen

underwent controlled cooling, during which the images of the specimen were recorded sequentially in 1-second intervals until the solid-liquid interface passed through the whole region of observation.

A series of images are shown in Figure 4. The first image denoted 0 seconds in the image before cooling. The top, featureless region is the liquid and the bottom is the unmelted sample. The feature in the bottom is similar to the flake graphite in Figure 3. A solid-liquid interface is also shown in the figure with a width of about 140 µm.

During the cooling process, austenite dendrites were first found to nucleate at the solid-liquid interface and grow into the liquid region, the size of the dendrite arm is in the range of several hundreds of micrometers. At 48 seconds, the length of the dendrite arm grew to around 290 µm and the newly solidified region was around 110 µm (i.e., 250 µm minus the original 140 µm before cooling). At this stage, no graphite phase was observed. As cooling continued past 53 seconds, some graphite particles were found to nucleate at the root of the dendrite arms. These graphite particles nucleated and grew individually. At the 64-second mark, the graphite particles nucleated not only at the root of the dendrite but also within the dendrite region. The contrast of dark dendrites in the image of 53 seconds and 64 seconds are due to diffraction extinction. It suggests that the whole dendrite is a large single crystal. When the dendrite structure rotates to a certain direction that fulfills the Bragg diffraction condition, the x-ray will be diffracted out and leave a dark spot on the transmitted radiography image. The majority of graphite particles formed in this period were identified as Type IV (per ISO 945) or Type-III (per American Society for Testing and Materials A247) graphite. It is aggregate, or a temper carbon with size ranging from 40 to 80 µm (diameter of the bounding circle).

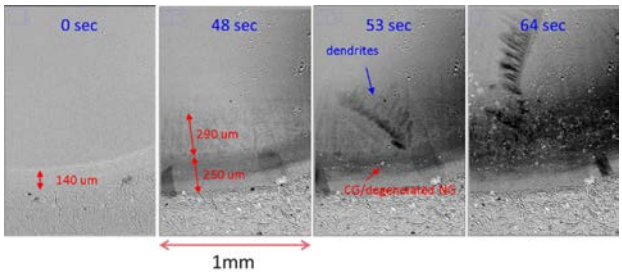

Figure 4: Radiography images of the sample during solidification. The time series is the first cycle of the cooling and it clearly shows the formation sequence of iron and graphite phases.

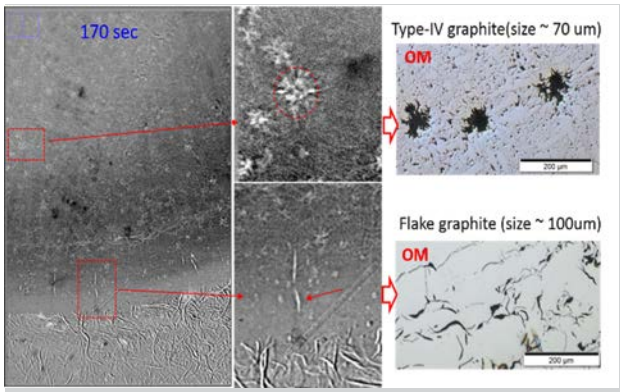

Figure 5: At 170 secs of first cycle cooling, different types of graphite were found in the sample. Center top is type-IV graphite and center bottom is conventional flake graphite. The typical metallurgical images of Type-IV and flake are shown on the right.

At a later stage, when dendrite growth passed through the whole region of observation, some flake graphite was also found to nucleate and grow in the solid region (Figure 5). The corresponding metallurgical images of the Type IV graphite and flake graphite are shown on the right of Figure 5. The metallography images were taken from different samples from the same casting block and re-melted/cooled under the sample cooling conditions.

Once the specimen was solidified, the same specimen was re-melted and cooled again to study the reproducibility of the phase formation sequence.

A series of images for secondary cooling are shown in Figure 6. The phase formation sequence in the second

cooling is similar to that in the first cooling. During the process, iron dendrite was formed first at the liquid-solid interface and grew into the liquid at a rate slightly slower to the first cycle cooling. Large austenite dendrite arms a few hundreds of micron meters in size were found throughout the process. However, the graphite formation behavior in the second cycle was different from the first cycle. No Type IV graphite was found in the second cooling, even though the sample was still the same. Only flake graphite was formed and it all nucleated at the root region of the dendrite and grew in military style following the growth of the iron dendrite. No flake was observed to form within or in-between dendrite. The growth speed of dendrite for the first and second cooling cycle was 25 to 28 µm/s and 10 to 14 µm/s, respectively.

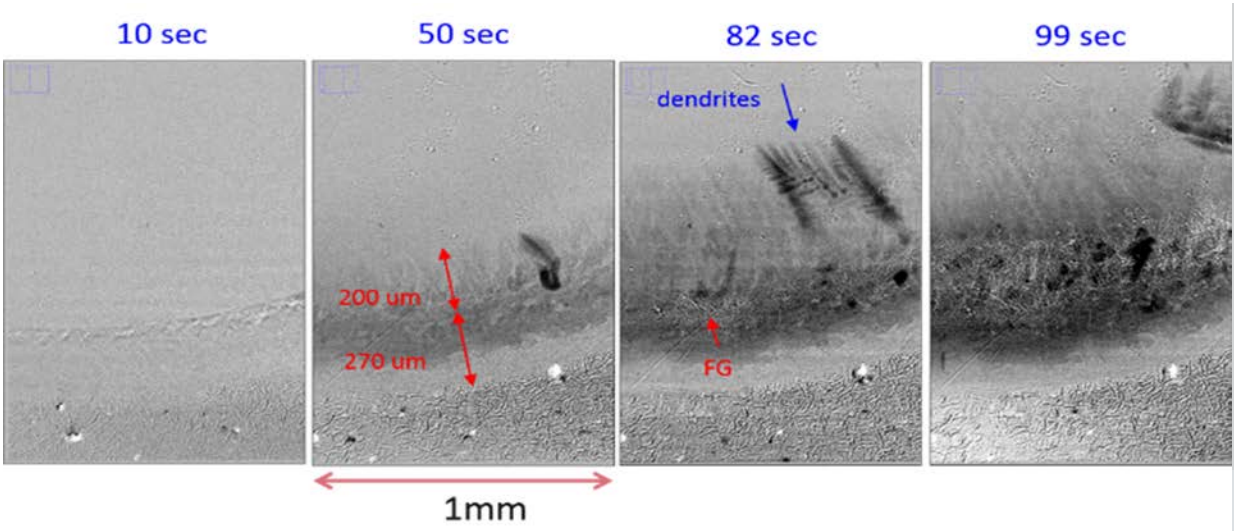

Figure 6: Radiography images of the sample during second cycle cooling. In second cycle cooling, only flake graphite phases were found in the sample. The nucleation of flake graphite is near the root of the dendrite and the growth is in military style.

Figure 7 shows the radiography of the first and second cycles of solidification. The size of the image is 350 µm x 250 µm. One can clearly see the differences between the two images. Type-IV graphite particles are scattered in the sample of the first cycle cooling. Only flake particles were found in the second cycle. It is well-known that magnesium and/or rare-earth elements will fade away (i.e., lose effectiveness) if the melt is held too long before pouring into the casting mold. Without proper magnesium in the material, flake graphite will form instead of nodular graphite. This observation suggests the possible fading effect of critical elements in the liquid, which significantly change the formation and growth of graphite particles and results in different graphite morphology between the first and the second cycle of cooling.

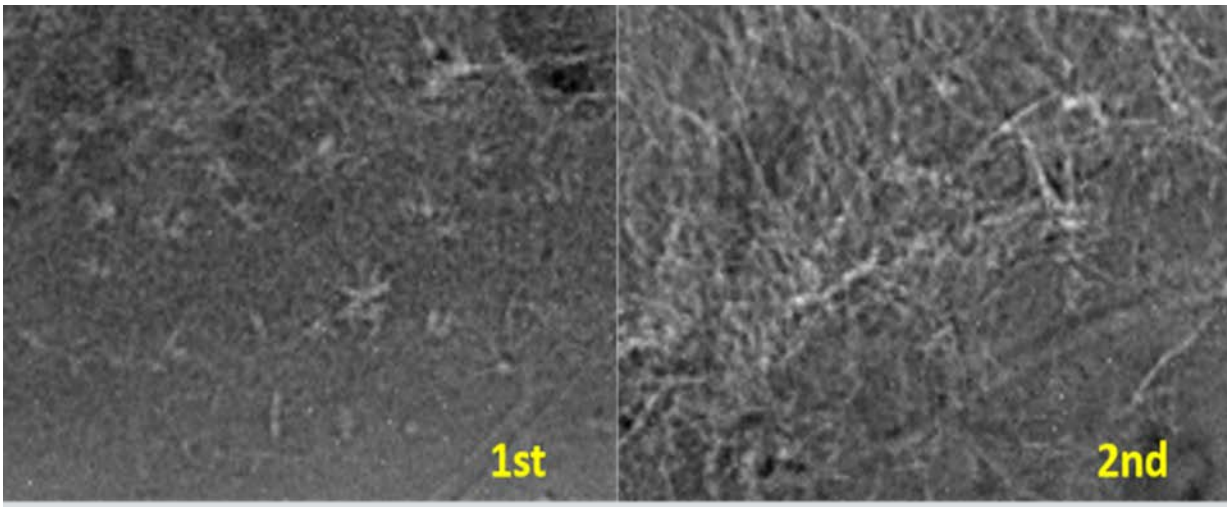

Figure 7: Radiography images of first and second cycle cooling. The graphite morphology is quite different due to the fading of critical elements in the liquid.

It is not clear at this current stage which element(s) is responsible for such changes. Further studies are required to understand the detailed mechanism for the different growth behaviors observed at different cooling cycles and identify the key elements affecting the graphite morphology.

Conclusions

The high-temperature apparatus for in-situ phase evolution studies was designed, tested, and validated. The system allows in-situ characterization of phase formation and dendrite growth during the alloy solidification process.

The first proof-of-concept in-situ experiment was conducted in the Advanced Photon Source at ANL. The phase formation sequence of a CGI sample during solidification was characterized successfully. Upon cooling, austenite graphite dendrite was formed first and followed by various types of graphite phases. In the first cycle cooling, Type-IV graphite and flake graphite was formed. The flake graphite forms at a later stage at the root area of the austenite dendrite arms and continue to grow up to about 100 µm in size. Subsequent melting and freeing showed a different evolution of microstructure. The flake graphite nucleated at the root of the iron dendrite and grew together as the iron dendrite advanced. The differences in graphite morphology between the first and second cooling suggests fading of a certain type of element, most likely Mg, in the liquid, which alters the chemistry of the liquid phase and results in a different graphite morphology.

The apparatus and experimental methodology will be applied to the cast steel alloys being developed for crankshaft application.

Project 21656 – Development of High-Strength Crankshafts

Agreement CEVT211 – High-Performance Cast Aluminum Alloys for Next Generation Passenger Vehicle Engines

Amit Shyam,* Shibayan Roy, Larry Allard, Dongwon Shin, Baishakhi Mazumder, Yukinori Yamamoto, Adrian Sabau, Wallace Porter, Thomas Watkins, and Phil Maziasz
Oak Ridge National Laboratory
1 Bethel Valley Road e
Oak Ridge, TN 37831
Phone (865) 241-4841; fax: (865) 574-6098; e-mail: shyama@ornl.gov

Christopher Glaspie, Seyed Mirmiran, and Lin Zhang
FCA US, LLC

Jose Talamantes, Andres Rodriguez, and Alejandro Gonzalez
Nemak, S.A.

DOE Technology Manager: Jerry L. Gibbs
Phone (202) 586-1182; fax: (202) 586-1600; e-mail: jerry.gibbs@ee.doe.gov

ORNL Technical Advisor: J. Allen Haynes
Phone (865) 576-2894; fax: (865) 574-4913; e-mail: haynesa@ornl.gov

Contractor: Oak Ridge National Laboratory, Oak Ridge, Tennessee
Prime Contract No.: DE-AC05-00OR22725

Objectives

- To develop high-performance cast aluminum alloys with improved castability, high-temperature strength, and fatigue performance compared to industry standard 319 and 356 baseline alloys. Engine cylinder heads cast with the new alloys will have a minimum of 25% strength improvement compared to those cast from the baseline alloys. The cost of engine cylinder heads manufactured from the new alloys will be less than 110% of heads manufactured by 319 or 356. The developed alloys will enable an increase in maximum component operating temperature by about 50^{o}C.
- To evaluate the adequacy of existing ICME models and codes for the prediction of properties and development of cast aluminum alloys. A gap analysis report for existing ICME codes for cast aluminum alloy development will be generated.

Approach

- Develop microstructure-property maps for baseline compositions
- Develop a predictive modeling and ICME approach for alloy development and material/component property prediction
- Perform casting and mechanical property measurements for select compositions
- Ensure components cast for materials meet cost and property requirements
- Perform Engine testing for components
- Perform a cost analysis for production of a large number (i.e., hundreds of thousands) of components
- Create a commercialization plan.

Accomplishments

- The evaluation of microstructural, tensile, thermal, and mechanical properties of some baseline 319 and 356-type cast alloys and two Al-5Cu alloys was completed.
- Microstructural coarsening was identified as a significant hurdle for design of high-temperature aluminum alloys and new coarsening-resistant compositions were proposed.
- Several compositions resistant to coarsening were cast and an invention disclosure was filed for new cast aluminum alloys that are capable of higher-temperature operation.
- It was demonstrated that the new alloys have superior tensile response at temperatures of up to 350°C.

Future Direction

- New compositions that have improved hot tear resistance will be proposed and cast.
- Hot tear resistance of the new alloys will be evaluated.
- Engine cylinder heads will be cast with new compositions and subjected to engine tests.

Introduction

Cast aluminum alloys that are standard across the automotive industry (such as 319 and 356 aluminum) have now been available for several decades. The design and implementation of higher-efficiency passenger automotive engines is currently limited by the absence of economical lightweight materials with improved castability, high-temperature strength, and fatigue performance. The next generation of lightweight alloys must allow a significant reduction in the total weight of automobiles while still maintaining vehicle performance and safety. Electrification of transportation vehicles has accorded an additional emphasis on light weighting because of the additional weight of power systems such as batteries.

Development of new cast aluminum alloys that allow improved performance will be dictated, to a large extent, by the ability to manipulate and enhance the desirable features of microstructural constituents. However, the alloy system is too complex to undertake this development process by trial and error. The trial and error alloy development approach is inefficient and expensive in the long run. In this regard, predictive modeling and ICME provide powerful tools for accelerating the development and deployment of new cast aluminum alloys. In the present project, we plan ICME-based iterative design and development of new cast aluminum alloys with

improved performance characteristics compared to industry standard 319/356 alloys. The new cast aluminum alloys will represent a significant opportunity for the automotive industry to increase engine efficiency.

Results

Cast and heat-treated aluminum alloy materials were received from Nemak S.A. The following seven alloys were cast and machined in the form of blocks (i.e., about 1-in. x 1-in. x 7-in.) from an area in a wedge casting with secondary dendrite arm spacing or a grain size of approximately 30 μm:

– 319 – T7
– 356 – T6
– A356 – T6
– A356 + 0.5 Cu – T6
– 206 – T6
– Al-5Cu-Ni – T6
– Al-7Cu-T6.

Previous reports have included progress on characterization of alloys. During the course of the present project, the high-temperature performance of aluminum alloys has been observed to be limited by the stability of microstructure at elevated temperature.

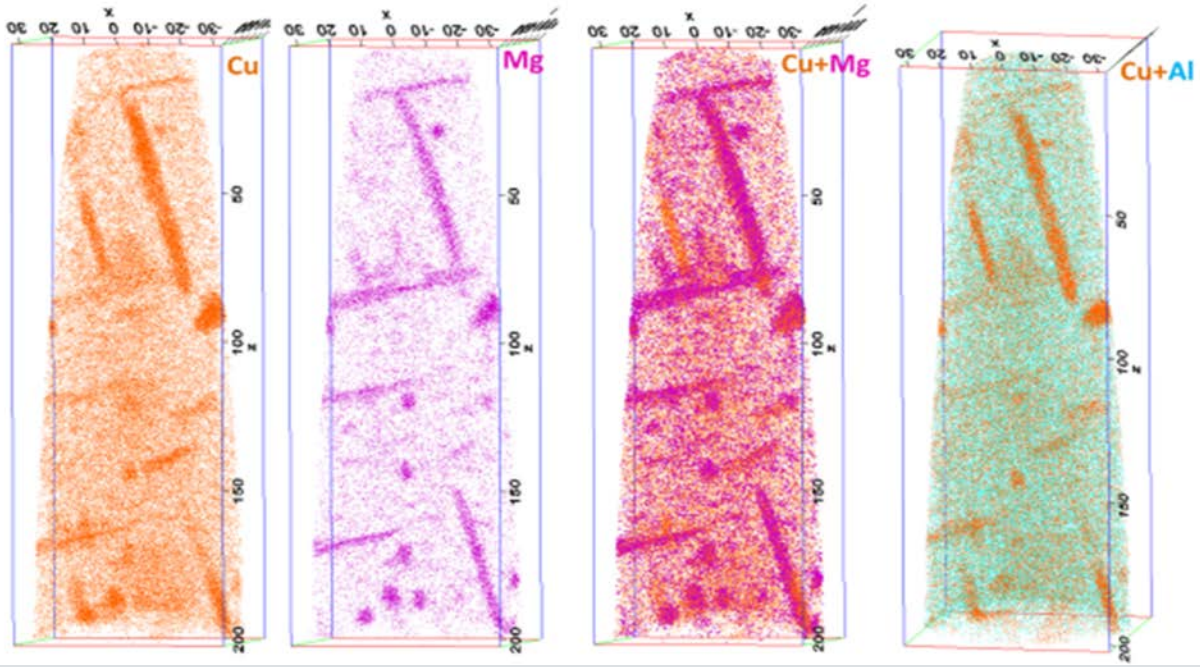

Figure 1: Atom probe tomography images for the most common elements in a 206-T6 alloy.

For example, the 206-T6 alloy (i.e., precipitate distribution illustrated in APT chemical images shown in Figure 1) has exceptional room temperature peak hardness values; this also corresponds to attractive tensile properties at lower temperature. However, at elevated temperature, the microstructure of this alloy can become unstable. Analysis of precipitate complexes that lead to elevated temperature instability is shown in Figure 2. The high-resolution transmission electron micrograph shows the so-called Q phase (Al-Cu-Mg-Si) that provides a heterogeneous nucleation site for multiple GPII zones. The GPII zones in different habit planes maintain an orthogonal relationship with each other. A similar Q-phase precipitate with two GPII precipitates around it is shown in the atom probe tomography analyzed image (right in Figure 2). In this atom probe tomography image, Si atoms are green, Mg atoms are magenta, and Cu atoms are orange. Because Mg has a much higher diffusion coefficient when compared to Al, it is not surprising then to see the Q-phase promoting the coarsening of these precipitates at elevated temperature.

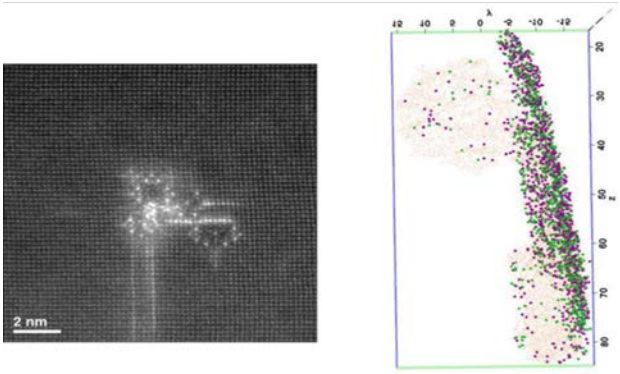

Figure 2: High-resolution transmission electron micrograph image (left) and atom probe tomography image (right) of a Q-phase precipitate that helps nucleate and then coarsen the Al-Cu type precipitates. Color code for the APT image: green – Si; magenta – Mg; and orange - Cu.

As stated earlier, coarsening resistance is an important characteristic of higher-temperature capable cast aluminum alloy. The evolution of the 206-T6 alloy microstructure was well-characterized by transmission electron microscopy, atom probe analysis, and X-ray synchrotron diffraction. The 206 alloy shown in Figures 1 and 2 has a fine distribution of precipitates that allow the system to coarsen and lower their excess interfacial free energy. The evolution of the microstructure and mechanical properties of the 206-T6 alloy at the ageing temperature of 190°C is shown in Figure 3.

After 5 hours of aging at 190^{o}C, the strengthening precipitates consist of GPI or GPII (i.e., two layers of Cu atoms sandwiching three layers of aluminum atoms) zones shown in the high resolution TEM images on the left in Figures 2 and 3. These fine strengthening features lead to exceptional peak strengths at room temperature. The same grain in the same alloy has been imaged after 16 hours of treatment at the aging temperature in the images on the right. The strengthening precipitates have coarsened to form the θ-ft precipitates with a corresponding lower hardness (Figure 3).

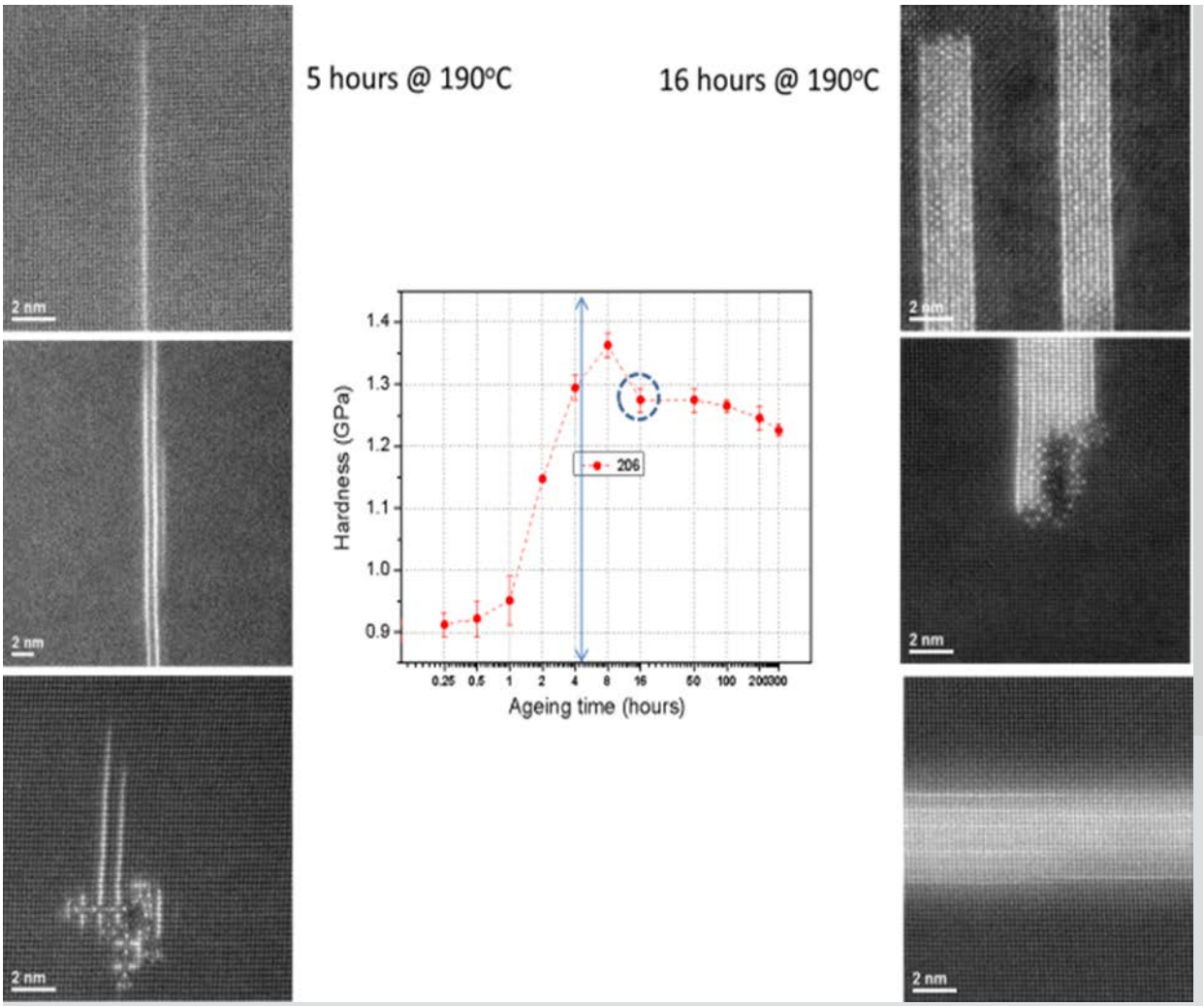

Figure 3: The effect of aging time on the microstructural stability and mechanical properties for a 206-T6 alloy.

Figure 4 shows further evolution in the microstructure of the 206-T6 alloy after prolonged preconditioning at 300°C by high resolution TEM. As can be seen, the initial fine transition phases (Figure 4b) have coarsened to the θ-ft phase after prolonged exposure at 300°C (Figure 4a). The equilibrium θ phase also formed at 300°C and this coarsening behavior leads to a decrease in mechanical properties.

In the present project, our team has now developed multiple higher-temperature-capable cast Al alloys that have stable microstructures; we will report on that effort in the future once IP is clearly established. We have cast a number of new alloy compositions (Figure 5) and the properties of the new cast alloys will also be reported in the future.

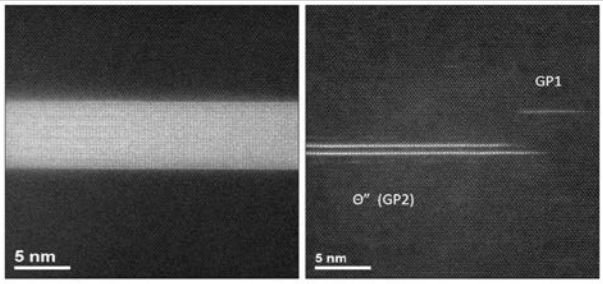

Figure 4: Evolution of the nanostructure in Alloy 206-T6 after (a) 200 hours at 300°C and (b) aging treatment.

An important aspect that determines the performance of for the cylinder head application is the

thermomechanical fatigue behavior. The low-cycle fatigue behavior of five candidate aluminum alloys was evaluated at 200 and 300°C. It is noted that the specimens were provided by Nemak, the testing was performed by Element in Wixom, Michigan, and the analysis was performed at FCA, highlighting the collaborative nature of the work being performed in this project. All specimens were preconditioned at the test temperature prior to testing. The stable (half-life) hysteresis loops for various strain ranges for both the 206-T6 and 319-T7 alloys at 300°C are compared in Figure 6. It is important to note that 300°C data on low-cycle fatigue is rare in the literature.

Figure 5: A summary of the alloy casting effort that was initiated at ORNL in FY 2015.

The "width" of the loop in Figure 6 is determined by the maximum and minimum strains imposed in the low-cycle fatigue test. Six different tests corresponding to six different maximum strains are reported in Figure 6. It is noted that the maximum stress in the stable hysteresis loop for the 206 alloy is higher compared to the 319 alloy corresponding to the higher copper content and 300°C strength in the former alloy. The data generated in this testing program corresponds to the baseline data that will be used to compare with the behavior of the new alloys that are being developed in this program.

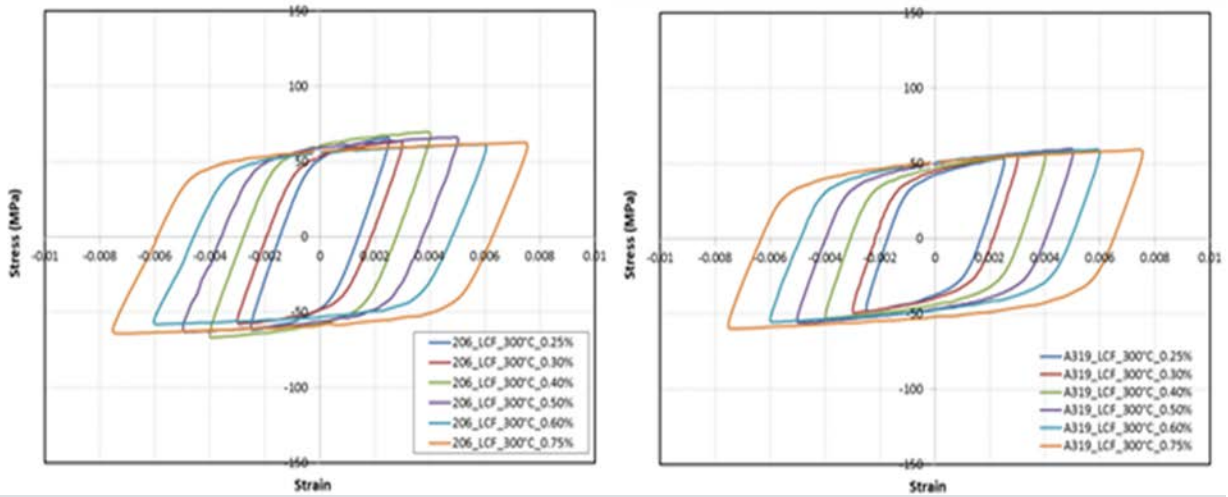

Figure 6: The stable hysteresis loops of two cast aluminum alloys at 300°C (a) 206-T6 and (b) 319-T7.

An important aspect that determines the performance of materials for the cylinder head application is high-cycle fatigue behavior. Previous reports have outlined how the endurance limit can be predicted by combining the pore size distributions with the fatigue crack propagation characteristic. In that regard, a new setup to measure the small crack propagation behavior of aluminum alloys up to elevated temperature was developed. Initial comparative small crack propagation curves for 206-T6 and 319-T7 (both preconditioned at 300°C for 200 hours prior to testing) are presented in Figure 7. It can be observed that consistent with the strength measurements reported earlier and LCF results reported above, at 300°C, the 206 alloy has improved small crack growth rates compared to the 319 alloy. In collaboration with FCA, we will perform pore size distribution characterization. The present results will allow the prediction of an endurance limit as a function of temperature

for the baseline aluminum alloys using computational models presented in the FY 2014 progress report.

Now that we have achieved success in developing aluminum alloys with improved mechanical properties at elevated temperature, the focus in FY 2016 for this project is to improve the fabricability of these alloys by improving the hot tear resistance of these new alloys.

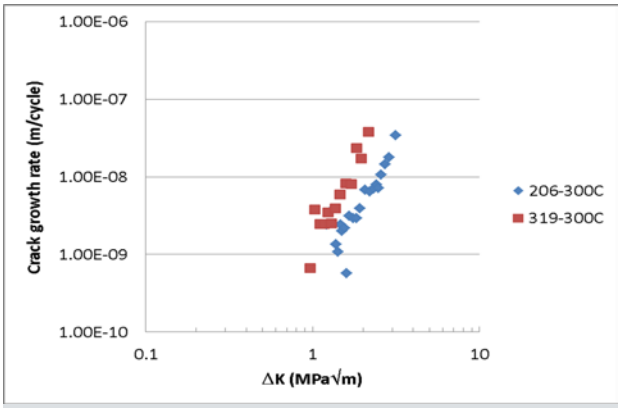

Figure 7: The small fatigue crack growth behavior of 206-T6 and 319-T7 alloys at 300°C. Specimens were preconditioned for 200 hours at 300°C prior to testing.

Conclusions

A series of baseline and newly developed aluminum alloys was fabricated and tested. Advanced characterization techniques (such as atom probe tomography, high-resolution TEM, and synchrotron x-ray diffraction) were applied to understand the basis of high-temperature instability in these alloys. Some of the new compositions proposed and cast have demonstrated exceptionally stable microstructures with attractive elevated temperature mechanical properties. The current focus is on improving the fabricability of these alloys.

ICME-based models for some selected properties were continually implemented in the present project. The ICME modeling for fabricability in conjunction with alloy development will be the focus of activities in the upcoming year.

Publications, Presentations, and Patents

Sabau, A .S., W. D. Porter, S. Roy, and A. Shyam, 2014, "Process Simulation Role in the Development of New Alloys Based on an Integrated Computational Materials Engineering Approach," (invited) paper IMECE2014-37982, *Proceedings of the ASME 2014 Int. Mech. Eng. Congress & Exposition IMECE2014*, Volume 14: Emerging Technologies; Engineering Management, Safety, Ethics, Society, and Education; Materials: Genetics to Structures, November 14 through 20, 2014, Montreal, Quebec, Canada.

Sabau, A. S., "Modeling of Casting Defects in an Integrated Computational Materials Engineering Approach," in *Advances in the Science and Engineering of Casting Solidification: An MPMD Symposium Honoring Doru Michael Stefanescu* (eds: L. Nastac, B. Liu, H. Fredriksson, J. Lacaze, C.-P. Hong, A. V. Catalina, A. Buhrig-Polaczek, C. Monroe, A. S. Sabau, R. E. L. Ruxanda, A. Luo, S. Sen, and A. Diószegi), John Wiley & Sons, Inc., Hoboken, New Jersey, USA, DOI: 10.1002/9781119093367.ch28.

Sabau, A. S., 2015, "Modeling of Casting Defects in an Integrated Computational Materials Engineering Approach," *2015 TMS Annual Meeting & Exhibition, Proceedings: Advances in the Science and Engineering of Casting Solidication: An MPMD Symposium Honoring Doru Michael Stefanescu*, Orlando, Florida.

Roy, S., C. S. Hawkins, D. McClurg, G. Muralidharan, and A. Shyam, 2014, "Microstructure-mechanical property correlation in several cast aluminum alloys," *Materials Science and Technology*, Pittsburgh,

Pennsylvania.

Shin, D., 2014, “High Performance Cast Aluminum Alloys for Next Generation Passenger Vehicle Engines,” (invited), *Materials Genome Initiative: Materials Data Workshop*, July 15 and16, 2014, Dayton, Ohio.

Shin, D., 2015, “Solute Cluster and Vacancy Interaction in Multi-Component Al Alloys,” 2015 *TMS Annual Meeting*, March 16, 2015, Orlando, Florida.

Roy, S., L. F. Allard, and A. Shyam, 2015, “Nano-scale strength modeling of cast aluminum alloys,” *2015 TMS Annual Meeting*, March 16, 2015, Orlando, Florida.

Roy, S., C. S. Hawkins, D. McClurg, G. Muralidharan, L. F. Allard, A. Rodriguez, A. Shyam, “Microstructure-mechanical property correlation in several cast aluminum alloys,” *MS&T 2014 – Materials Science & Technology Conference*, October 12 through 16, 2014, Pittsburgh, Pennsylvania.

Cooper, R.C., S. Roy, A. Sabau, C. S. Hawkins, and A. Shyam, 2015, “Defect modeling and endurance limit prediction for cast aluminum alloys,” (invited) *2015 TMS Annual Meeting*, March 16, 2015, Orlando, Florida.

Shyam, Amit, Yukinori Yamamoto, Dongwon Shin, Shibayan Roy, J. Allen Haynes, Philip Maziasz, Andres Rodriguez, J. Alejandro Gonzalez, Jose Talamantes, Lin Zhang, and Christopher Glaspie, “Cast aluminum alloys with improved microstructural stability and strength at 350^{o}C,” invention disclosure filed in ORNL in July 2015.

Project 21656 – Development of High-Strength Crankshafts

Development of Advanced High-Strength Cast Alloys for Heavy-Duty Engines

Richard K. Huff
Caterpillar Inc.
14009 N. Old Galena Road
Mossville, IL 61552-7547
Phone (309) 494-7349; fax: (309) 578-2764; e-mail: huffrk@cat.com

DOE Technology Manager: Jerry L. Gibbs
Phone (202) 586-1182; fax: (202) 586-1600; e-mail: jerry.gibbs@ee.doe.gov

Contractor: Caterpillar Inc., Mossville, Illinois
Prime Contract No.: DE-EE0005980

Objectives

- Develop new high-strength ferrous alloys to enable higher cylinder pressures for improved performance and fuel efficiency of heavy-duty engines.
- Provide at least 25% improvement in component strength relative to A842 CGI.
- Identify a pathway to meet incremental cost targets of less than 120% of current A48 cast iron component costs.

Approach

- Utilize an ICME approach to computationally engineer new material compositions and manufacturing processes to achieve improved material performance.
- Utilize a systems design approach that is focused on understanding the process-structure-property relationships.
- Produce experimental cast heats and conduct design of experiments using specially designed test castings to produce a range of casting conditions present in the production of actual engine component castings.
- Utilize high-resolution three-dimensional x-ray tomography to identify and characterize graphite structures and distributions, SEM/EDX serial-polishing for nucleant identification, atom probe tomography for nano-precipitate particle dispersions to obtain a mechanistic understanding of cast iron.

Accomplishments

- Conducted comprehensive three-dimensional structure analysis of graphite particles in developed alloys from tomographic data and demonstrated the superiority of the three-dimensional method over the traditional two-dimensional-based techniques.

- Identified graphite nucleants using electron microscopy methods (TEM/SEM/EDS) and calculated inoculant potencies based on the disregistry of the nucleate and graphite lattices.
- Analyzed nano-precipitation strengthening cast samples and verified precipitate dispersions with local electrode atom probe tomography (LEAP) in a pearlitic microstructure. Initial high-throughput density functional theory identified precipitation concepts and sub-scale buttons were cast (initial analysis complete).
- Twenty-four high-potential alloy concepts were cast, with many achieving the strength targets of this project.

Future Direction

- Complete three-dimensional reconstructions of graphite structures in various cast irons and establish correlations between graphite morphology and alloying and inoculant additions.
- Analyze remaining samples from high-throughput density functional theory concepts and continue to identify additional inoculation/precipitate strengthening concepts. Cast and analyze additional concept sample buttons and implement optimal approach.
- Using high energy x-rays, investigate phase evolution from iron melts in a time-resolved manner.
- Develop empirical and mechanistic processing/structure and structure/properties (e.g., strength) models, optimize final cast iron designs using advanced strength model calculations, and demonstrate through casting trials.

Introduction

Today, customers are demanding that heavy-duty engine manufacturers develop and produce engines with lower weight and improved efficiency to reduce fuel consumption, emissions, and costs associated with vehicle use without sacrificing performance and productivity. Resource limitations leading to rising fuel costs and concern about environmental effects are rapidly increasing the need for these improvements. A significant challenge for heavy-duty engine manufacturers to meet these customer requirements is cost-effective material solutions for engine blocks and heads.

Because of the high number of loading cycles an engine experiences over its life, improving the high-cycle fatigue properties over the materials is key to improving engine efficiency. Thus, the DOE target fatigue strength of 31 Ksi (214 MPa) will be used as the primary objective. Secondary goals will be to achieve increased yield and tensile strengths in the new alloys. Another important property is thermal conductivity. A high thermal conductivity can lower the thermal gradients in the component and reduce the stress ranges a component must endure. A barrier to implementation of a new material is the production costs, thus machinability and castability requirements need to be achieved.

Currently, higher strength cast irons are difficult to cast in complex shapes with thin walls, have lower thermal conductivity, and can require expensive heat treatments in addition to the higher casting costs. Over the years, improvements in cast iron materials have largely occurred by accident. The austenite-graphite eutectic solidification is still not completely understood and can be difficult to control in practice. This project aims to fully study the solidification of cast iron materials and utilize a state-of-the-art integrated computational materials engineering approach to optimize alloy design to improve key properties.

In most alloys, the grain/cell size is an important factor that influences the fatigue strength of the material. This is also the case in cast iron; Caterpillar has demonstrated a strong correlation between fatigue strength and eutectic cell size. Unique to cast irons is the strong influence of the graphite size and shape on the fatigue performance. This can be understood by realizing that fatigue failures initiate at the graphite structures and propagate through the cells along the graphite interface. The larger the graphite, the larger the initiation sites and crack propagation paths. The shape of the graphite structures influences the local stress field. Flake-type graphite acts more like a preexisting crack, while round-shaped graphite lowers the stress concentration and improves fatigue performance. As cracks nucleate and grow, they eventually will have to connect by propagating through the matrix and, ultimately, lead to a failure. Matrix hardness is a result of the austenite decomposition products and will significantly influence the strength of the different cast iron materials.

The project team is focusing on refining cell/grain size in the material by optimizing inoculation and treatment to maximize the number of nuclei during solidification. The project team is concentrating on alloy regimes that result in compacted and spheroidal graphite shapes and maximize the matrix strength. In addition to alloying and inoculation of the iron, novel casting methods can be explored to better control the cooling rates during solidification and the eutectoid transformations. Secondary thermal processing is another approach for modifying the austenite decomposition to achieve preferred phases with improved properties or precipitate strengthening particles/phases in the matrix.

Results

Experimental Nucleant Identification

The inoculation process in cast iron can be described as addition of elements that will form sufficient nucleation sites for the dissolved carbon to precipitate as graphite rather than iron carbides. Currently, the effectiveness of an inoculant is determined by the atomic lattice disregistry between the inoculant and graphite. A number of new techniques have been explored that will enable a more efficient and comprehensive analysis of the nucleants within cast iron alloys. The identification of nucleants within graphite particles will be used to further understand the origins of graphite size and morphology via inoculant potency determinations.

A serial polishing approach has been performed on samples to identify and track the nuclei through the depth of several graphite particles. An indent in the corner of the sample was used to track the removed thickness of each layer of the sample while performing nucleant identification. SEM/EDS microscopy was used with EDS point scans and mapping for selected particles in each layer. In summary, 23 unique inoculant particles were examined in five layers of analysis. Of these, 20 particles were located in the center of nodular graphite particles and three were located in vermicular graphite particles. Figure 1shows the nuclei in 5 different particles at various layers in the serial polishing steps. Using SEM/EDS, most particles were identified as primarily (La,Ce)S. However, as layers were uncovered deeper in the graphite samples, both Mg and Ca were observed. This indicates that these sulfide particles had excess Mg and Ca away from the graphite/sulfide interface or were composed of a dual-layer Mg-based oxide core surrounded by a RE-sulfide. Both situations were observed. Previous density functional theory studies have indicated that RE-sulfides have a lower mismatch than Ca or Mg-based sulfides, which is in agreement with these SEM/EDS findings.

Along with sulfides, oxides were also observed (at lower frequency) in both nodular and vermicular particles (see Figure 2 for a summary of nuclei findings). Three categories of nuclei were previously identified with traditional metallography: Mg/Si/Al, MgS (+Ca), and (La,Ce)S + MgS (+Ca). A similar grouping of particles were observed in serial sectioning investigations of 23 distinct nuclei. However, more types of sulfides were detected during serial sectioning due to the possibly of examining layered structures that include changes to the cation species of the sulfide particle.

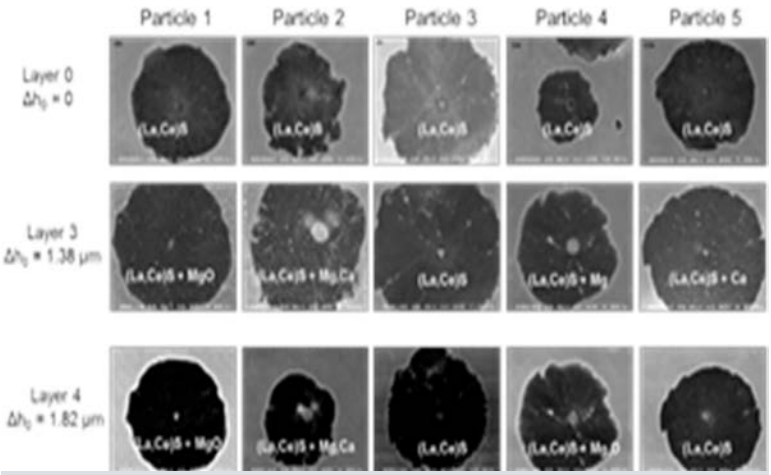

Figure 1: Serial sectioning and particle tracking for five nodular graphite particles in Sample 19B at various polishing depths. Compositions of the nuclei are listed in each figure.

	ANL "type I"?	ANL "type II"	ANL "type III"		
Graphite type	(Fe,Si,Ca)O-type oxide	(Mg,Ca)S only	(La,Ce)S only	(La,Ce)S + Mg/Ca	(La,Ce)S + MgO
Nodular	2	1	9	5	3
Vermicular	1	0	2	0	0

Figure 2: Summary table of types of nuclei observed with serial polishing in both nodule and vermicular graphite structures for sample 19B.

Three-Dimensional Characterization of Graphite Structures

Three-dimensional morphologies of graphite, its spatial arrangement in the alloy, and its phase connectivity are key factors that determine the properties of cast iron. These parameters cannot be attained reliably with the current two-dimensional-based industry standard test methods. The alloys developed through this project are characterized by high-energy x-ray tomography at the Advanced Photon Source located at ANL. The selected specimen is EDM-cut from cast samples into cylindrical rods of about 2-mm diameter and about 20-mm (Figure 3).

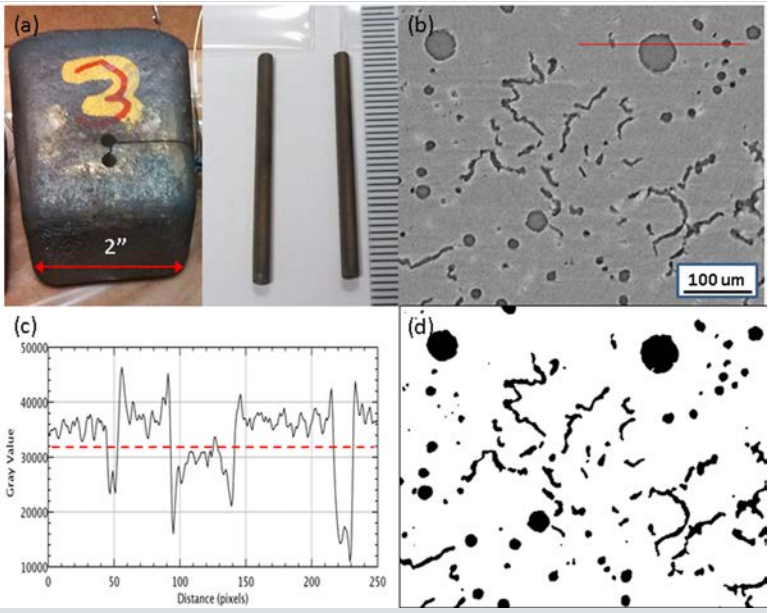

Figure 3: (a) The 2-in. casting block and the cylindrical rods that were EDM cut from the block. (b) Typical tomographic image after reconstruction. (c) Intensity profile along the red line in (b). (d) Binarized image after image segmentation using intensity-based thresholding.

The tomography images reveal the internal structure of the specimen. A typical tomographic image is shown in Figure 3(b), where graphite particles are in dark gray and iron matrix is in light gray. The intensity profile [Figure 3(c)] along the red line in Figure 3(b) shows how x-ray intensity changes within the

sample. The variation of intensity comes from the differences in the x-ray mass absorption coefficient of the phases. With a proper choice of threshold, intensity-based image segmentation is performed on the image to separate graphite phases from the iron matrix. After image segmentation, the binarized version of Figure 3(b) is shown in Figure 3(d).

Once the tomography images are binarized in two dimensions, the three-dimensional model of the particle is built from series of two-dimensional images. All graphite particles in the probed volume were identified and separated. The geometrical parameters (such as volume [Vp], surface area [Ap], sphericity [Ψ], mean radius [$\bar{r}$]) of each individual particle and size of its bounding sphere are calculated.

Once the geometrical parameters of each particle in the measured volume are identified, statistical analyses regarding the distributions of particle size and morphology can be performed. Figure 4 shows the size (in terms of volume) distribution of particles in one measured volume (1.8-mm in diameter x 1.2-mm in length) in the sample as a function of sphericity. It has been found that graphite particles in the sample have a wide distribution of sizes and shapes. From the mathematical definition of sphericity, we know that particles on the right part of the figure (i.e., with higher sphericity) will have a sphere-like shape, while particles on the left have more complex geometry. Based on sphericity, we roughly categorize them into three types: (1) spheroidal graphite (SG), (2) transitional/intermediate graphite (IG), and (3) vermicular graphite (VG). A typical morphology of SG, IG, and VG are shown in the bottom of Figure 4 from left to right. The sphericity of these particles is 0.51, 0.33, and 0.08. In general, low sphericity particles are larger in size. The diameter of minimum bounding sphere of the particles in the bottom of Figure 4 are (left to right) 51µm, 81 µm, and 310 µm.

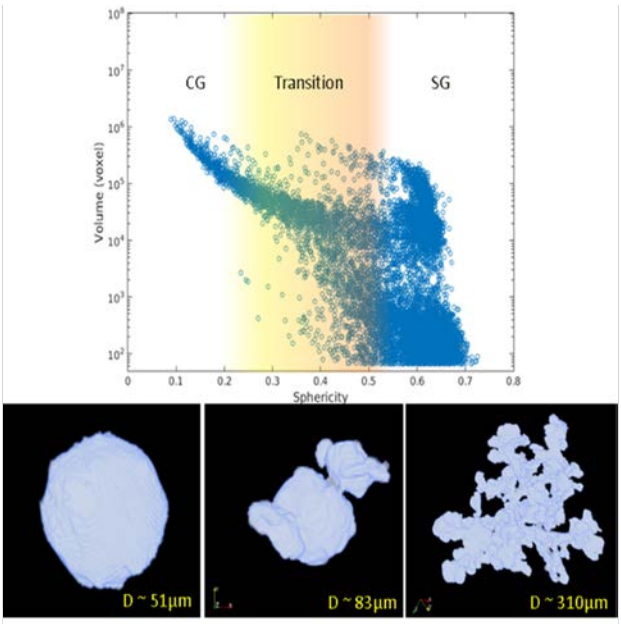

Figure 4: (Top) Size distribution of all graphite particles as a function of sphericity. Graphite particles are categorized based on sphericity. Typical morphologies of spheroidal, transitional, and vermicular graphite particles are shown on the bottom row (from left to right). Pictures shown here are in different scales.

A particle with sphericity equal and larger than 0.5 was considered SG; otherwise, it was VG in the present three-dimensional analysis. The choice of 0.5 was based on the manual review of the three-dimensional models of many particles with different sphericities. With that criterion, the calculated three-dimensional nodularity of the sample is 36.2%. The number obtained from three-dimensional analysis is lower than that from traditional two-dimensional analysis because in two-dimensions, a CG particle might be misinterpreted as a SG particle, depending on the orientation of the cutting surface.

The current industrial standard for evaluating the types of graphite in cast iron relies mainly on the comparison of two-dimensional metallography images of the specimen with American Society for Testing and Materials/ISO standard images. The results from the current three-dimensional analysis were compared to the results from the standard two-dimensional-based analysis. A typical tomography image from the sample is

shown in Figure 5. We have shown previously that graphite morphology from the tomography technique is identical to that obtained from metallography. The sectioning plane cuts through the graphite particles at random, producing images of graphite particles with circular or non-circular peripheries with various dimensions. The traditional two-dimensional analysis method was applied to the sectioning images to calculate the nodularity of the specimen. The analysis followed the ISO/16112 standard, which defines the percent nodularity as

$$Percent\ Nodularity = \frac{\sum A_{nodule} + 0.5 \times \sum A_{intermediates}}{\sum A_{all\ particles}}$$

where nodules (or SG) are defined as particles with roundness larger than 0.625, intermediates are defined as particles with roundness between 0.525 and 0.625, and the rest (roundness smaller than 0.525) is defined as VG. Particles with a maximum Feret diameter smaller than 10 pixels (1 pixel = 1 µm) were excluded. Two-dimensional nodularity was calculated and the percentage of each type of particles for Figure 5 (left) were plotted in Figure 5 (right).

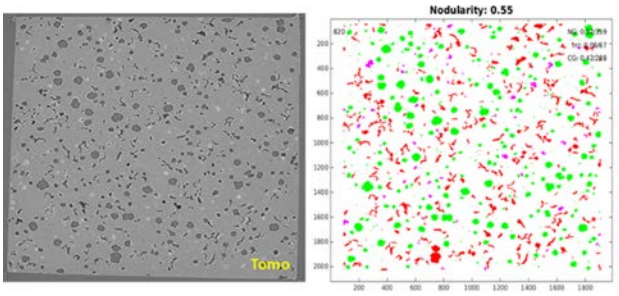

Figure 5: Graphite morphology in tomography (left) and computer-assisted two-dimensional nodularity analysis (right) in the sample.

Two-dimensional nodularity analysis of the sample is shown in Figure 6. The figure presents the area percentages of the different categories of particles within a probed volume in the sample (a 1.8-mm diameter [X-Y] x 1.2-mm length [Z] volume; 1,200 slices of two-dimensional image with 1-µm per slice). The analysis is equivalent to serial sectioning of a sample 1,200 times, with a layer thickness of 1 µm. With the area percentage data, the nodularity rating (%) was calculated and the two-dimensional nodularity of this specimen ranges from 43 to 58%, with an average of 49.6% and a standard deviation of 3.35. The result indicates the sample is a mixed graphite iron with roughly half of the graphite is SG (i.e., 46.5% area) and the other half is VG (47.1% area). Also, 6.3% area graphite was categorized as IG.

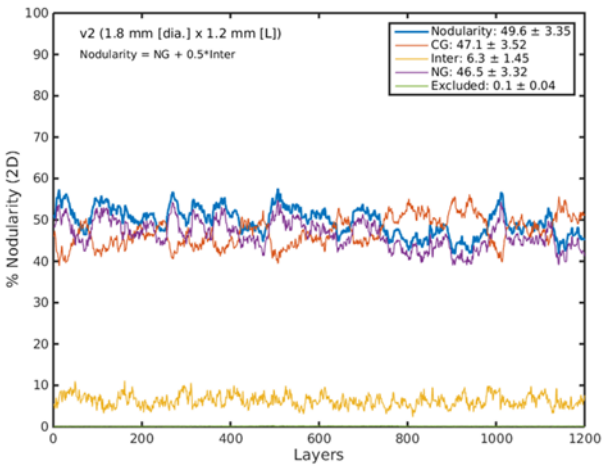

Figure 6: Two-dimensional analysis of percent nodularity through the analyzed volume. The area percentages of each type of particle and calculated two-dimensional nodularity are plotted as a function of position.

The same dataset was further analyzed in three dimensions and the quantitative analysis of the particle distributions are shown in Figure 7. There are total of 21,619 individual graphite particles, whose equivalent diameter is larger than 5 µm (i.e., the cut-off size). Distribution of the particle as a function of sphericity is shown in Figure 7(a). All particles have a sphericity between 0.08 to 0.75 and about 70% of them are between 0.55 to 0.7. The percentage of cumulative total graphite volume and the percentage of accumulative total particle counts were also plotted in Figure 7.

The curve of accumulative volume rises faster than the accumulative particle counts, indicating that the low

sphericity particles (CG) are, in general, larger in size. The volume distribution of graphite particles in Figure 7(b) clearly shows this trend. Only half of the total 21,619 particles are shown in Figure 7(b) for clarity. For those particles considered as VG (i.e., particles with small sphericity), it shows that the smaller the sphericity of a particle, the larger the size of that particle. The largest particle has a volume of about 1.37 x 10^6 voxels with a sphericity around 0.1. This volume is equivalent to a ball with a diameter of 138 µm. The DMBR of this particle is 607 µm. On the other hand, there were various sizes for SG particles, from as small as 66 voxels (cut-off size) up to about 3 x 10^5 voxels (equivalent to about 84 µm in diameter sphere). The size distribution of the SGs is not uniform, but instead it is grouped into two or three clusters. There are 16,513 SG particles (sphericity greater than 0.5) that account for 76.4% of the total particles. The size distribution of SG shows the complexity of graphite formation in cast iron and has many implications. It could be they were nucleated at different stages of the solidification process. Some were nucleated early in the melt and had more time to grow into a larger size; some were nucleated just before the completion of solidification. Moreover, the sizes could just be the result of different SG growth rates, depending on the chemistry of the local nucleation sites. Additional studies are required to obtain better mechanistic understandings of the graphite-forming behavior.

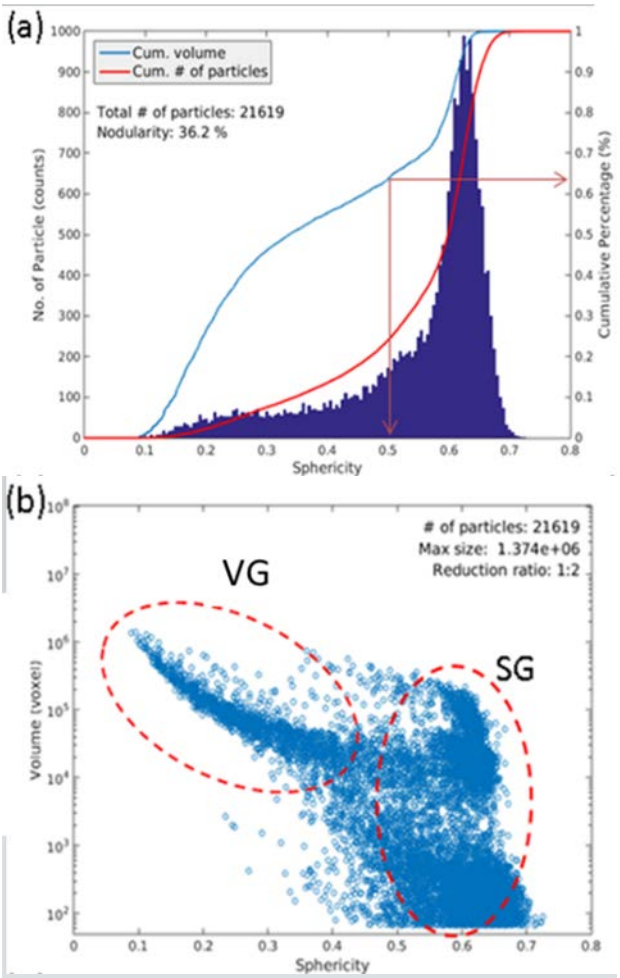

Figure 7: Distribution of graphite particles in the sample: (a) number of particles as a function of sphericity and (b) volume distribution.

Analysis of Cu-Ni-Al Precipitate Strengthening Concepts

One approach being considered for strengthening of cast iron has been to stabilize a bcc-structure (B2) to increase shear resistance. Because copper is a faster diffuser in iron, slower diffusers (i.e., Ni and Al) will be used to reduce the coarsening of this phase. The phase space between NiAl (B2) and Cu_3Al has been targeted for this strengthening dispersion, and effective strengthening was previously demonstrated in ferrite samples (Fe-CuNiAl-Si). This concept was then utilized in a step block casting DOE to determine the effect of Cu-based precipitation strengthening in the pearlitic and ferritic microstructural regions in cast iron.

To confirm the existence of these precipitates and their hardening potential, local electrode atom probe tomography, or LEAP, was used to measure the Cu-based precipitation. LEAP is a destructive tomographic technique where an atomically-sharp tip (r about 50 nm) is analyzed using field evaporation of single atomic planes at the tip surface. Tips were extracted from a cast iron sample using focused ion beam cutting and lift out since electro-polishing methods were unsuccessful due to graphite's interaction with the etchant. Phases/phase

interfaces may be visualized using iso-concentration surfaces, along with one-dimensional compositional profiles across individual interfaces. Both phase composition analysis and identification of interfacial segregation are enabled with this method, as well as statistical analysis of nanoscale precipitate size/shape/spacing.

The reconstructed LEAP tip is shown in Figure 8. An interface of cementite with ferrite was found within the sample. Along the ferrite/cementite interface, three Cu-based precipitates were observed. The cementite lamella was approximately 50 to 80-nm thick and cementite was 100s of nm apart in the current sample region. The concentration profile in Figure 9 shows the composition as a function of distance through one of the Cu-based precipitates found at the cementite/ferrite interfaces. Ni was found to segregate to these precipitates; however, no aluminum was present in the precipitate phase or around its interface. The size of these precipitates was on the nano-scale around 0 to 40 nm. Additional expected segregation trends were observed, including segregation of Si and Al to the ferrite region and slight Mn preferential segregation to cementite.

While the existence of precipitates was confirmed for this step block (heat number 18.4), which contained the Cu-Ni-Al additions, it is still unknown whether these precipitates caused the increase in yield strength that was observed over the baseline casting. Additional LEAP will be performed in future work to determine if Cu-based precipitation has occurred in the control sample (18.2) and the ferritic microstructures.

To determine if yield strength changes in Cu-alloyed step block castings were due to precipitate strengthening or other effects, the pearlite microstructure of each casting was analyzed. Samples were etched and observed with SEM. SEM images were then analyzed with imaging software to determine the area fraction of cementite, ferrite, and thickness of ferrite/cementite lamella in the pearlitic microstructure. Small alloying additions led to an

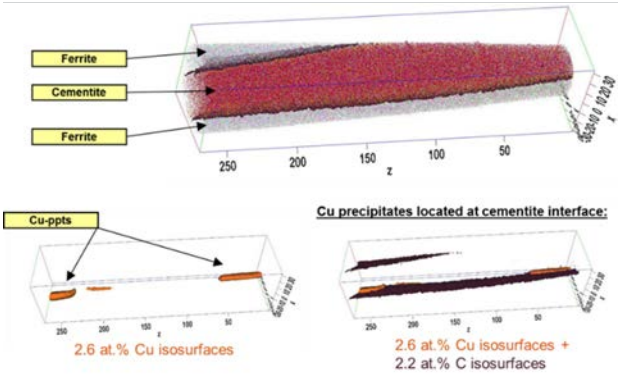

Figure 8: LEAP reconstruction showing the ferrite/cementite and precipitate regions. Precipitates and cemenite interfaces were visualized using 2.6% Cu and 2.2% C isosurfaces.

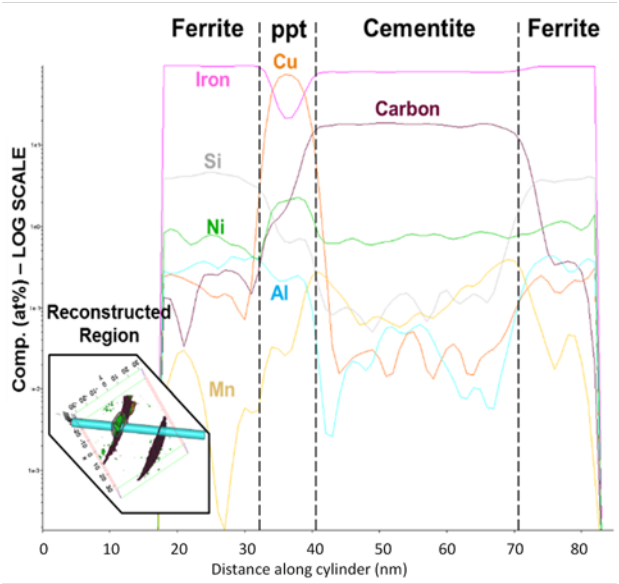

Figure 9: One-dimensional concentration profiles across cementite/precipitate/ferrite interface.

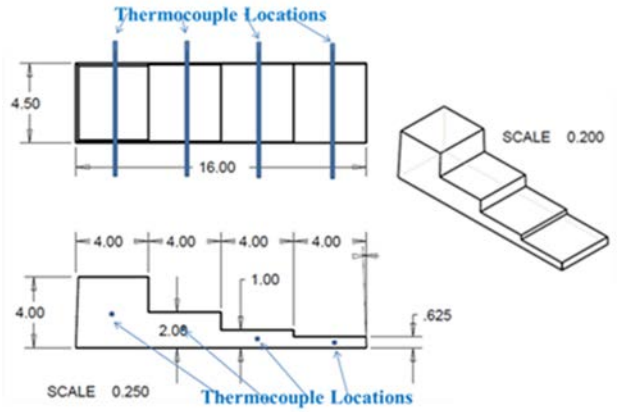

Figure 10: Schematic of step block casting.

increase in the cementite phase fraction, but only a slight change in lamellar spacing over the baseline casting (18.2). Given these results, it is possible that strength increases are due to both increased phase fraction of cementite and decreased lamellar spacing. However, the trend in lamellar spacing and cementite phase fraction do not follow the linear increase in yield strength; it is quite possible that the Cu-based precipitation contributed to the enhanced strength of the alloy.

Process-Structure-Property Relationships

The project team is using a system design approach that is focused on identifying and quantifying process-structure-property relationships in advanced high-strength cast iron materials. Based on past work, 24 high potential alloy concepts were developed and experimentally cast during the past year. Step block castings (Figure 10) were used to prototype each alloy. The step blocks provide a range of cooling rates during solidification that are representative of what can be expected in an actual engine component.

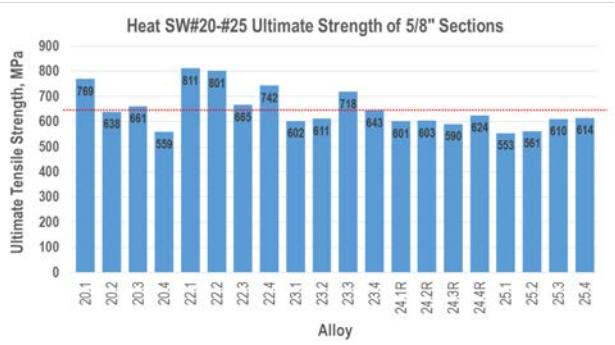

Figure 11: Comparison of ultimate tensile strength for the high-potential alloy concepts developed and prototyped.

Tensile specimens are extracted from the center of the 5/8-in. and 4-in. sections of the step block castings to measure the properties at the extremum cooling rates during solidification and in-mold cooling. Figure 11 shows the ultimate tensile strength in the as-cast condition for twenty of the high-potential alloys. The CuNiAl precipitation alloy concepts previously discussed are omitted because they are being designed for a heat treatment process to optimize precipitate formation and the as-cast properties are not directly comparable to the as-cast properties of the alloys in Figure 11. It can be seen that the properties of all alloys are higher than the current production CGI grade, which is 450 MPa. Several of the alloys are close or even exceed the targets for this project, which is indicated by the red line. Figure 12 shows the percent elongation measured for each alloy. All alloys generally exhibited good elongations and would be considered acceptable for meeting requirements.

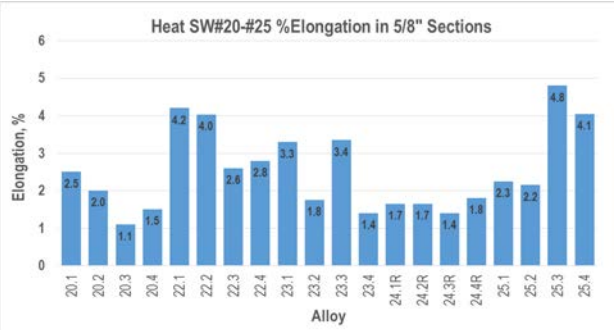

Figure 12: Comparison of %elongation for the high-potential alloy concepts.

The microstructure of each tensile specimen was characterized using conventional two-dimensional metallography. Figure 13 illustrates how the metallography samples were extracted from the tensile specimens and the location (i.e., about 4 mm from the fracture face) where the ratings were made (marked

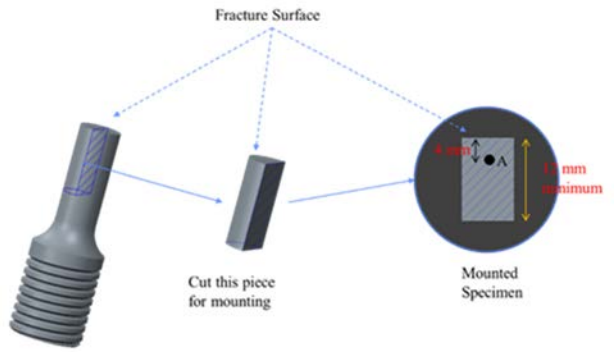

Figure 13: Illustration of the location of the metallographic sample extraction from the tensile specimens.

A). Ratings were made by visually comparing the optical microscope images to the AFS standards. The graphite is characterized by the nodularity (Figure 14). The nodularity values are all within the expected range for CGI, although the typical specification in today's CGI grades is usually less than or equal to 25%. Alloy 20.1 is actually a nodular iron, which is why the nodularity is more than 90%. Series 22 alloys general have high nodularity for CGI, which is certainly contributing to the fact that alloys from this heat had some of the highest ultimate tensile strength values. The alloys in Series 22 are actually considered to be a mixed graphite iron). As discussed previously in this report, the use of three-dimensional x-ray tomography has shown that the two-dimensional measurements usually overestimate the actual nodularity measured in a three-dimensional sample volume. Series 24 alloys have the lowest nodularity and higher carbide fractions were observed, which contributes to the lower elongation. As can be seen in Figure 15, most of the alloys had a primarily pearlitic matrix structure. Series 25 alloys were the first attempt at high-strength ferritic irons and the strengths deemed them worth further investigation.

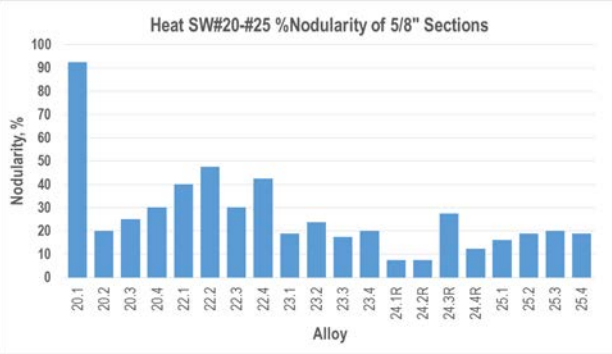

Figure 14: Nodularity measurements for the high-potential alloys.

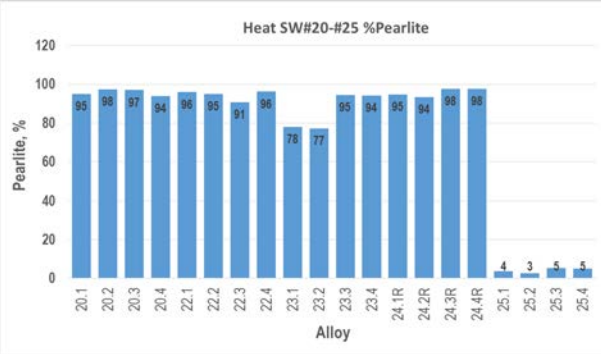

Figure 15: Pearlite fraction measurements for the high-potential alloys.

Summary and Next Steps

Serial polishing with SEM/EDX enabled the identification and classification of graphite and the inoculant particles that serve as nuclei for the graphite. Three-dimensional tomography has enabled the team to visualize the three-dimensional morphologies of graphite, its spatial arrangement in the alloy, and its phase connectivity, which are key factors that determine the properties of cast iron. Using this knowledge, the team successfully developed and prototyped high-performance alloy concepts that show promise for achieving project objectives. Directional solidification, interrupted solidification, and in-situ radiography solidification experiments are in process to further the understanding of cast iron solidification.

LEAP will be performed on as-cast CuNi designs at both cementite/ferrite interface and bulk ferrite regions to optimize precipitation concepts and apply these concepts in final cast iron designs. Precipitate growth and coarsening models will be developed based on LEAP results.

Additional concept generation will be achieved by performing analysis on high-throughput density functional theory concept samples. Using additional results on precipitate phases and austenite and graphite inoculants, new concept sample buttons will be cast and analyzed. Promising concepts will be implemented into final cast iron designs.

Empirical and mechanistic processing/structure and structure/properties models will be developed using experimental data generated from these investigations. After compiling strength data in the literature and from

prototype castings, empirical strength models will be built. Mechanistic strength models will be developed from initial empirical strength models; final cast iron designs will be optimized using advanced strength model calculations.

Focus will shift to characterizing the fatigue performance of the high potential alloys. Future alloy optimization will focus on the concepts that can achieve the greatest improvement in the critical material properties. Using fatigue and other design data, a concept design will be developed for a new engine component that will demonstrate the potential benefits of implementing the new alloy. Caterpillar's new Micro-foundry, which is now starting operations, will enables prototypes of the new component design to actually be produced.

Project 21656 – Development of High-Strength Crankshafts

Caterpillar: Development of High-Performance Cast Crankshafts

Richard K. Huff
Caterpillar Inc.
14009 N. Old Galena Road
Mossville, IL 61552-7547
Phone (309) 494-7349; fax: (309) 578-2764; e-mail: huffrk@cat.com

DOE Technology Manager: Jerry L. Gibbs
Phone (202) 586-1182; fax: (202) 586-1600; e-mail: jerry.gibbs@ee.doe.gov

Contractor: Caterpillar Inc., Mossville, Illinois
Prime Contract No.: DE-EE0006428

Objectives

- To improve the power density of today's gas and diesel engines, material and process technologies will be developed that enable production of cast crankshafts meeting or exceeding the performance of current state-of-the-art high-performance forged crankshafts.
- Achieve minimum core material properties of 850 MPa tensile strength and 615 MPa yield strength. Material must also be able to meet the local ultra-high cycle fatigue properties required in a crankshaft.
- Identify a pathway for meeting incremental cost targets of less than 110% of current production cast units.

Approach

- Utilize an ICME approach to computationally engineer new material compositions and manufacturing processes to achieve improved performance of cast steel alloys.
- Process-structure modeling techniques will be integrated with finite element analyses by crankshaft designers to optimize crankshaft life-cycle cost and performance.
- Prototype melts will be produced and characterized iteratively for an alloy design within a stage-gate process to validate the alloy performance and provide feedback to material design and manufacturing process models.
- Utilize the Advanced Photon Source at ANL to conduct innovative in-situ measurements of phase evolutions and damage during heating and cooling under various loading conditions.
- Production and validation of prototype crankshafts will be performed using standard bench tests at Caterpillar and General Motors. A full engine test is planned for the prototypes to test the crankshaft and con-rod bearing system.

Accomplishments

- ICME-based alloy design completed for initial concepts and a matrix of 14 alloys developed.
- Casting trials completed for 10 of the 14 alloys in the initial alloy matrix.
- Initial structure-property characterization completed for eight of the ten alloys produced to date.
- Simulation-based evaluation of several casting concepts has been completed. A horizontal orientation casting concept was fully developed and two prototype castings were produced using three-dimensional printed sand molds.
- A vacuum-assisted counter-gravity system has been designed and fabricated for laboratory-scale casting trials.

Future Direction

- Cast remaining alloy concepts and complete structure-property characterization. Generate CCT and TTT curves for high-potential alloy concepts.
- Update ICME tools using experimental data and utilize to further optimize the high-potential alloy concepts.
- Develop optimized crankshaft design concepts and processing methods for producing quality cast steel crankshafts.
- Scale up laboratory experiments using concept crankshaft geometry to investigate high potential alloy concepts.
- Develop plans and execute evaluation of post-casting processing methods on scaled prototype crankshafts.

Introduction

Vehicles of the future need to meet increasing fuel efficiency standards with low exhaust emissions, while meeting the performance and cost expectations of consumers. This is true whether considering light-duty automotive or heavy-duty vehicle segments. A vehicle's power source is a critical component in meeting these objectives. Engine manufacturers will need to produce engines that are lighter weight and operate in more efficient combustion regimes in order to deliver fuel efficiency, emissions, and power requirements. Increasing the power density of the engine is a direct approach to achieving these objectives. However, increasing engine power and efficiency requires higher operating cylinder pressures, resulting in increased loads on the crankshaft. For higher-performance applications, the loads on the crankshaft are too high for today's cast materials and, thus, are required to be produced from more expensive steel forgings. Enabling the use of cast crankshafts for high-performance engines will enable designers at General Motors and Caterpillar to optimize material utilization to develop lighter-weight crankshafts while maintaining torsional and bending stiffness requirements. Reducing the rotating mass of the crankshaft will enable further reduction in the engine block weight as it supports crankshaft loads. Replacing current cast ductile iron crankshafts used in smaller engines with higher-strength castings will enable the power and efficiency of the engine to be increased. Thus, smaller more efficient engines may be able to replace larger engines, which could greatly reduce demands on petroleum resources and the amount of greenhouse gasses emitted annually from automobiles and heavy-duty trucks and equipment.

The objective of this project is to develop technologies that enable production of cast crankshafts that can

replace high-performance forged crankshafts. To achieve this, the ultimate tensile strength of the new material should be 850 MPa, with a desired yield strength (0.2% offset) of 615 MPa. Perhaps more challenging, cast material needs to be able to achieve sufficient local fatigue properties to satisfy durability requirements in today's high-performance gasoline and diesel engine applications. The material and process developed should produce high-performance crankshafts at no more than 110% of the cost of current production cast units.

The project team is focused on development of cast steel alloys for application in crankshafts to take advantage of the higher stiffness over other potential material choices. The current alternative material for cast crankshafts (i.e., ductile iron) has a lower Young's Modulus than steel (typically 14% lower), which results in a significant drop in crankshaft stiffness if mitigating redesign (addition of more material) is not considered. The drop in stiffness leads to increased force transmission into the cylinder block, which can lead to both structural implications and an increase in noise levels. Utilizing the casting process and the stiffness advantage of steel will allow the weight reduction potential to be maximized without sacrificing performance.

The significant challenge in this project is developing production methods for steel castings that can meet performance and cost requirements. To minimize costs, the primary alloy design strategy is to design compositions that can achieve the required properties with minimal alloying and post-casting heat treatments. The team is exploring approaches for achieving higher strength microstructure phases from lower cooling rates, optimizing the solidification freezing range, refining the solidification grain structure, and precipitating nanostructures that strengthen and improve the toughness of the material. New filling, feeding, and molding techniques are being investigated to achieve the desired liquid metal flow and solidification behavior to yield castings with minimal porosity and inclusions.

An ICME-based approach is being utilized, rather than relying only on traditional trial-and-error methods, which has been proven to accelerate alloy development time. The multi-disciplinary effort will integrate finite element analyses by engine designers and geometry-specific casting simulations with existing materials models to optimize crankshaft cost and performance.

Results

Alloy Design Concepts

For a cast steel alloy, solidification takes place in the liquid region around 1500°C, while solid transformation occurs around 705°C, at which the cooling rate would give the most significant impact on the final transformation microstructure for a given composition. Thus, the microstructure and performance of an alloy not only depends on chemical composition, but on heat treatment after casting. Optimization of the initial alloy concepts was performed using various ICME tools. The first step was to simulate the casting and heat treat processes for a representative crankshaft to determine the cooling rates at critical temperatures. Figure 1 shows the

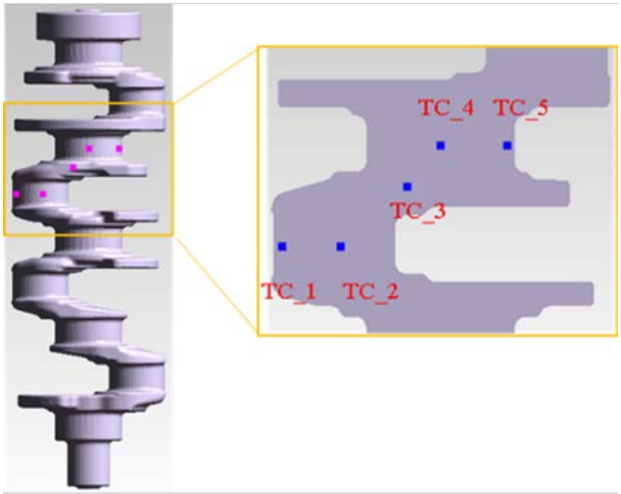

Figure 1: Typical crankshaft geometry with a section view showing the location of virtual thermocouples.

casting orientation and locations of virtual thermal-couples that are set to examine their cooling rates during solidification and heat treatment. For the baseline case, casting was solidified in a sand mold and shaken out after 8 hours, followed by austenization at 950°C and air cooled to 50°C. The cooling rates at the virtual thermocouples at 704°C were around 0.02°C/s during solidification and in-mold cooling and between 0.3°C/s and 0.4°C during austenization and cooling in still air.

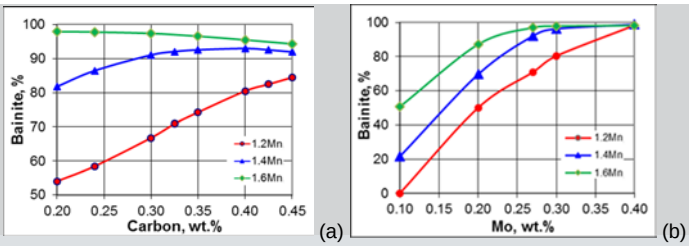

Figure 2: (a) Effect of carbon and (b) effect of molybdenum on bainite transformation in steel.

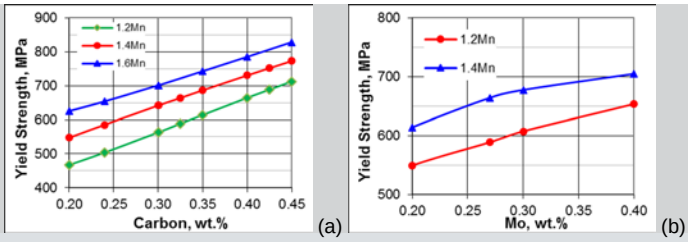

Figure 3: (a) Effect of carbon and (b) effect of molybdenum on the yield strength in steel.

The next step was to examine the effect of alloying elements on structure formation and mechanical properties. In this approach, for each concept, a base composition and elements of interest are selected as design variables with ranges specified based on cost, solubility, and other thermodynamic factors. Design optimization is iterative in nature, where each design variable is adjusted independently while holding the other elements in the composition constant. A cooling rate of 0.4°C was then used for calculations of the microstructure phases and properties through the defined range for each design variable. Figure 2 shows and example of the calculated results for the effect of carbon (C) and molybdenum (Mo) on bainite transformation for a given steel for three different manganese (Mn) levels. It is seen that C has less effect when Mn is above 1.4%, while Mn exhibits strong effect until its addition reaches to 1.4% and is most influential for lower C levels. Mo additions are seen to strongly influence the bainite formation. Obviously, the degree of the Mo effect changes not only with its addition, but also with the Mn content in the steel. As a consequence, it is better to first determine levels of C and Mn and then determine the Mo level based on the structure-property requirements.

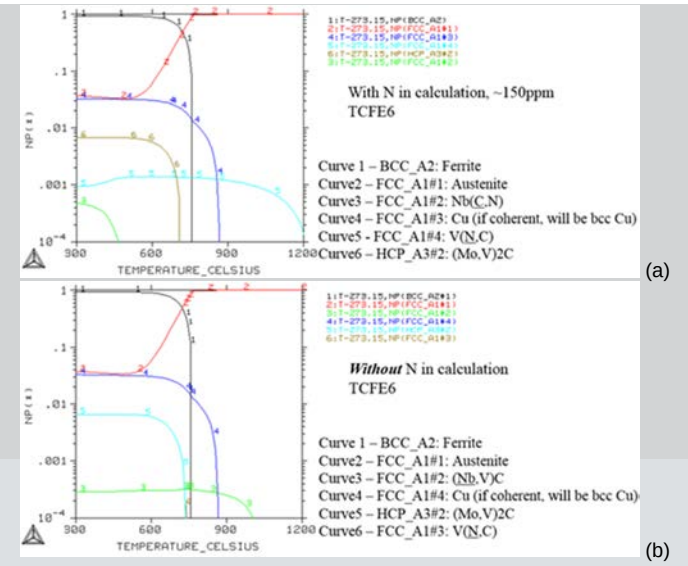

Figure 4 Example step diagrams for a given steel alloy concept (a) 150 ppm N and (b) 0 ppm N.

Mechanical properties are calculated using JMatPro based on the predicted phase fraction. Calculations have shown that JMatPro predicts the same trend for both yield strength and tensile strength for a given steel at a certain cooling rate. For simplicity, examples of the effect of alloying elements on yield strength only are presented. Figure 3 shows the effect of C on the calculated yield strength for a given steel with three different Mn levels. It is seen that addition of C leads to a linear increase of yield strength within a wide composition

range. A similar effect is also predicted for Mo.

In addition to designing alloys with primary phase fractions needed to meet the strength requirements through only air cooling, low carbon steels with good castability are being investigated that rely on precipitation hardening processes to achieve strength requirements. The current design concepts have adopted the same strengthening concept from Blastalloy160 steel developed by Professor Greg Olson's research group at Northwestern University, which relies on precipitation of coherent Cu and M_2C, i.e. $(Mo,V)_2C$ carbide phases. In order to improve toughness, grain refining of the cast alloy is an important step. Strategic formation of MC carbides is being investigated to assist in pinning the grains during subsequent heat treatment, which will help refine the grains. Inoculation strategies are also being investigated to assist in heterogeneous nucleation of ferrite or austenite grains. Toughness is also significantly impacted by the formation of microporosity, carbo-nitrides, and other non-metallic inclusions. Nitrogen content during melting needs to be controlled, which can be difficult, because excess nitrogen leads to microporosity and embrittling phases. Step diagrams are calculated to optimize the composition and processing path for desired precipitate formation. Figure 4 shows example step diagrams for different nitrogen levels in a particular steel composition. It can be seen that nitrogen strongly influences the V(C,N) formation, which will be significant for high nitrogen. It should be noted that processing temperatures and times will be further revised according to initial experimental results. For example, by controlling tempering time, we will be able to study the kinetics of precipitate nucleation and coarsening.

Based on the ICME materials design work, a test matrix of 14 alloys has been developed. Table 1 shows a list of the alloy concepts with the ICME predictions for the microstructure phase fractions (i.e., B – bainite, F – ferrite, P – pearlite, and M – martensite) and the yield strength, tensile strength, and hardness. The properties reported in Table 1 are for air cooling at 0.4^{o}C/s. Two of the alloys are industry standard grades and one is a standard micro-alloy forging steel. Three of the alloys are duplicate compositions, but have a grain refiner addition during the melting and treatment process. It is not possible to predict the effect of the grain refiner on the mechanical properties; however, the aim is for the biggest effect to be increasing toughness, which is not a property that can currently be predicted with IMCE tools.

Table 1. Matrix of cast steel alloy design concepts.

Steel	Designation	Phases	YS	UTS	HRc	Steel	Designation	
		B	F	P	M	MPa	MPa	Phases
1	V-MA650-1	97.8	0.5	1.7	–	654	901	27.2
2	V-MA650-2	86.4	8.4	27.0	–	650	889	27
3	V-MA650-2 + GR							
4	V-MA650-3	72.6	15.0	12.4	–	662	910	27.6
5	V-MA650-3 + GR							
6	SiV-MA700	31.1	14.2	54.8	–	707	959	30
7	SiV-MA650	36.2	30.5	33.4	–	661	902	27.6
8	SiBo9 Steel	17.7	9.9	1.1	71.1	1,364	1,603	49.8
9	SiBo9 Steel + GR							

10	NW-Cast1000	98.8	0.01	–	1.24	1,024	1,283	42
11	NW-Cast700	86.2	13.8	–	–	724	977	30.8
12	GM 1536MV	–	19.2	80.8	–	531	761	19.2
13	4140	82.9	16.2	0.9	–	656	903	27.3
						635*	972*	30*
14	1330							

Alloy Trials

As reported in last year's report, the team developed a new test casting design to produce samples in support of the alloy development effort. Key requirements for the test casting are to have good filling and solidification, with varying sections resulting in cooling rates during solidification and heat treatment that are representative of the range of cooling rates reported earlier in this report for an actual crankshaft. After several design revisions and simulations, a final design was selected as shown in Figure 5. The test casting consists of a 1-in., 2-in., and 3-in. test bar. A large draft is applied to each bar to promote directional solidification toward the open top risers. A tapered runner is designed to flow under the bars to promote smooth bottom filling.

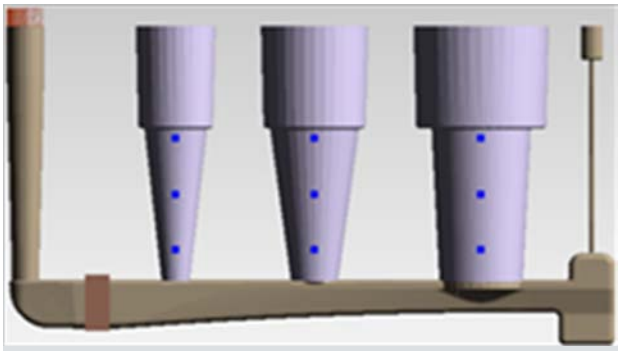

Figure 5: Geometry of the final test casting design.

General Motors issued a purchase order to National Pattern to produce the pattern and mold boxes for the test bar casting design (shown in Figure 6).

Figure 6: Test bar pattern and mold box assemblies for alloy casting trials.

To-date, test bar castings have been poured for 10 of the 14 alloy concepts in Table 1, all except for Alloys 4, 5, 8, and 9. Figure 7 shows three test bar sand molds made from the mold boxes and filled with liquid steel of the composition specified for one of the alloy concepts. Figure 8 shows the test bar castings during hot shakeout from the molding sand. Several of the test bar castings produced to-date have been through x-ray to check for macro-defects. Digital radiography images of three test bars with different diameters are shown in Figure 7 and the porosity is contained to the riser heads and the tapered bars were completely filled and free of macro-defects.

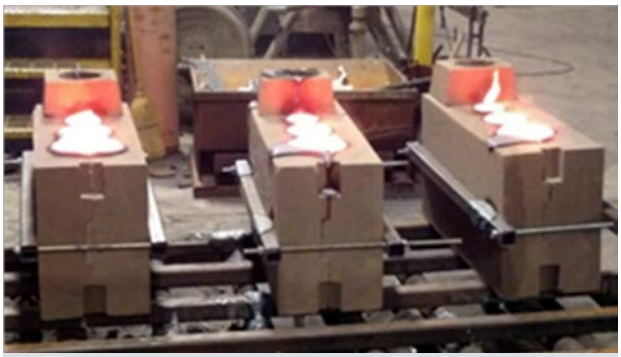

Figure 7: Three test bar casting molds filled with an early steel alloy design concept.

As results of mechanical testing became available, the elongations of several alloys were lower than required. Examination of the fracture surface revealed microporosity that is too small to see on the x-rays, but was present in many tensile specimens. This possibility was expected for specimens taken from the centerline of the bars, but microporosity was still present in specimens extracted off the centerline. Thus, the team decided to start casting keel block samples (shown in Figure 8) in addition to the conical test bars. The keel block geometry has two "legs" where tensile bars can be extracted and a large block on top to feed the "legs" during solidification. The advantage of the keel block is that the feeding distance to the legs is very small, which minimizes the potential for microporosity to form.

Figure 8: Test bar casting during hot shakeout.

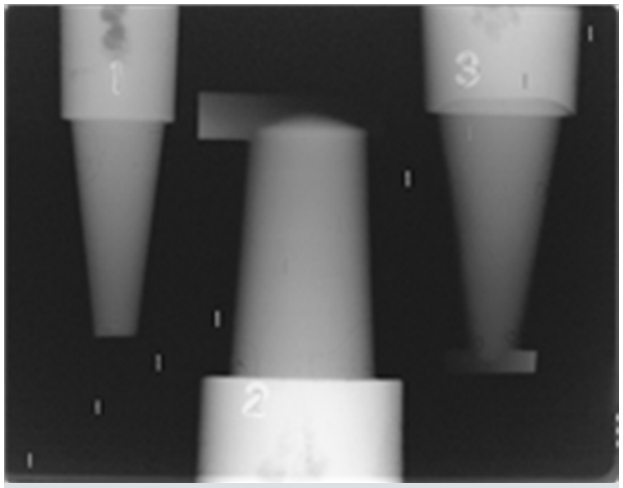

Figure 9: X-ray radiography results for test bars.

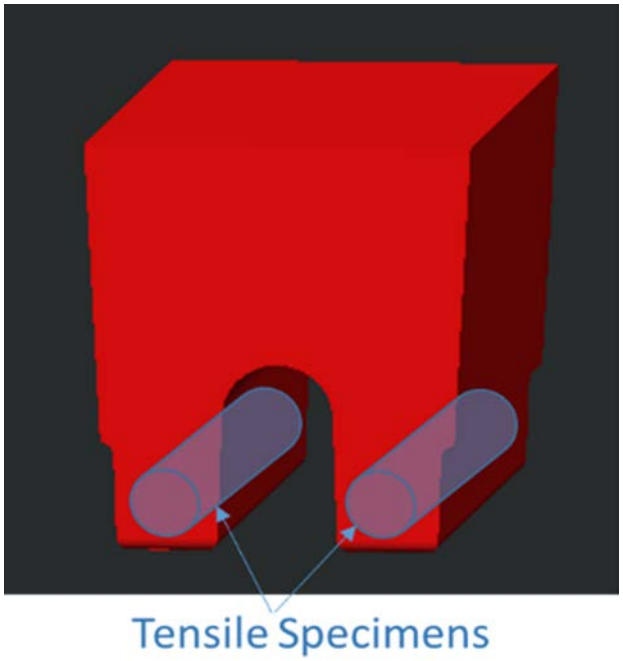

Figure 10: Keel block geometry used for producing alloy samples with the tensile bar locations indicated.

Structure-Property Characterization

For each alloy, two molds were cast and cooled in the mold overnight and then shaken out and shot blasted to remove any stuck on sand. The test bars were then cut off the runner bar and shipped to Caterpillar's Technical Center where all the 1-in. and 3-in. test bars were normalized for 3 hours at a specifically defined temperature for each alloy. All normalized bars were removed from the furnace and cooled in still air. The 2-in. bars were left in the as-cast condition. After heat treatment, one set of bars for eight of the ten alloys produced were sent to Element Materials Technology for metallurgical and mechanical property characterization. Two sets of bars from Alloys 12 and 14 were sent to Element Materials Technology as one set of each of these alloys had a quench and temper process performed to compare against the samples in the normalized and as-cast conditions. General Motors is coordinating the sample evaluations with Element Materials Technology, which includes x-raying all bars, extracting tensile specimens from each bar, and characterizing the microstructure and defects of each tensile bar near the fracture surface. Hardness measurements are also being made at the surface and the center of each bar. Samples for two of the alloys were sent directly to Northwestern for optimal heat

treatment determination.

The mechanical properties of each alloy in the heat-treated condition are shown in Table 2. The results in the 1-in. heat-treated bars have low elongations due to microporosity at the centerline of the bars. In some cases, the properties in these bars did not change much from the as-cast condition. This indicates that the microporosity is likely dominating the properties, making it difficult to directly compare the alloys at this location. The tensile specimens were extracted from the mid-radius location in the 3-in. bars. The ultimate tensile strengths and elongations at this location were higher than at the centerline due to less microporosity. However, some microporosity was still present, which resulted in low elongation even at the mid-radius in many cases. Despite the microporosity, several of the alloys had tensile strengths in the 3-in. bars near the target, namely Alloys 2, 3, 6, and 12. To make a better direct comparison of the alloys, keel blocks are being cast for the promising alloys. It can be seen that the tensile strength and elongation targets (i.e., 850 MP ultimate tensile strength and 10% elongation) were achieved in the Alloy 2 keel block. This is promising, because this alloy was thought to be a leading candidate and was chosen for prototype crankshafts cast this year as discussed later in this report. Results from the different casting geometries and the different specimen locations can be used to quantify the effect of microporosity on material performance. This will be valuable for establishing allowables in new material specifications and developing alloys with lower tendency for microporosity to form.

Table 2. Summary of the mechanical properties of the heat-treated 1-in. and 3-in. bars.

Alloy	Casting Size	Sample Location	Heat Treatment	Ultimate Tensile Strength (MPa)	Yield Strength (MPa)	% El
1	1-in.	centerline	Normalized	672	405	3
	3-in.	mid. radius	Normalized	748	420	5.8
2	1-in.	centerline	Normalized	741	521	2.9
	3-in.	mid. radius	Normalized	811	533	4.7
	K-block	centerline	Normalized	883	550	13.7
3	1-in.	centerline	Normalized	656	560	0.9
	3-in.	mid. radius	Normalized	778	538	1.6
6	1-in.	centerline	Normalized	735	584	1.1
	3-in.	mid. radius	Normalized	837	552	6.9
7	1-in.	centerline	Normalized	693	496	1.8
	3-in.	mid. radius	Normalized	744	507	2.1
12	1-in.	centerline	Normalized	768	656	0.6
	3-in.	mid. radius	Normalized	795	538	2.7
	1-in.	centerline	Q&T	1,089	970	2.1
	3-in.	centerline	Q&T	944	843	1.7
13	1-in.	centerline	Normalized	684	498	5.6
	3-in.	mid. radius	Normalized	737	491	9
14	1-in.	centerline	Normalized	679	443	6.8

	3-in.	mid. radius	Normalized	689	430	8.9
	1-in.	centerline	Q&T	770	597	6.9
	3-in.	mid. radius	Q&T	754	562	14.2

Only a few of the alloys were at or near the minimum yield strength target of 580 MPa. Figure 11 shows a representative microstructure from 3-in. bars in the normalized condition (i.e., Alloys 6 and 7 in this case). It can be seen that a multiphase structure is present, where the white areas are ferrite, the dark areas are pearlite, and the bluish-tan areas are assumed, but not confirmed, to be a bainitic structure. The black areas in Figure 11 (b and d) are microporosity voids. Many of the microstructures did not exhibit significant changes from the as-cast microstructure after normalization. This indicates the alloys may not be optimized for achieving the required microstructure under air cooling conditions. Also, the normalization time and temperature may need to be better optimized for the alloys. Dilatometry and x-ray diffraction experiments are in process to develop CCT and TTT curves for the higher potential candidates to use in ICME tools to optimize the alloy composition and heat treatment to achieve the desired structures.

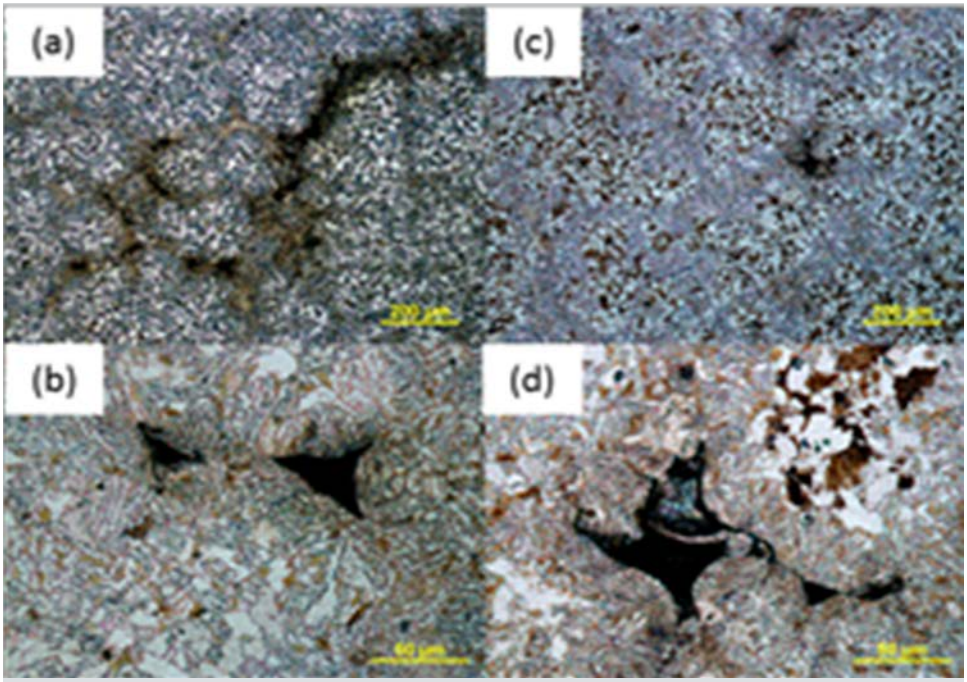

Figure 11: Optical microstructure of Alloy 6 (a) and(b) and 7 (c) and (d) after normalizing and air-cooliing. Both alloys show considerable defects (e.g., pores, shrinkages, and inclusions) in the microstructure. Etched by 2% Nital.

Process Design Concepts

The project team has investigated the castability of multiple Caterpillar and General Motor crankshaft designs. These crankshafts consisted of both current forged and cast ductile iron crankshafts. ICME process simulation tools have been used to investigate a broad range of processing concepts. These concepts included casting orientation, various mold and core materials, and various filling and feeding strategies. Each crankshaft was first simulated without gating and risers, which is termed natural solidification. The natural solidification results were used as a baseline for the strategy development for each concept. The goal was to identify the benefits and challenges of each concept and feed that information to designers to develop a crankshaft design more suitable for a given concept. The challenges identified also serve as a basis for prioritizing focus areas for new process technology development specific to crankshafts.

In general, bottom filling the crankshaft in a vertical orientation showed the best filling. However, there were many challenges identified in feeding a steel crankshaft casting in the vertical orientation. Casting the crankshaft in the horizontal orientation was much easier to feed the numerous hotspots. The use of both highly conductive and insulating mold and core materials was also investigated, but a broad change of the mold or core material alone would not significantly improve the feeding challenges and, in some cases, a conductive mold made the feeding conditions worse.

In order validate the ICME process simulation tools, the team decided to prototype a crankshaft using a fully developed process that was predicted to be free of macro-porosity defects. A General Motors small gas engine crankshaft was selected for this case study. A process was developed using a simple end filling gravity casting approach with a horizontal crankshaft orientation. Several simulations were run to develop a riser and chill strategy that predicted a porosity-free crankshaft (Figure 12). It can be seen that the porosity (i.e., blue areas) is predicted only in the risers, which is the purpose of the risers to feed liquid metal to the crankshaft to compensate for contraction during cooling.

Two sand molds were three-dimensionally printed at University of Iowa's Metal Casting Center, directly using the three-dimensional model from the simulations. The sand molds consisted of four parts: a cope, a drag, the journal cores (which are all shown in Figure 13), and a filter access plug in the bottom of the drag. A two-piece chill was also utilized at the center main journal location. The two prototype castings were poured at St. Louis Precision Casting Company using Alloy 2 from Table 1. Figure 14 shows one of the cast crankshafts after going through the shot blasting process to remove any stuck-on sand. There were no visible surface defects and overall the casting looked very good. The castings were sent to Caterpillar, where they were normalized. After heat treatment, the casting was sent to Element for evaluation. X-ray radiography was conducted with the

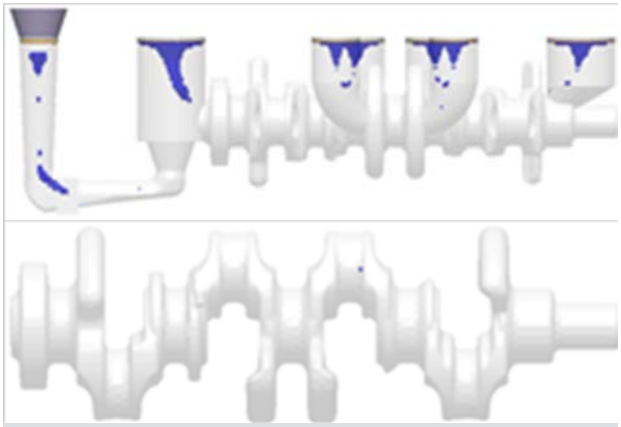

Figure 12: X-ray view of the General Motors small gas engine crankshaft porosity prediction. The blue indicates porosity locations within the crankshaft and feeders: (top) side view with risers, (bottom) top view without risers.

Figure 13: Three-dimensional printed sand molds (a) cope and (b) drag with journal cores installed.

Figure 14: Prototype cast crankshafts after going through the shot blasting process.

risers still attached. The riser piping (i.e., feeding) agreed very well with predictions. There were some small indications in the crankshaft that were likely filling-related defects, which are difficult to predict. Overall, the feeding predictions look very good; however, detailed correlation of the experimental and predicted results is still ongoing.

As many inclusions have been observed in the test bar castings, methods are being investigated to produce clean steel castings. The team is investigating counter-gravity filling processes that have shown through simulations to be able to fill the crankshaft with little turbulence in the liquid metal, regardless of the casting orientation. Eliminating turbulence and splashing in the liquid metal can significantly reduce the formation of harmful oxide inclusions.

The University of Iowa has developed an experimental vacuum-assisted counter-gravity system to further investigate the application of this process for cast crankshaft production. The vacuum-assisted counter-gravity system (Figure 15) consists of four major components: the vacuum pump, accumulator tank, pressure regulator, and vacuum chamber. The vacuum chamber (shown in Figure 16) is a welded steel box with a lid, which seals to the chamber with a high-temperature silicone rubber gasket.

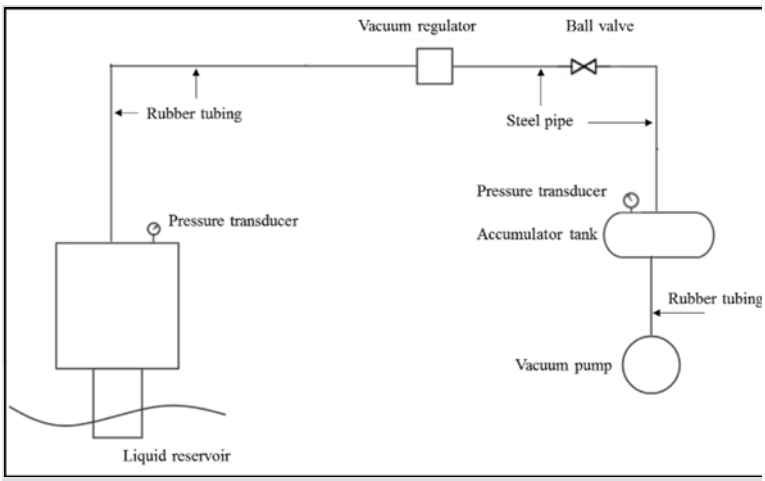

Figure 15: Vacuum-assisted counter-gravity system diagram.

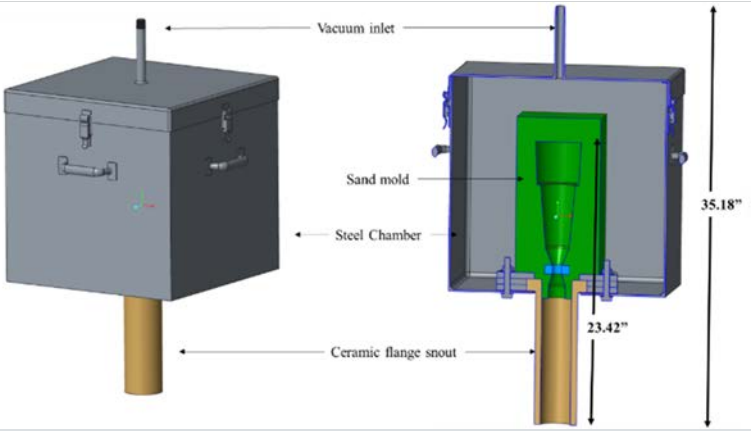

Figure 16: Vacuum chamber with internal components.

The Vacuum-assisted counter-gravity process is as follows: first, with the ball valve in front of the accumulator tank closed, the vacuum pump will draw air out of the accumulator, creating a lower vacuum than needed to draw up the liquid steel into the mold. When the pressure in the tank reaches a suitable range the ball valve will be opened and the vacuum regulator will regulate the pressure inside the vacuum chamber. With a sacrificial seal over the inlet to the ceramic snout, a small vacuum will be drawn within the vacuum chamber. Next, the vacuum chamber's ceramic flange snout will be lowered into the furnace melt, destroying the sacrificial seal and allowing liquid to rise into the sand mold within the chamber. The pressure in the chamber will be regulated in a way that allows for the mold to fill completely and quiescently.

The geometry of the test casting that will be used to validate the vacuum-assisted counter-gravity system was

developed by simulating filling and solidification with different inlet designs and time-dependent pressure profiles. The top section of the part is based on the middle (i.e., 2-in.) test bar used for gravity casting alloy trials (see Figure 5). The effects of vacuum-assisted casting on the metal quality will be directly compared to a gravity-pour casting that has been produced and discussed earlier in this report.

Summary and Next Steps

During the past year, ICME-based design of several alloy concepts was completed and a matrix of 14 alloys for investigation was developed. Casting trials were completed for 10 alloys. Preliminary structure-property characterization work was completed for 8 of the 10 alloys produced. A few of the concepts showed promise in meeting the property requirements for application of cast crankshafts. Keel block samples were cast and show fewer casting-related defects, which makes it easier to compare the capabilities of different materials. Several casting concepts have been explored using ICME process simulations. A horizontal orientation casting process was fully developed for a General Motors small gas engine crankshaft. Prototypes of the General Motors small gas engine crankshaft have validated the ICME predictions and the team has gained some confidence for designing and optimizing complex processes in the future.

In FY 2016, the team will continue to cast the remaining alloy concepts and complete the standard structure-property characterization work. Additional suppliers for alloy casting trials are being identified that have better melting, treatment and handling, and pouring practices. The remaining alloys require a ladle pouring process, because special alloy and treatment additions are required in the ladle rather than the furnace. The preference is for either a bottom or teapot-style pouring ladle. Alloy trials for the high-potential alloy candidates will be repeated at the new supplier(s) to evaluate the effects of various foundry practices on material quality (e.g., microporosity and inclusions).

In-depth microstructure characterization work will continue for each alloy at Element, Northwestern, and Caterpillar. Correlation of the microstructures with ICME predictions will continue and the models will be updated to improve the predictive capabilities of the ICME tools. Dilatometry experiments will be performed at ANL on a few of the high-potential alloy candidates to develop TTT and CCT diagrams, which will be used to improve the ICME models and facilitate a better understanding of the phase evolutions. Additionally, in-situ x-ray diffraction experimental methods are being explored at ANL to further develop CCT and kinetic models for the phase evolutions. Updated ICME models will be used by Northwestern and Caterpillar to further optimize the high-potential alloy concepts, including compositions and heat treatments.

Microporosity has been shown to significantly affect the critical properties of the cast material. Attempts will be made to further quantify the microporosity in the samples cast to-date. Microporosity predictions will be made in the ICME simulations for the test bars, keel blocks, and crankshaft castings. These predictions will be compared with the actual castings to determine if the microporosity levels can be accurately predicted and the microporosity predictions can be correlated to material performance. A criterion for the level of predicted microporosity can be developed for use in crankshaft process development. Caterpillar will update the microporosity model in its internal solidification software, SolCAT3D, in order to evaluate the effects of nitrogen levels in the liquid steel on the microporosity formation during solidification.

Casting process concepts will continue to be explored through both simulation and experiments. A detailed inspection plan for the two prototypes already produced will be developed and the results will be used to

correlate the simulation models. The vacuum-assisted counter-gravity system developed will be tested using water as the fluid. PVC piping will replace the ceramic flange snout and no mold will be used. The water experiment will reveal difficulties within the system and a finalized plan will be developed for the liquid steel trials to being in December 2015. Metal quality from the vacuum-assisted counter-gravity experiments will be compared to traditional gravity cast samples to quantify the benefits of the clean steel casting process.

Based on high-potential alloy and process concepts identified, new crankshaft design concepts will be generated that take advantage of the casting process to minimize the component weight while optimizing the castability. A scaled model (i.e., single throw) of the crankshaft optimized for structural performance and castability will be developed. Casting process simulation will be used to optimize the gating and risering design for this crankshaft design. A pattern for this section of a crankshaft will be produced in the second quarter of FY 2016 for future testing of high potential alloy concepts.

Project 21656 – Development of High-Strength Crankshafts

Computational Design and Development of a New, Lightweight Cast Alloy for Advanced Cylinder Heads in High-Efficiency, Light-Duty Engines

Mike J. Walker
General Motors Research and Development Center
30500 Mound Road
Warren, MI 48090-9055
Phone (586) 651-3757; e-mail: mike.j.walker@gm.com

Qigui Wang
General Motors Global Powertrain Engineering
823 Joslyn Avenue
Pontiac, MI 48340-2925
E-mail: qigui.wang@gm.com

DOE Technology Manager: Jerry L. Gibbs
Phone (202) 586-1182; fax: (202) 586-1600; e-mail: jerry.gibbs@ee.doe.gov

Contractor: General Motors, LLC
Prime Contract No.: DE-EE0006082

Objectives

- This collaborative project between General Motors, QuesTek Innovations LLC, Northwestern University, Massachusetts Institute of Technology, Camanoe Associates, AFS, and Dr. Fred Major used ICME tools, expert knowledge, and experimental validation to accelerate development of an alloy capable of handling the higher temperatures and pressures utilized in the smaller, more efficient engines.

Approach

- For FY 2015, General Motors and its partners have evaluated four alloy concepts developed through ICME methods.
- Evaluation has included microstructural analysis with advanced analytical techniques such as LEAP and TEM imaging, isochronal and isothermal hardness, and tensile testing using samples made from button and chill plate castings.
- Thermodynamic databases, kinetic growth models, and alloy strength models have been calibrated and validated using experimental results.

Accomplishments

- Subscale concepts and models validated (Milestone 6)
- First generation alloy designs completed (Milestone 7)
- Laboratory-scale castings completed (Milestone 8).

Future Direction

- Develop final alloy chemistry and process and complete laboratory-scale test casting plates and full-scale head castings.
- Measure thermal conductivity, tensile, and fatigue properties.
- Evaluate castability.
- Establish chemistry and heat treatment tolerances for the optimal alloy.
- Conduct full recyclability analysis of the optimal alloy.
- Develop alloy and process cost models for full production implementation using the new high-temperature-capable aluminum alloy.

Technology Assessment

- Target 1: 40 KSI (276 MPa) room temperature tensile strength and 30 KSI (207 MPa) room temperature yield strength.
- Gap: Our selected high-temperature alloy has achieved 51 KSI (350 MPa) room temperature tensile strength and 41 KSI (286 MPa) room temperature yield strength; therefore, we are able to meet these targets.
- Target 2: Maintain 3.5% elongation at room temperature.
- Gap: Our selected alloy achieved 6% elongation in the fine microstructure and 3.8% in a relatively coarse microstructure, which covers the microstructure variation normally seen in a cylinder head. Thus, this alloy is able to provide sufficient room temperature ductility for maintaining low-cycle fatigue strength.
- Target 3: Achieve 9.5 KSI (65.5MPa) tensile strength and 6.5 KSI (49 MPa) yield strength at 300°C.
- Gap: Our selected alloy achieves 7.4 KSI (51 MPa) tensile strength and 5.6 KSI (38.5 MPa) yield strength at 300°C. There is still a significant (i.e., greater than 20%) gap that we are attempting to address through minor element additions that have higher-temperature stability but are difficult to put into solution.

Introduction

The DOE Energy Efficiency and Renewable Energy Program is targeting a 25% lighter powertrain by 2025 and 40% lighter powertrain by 2050. As a result, the engine power density will be increased significantly. This will result in higher exhaust temperatures and a doubling of the cylinder peak pressures by 2050. To meet these requirements and achieve the stated goals, the properties of the state-of-the-art materials (like cast aluminum alloys) must increase substantially. Historically, it has taken about 10 years to develop and implement a new alloy and it has taken about 100 years to improve the performance of a material such as cast aluminum by 50%. Thus, traditional methods of experimental trial and error are no longer sufficient. Fortunately, both computational and analytical methods have been vastly improved in the last few decades. ICME and advanced

analytical tools such as focused ion beam microscope, high-resolution scanning TEM, and LEAP experimental techniques are now available to accelerate the timeframe to develop new alloys. Combining ICME tools with expert knowledge from the field and judicious experiments for verification and validation is the quickest and the most effective way to achieve the goals of developing a new high-temperature capable aluminum alloy for head production.

Approach

State-of-the-art ICME tools (such as first principles calculations, computational thermodynamic and kinetic models, virtual casting modules, commercially available casting process simulation, and structural and durability analysis software) will be used to design a new, lightweight cast alloy with ideal multi-scale microstructures and a minimum tendency for casting defects to achieve the desired high-temperature strength and fatigue performance requirements in complex castings. The *iCMD*™ platform is used in this project to develop concepts and to perform modeling, validation, and alloy refinement. QuesTek's proprietary *iCMD*™ platform is a core modeling software system that integrates proprietary and commercial mechanistic modeling tools to facilitate rapid design and development of new materials (see Figure 1).

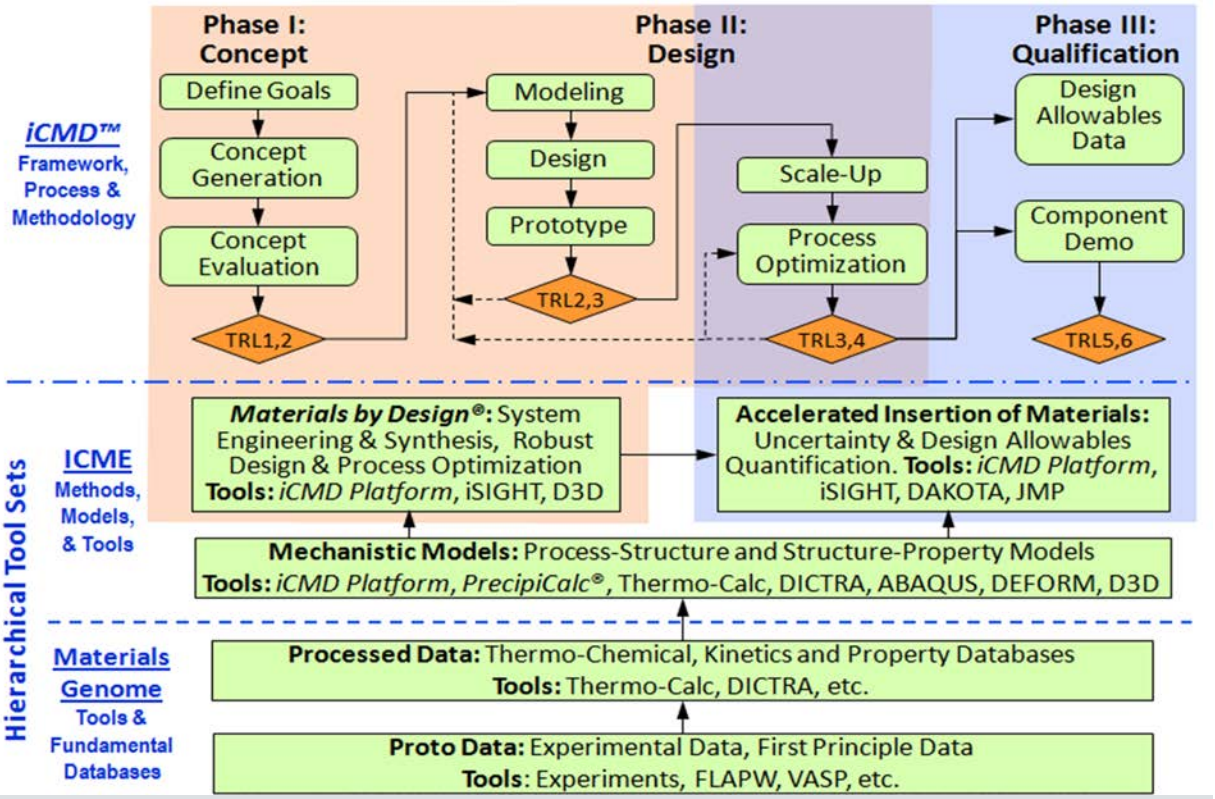

Figure 1: QuesTek's iCMD and ICME technology.

General Motors' Virtual Cast Component Development Program uses an integrated state-of-the-art modeling and simulation methodology for cast aluminum components, starting from computational alloy and casting design through casting and heat treatment process modeling, multi-scale defect and microstructure simulation and culminating in casting property and durability prediction (see Figure 2).

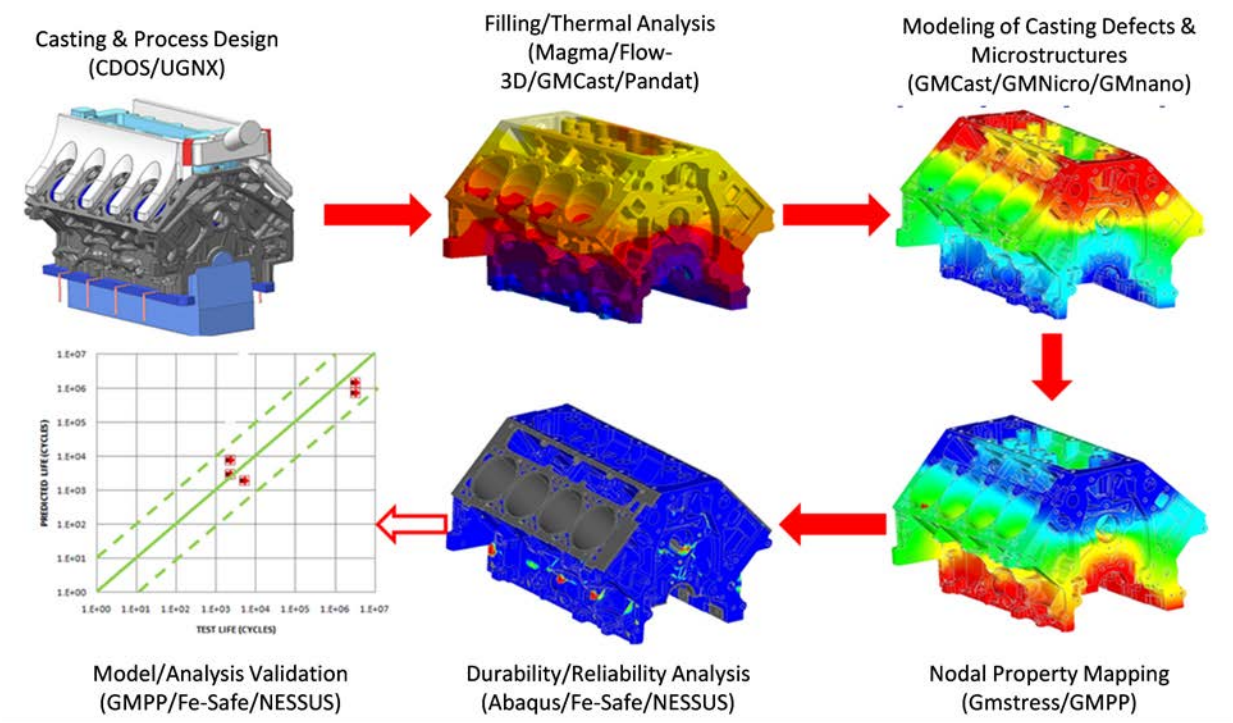

Figure 2: GM Virtual Cast Component Development Program modeling and simulation method for cast product property and life prediction.

During the first stage of the project, a material requirement matrix was developed to guide alloy development. The first generation of the matrix was based on property requirements in the original DOE Funding Opportunity Announcement and the best achievable properties of current cast aluminum alloys used in the heads. Improvements to the matrix were based on a design for six sigma optimization.

QuesTek's iCMD and ICME technology was used to develop the alloy concepts. Beginning with expert knowledge and past research as a guide, thermodynamic and kinetic databases were utilized to create the initial alloy concepts. Precipitation modeling was used to design peak strengthening heat treatment cycles for targeted precipitate structures. Density functional theory calculations were used to determine key input parameters beyond the reach of experimental methods. These inputs for thermodynamic and kinetic models include interfacial energies and accompanying changes with solute additions, high-throughput searches of new stable crystal structures, and solute partitioning energies to interfaces and precipitate phases. Once concepts have been developed, buttons are cast and analyzed to find the precipitate phases through LEAP or TEM. Isothermal and isochronal hardness measurements are conducted to establish the long-term stability of precipitates from the various concepts. Isochronal hardness plots are used to find the temperature to achieve peak hardness in an hour and to confirm precipitation. Isothermal hardness plots are utilized to determine time for peak aging and a first look at the strength and long-term stability of a concept.

Data collected from these experiments is also used as inputs in the strength models for future alloy calculations. Continuing with QuesTek's iCMD and ICME approach, substitutional elements are selected that may reduce coarsening of the precipitate phase or otherwise enhance the high-temperature mechanical properties of the

alloy. Parametric models are created for the alloys using the initial alloy concepts. These parametric models are used to design prototype alloys that strive to meet the multifaceted criteria of the material requirement matrix. Tensile strength, fatigue resistance, thermal conductivity, and good castability are all necessary to create a viable alloy. At this stage, General Motors' Virtual Cast Component Development Process is utilized to predict casting defects such as macroporosity, microporosity, hot tears, and overall mechanical performance and product durability. In conjunction with the modelling approach, chilled plate castings are made for microstructure and mechanical property validation. Castability studies are carried out using fluidity spirals, N-Tek MetalHealth® Fluidity molds, hot tear molds, and Tatur shrinkage molds. After the parametric model and prototype stage, the alloy and process is scaled up to reflect a real application, which in this case is a production head. The alloy and process is optimized in terms of alloy elemental tolerances, casting process variation, heat treatment temperatures and times, costs, and recyclability evaluation. In 2015, the goals were to validate the subscale concepts, create parametric designs of the new alloys, produce laboratory-scale casting of these alloys, and begin development of the final alloy embodiment through selection of the best concepts.

Results and Discussion

By 2015, the material requirements matrix, subscale alloy concepts, and initial data development had all been completed. In 2015, validation of the ICME models for phase precipitation predictions and alloy strength was the first milestone to be achieved. Multi-precipitate growth simulations backed by both LEAP imaging and TEM results from samples aged up to 100 hours were used for validation of these models. In Figure 3, the radius, number, and volume fraction of two precipitate phases were predicted. These results were then used in the alloy strengthening models. These models incorporated particle shear, Orowan-looping, and solid-solution hardening. Initial precipitate growth models were based on a spherical precipitate; however, models have now been updated to better reflect the rod-shaped structure. In Figure 4 comparisons of the simulations to both the precipitate radii and the resulting predictions of alloy strength are shown. At 200°C, the predictions of precipitate size and yield strength are excellent. At higher temperatures, the simulations appear to underpredict yield strength, particularly in the overaged condition. Further advances to the model will include the effect of the Al-Si eutectic, which has been shown by tensile testing at higher temperatures to have a positive effect on yield strength. This might account for some of the discrepancy. Additional high-temperature in-situ TEM imaging has been carried out to observe precipitate growth at even higher temperatures and these data will also be used to improve the accuracy of the growth models.

The second milestone achieved in 2015 was completion of the first generation of alloy designs, including parameterization of selected alloy concepts. Four base alloy designs were developed and two additional modifications of these were also researched.

The concept alloy designs include a Theta phase-based alloy, a Q phase-based alloy, a Theta and Q-based alloy, and a Beta phase alloy. The two other alloys were modifications of one of these four alloys together with heat treatment variation. Of those six alloy concepts, two showed the greatest promise as high-temperature alloys for heads. These two were parameterized with regards to silicon level and heat treatment condition. Additional laboratory-scale plate castings for these two concepts were produced and mechanical properties were measured. A comparison of A356 to these two designs is shown in Figure 5.

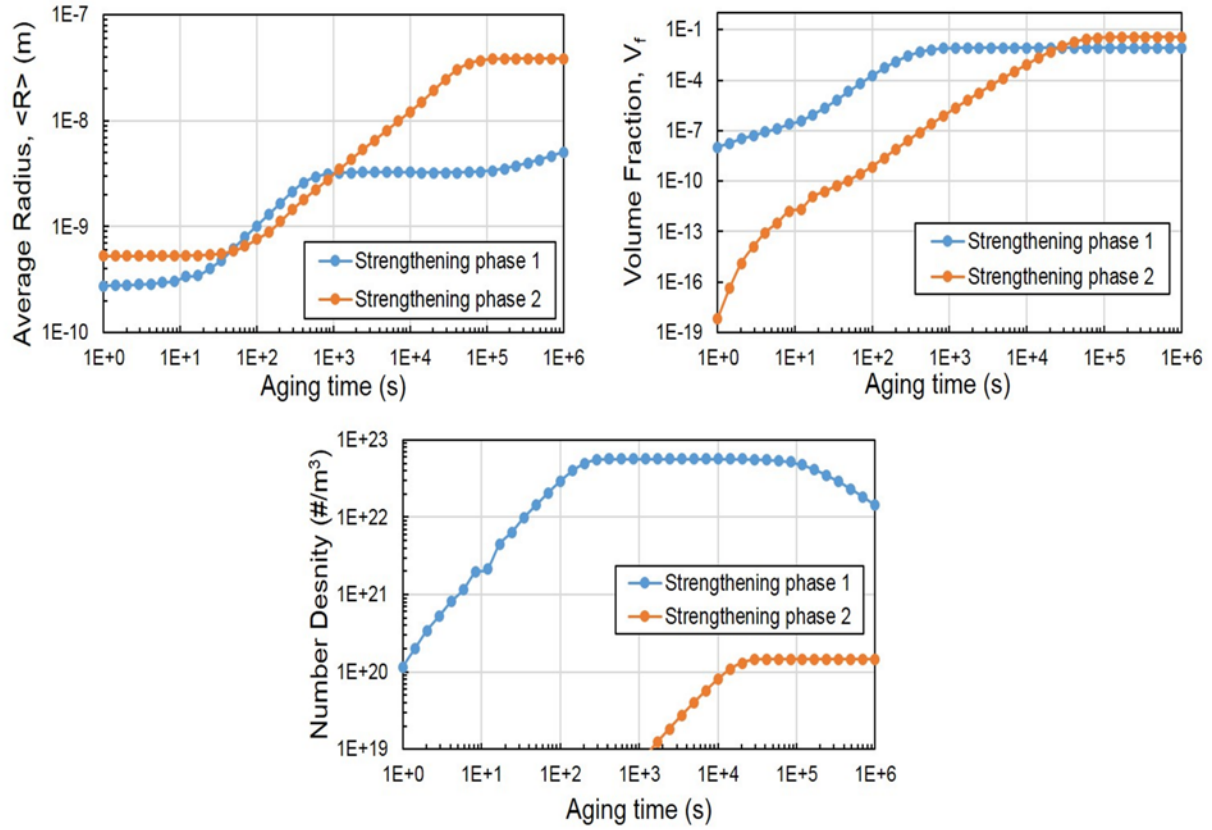

Figure 3: Average radius, volume fraction, and number density of precipitate phases at 200°C over time.

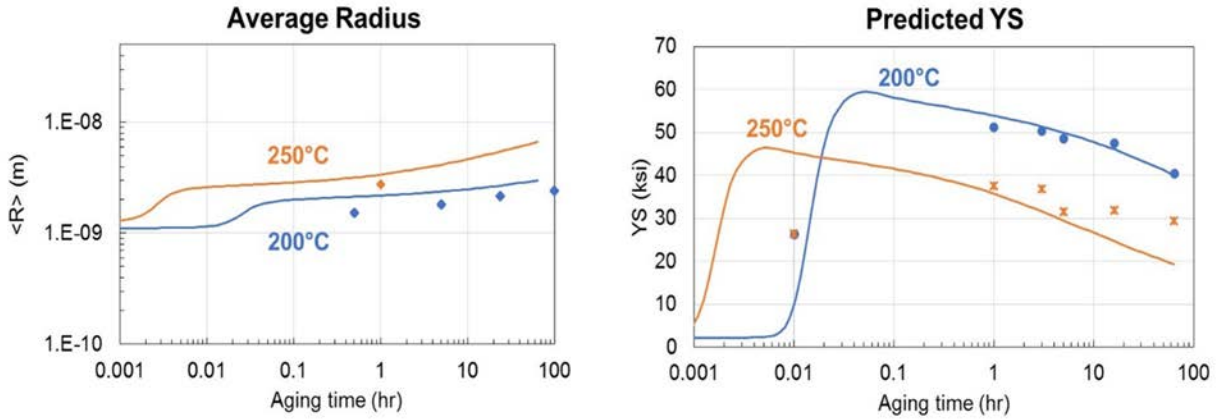

Figure 4" Precipitation radii growth (left) and alloy yield strength (right) predictions (lines) versus experiment (points) at 200°C and 250°C.

In 2014, we investigated the potential of additional minor elements on the increased temperature stability of the alloy concepts. Density functional theory calculations had also showed some potential for a few of these elements. Unfortunately, isothermal hardness studies on cast buttons did not show any benefit with these

singular additions. In 2015, we have chosen to revisit the addition of these elements on the selected final alloy embodiment. Cast buttons of 16 different alloy combinations using design for six sigma methodology have been produced. By using this methodology, we are not only able to explore the impact of individual elements on the long-term temperature stability but also understand the effect of element combinations. The matrix is shown in Table 1. A value of zero means either a baseline concentration of the element or no addition. The buttons are now being heat treated for up to 100 hours and isothermal hardness studies are being carried out. Elemental combinations that show potential will be cast into chill plates and, potentially, cylinder heads.

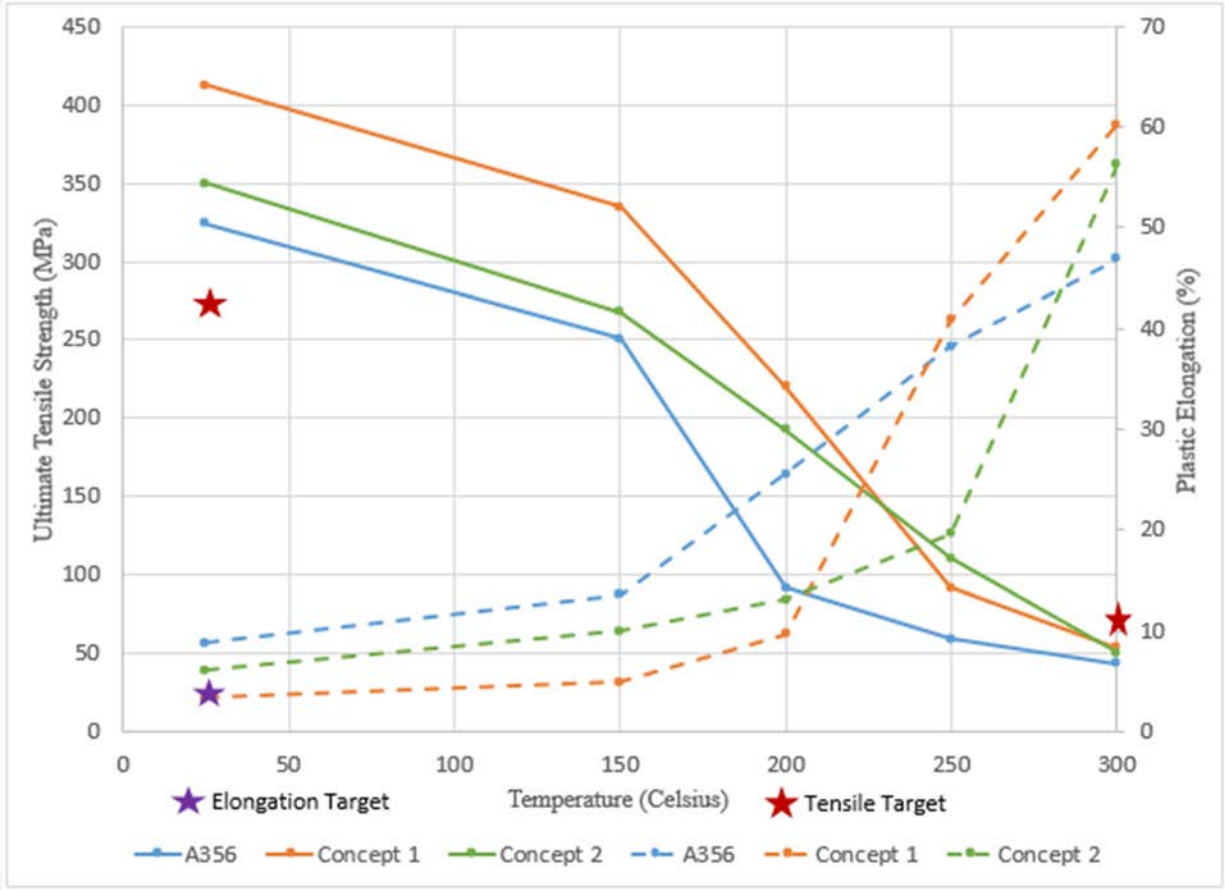

Figure 5: A comparison of tensile properties of baseline A356 alloy to Concept Alloys 1 and 2.

Table 1. Design of the element experiment matrix to evaluate high-temperature stability.

Run	Mn	Cr	B	Ba	Ti	V	Co	Mo	Zr
1	0	0	0	0	0	0	0	0	0
2	0	0	0	0	+	+	+	+	+
3	0	0	+	+	0	0	+	+	+
4	0	0	+	+	+	+	0	0	0
5	0	+	0	+	0	+	+	0	+

Run	Mn	Cr	B	Ba	Ti	V	Co	Mo	Zr
6	0	+	0	+	+	0	0	+	0
7	0	+	+	0	0	+	0	+	0
8	0	+	+	0	+	0	+	0	+
9	+	0	0	+	0	+	0	0	+
10	+	0	0	+	+	0	+	+	0
11	+	0	+	0	0	+	+	+	0
12	+	0	+	0	+	0	0	0	+
13	+	+	0	0	0	0	+	0	0
14	+	+	0	0	+	+	0	+	+
15	+	+	+	+	0	0	0	+	+
16	+	+	+	+	+	+	+	0	0

Technology Transfer Path

In the last year of the project, when the final alloy and process is established, a casting trial on production heads will be carried out. The purpose of this trial is to measure tensile and fatigue properties and, particularly, to evaluate the castability of the alloy in a head. This will also be the first step in evaluating the alloy for production.

Secondly, an evaluation of the recyclability will be carried out. It is essential that any alloy put into production will not adversely affect the aluminum recycling stream.

Thirdly, as required by the Funding Opportunity Announcement and implemented into the second phase of the project, comprehensive cost models will be developed to include materials production, component casting, heat treatment, and machining costs for annual production runs up to 500,000 units of cylinder heads using the new alloy. A technology transfer and commercialization plan will be developed for the new alloy using the material properties and results of the cost model.

Once these steps have been established, General Motors would evaluate and select what future head would be the best first candidate for this new alloy. The head design would take into account the improved higher temperature properties offered by this alloy. Prototype tooling would be made and additional casting trials would be carried out. These casting trials would again collect material property data but also heads would undergo various benchmark tests and, finally, engine build and dyno-tests. General Motors would either select a supplier to conduct the trials or plan for production at one of our captured foundries. After patent protection has been established, Tier One suppliers will be given full access to the knowledge of how to produce the alloy and process the alloy for production purposes.

Conclusion

In 2015, General Motors and its partners have validated four alloy concepts and developed precipitate growth and strength models. Thermodynamic and kinetic databases have been updated to reflect observations obtained by a combination of TEM and LEAP input. Two alloy concepts were selected for further parametrization to study the effect of silicon and heat treatment on properties. Thereafter, one alloy concept was chosen to construct the final alloy embodiment. This alloy displays excellent room temperature tensile properties and good castability, but still needs further improvement in high-temperature strength. A design for six sigma study has been conducted to find minor element combinations that will hopefully improve the high-temperature strength of this alloy. In 2016, head casting trials will be carried out to study tensile and fatigue properties in the semi-production environment to provide critical data to the powertrain before the alloy can be accepted as part of the bill of process for making engine heads.

Project 21656 – Development of High-Strength Crankshafts

Agreement DE-EE0006845 – Next Generation Three-Way Catalysts for Future, Highly Efficient Gasoline Engines

Dr. Christine Lambert
Ford Motor Company
2101 Village Rd
Dearborn, MI 48121
Phone (313) 323-1038; fax: (313) 594-2963; e-mail: clamber9@ford.com

Dr. Todd Toops
Oak Ridge National Laboratory
2360 Cherahala Boulevard
Knoxville, TN 37932
Phone (865) 946-1207; fax: (865) 946-1354; e-mail: toopstj@ornl.gov

Dr. Johannes Schwank
University of Michigan
2300 Hayward
Ann Arbor, MI 48109
Phone (734) 764-3374; fax: (734) 763-0459; e-mail: schwank@umich.edu

DOE Technology Manager: Jerry L. Gibbs
Phone (202) 586-1182; fax: (202) 586-1600; e-mail: jerry.gibbs@ee.doe.gov

DOE NETL Program Manager: Aaron Yocum
Phone (304) 285-4852; fax: (304) 285-4403; e-mail: aaron.yocum@netl.doe.gov

Contractor: Ford Motor Company, Dearborn, Michigan
Prime Contract No.: DE-EE0006845

Objectives

- Develop new TWCs and/or catalyst systems capable of achieving durable 90% activity [HC, CO, NO_x] at 150°C.

Approach

- Establish common test protocols between the three partners.

- Identify and characterize new materials and predict performance and costs.
- Leverage cross-laboratory analytical capabilities.

Accomplishments

- Reactor compatibility between the three partners was confirmed by testing the same commercial TWC.
- Mixed oxide support materials show promise for activity at least 100°C lower than the commercial catalyst.
- A microemulsion procedure was developed to successfully prepare core@shell catalysts with Pd at the core.

Future Direction

- Identify and capitalize on synergies between various catalyst materials.
- Demonstrate full aging and performance from coated monolith cores using most promising materials.
- Identify system solutions and estimate vehicle performance and cost.

Introduction

Ford Motor Company has a nearly 40-year history of successfully using catalysts on cars and trucks to control emissions. Changes in gasoline engine technology have allowed the use of "high tech" TWC to simultaneously control HC (hydrocarbons), CO (carbon monoxide), and NO_x (nitrogen oxides) at nearly 100% efficiency. Waste heat is used upon engine start to bring the catalyst up to its full operating temperature of greater than 350°C, lowering fuel economy and creating particle matter. The goal of this project is to develop and test new catalysts for lower operating temperatures that may occur with future, more efficient gasoline-powered vehicles. The work includes laboratory preparation, aging, and poisoning of catalyst materials, activity tests, and chemical analyses. The work is expected to result in new TWCs and/or catalyst systems capable of achieving durable 90% activity HC, CO, and NO_x at 150°C.

Results

Testing Protocols and Commercial Three-Way Catalysts

Recommended test protocols for catalysts operating under stoichiometric exhaust conditions were derived from the recommendations of the Advanced Combustion and Emission Control Tech Team of USDRIVE. Detailed test conditions are as follows:

- 525 ppm C_2H_4, 500 ppm C_3H_6, 150 ppm C_3H_8, and 1,000 ppm NO
- 0.5% CO, 0.17% H_2, 0.74% O_2, 10% H_2O, and CO_2
- Ramp oven temperature up and down between

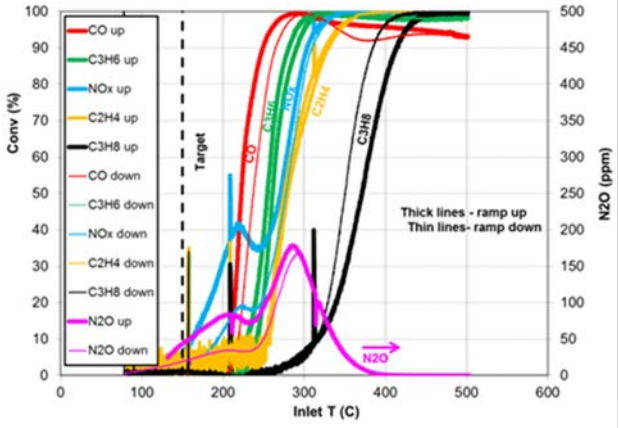

Figure 1: Aged TWC powder sample stoichiometric evaluation (1.8 g, 5°C/min ramp, C_3H_6, C_3H_8, C_2H_4, NO, and CO, 3.5 L/min). The results are plotted against catalyst inlet temperature.

70 and 500°C.

The results of testing a commercial TWC sample at each partner are shown in Table 1. Relatively good agreement was found for the T_{50} (temperature of 50% conversion) of each chemical species. It was confirmed that reactors at three locations (including two at the University of Michigan) are operating in a similar manner. In an example of reactor output (Figure 1), the conversions of CO, various hydrocarbons, and NO_x may be noted, as well as formation of nitrous oxide (N_2O).

Table 1. Cross-laboratory comparison of temperatures for 50% conversion (T_{50}) for each chemical species over a commercial TWC.

	Species	University of Michigan 1	University of Michigan 2	ORNL	Ford
T_{50}	Co	230	238	230	225
	C_2H_4	273	281	273	275
	C_3H_6	273	252	255	250
	C_3H_8	320	362	320	370
	NO	NA	255	280	273

Mixed Oxide Support Materials

One interesting way to create high surface area mixed oxide support materials is to begin with metal alkoxides and hydrolyze them in an aqueous solution, which is called sol-gel synthesis. Adding the active metal precursor before the oxides are formed is a one pot synthesis (Figure 2). Alternatively, the active metal may be added later via impregnation or incipient wetness techniques. Using these methods, it was found that adding SiO_2 stabilized the Al_2O_3 surface area for an active and durable catalyst and a comparable support material was obtained from a supplier. Creating a layer of sol-gel-derived titania or zirconia on the stabilized Al_2O_3 and then adding Pd resulted in T_{90} of 250 to 300°C (titania-containing example in Figure 3), with a notable large improvement in propane conversion over the commercial TWC.

Another example of mixed oxide synthesis is presented in Figure 4, where a shell of a low surface area material (ZrO_2) is formed on the core of a high

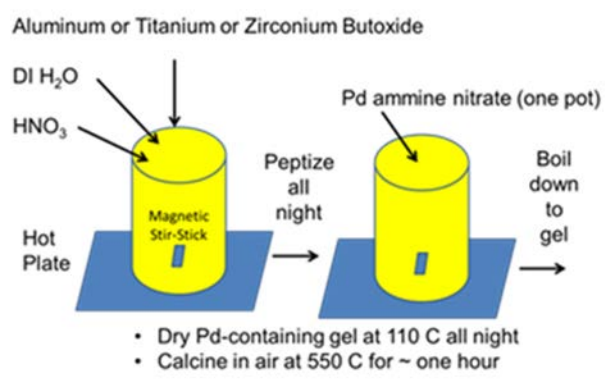

Figure 2: One pot synthesis of supported Pd catalyst material.

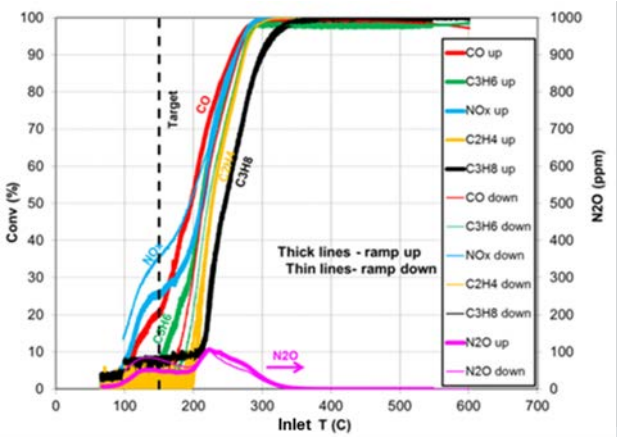

Figure 3: Reactor test with full exhaust mix for fresh 2 wt% Pd/8 wt% titania (TiO_2)/commercial silica-stabilized Al_2O_3. The results are plotted against the inlet temperature. Also, 1 g of sample was used at 3.6 L/min.

surface area material (SiO_2).

Scanning TEM confirmed the core-shell structure was obtained (Figure 5). A $Pd(NO_3)_2$ precursor was impregnated (incipient wetness) onto the SiO_2@ZrO_2 oxide support, leading to 1 wt% Pd/SiO_2@ZrO_2 catalysts. The T_{50} of CO conversion was around 202°C and remained the same after desulfation at 600, 700, and 800°C, as well as after hydrothermal aging at 800°C (Figure 6).

Ternary Oxide Materials as Precious Metal Substitute

Excellent low temperature reactivity was found with a precious metal-free ternary oxide mixture of Cu, Co, and Ce, with light-off temperatures below 100°C. Even after calcining at 800°C, the light off temperature continued to be below 200°C in the presence of HCs and NO_x (Figure 7).

The current synthesis route involves a co-precipitation technique utilizing $Cu(NO_3)_2$, $CoCl_2$, and $Ce(NO_3)_3$. This technique results in a catalyst with a metal molar ratio of 1:5:5 (Cu:Co:Ce). Figure 8 shows a representative EDX elemental mapping of the CuOx-$CoOy$-CeO_2 catalyst for each of the relevant metals. Again, distinct regions of cobalt oxide and ceria are evident though there is considerable mixture of these

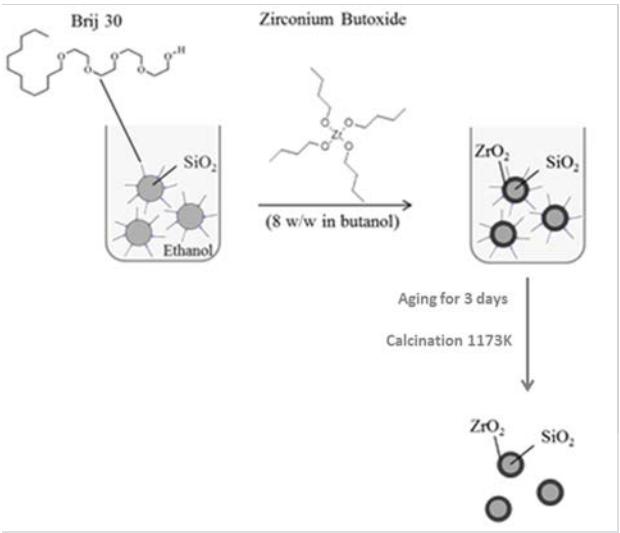

Figure 4: Synthetic procedure of SiO_2@ZrO_2 oxide supports.

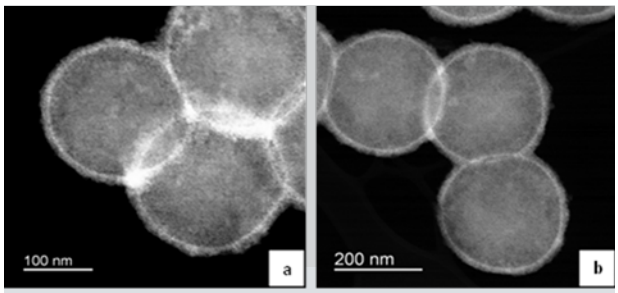

Figure 5: Scanning TEM micrographs of SiO_2@ZrO_2 oxide supports calcined at (a) 700°C and (b) 900°C.

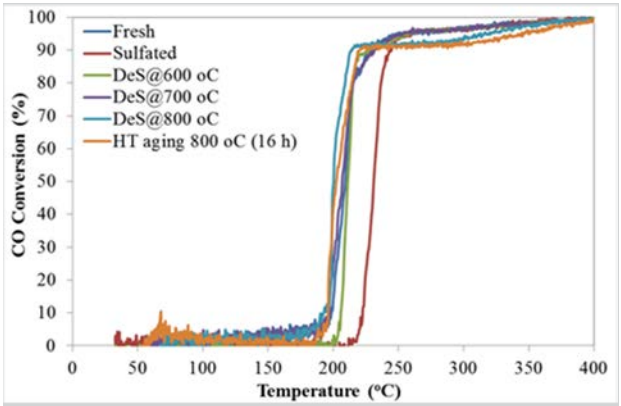

Figure 6: Catalytic performance of Pd/SiO_2@ZrO_2 in the oxidation of CO with a total flow rate of 200 ml/min (4,000 ppm CO/1,000 ppm C_3H_6/500 ppm NO+10% O_2 + 5% H_2O + Ar balance) for fresh, sulfated, desulfated at 600, 700, and 800°C and hydrothermally aged at 800°C (16 hour) states.

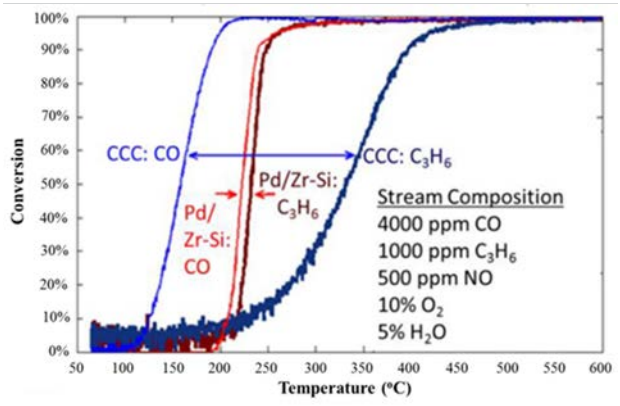

Figure 7: CO (thin/light) and C_3H_6 (thick/dark) light-off curves of CuOx-$CoOy$-CeO_2 (blue) and PGM (red) catalysts in simulated exhaust conditions. Arrows highlight significant change in the response to propylene.

distinct phases throughout. The copper signal can be seen throughout the sample with no particular focus on either the Co_3O_4 or CeO_2 phases. Because no copper phase was seen via TEM or x-ray diffraction, it is evident that the copper component is imbedded into the lattices of both Co_3O_4 and CeO_2 phases. As a result of this catalyst's unique inhibition resistance, we have looked for other possible candidates for mixed oxide catalysts. Table 2 provides a list of catalysts synthesized via a modified co-precipitation route that are awaiting further characterization.

Table 2. Synthesized catalysts.

Sample (Shorthand)	Molar Ratio
ZnO-Co_3O_4-CeO_2 (ZCC)	1:5:5 (Zn:Co:Ce)
NiO-Co_3O_4-CeO_2 (NCC)	1:5:5 (Ni:Co:Ce)
PdO-Co_3O_4-CeO_2 (PCC)	1:5:5 (Pd:Co:Ce)

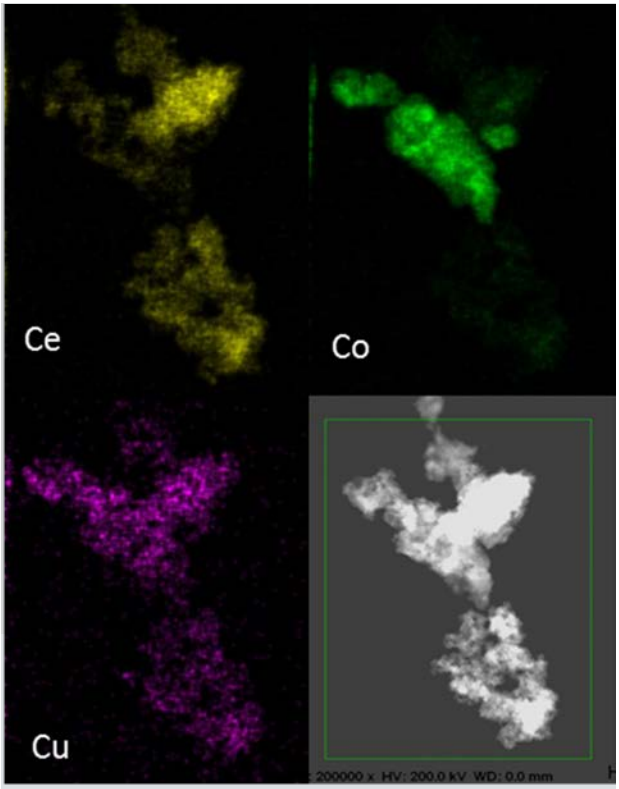

Figure 8: EDX elemental mapping of CuOx-CoOy-CeO_2 catalyst particle. Copper signal is seen throughout both the Co_3O_4 and CeO_2 regions.

Core-Shell Model Catalysts

A microemulsions method was used to prepare Pd@SiO_2 powders with different metal loadings. SiO_2 is formed as a shell around a Pd core to protect the active Pd site from contamination and thermal sintering that would cause losses in surface area. TEM micrographs of Pd@SiO_2 particles with different loadings are shown in Figure 9. There appears to be a relationship between metal loading and shell thickness. The particles in the sample with a nominal Pd loading of 4 wt% have a shell thickness of about 20 nm, while the sample with a lower Pd loading (0.4 wt%) has much thicker shells in the range of about 40 nm. CO conversions of 90% were found below 200°C (Figure 10).

A method was also developed for preparing active Pd@CeO_2 core@shell particles (shown schematically in Figure 11). A preliminary result is shown in Figure 12, where CeO_2 particles are observed on the surface of the

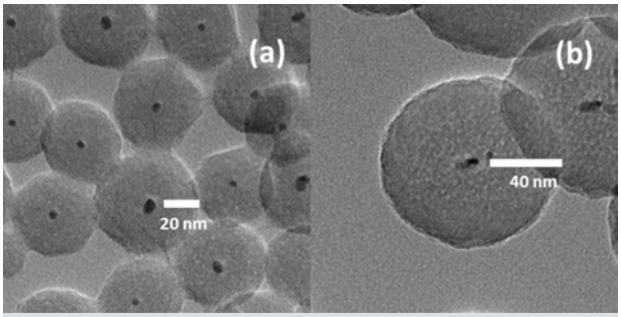

Figure 9: Pd@SiO_2 particles with different loadings. The left panel (a) presents a 4 wt% Pd loading, while the right panel (b) presents a 0.4 wt% Pd loading.

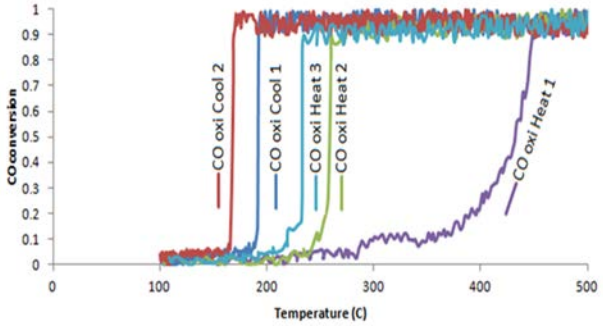

Figure 10: Multi-cycling CO oxidation test for Pd@SiO_2 core@shell particles (4% loading).

particle.

Conclusions

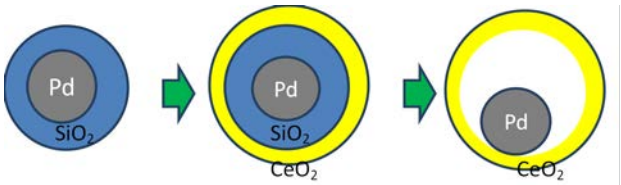

Figure 11: A new schematic for preparing core@shell nanoparticles with palladium core and an oxide material (CeO_2 for the first choice of material) other than silica.

A cross-laboratory reactor comparison of commercial TWC activity was comparable and demonstrated similar temperatures for 50% conversion of various chemical species typically present in gasoline engine exhaust (i.e., HC, CO, and NO_x). Sol-gel techniques were successfully applied to create supported metal catalyst materials with improved activity at lower temperatures than the commercial catalyst. Successful materials included Pd/titania (or zirconia) on silica-stabilized alumina, Pd supported on a core of SiO_2 and shell of ZrO_2 ($Pd/SiO_2@ZrO_2$), ternary metal oxides made of 1:5:5 (M:Co:Ce) where M = Cu, Zn, Ni, or Pd, $Pd@SiO_2$ with Pd core and SiO_2 shell, and $Pd@CeO_2$ (Pd core, CeO_2 shell). A large improvement in propane oxidation activity was noted for Pd/titania/silica-alumina over the commercial TWC. A potential cost saving opportunity was found with precious-metal free 1:5:5 (Cu:Co:Ce). The formation of Pd cores within SiO_2 and CeO_2 shells was confirmed via microscopy.

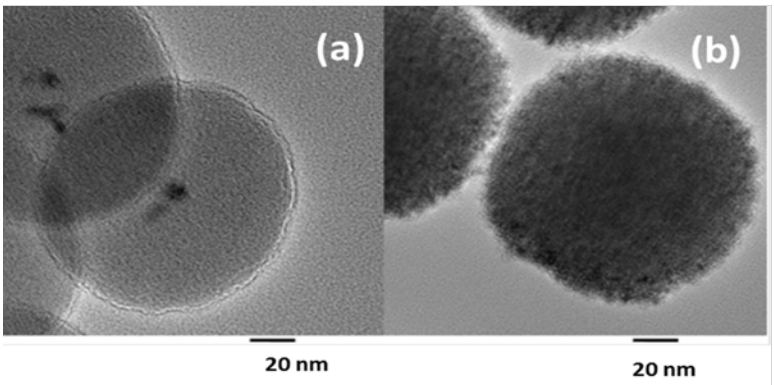

Figure 12: Preliminary result with $Pd@SiO_2@CeO_2$ particle preparation. The surface of $Pd@SiO_2$ (a) is coated with cerium oxide nanoparticles to produce $Pd@SiO_2@CeO_2$ particles (b). The scale bar represents 20 nm for both images.

Project 21656 – Development of High-Strength Crankshafts

Cummins Sustained Low-Temperature NO_X Reduction

Yuhui Zha
Catalyst Technology and Integration
1900 McKinley Avenue
Columbus, IN 47201
Phone (812) 377-7050; e-mail: yuhui.zha@cummins.com

DOE Technology Manager: Jerry L. Gibbs
Phone (202) 586-1182; fax: (202) 586-1600; e-mail: jerry.gibbs@ee.doe.gov

Contractor: Cummins, Inc.
Prime Contract No.: DE-EE0006795

Objectives

- The objective of this project is to develop the catalyst and system technology needed to enable a commercially viable system to sustain at least 90% conversion of NO_x emissions entering the SCR catalyst at 150°C.

Approach

- The project will develop the catalyst technology needed to enable sustaining at least 90% conversion of NO_x emissions entering the SCR catalyst at 150°C; demonstrate, using a prototype system and relevant emulated exhaust gas composition and temperatures, sustained low-temperature NO_x reduction (SLTNR); and develop a cost model to assess the commercial viability of the proposed SLTNR system.
- Development of a zeolite catalyst and catalyst architectures with enhanced catalytic activity at 150°C, targeting 90% conversion at an inlet NO_2/NO_x ratio of 0.50.
- Development of an integrated catalyst system capable of providing inlet SCR catalyst NO_2/NO_x ratios in the range of 0.40 to 0.50 at turbine outlet temperatures of 150°C.
- Determination and development of an appropriate means for robustly delivering reductant under sustained operation at low-temperature SCR catalyst inlet conditions.
- Development of SCR and oxidation catalyst models under conditions relevant to the SLTNR system.
- Budget Period 1: SLTNR System Analysis and Model Development – Model development for oxidation catalyst, tradeoff analyses, SCR mechanistic studies, and define SLTNR requirements/design configurations.
- Budget Period 2: SLTNR System Technology Development – SCR technology formulations, reductant delivery systems design, and commercial potential assessment. SLTNR system procurement and subsystem demonstration.
- Budget Period 3: SLTNR System Demonstration – SLTNR subsystem testing and system demonstration.

Accomplishments

- Developed an SCR formulation and preparation technique that the finished powder catalyst could achieve over 90% NO_x conversion under a fast SCR reaction condition.
- Developed DOC integration concepts that could generate high NO_2 generation to enable fast SCR reaction at low temperature.
- Demonstrated a new diesel emissions fluid (DEF) dosing concept: ultrasonic vaporizer technology with bench equipment.
- Developed an assessment criterial and evaluation approach for assessing the commercial viability of the developed system.

Future Direction

- Develop SCR monolith formulation from powder formulation and test performance and make improvements.
- Pre-turbo catalyst design and FMEA.
- DEF ultrasonic vaporizer device design and integration.
- Decision point at mid2016 to decide path forward on prototype system and technology demonstration.

Introduction

The objective of this project is to develop the catalyst and system technology needed to enable a commercially viable system to sustain at least 90% conversion of the NO_x emissions entering the SCR catalyst at 150°C.

The project will develop the catalyst technology needed to enable sustained at least 90% conversion of NO_x emissions entering the SCR catalyst at 150°C; demonstrate, using a prototype system and relevant emulated exhaust gas composition and temperatures, SLTNR; and develop a cost model to assess the commercial viability of the proposed SLTNR system.

The objectives for the project management portion of the work are to provide project planning, coordination, and reporting as required to successfully achieve the overall objectives of the project.

Budget Period 1: SLTNR Systems Analysis and Model Development

Task 1.0 –Zeolite Catalyst Development with Enhanced Intrinsic Catalytic Activity

This task includes SCR mechanistic studies, chemical and physical properties of various SCR formulations, and performance model development.

Task 1.1 – SCR Mechanistic Studies

The limiting mechanisms that result in light-off temperatures of 200°C for the commercially available SCR materials will be determined. A range of catalyst compositions that vary the metal (i.e., Cu and/or Fe) content, the zeolite composition (e.g., Si/Al ratios), and varied acidity will be selected to address ammonia storage, NO_2/NO_x ratios and N_2/N_2O selectivity. The differences in ammonium nitrate formation and varying selectivity to NO_2 during standard and fast SCR on Cu and Fe will be determined. Low-temperature light-off on metal

(i.e., Cu and/or Fe) reducibility will also be determined with variations in the metal (i.e., Cu and/or Fe) content and zeolite Si/Al ratios.

Task 2.0 – Integrated Catalyst System Development

This task will specify and design integrated catalyst systems through analysis and reactor testings that are expected to meet the SLTNR NO_2/NO_x ratio requirements.

Task 2.1 – Develop Models for Oxidation Catalysts

Reaction engineering and kinetic modeling will be applied to develop oxidation catalyst models under conditions representative of a pre-turbine location. Laboratory tests to confirm oxidation catalyst performance will be performed.

Task 2.2 – NO_2/NO_x Ratios Assessment for Pre-turbine Oxidation Catalysts

Oxidation catalyst models and reaction engineering principles will be applied to perform trade-offs regarding oxidation catalyst functions and size required to meet the SLTNR NO_2/NO_x ratios. Both pre-turbine and close-coupled oxidation catalysts will be considered.

Task 2.3 – Pre-Turbine Catalyst Performance Testing

Laboratory tests will be performed to characterize oxidation catalyst performance under conditions representative of the pre-turbine location. The oxidation catalyst models will be updated, as needed, based on the test results.

Task 2.4 – Catalyst System Integrated Oxidation Options

Engine cycle simulation tools, in combination with the developed catalyst models and practical design considerations, will be used to estimate the potential benefits and trade-offs of the pre-turbine and close-coupled oxidation catalyst locations. Based on the simulation results, integrated catalyst systems for testing will be recommended.

Task 3.0 – SLTNR System Designs

Specify and design low-temperature reductant delivery systems that are expected to meet the SLTNR requirements. Designs for the recommended testing configurations will be developed and preparatory work for procurement of the systems will be completed.

Task 3.1 – Assess Options Available to Deliver Reductant for Continuous Operation

Available reductant options for low-temperature operation will be assessed. The advantages and disadvantages of the low-temperature reductant delivery options will be developed. A literature survey and a concept generation process will be completed to create a list of options to assess against the requirements. The available options will be rated and recommendations made as to the reductant delivery system(s) to integrate as part of the SLTNR systems to assess through engine testing.

Task 3.2 – Design and Prepare to Procure the Recommended Reductant Delivery System(s)

The most promising low-temperature reductant configurations will be designed and integrated into the engine system. Practical design and standard analysis work to assess the robustness of the required changes will be carried out. Drawings to procure the new components will be created. Suppliers for manufacturing the prototype hardware will be identified and estimates for procurement lead times will be obtained.

Task 4.0 – Commercial Potential and Capability of the SLTNR Configurations

The commercial potential and capability of the proposed SLTNR configurations will be assessed. The SLTNR configuration against both medium-duty vehicle and heavy-duty engine system requirements will be evaluated.

Task 4.1 – SLTNR Options Assessment

The key requirements and baseline configurations against which to assess the integrated SLTNR options will be defined. A cost model will be developed to assess the commercial potential of the integrated SLTNR configurations. The relevant cycles for both medium-duty vehicle and heavy-duty engine systems will be used to assess the commercial potential of the SLTNR configurations.

Table 1. Budget Period 1 project milestones.

Milestone	Type	Description
SLTNR Requirements	Technical	Document key requirements against which to assess the commercial viability of SLTNR concepts
Catalyst Formulation and Reaction Unit Design	Technical	Analysis complete for catalyst formulation and reaction unit design
Oxidation Catalyst	Technical	Oxidation catalyst received for laboratory testing
Low-Temperature SCR Formulations	Technical	Low-temperature SCR formulations of critical functions established
Technology Development Assessment	Go/No Go	Analysis indicates 90% conversion of NO_x emissions entering the SCR catalyst is achievable at 150°C with NO_2/NO_x at 0.5

Continuation: In accordance with the award terms and conditions, specifically the provision named "CONTINUATION APPLICATION AND FUNDING," and the go/no go technical criteria outlined above, the recipient is **NOT** authorized to proceed beyond Budget Period 1 without the DOE Contracting Officer's approval of acceptable technical progress associated with the go/no go technical criteria and the submission of a continuation application no later than 90 days prior to the end of the current budget period. If selected to continue into a subsequent budget period, the recipient will continue to perform the overall tasks listed in this statement of project objectives, or, adjusted tasks as deemed necessary and negotiated during the negotiation of subsequent continuation application(s). If the recipient unilaterally decides to continue into the subsequent budget period prior to the DOE Contracting Officer's approval, all costs are incurred at the recipient's risk and no DOE funds may be utilized for such costs prior to the DOE Contracting Officer's approval of the technical go/no go criteria and continuation application.

Budget Period 2: SLTNR System Technology Development

Task 1.0 – Develop a Zeolite Catalyst with Enhanced Intrinsic Catalytic Activity (Continued)

This task includes SCR mechanistic studies, chemical and physical properties of various SCR formulations, and performance model development.

Task 1.1 – SCR Mechanistic Studies. (Continued)

The limiting mechanisms that result in light-off temperatures of 200°C for the commercially available SCR materials will be determined. A range of catalyst compositions that vary the metal (i.e., Cu and/or Fe) content, the zeolite composition (e.g., Si/Al ratios), and varied acidity will be selected to address ammonia storage, NO_2/NO_x ratios and N_2/N_2O selectivity. The differences in ammonium nitrate formation and varying selectivity to NO_2 during standard and fast SCR on Cu and Fe will be determined. Low-temperature light-off on metal (i.e., Cu and/or Fe) reducibility will also be determined with variations in the metal (i.e., Cu and/or Fe) content and zeolite Si/Al ratios.

Task 1.2 – Chemical and Physical Properties of the Low-Temperature SCR Formulations

Experiments will be performed to establish the chemical and physical properties of the alpha SCR catalyst. The requirements for a beta version of the low-temperature SCR will be defined.

Task 1.3 – Alpha Low-Temperature SCR Performance Model

Reactor tests will be used to characterize the alpha low-temperature SCR catalyst functionality. Experimental data will be used to calibrate and/or develop a SCR catalyst model. The model will be refined as required to characterize the beta low-temperature SCR formulations.

Task 1.4 – Low-Temperature SCR Formulations for Thermal Stability and Sensitivity to Poisoning

Laboratory-scale testing will be conducted to verify that the low-temperature SCR catalysts possess sufficient hydrothermal stability and resistance to poisoning from fuel and engine oil impurities (such as sulfur).

Task 2.0 – Integrated Catalyst System Development (Continued)

This task will specify and design integrated catalyst systems through analysis and reactor testing that is expected to meet the SLTNR NO_2/NO_x ratio requirements.

Task 2.3 – Pre-Turbine Catalyst Performance Testing (Continued)

Laboratory tests will be performed to characterize oxidation catalyst performance under conditions representative of the pre-turbine location. The oxidation catalyst models will be updated, as needed, based on the test results.

Task 2.4 – Catalyst System Integrated Oxidation Options (Continued)

Engine cycle simulation tools, in combination with developed catalyst models and practical design considerations, will be used to estimate the potential benefits and trade-offs of the pre-turbo and close coupled oxidation catalyst locations. Based on simulation results, integrated catalyst systems for testing will be recommended.

Task 2.5 – Exhaust Manifold with Integrated Pre-Turbine Oxidation Catalysts Design

Exhaust manifold designs integrating the oxidation catalysts for the most promising configurations will be prepared. The robustness of the required exhaust manifold changes to accommodate the configurations of oxidation catalysts will be established. Drawings to procure new engine system components will be prepared. Suppliers to manufacture the prototype hardware will be identified and estimates for procurement lead times will be obtained.

Task 3.0 – SLTNR System Designs

Specify and design low-temperature reductant delivery systems that are expected to meet the SLTNR requirements. Designs for the recommended testing configurations will be developed and preparatory work for procurement of the systems will be completed.

Task 3.2 – Design and Prepare to Procure the Recommended Reductant Delivery System(s) (Continued)

The most promising low-temperature reductant configurations will be designed and integrated into the engine system. Practical design and standard analysis work for assessing the robustness of the required changes will be carried out. Drawings to procure the new components will be created. Suppliers to manufacture the prototype hardware will be identified and estimates for procurement lead times will be obtained.

Task 4.0 – Commercial Potential and Capability of the SLTNR Configurations (Continued)

The commercial potential and capability of the proposed SLTNR configurations will be assessed. The SLTNR configuration against both medium-duty vehicle and heavy-duty engine system requirements will be evaluated.

Task 4.2 – Commercial Potential of SLTNR Configurations

The SLTNR system configurations will be assessed against the key requirements relative to baseline systems. The commercial viability of the systems will be assessed based on initial and operating costs.

Task 5.0 – SLTNR Prototype Systems

This task includes design, procurement, and testing of SLTNR prototype systems.

Task 5.1 – SLTNR Systems Final Design and Procurement

Design of the SLTNR subsystems (i.e., oxidation catalyst, exhaust manifold changes, SCR catalyst configuration, and low-temperature reductant dosing) will be finalized. Parts will be procured and assembled. Control modifications and other preparations for testing in the test cell will be completed. The base engine system configuration for testing will also be procured. Detailed test plans to assess subsystem performance will be developed.

Task 5.2 – SLTNR Subsystems Performance Characterization

The base engine will be installed and commissioned in a test cell. Baseline configuration performance will be validated. It is anticipated that the subsystems will be characterized independent of one another. A specific test

plan to characterize the capability of the different integrated oxidation catalyst systems to generate target NO_2/NO_x and the impact on engine performance will be measured without the presence of low-temperature reductant dosing or SCR catalysts. Similarly, performance of the low-temperature reductant delivery systems will be assessed independently of the other subsystems; the low-temperature SCR catalyst performance will be tested with and without the integrated oxidation catalysts and low-temperature dosing system. The tests will be designed to collect data in support of system model validation.

Performance of the subsystems will be assessed against expectations. Based on the test results, SLTNR subsystems will be selected for additional testing.

Task 5.4 – Risk and Programmatic Impact Assessment

A cross-functional team will be assembled to assess the risks associated with the proposed SLTNR configurations. The high-risk areas associated with the proposed changes to the system architecture will be identified and action items developed to mitigate the highest risk factors.

Table 2. Budget Period 2 project milestones.

Milestone	Type	Description
Low-Temperature SCR Models	Technical	Alpha low-temperature SCR model completed
Integrated Catalyst System	Technical	Bench-scale testing confirms catalyst system meets NO_2/NO_x targets
Cost Benefit Analysis	Technical	Initial cost benefit analysis complete and SLTNR systems selected for testing
Prototype SLTNR Systems	Technical	SLTNR subsystems complete and ready for engine testing
SLTNR System Procurement and Testing	Go/No Go	Reaffirm decision to proceed with procurement of hardware and testing of SLTNR systems

Continuation: In accordance with the award terms and conditions, specifically the provision named "CONTINUATION APPLICATION AND FUNDING," and the go/no go technical criteria outlined above, the recipient is **NOT** authorized to proceed beyond Budget Period 2 without the DOE Contracting Officer's approval of acceptable technical progress associated with the go/no go technical criteria and the submission of a continuation application no later than 90 days prior to the end of the current budget period. If selected to continue into a subsequent budget period, the recipient will continue to perform the overall tasks listed in this statement of project objectives, or, adjusted tasks as deemed necessary and negotiated during the negotiation of subsequent continuation application(s). If the recipient unilaterally decides to continue into the subsequent budget period prior to the DOE Contracting Officer's approval, all costs are incurred at the recipient's risk and no DOE funds may be utilized for such costs prior to the DOE Contracting Officer's approval of the technical go/no go criteria and continuation application.

Budget Period 3:

Task 1.0 – Develop a Zeolite Catalyst Development with Enhanced Intrinsic Catalytic Activity (Continued)

This task includes SCR mechanistic studies, chemical and physical properties of various SCR formulations, and performance model development.

Task 1.2 – Chemical and Physical Properties of the Low-Temperature SCR Formulations

Experiments will be performed to establish the chemical and physical properties of the alpha SCR catalyst. The requirements for a beta version of the low-temperature SCR will be defined.

Task 1.4 – Low-Temperature SCR Formulations for Thermal Stability and Sensitivity to Poisoning

Laboratory-scale testing will be conducted to verify that the low-temperature SCR catalysts possess sufficient hydrothermal stability and resistance to poisoning from fuel and engine oil impurities (such as sulfur).

Task 5.0 – SLTNR Prototype Systems (Continued)

This task includes design, procurement, and testing of SLTNR prototype systems.

Task 5.2 – SLTNR Subsystems Performance Characterization (Continued)

The base engine will be installed and commissioned in a test cell. Baseline configuration performance will be validated. It is anticipated that the subsystems will be characterized independent of one another. A specific test plan for characterizing the capability of the different integrated oxidation catalyst systems to generate target NO_2/NO_x and the impact on engine performance will be measured without the presence of low-temperature reductant dosing or SCR catalysts. Similarly, performance of the low-temperature reductant delivery systems will be assessed independently of the other subsystems; the low-temperature SCR catalyst performance will be tested with and without the integrated oxidation catalysts and low-temperature dosing system. The tests will be designed to collect data in support of system model validation.

Performance of the subsystems will be assessed against expectations. Based on test results, SLTNR subsystems will be selected for additional testing.

Task 5.3 – Prototype SLTNR System Demonstration

A limited number of SLTNR configurations will be tested as full systems. The SLTNR system test plan will be developed. SLTNR system performance will be characterized at a number of key operating points.

Task 5.4 – Risk and Programmatic Impact Assessment (Continued)

A cross-functional team will be assembled to assess the risks associated with the proposed SLTNR configurations. The high-risk areas associated with the proposed changes to the system architecture will be identified and action items will be developed to mitigate the highest risk factors.

Task 5.5 – SLTNR System Performance and Robustness Testing

A single SLTNR system will be selected for performance characterization and preliminary robustness testing. A test plan will be developed and engine testing will be performed.

Table 3. Budget Period 3 project milestones.

Milestone	Type	Description
Low-Temperature SCR Beta Formulation	Technical	Deliver SCR beta formulation
SCR Thermal Stability and Sulfur Sensitivity	Technical	Quantify thermal stability and sulfur sensitivity of low-temperature SCR catalyst formulations
Prototype SLTNR Systems Testing	Technical	Select SLTNR system for engine demonstration
SLTNR Demonstration System	Technical	Complete SLTNR system engine performance and robustness testing

Results

Low-Temperature SCR Formulation Development

During the first and second quarters, SCR reaction tests carried out at PNNL led to identification of two key factors that influence low-temperature fast SCR performance: (1) the NH_3 storage capability of the SCR catalysts and (2) the density of the redox sites of the SCR catalysts. It was further concluded that the minimization of NH_3 storage capability and the maximization of the density of redox sites led to enhancement in low-temperature SCR performance. Based on the extensive experimental work during the first and second quarters, Fe/beta has been identified as our best catalyst for low-temperature fast SCR.

However, although the Fe/beta catalyst performs the best under fast SCR (NO_2/NO_x = ½) conditions, this catalyst displays much less activity for standard SCR (NO_2/NO_x = 0) at low reaction temperatures (i.e., less than 250°C) when compared to Cu/CHA. In this research, NO_2 is generated by a DOC catalyst placed upstream of the SCR catalyst. Preliminary results from Cummins indicate that unburned hydrocarbons convert NO_2 back to NO in DOC. Therefore, NO_2/NO_x = ½ is not always maintained. Rather, the NO_2/NO_x ratio for SCR can fluctuate in a wide range from 0.3 to 0.7. In order to maximize NO_x conversion at various NO_2/NO_x ratios, a dual-layer SCR catalyst design is proposed and detailed below. The dual layer catalyst design is schematically shown in Figure 1.

Figure 1: Schematic of the dual-layer SCR catalyst design.

From this design, it is critical to determine the gas compositions at point “A” (i.e., gas compositions at the outlet of the Fe/beta first layer). This follows because gas composition determines which catalyst should be used in the second layer to maximize NO_x conversion.

To determine gas compositions at point "A," SCR reactions were carried out at a relatively high GHSV of 300k h^{-1} at various NO_2/NO_x inlet ratios from 0.3 to 0.7 on a Fe/beta catalyst formed via solid-state ion exchange. The results are displayed in Figure 2.

From these results, it has been found that outlet NO_x and NH_3 concentrations depend heavily on inlet NO_2/NO_x ratios: (1) at inlet NO_2/NO_x less than 0.5, outlet $NO_2 \approx 0$ ppm and $NO \approx NH_3$ (in other words, the unreacted portion has a standard SCR composition); (2) at inlet $NO_2/NO_x = 0.5$, outlet $NO \approx NO_2 \approx ½\ NH_3$ (i.e., the unreacted portion still has a fast SCR composition); (3) at inlet NO_2/NO_x greater than 0.5, outlet NO_2/NO_x becomes even higher. These results are fully expected such that within the first Fe/beta catalyst layer, only fast SCR reaction proceeds. These results allow the second catalyst to be determined fairly readily.

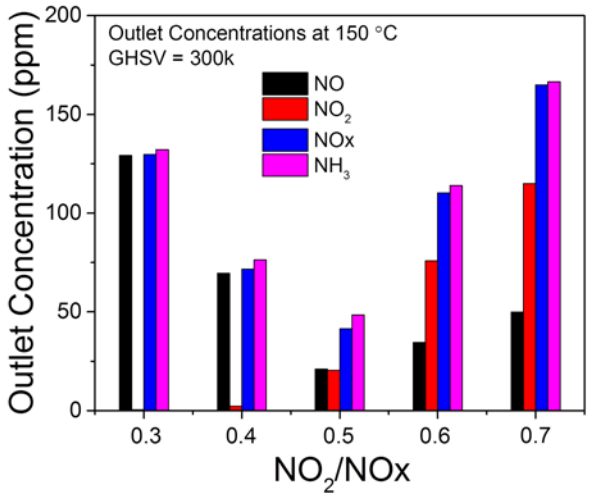

Figure 2: NO_x and NH_3 outlet concentrations as a function of inlet NO_2/NO_x ratio during NH_3–SCR on a hydrothermally aged Fe/beta catalyst. Reactant feed contains 350 ppm $NO+NO_2$ ($0.3 \le NO_2/NOx \le 0.7$), 350 ppm NH_3, 14% O_2, 2.5% H_2O balanced with N_2 at a GHSV of 300,000 h^{-1}. Reaction temperature is 150°C.

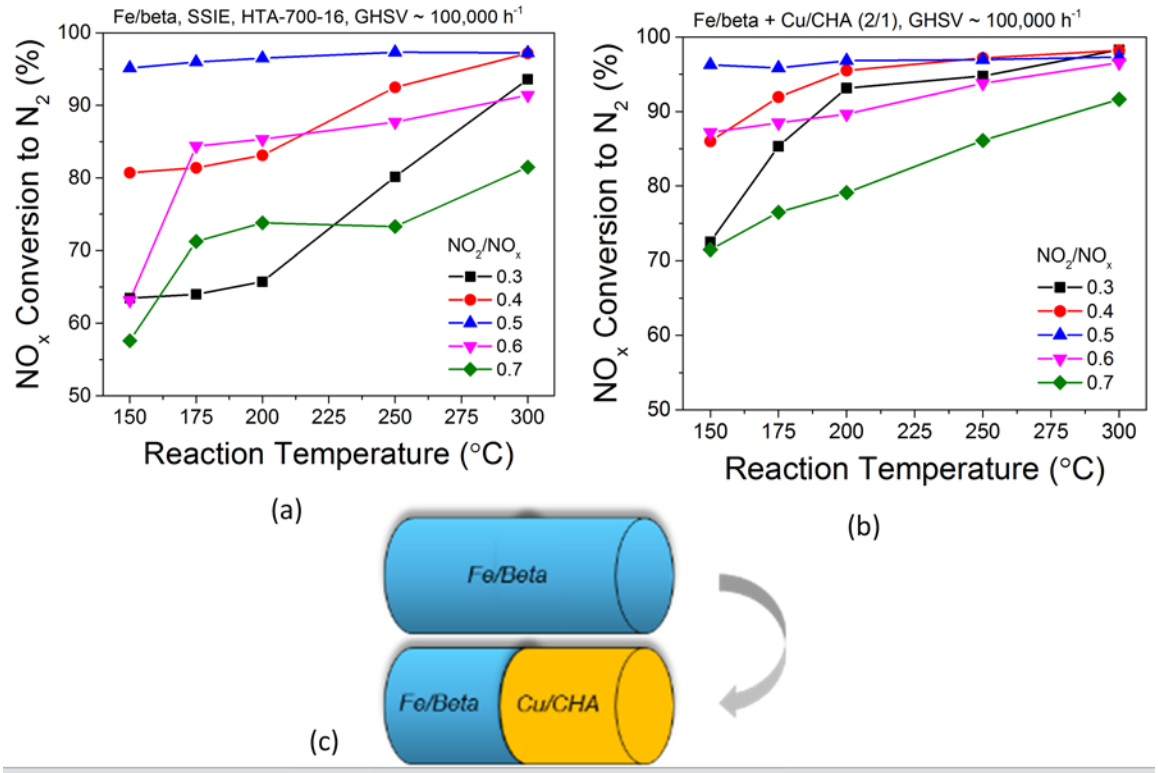

Figure 3: NO_x conversion as a function of reaction temperature on (a) Fe/beta, and (b) Fe/beta + Cu/CHA (2/1) dual-layer catalyst. Reactant feed contains 350 ppm $NO+NO_2$ ($0.3 \le NO_2/NOx \le 0.7$), 350 ppm NH_3, 14% O_2, 2.5% H_2O balanced with N_2 at a GHSV of 100,000 h^{-1}. (3) A schematic of the dual-layer catalyst design where Fe/beta is placed upstream and Cu/CHA downstream.

When inlet NO_2/NO_x is less than 0.5, a Cu/CHA second layer is preferred because this catalyst is much more active for low-temperature standard SCR. When inlet NO_2/NO_x = 0.5, a Fe/beta second layer is preferred, but a Cu/CHA second layer is acceptable because a Cu/CHA catalyst can reach about 80% total NO_x conversion at 150°C. When inlet NO_2/NO_x is greater than 0.6, NH_4NO_3 inhibition becomes severe enough that neither Fe/beta nor Cu/CHA could achieve high NO_x conversions.

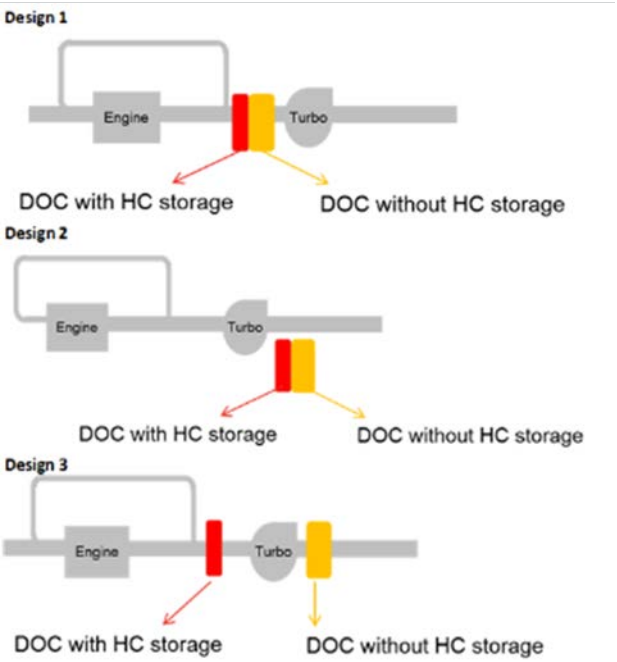

Figure 4: DOC location design layout (Design 1 – pre-turbo, Design 2 – post-turbo, Design 3 – split).

From these preliminary reaction tests, a few key conclusions can be reached. First, at NO_2/NO_x less than or equal to 0.6, a downstream Cu/CHA layer is beneficial for low-temperature NO_x conversion. This effect is the most obvious when NO_2/NO_x ratios vary from 0.4 to 0.6. However, without more detailed knowledge on the precise NO_2/NO_x ratios, a weight (or volume) ratio between the two layers is difficult to determine. In fact, when inlet NO_2/NO_x ratios fluctuate extensively, optimizing SCR catalyst performance can be very challenging. Meanwhile, a NO_2/NO_x greater than 0.6 situation, if possible, should be avoided.

Finally, PNNL has identified three near-term focuses: (1) effects of hydrocarbon to low-temperature fast SCR; (2) beta zeolite modification (e.g., sialylation to heal defects and improve hydrothermal stability); (3) test dual-cation catalysts (Cu and Fe in the same catalyst).

Integrated System Development for High NO_2

A zoned DOC concept was proposed to meet the NO_2/NO_x ratio (at SCR inlet) requirement for the SLTNR program. The front zone is designed for efficient HC storage and oxidation, while the rear zone is mainly responsible for NO oxidation to NO_2. Johnson Matthey has started simulation work for DOC optimization in order to hit the targeted NO_2/NO_x ratio (i.e., about 0.5).

The engine condition provided by Cummins (Table 4) was used for the preliminary DOC simulation. Some criteria are fixed for the initial assessment: volume of front zone (HC removal) = 1 L and volume of rear zone (NO oxidation) = 3 L. A Johnson Matthey-proprietary DOC model was used for the simulation work. A pipe module is added at the turbo location to represent the temperature loss across. Three designs (1, 2, and 3) are considered (Figure 4) for the different DOC locations: Design 1 has both zones located pre-turbo; Design 2 has both zones located post-turbo; Design 3 has the front zone located pre-turbo and the rear zone post-turbo. The model was based on the volume of each DOC module. Since 4.66-in. and 5.66-in. diameter substrates are typical for 1 L and 3 L DOC, the sizes of 4.66-in. x 3.6-in. for the front DOC and 5.66-in. x 7.3-in. for the rear DOC were chosen for simulation.

Table 4. First set of engine condition for DOC simulation (a: EGR=0, b: EGR=0.2, c: EGR=0.4, d: EGR=0.5).

Condition Index		1a	1b	1c	1d	2a	2b	2c	2d	3a	3b	3c	3d
Pre Turbo Temperature	deg C	225	212	229	232	229	232	232	236	243	242	241	
Post Turbo Temperature	deg C	202	188	189	188	209	209	204	201	217	217	216	
SCR in Temperature	deg C	149	135	134	138	163	161	149	149	180	176	173	
pre & post turbo Composition													
NO	ppm	416	167	46	11	151	86	26	7	88	58	22	
NO2	ppm	43	45	31	20	36	42	32	21	33	38	32	
CO	ppm	87	117	207	355	157	196	337	609	219	267	430	
HC	ppm	149	166	186	229	208	233	298	413	268	297	396	
CO2	%	3.78	4.58	6.2	7.29	2.95	3.72	5.03	6.01	2.62	3.21	4.28	
O2	%	15.3	14.1	11.5	9.7	16.5	15.3	13.3	11.7	17	16.1	14.5	
II2O	%	5.56	6.33	8.03	8.88	4.91	5.55	6.8	7.72	4.62	5.14	6.12	
Flow rate	g/s	42	33	26	22	58	45	33	28	74	60	44	
EGR Frac	none	0	.02	.04	.05	0	0.2	0.4	0.5	0	0.2	0.1	

Figure 5 shows the preliminary simulation results. Design 1 clearly exhibits the best HC removal efficiency, which is probably due to the higher-temperature pre-turbo. However, the NO_2/NO_x ratio is generally higher than 0.5 for all flow rates simulated. Design 2 and 3 show very close HC removal efficiency (i.e., greater than 87%) and NO_2/NO_x ratios (i.e., $0.3<NO_2/NO_x<0.7$) at Conditions 2 and 3. At Condition 1, Design 2 exhibited a lower HC conversion and NO_2/NO_x ratio compared to Design 3. It can be implied by the simulation that the proposed DOCs might be able to hit the targeted NO_2/NO_x under the engine condition shown in Table 4.

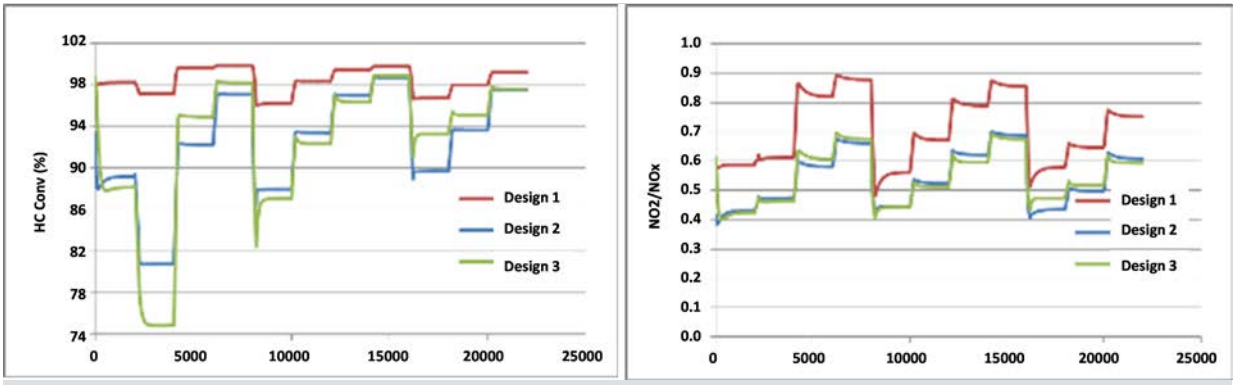

Figure 5: DOC simulation results (left – HC conversion, right – NO_2/NO_x ratio) based on the engine condition (11 mode, 1a-3c) in Table 4.

Based on simulation work, the team recommended that engine testing with a full part be completed. Because reasonably high HC conversion with an operational NO_2/NO_x ratio could be achieved by modeling, the DOC parameters in the model work were used without modification to make these parts. Per Cummins' request, the actual DOC parts were all made 5.66-in. in diameter (while keeping the volume unchanged) for easy test cell setup at Cummins. Two pairs of DOC sets were made and delivered to Cummins in time.

In order to confirm model simulation results, Johnson Matthey provided prototype DOCs to Cummins in October 2015. The specification of DOCs received are listed as follows:

– 5.66-in. x 2.5-in. PGM: 2:1:0/50, 400/4

– 5.66-in. x 4-in. PGM: 5:1:0/30, 400/4

– 5.66-in. x 3.3-in. PGM: 5:1:0/30, 400/4.

The DOCs were canned at Cole Tech and tested in Test Cell 221 at Cummins Tech Center. The DOC set was installed post-turbo and in A-B-C sequence as shown in Figure 6.

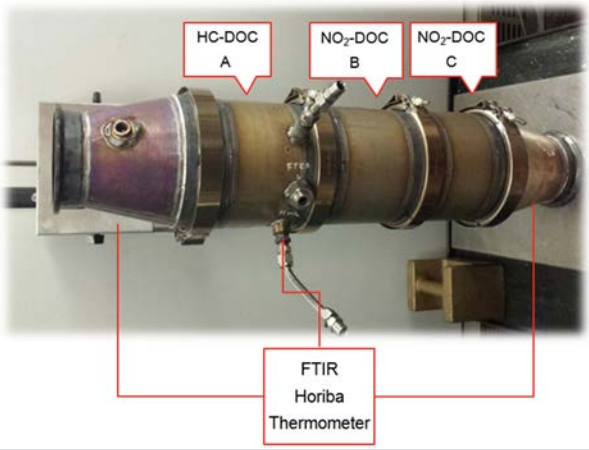

Figure 6: The installation of canned prototype DOC set is A-B-C with three measurement location for HC, NO, NO_2, and temperature.

The engine was operated to target the 12 modes stated in the previous section, where EGR sweep from 0 to around 0.6 and flow from low to high at the same time SCR inlet temperature remained around 150°C. Among these 12 modes, the DOC set inlet temperature (DOC A inlet) is in range of 180 to 220°C. In addition, a few points at the higher DOC A temperature were also tested to simulate pre-turbo location, where temperature could be in the range of 220 to 350°C.

Testing results were plotted in Figure 7. The NO_2/NO_x ratio after the DOC set reaches acceptable range (i.e., greater than 0.4) above 225°C and get on target (about 0.5) at around 270°C. In order to understand the limiting factor that causes this lower NO_2/NO_x fraction in comparison with the simulation result, HC conversion over DOC A was also plotted. It is observed that the HC conversion rate is much lower than expected, especially in the low-temperature region, which could be the key inhibitor for NO_2 generation on DOC B and C. For future confirmation, the HC/NO_x ratio was plotted and the trend was well in line with the NO_2 fraction, which indicates that HC most likely is the key inhibitor to diminishing the

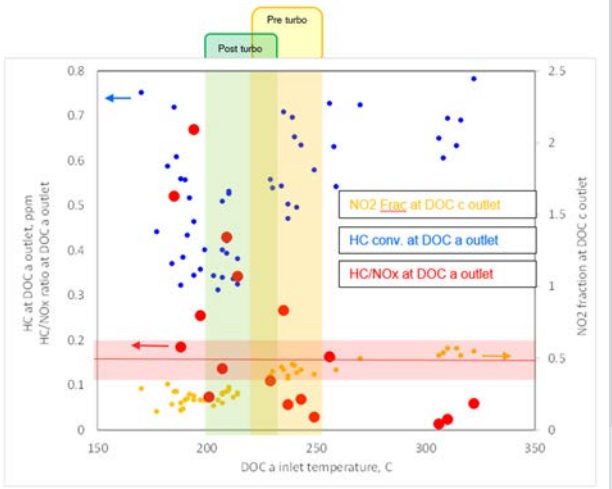

Figure 7: DOC engine test results: NO_2/NO_x ratio at tailpipe (red dots), HC conversion over DOC A (blue dots-left Y axis), and HC/NOx ratio at DOC A outlet;

DOC B and C performance.

The observation of the NO_x conversion (i.e., NO_x concentration decrease) as the N_2O concentration increases over DOC A provides strong evidence that indicate the HC-SCR reaction (Equation 1) occurs on a PGM-based DOC catalyst, which consume NO_2, NO, and HC to generate N_2O as one of the major products. Even over DOC B and C, the function of NO_2 generation is significantly inhibited by HC-SCR reaction and is based on the increase of the N_2O rate over DOC B/C (see Figure 8).

$$HC + NO + NO2 + O2 => N2 + N2O + CO + CO2 + H2O \quad \text{(Equation 1)}$$

Based on the above engine test results, we consider the following three paths for improving the HC control capability over HC-DOC:

- Optimize size of HC-DOC (A) to limit HC-SCR reaction on NO_2-DOC (B/C)
- Optimize location of HC-DOC (A) to increase temperature of HC-DOC
- Optimize PGM loading of HC-DOC(A) to shift HC-SCR reaction
- Develop reductant delivery system.

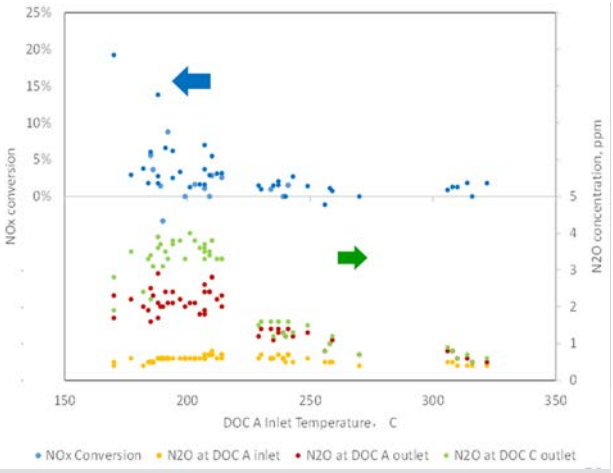

Figure 8: N_2O generation versus NO_x conversion as function of temperature.

Laboratory testing of commercially available ultrasonic dosers was performed on schedule and an initial prototype design was completed in computer-aided design (CAD). A bill of materials has been completed, with all items off-the-shelf, except for the DEF drain valve and the rapid prototype plastic parts. The drain valve is expected to be available in January 2016, pushing the prototype build into the first quarter of 2016. Work to design an appropriate decomposition chamber will run through the end of 2016.

Laboratory testing of a heated exhaust chimney to address the recorded failure mode of DEF condensation is planned for the fourth quarter of 2016.

Rescheduling the prototype build to the first quarter allows for incorporation of test results and failure mode resolutions into the design. The Task 3 schedule is on-track to provide a working prototype to support all system-level tests. Tasks that have been delayed are under evaluation for modification or elimination, depending on impact and risk.

Testing of droplet size mean diameter (Sauter mean diameter [SMD]) was performed earlier in 2015, with 5 to 7 micron droplet sizes recorded, depending on test conditions. An example plot of SMD at two different volumes measured 50 mm from the vaporizer spout is shown in Figure 9. Taking the averages of all tests, SMD is measured to be between 5.5 and 7.5 µ. For comparison, test data showing several current product DEF dosing technologies is seen in Table 6, with SMD readings between 33 and 72 µ.

It is not clear what impact the small fraction of large droplets represented by the DV90 values (i.e., size in the

distribution where 90% of the droplets are smaller than the DV90 value) have on deposit formation; however, larger droplets take longer to decompose and may be linked to deposits. For comparison, the DV90 measurements for current product in Table 6 range from 150 to 222 µ. The ultrasonic vaporizer measured DV90 value is 27 µ. It should be noted that ultrasonic droplet size testing was performed using water due to laboratory concerns of aerating DEF. The current plan is to repeat this testing using DEF by the end of January 2015 to confirm performance.

Table 5. Ultrasonic DEF vaporizer team RACI chart, showing tasks, responsibilities, and timelines.

8/24	8/31	9/7	9/14	9/21	9/28	10/5	10/12	10/19	10/26	11/2	11/9	11/16	11/23	11/30	12/7	12/14	Task or Milestone Definition	Yuhui	John Heichelbech	Samuel J	Sanjay B	Karan S	Rei T	Danielle H	Taren D	ColeTech	R-Y-G-C	Comment
																	Testplan											
																	Obtain OTS hardware		R								C	
																	Spray test plan		A				R				C	
																	Spray testing		A				R				C	
																	DEF droplet size testing		A	R							G	28OCT2015: Capability should be in place by end of Dec; testing in Jan.
																	Obtain lab space		A	R							C	
																	Evaluation of prior (Crane) vaporizer		A	R							C	
																	Create deposit formation testplan		A	R		R					C	
																	Determine hardware needed		A	R		R					C	
																	Provide hardware		R								C	
																	Perform deposit testing		A	R		R					C	
																	Create NH3 derivation test plan		A					R			Y	12AUG2015: CTC lab unable to fullfill request; looking at alternative suppliers
																	Determine hardware needed		A					R			Y	
																	Provide hardware		R					A			Y	
																	NH3 derivation testing		A					R			Y	
																	Product Profile		A		A						C	
																	Design requirements		A							R	C	12AUG2015: Requirements delivered to supplier; quotation due by 14AUG
																	Creo design 1		A							R	C	27OCT2015: initial draft complete
																	Design review 1		A							R	Y	27OCT2015: Design review not yet scheduled
																	Creo design 2		A							R	Y	27OCT2015: Completion targeted for Jan 2016
																	Design review 2		A							R	Y	27OCT2015: Completion targeted for Jan 2016
																	Finalize design		A							R	Y	27OCT2015: Completion targeted for Jan 2016
																	ALD Scope statement		R						C		R	27OCT2015: Looking for available resources
																	Iterate ALD based upon Creo design										R	
																	Complete ALD recommendations										R	
																	Bench testing at CEP		A	R								
																	Burner rig test plan		A							R	G	16SEP2016 moved to Q1 2016
																	Test plan execution		A							R	G	16SEP2016 moved to Q1 2016
																	Document results		R		A					R	G	16SEP2016 moved to Q1 2016

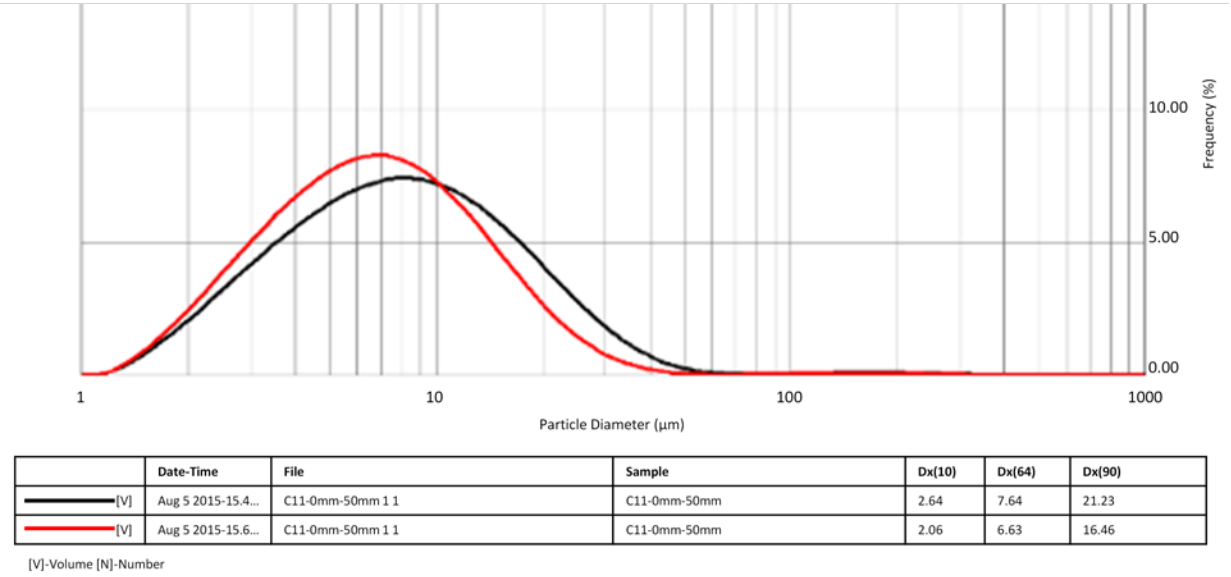

	Date-Time	File	Sample	Dx(10)	Dx(64)	Dx(90)
[V]	Aug 5 2015-15.4...	C11-0mm-50mm 1 1	C11-0mm-50mm	2.64	7.64	21.23
[V]	Aug 5 2015-15.6...	C11-0mm-50mm 1 1	C11-0mm-50mm	2.06	6.63	16.46

[V]-Volume [N]-Number

Figure 9: Ultrasonic vaporizer droplet size testing results showing plots of approximately 7 and 8 micron averages (Cummins Emission Solutions, A&TT Tech Report TR-128, Rei Tangko).

Table 6. Current product DEF droplet sizes, taken from spray angle and droplet size comparisons (Bosch and UL2 Dosers, May, 2014, Rei Tangko and Achuth Munnannur).

Averaged Derived Parameter	UL2 K4.3	UL2 S5.3	Bosch 2.2 A030P707	Bosch 2.2 A045N270	Bosch 2.6 A043C088
SMD (micron)	33.2	35.6	72.5	66.5	54.7
Dv90 (micron)	93.2	125	222	187	150

Laboratory testing earlier in 2015 confirmed ultrasonic vaporizer performance, including behavior of DEF, material compatibility, and key failure modes of deposit formation and condensation. This testing used a commercial off-the-shelf home vaporizer made by Crane that was tested previously using DEF. The system performed without catastrophic failure or failure to operation, although some undesirable characteristics were observed and documented. The tendency of the DEF vapor to condense on the chimney or connection hose walls was noted, as was the appearance of small DEF crystals on the air passages around the fan. These failures are noted in Table 7.

The testing also allowed for observation of the characteristics of DEF vapor, PZT behavior in DEF, and the general suitability of the materials and the component design when applied to an automotive DEF vaporizer.

Table 7. Observed failure modes from commercial vaporizer testing with DEF (by Samuel Johnson, Cummins Emission Solutions).

Date of Failure	UHV Model	Test Running	Failure
20-Jul	Crane	Initial Deposit	Chimney was oriented in sideways 'S' curve. Condensed/coalesced droplets begin collecting in low spot of the tube. Eventually restricted flow to the chimney.
29-Jul	Crane	Long Duration Deposit	DEF dripping back to the tank collected at the barbed fitting between the hose chimney and the fitting. The pooling DEF eventually leaked through the seal of the fitting and began to crystallize on top of the UHV.
7-Aug	Crane	Long Duration Deposit	Crystals found inside fan. Probable cause is equilibrium diffusion of urea droplets after shutdown. Eddy current recirculation to the fan is possible, but not likely due to droplet size and positive air flow to the base pool of the UHV.
17-Aug	Crane	Long Duration Deposit	Low-level sensor apparently does not function with DEF. Does function with water as working fluid (i.e., low-level light comes on with water, does not with DEF; will check system response).
17-Aug	Crane	Long Duration Deposit	Crystals formed over PZT during weekend sit. Possible reduction in performance if crystals cover PZT.

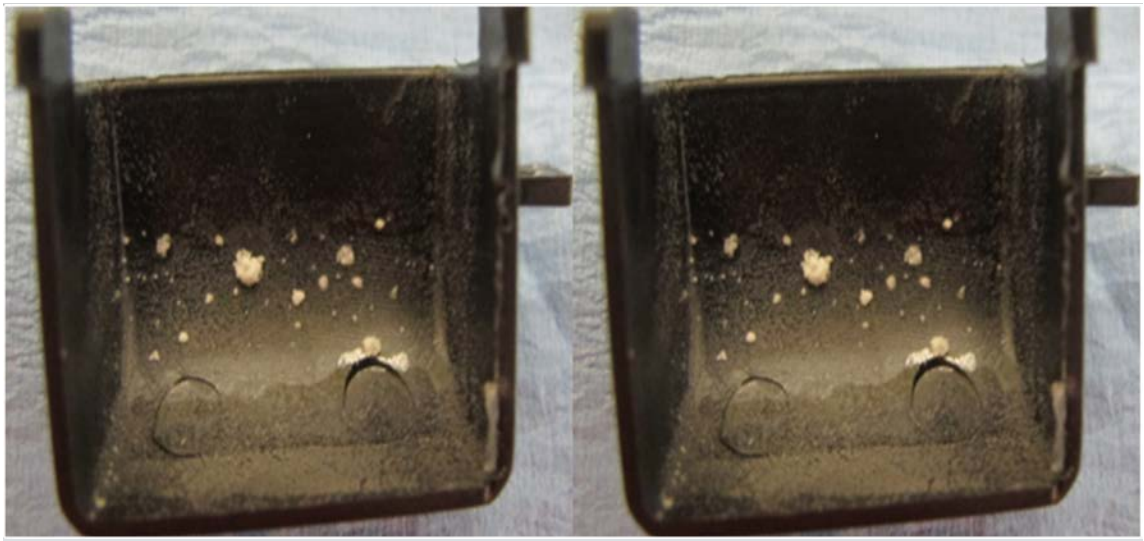

Figure 10: (A) DEF deposits on fan blade tips (results of laboratory testing of commercial vaporizer with DEF). (B) DEF deposits on fan shroud (results of laboratory testing of commercial vaporizer with DEF).

Test cell data were collected for the representative SLTNR operating conditions of exhaust flow, temperature, and NO_x concentration. These operating conditions represented the operating characteristics for an SCR inlet temperature of 134 to 180°C. The prototype reductant delivery system being proposed exceeds the requirements for exhaust temperature, flow rate, and NO_x concentration. The one per hour of DEF required was estimated by calculating the molar concentration of NO_x from the engine NO_x sensor and is calculated using an ammonia to NO_x ratio of 1:1.

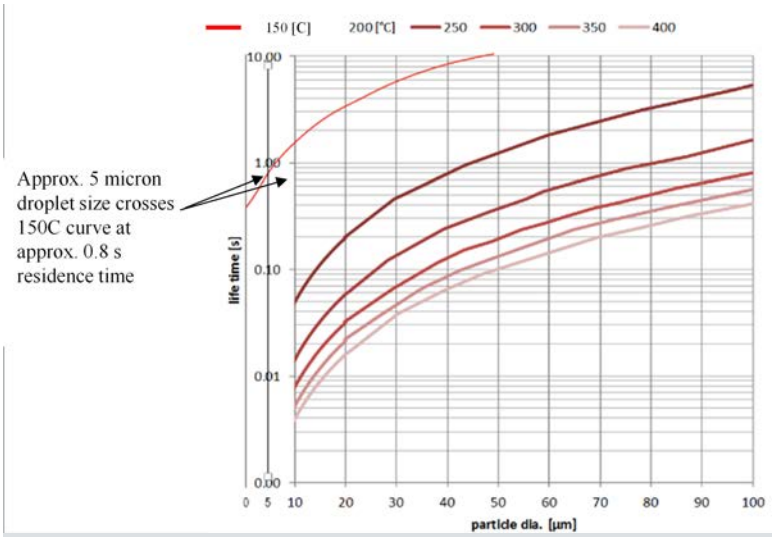

Figure 11: DEF droplet residence time as a function of droplet size and temperature. The 150°C curve and the sub-20 micron data have been extrapolated from Lundström, Andreas, Henrik Ström, and Magnus Skoglundh. 2013, "Dispersion Aspects of NH3-Delivery Strategies for NH3-Based SCR Systems." *Topics in Catalysis*: 1-5.

The listed conditions are valid for the SLTNR testing at 150°C. In production, the ultrasonic doser would need to accommodate the full range of exhaust characteristics from idle to peak power. The prototype being proposed would likely need to be scaled up to meet these flow rates, utilizing multiple and possibly higher-capacity PZTs.

The residence time shown at the bottom of Table 8 was estimated using a 10-in. diameter x 24-in. long decomp reactor. This sizing may be appropriate for the demonstration, but may be overly bulky for production, particularly for smaller engines.

Table 8. Ultrasonic vaporizer design requirement for SLTNR demonstration (test data courtesy of Ravi Lakkireddy, CMI Catalyst Technology and Integration).

Characteristic	System Required Min Value	Vaporizer Deliverable	Status
SCR exhaust pressure	0.688 kPa max	2.0 kPa nom	Good
SCR exhaust flow rate	74 g/s	-	NA
Max NO_x flow	–	6.3 Mol/hour	NA
Temperature range at SCR	150°C	134 to 180°C	Good
Max DEF flow rate	0.541/hour	0.71/hour	Good
Calculated residence time	0.8 s	0.5 s	Monitor

Determination of requirement for residence time is particularly ch allenging via calculation methods due to the low operating temperature of 150°C and the known behavior of DEF droplets. Literature exists for droplet size decomposition at temperatures of 200°C and higher, but the behavior at 150°C is not understood. Based on prior studies, the residence time, or time to decompose fully (some studies use 90% decomposition), can be estimated. Figure 11 shows an extrapolated curve for DEF droplet time to decompose as a function of temperature.

A draft design of the demonstration DEF vaporizer was completed using Creo 2.0 CAD software. See Figures 12, 13, and 14 for a cross section showing internal components. Key features included in this design iteration are as follows:

- A metering DEF pump to enable metering control
- Umbrella-style check valves to protect the air system from DEF crystal migration
- Addition of space for electronics
- Addition of a sealing gasket between the plastic components (i.e., o-ring, shown in yellow between top and body)
- Addition of two fans for air control.

The control strategy presented is dependent on inclusion of a metering DEF pump within the system. While any metering pump could be used, Cummins Emission Solutions has been working with the firm Thomas Magnate to produce a plastic metering pump as a cost reduction opportunity. The control opportunity and requirements to enable use of the Thomas Magnete pump are discussed in the following sections.

Control of DEF dosing within an SCR aftertreatment system requires accurate calculation of DEF volume delivered to the SCR catalyst per unit time.

For a PZT-based system, due to the absence of an injector, the flow rate is only known with accuracy by calculating volume metered into the PZT bowl per unit time, assuming no DEF is lost to solid deposits or other nitrogen-containing byproducts.

A liquid level sensor is used to detect when the DEF level is below the full level, at which time the pump turns on until sensor contacts close again. Resulting volume (i.e., number strokes x pump swept volume) is the quantity metered between sensor "full" readings. This volumetric flow rate Q is determined by where the theoretical limit of ΔV results from the commanded pump frequency (i.e., number of strokes/unit time) and ranges from 0 to 32 Hz. The

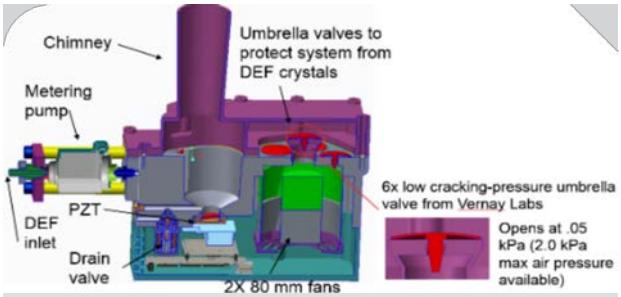

Figure 12: CAD model cross section of prototype ultrasonic vaporizer showing key features

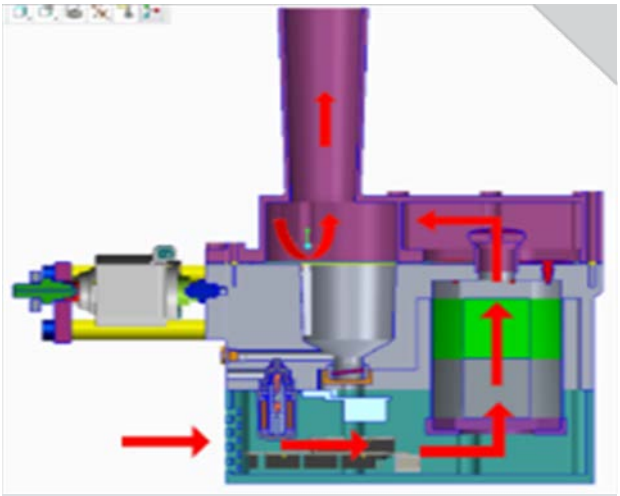

Figure 13: CAD model cross section of prototype ultrasonic vaporizer showing airflow path. Curved red arrow indicates airflow behind the chimney and exiting as shown.

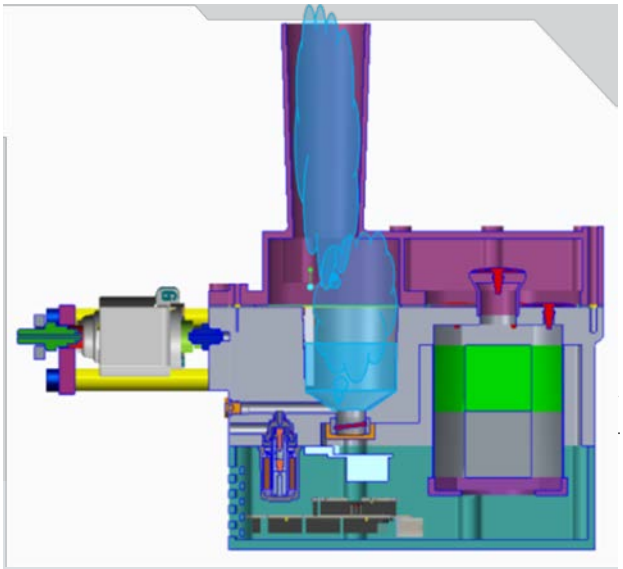

Figure 14: CAD model cross section showing DEF level in blue, with vapor clouds indicated above pool and exiting through chimney

resulting Q value is used as a feedback control algorithm to relate required PZT voltage to actual quantity commanded.

The PZT voltage can then be continuously modified using Q as feedback. It should be noted that the PZT voltage requested will also vary with liquid temperature and fluid level. These factors will be incorporated as lookup values and originate from the sensor readings. See Figure 15 for lookup values supplied by the PZT manufacturer.

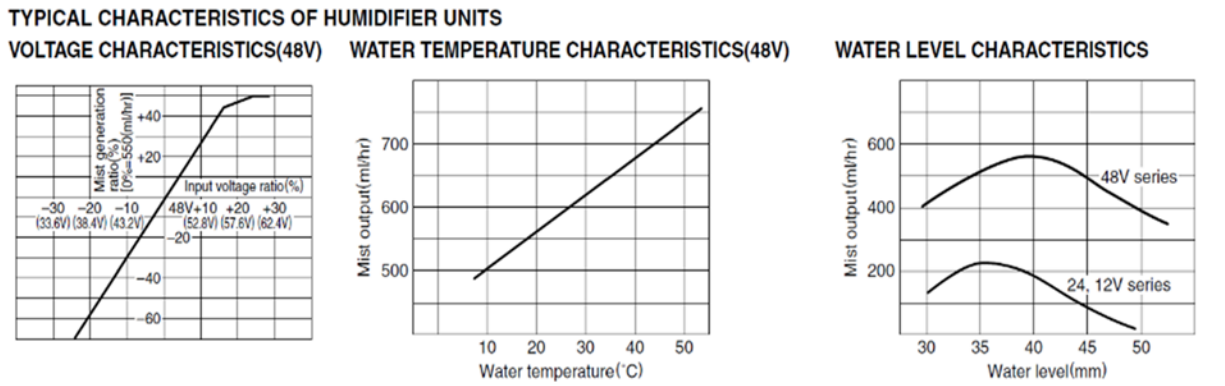

Figure 15: Lookup tables provided by the PZT manufacturer, TDK p/n NB-59S-09S-0, illustrates flow rate as a function of PZT voltage, water temperature, and water level.

All electronic/electrical components (Table 9) are expected to be off-the-shelf, with the exception of a DEF metering pump and DEF drain valve, which are both under development for Cummins Emission Solutions. Samples are expected in the first quarter of 2016. An electrical transformer has not been selected and may require modification to an existing product to provide 48 VAC, which is not a common voltage.

Table 9. Control system bill of materials for prototype.

Item	Quantity	Description	Vendor	Vendor P/N	Voltage	Watts	Signal
1	2	Fan, 80 mm PWM with digital tachometer	San-Ace	9HV0812P1G001	12	40.8	PWM
2	1	Sensor, liquid level	Hamlin	59630	12	0	Open/closed
3	1	Vaporizer, ultrasonic PZT	TDK	NB-59S-09S-0	48	35	Variable input voltage
4	1	Transformer, 12-VDC to 48 VAC			12		
5	1	Pump, metering	Thomas Magnete	P1300	12	21	PWM
6	1	Sensor, temp			12		0 to 5 VDC
7	1	Sensor, humidity			12		0 to 5 VDC
8	1	Valve, solenoid	IMI Webber	90X-20950	12		PWM

Item	Quantity	Description	Vendor	Vendor P/N	Voltage	Watts	Signal
		drain					

Several key control system tasks still need to be addressed, including the following:

- Interfacing with the engine ECM via CAN (J1939 automotive communication protocol); the expectation is to address this with current SLTNR team resources
- Choice of microcontroller to integrate the vaporizer electronic devices
- Control software selection language and writing the actual code
- Qualified controls engineering resources have not been selected/secured.

Controls resources are typically in high demand; therefore, establishing these resources will be a key task. It is anticipated that the resources will be in place sometime during the first quarter of 2016.

Architecture Selection

We brainstormed the potential aftertreatment system architectures to meet project objectives. A series of architectures were considered that had various strengths depending on other key decisions within the project. Based on the current status of the other work objectives, the promising architectures have been downselected to three (summarized in Figure 16).

The architectures in this figure that are marked out with an ‘X-1’ indicate the concepts that were designed to favor an NO_2 production method relying on engine out combustion to generate the 50% NO_2/NO_x ratio target. Although the engine can generate the necessary target ratio, this also generates high levels of hydrocarbon, which can have a negative impact. Based on this, the current direction is to utilize combustion to generate some NO_2, but ensure it is balanced to keep the engine out hydrocarbons levels low. Based on this, half of the concepts can be eliminated.

The architectures marked out with an ‘X-2’ indicate the concepts that favored a urea delivery system, which uses an untreated slip-stream of pre-turbine exhaust gas. In this case, this side-stream must be treated for particulate without oxidizing the ammonia; therefore, these concepts use an uncatalyzed DPF or with the filter downstream of the SCR catalyst. Based on the current direction for ammonia delivery, it does not appear that these concepts will be required.

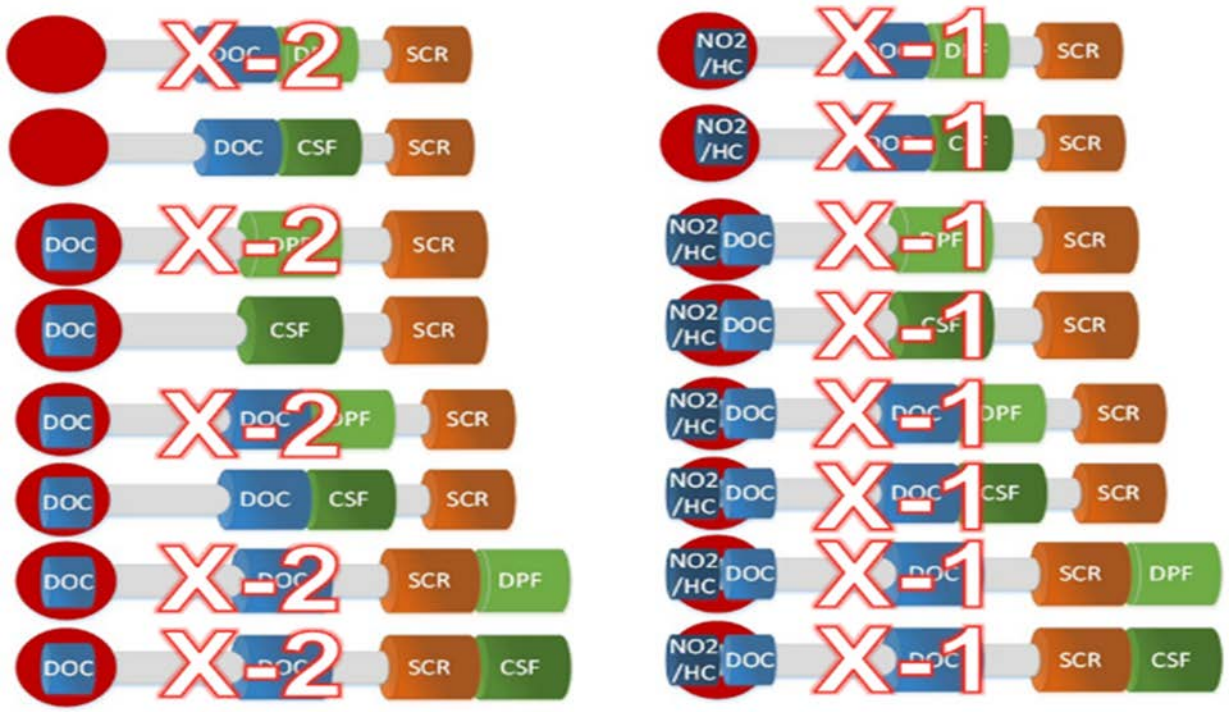

Figure 16: Summary of aftertreatment architecture concepts, with down-selected architectures denoted with an X.

Figure 17: Summary of top aftertreatment architectures currently under consideration.

The final three concepts are summarized in Figure 17, along with radar plots that show their key performance characteristics. The concepts are numbered in terms of current likelihood, with Concept 3 being most unlikely due to its lack of capability to meet hydrocarbon control requirements with only a pre-turbo DOC. Although Concept 2 would be the most cost-effective option and most like our baseline systems, the current DOC testing is suggesting that we will most likely need to rely on Concept 1. This concept will use a pre-turbine DOC, a post-turbine DOC followed by a catalyzed soot filter, and the SCR catalyst system. This down-selection has been completed based on other the directions of the other tasks within this project, and may be re-visited if those tasks determine that another path is required.

Commercial Viability Assessment

Some revisions have been made to the proposed plan for assessment of commercial viability. The new proposal is summarized in Table 10. The baseline system of a Mid-Range ISB 6.7L engine with a 2017 aftertreatment system and urea dosing system will remain in accordance with the previous report.

Table 10. Summary of commercial viability assessment method.

Aspect	Evaluation Criteria / Baseline	Current Feasibility	2 Yr. Potential	4 Yr. Potential	6 Yr. Potential	8 Yr. Potential
Initial Purchase Price						
System Cost	Current cost of baseline system = 1x	Rate with a feasibility percentage utilizing baseline and anticipated system cost				
Operating Cost						
Active Regen Frequency (Reduced Passive Regeneration)	Time between active regens over operating duty cycle	Rate with a feasibility percentage utilizing baseline system values and anticipated performance of final system				
Fluid Economy over drive cycle	Fuel + Urea consumption over cold FTP + warm FTP					
Fluid Economy over low temperature operation	Fuel + Urea consumption over low temperature cycle					
Backpressure	Exhaust manifold pressure at rated temperature and flow					
Maintenance Cost						
RF 1 - Durability of Fe-Beta SCR	Hydrothermal aging comparison to Cu-CHA SCR	Percentage confidence in ability to develop countermeasures				
RF 2 - Durability of Pre-Turbo DOC	Hydrothermal aging of DOC at elevated temperatures					
RF 3 - Durability of engine system with Pre-Turbo Catalyst	Assessment of DOC debris, impact on engine life					
RF 4 - Robustness of DOC to maintain 0.5 NO2/NOx Ratio	Assessment of aging impacts					
RF 5 - Durability / Useful Life of Urea Vaporizer	Assess lifetime compared to current urea dosing system					
OEM Development Cost						
Packaging Impact to Vehicle	Baseline engine/aftertreatment space claim envelope	Percentage confidence in ability to develop countermeasures				
Estimated System Feasbility		Multiply rows to develop overall estimated confidence measure				

The four main aspects and evaluation criteria remain the same as previously reported, with the exception of the maintenance cost section. We were struggling with how to assess this category well and we have determined that identifying the significant risk factors that any new technology that is being added via this project will bring. At this time, we have identified five risk factors associated with the durability of the proposed Fe-Beta SCR catalyst, the pre-turbine catalyst, the ability to meet the 0.5 NO_2/NO_x target over time, and the durability of the proposed urea delivery system. These technologies will continue to be assessed throughout the project, and, before the final commercial assessment, a thorough risk factor listing will be reviewed.

The other change is to the feasibility ranking shown in the last five columns of the figure. It was determined that a meaningful way of assessing the commercial viability was to judge each aspect's ability to evolve with time and development maturity. It is expected, as with any new technology, that it will be difficult to apply off-the-shelf and will take some development efforts to develop sufficient robustness to have a viable product. In order to reflect this, we will assess the maturity of each aspect by current status at the end of this contract period; then

project development over the next 8 years in 2-year intervals as a percent rating from 0 to 100% compared against the baseline system proposed.

The final addition is an overall estimated system feasibility, which will provide a roll-up of the overall system. This will be calculated by multiplying all individual elements to achieve an overall system percentage in the 0 to 100% range. The maturity of this feasibility will also be shown as a function of time.

Conclusions

The Cummins SLTNR Program has completed the third quarter of the project. The annual review was held on October 14th in Columbus, IN, and was attended by personnel from DOE and the National Energy Technology Laboratory, including Jerry Gibbs, Jerry Parker, and collaboration partners (i.e., people from PNNL, Johnson Matthey Inc., and Cummins Inc.). We reviewed the technical achievements in the first year (i.e., 2015), including testing data/analysis, model simulation, design concepts, challenges, and mitigation proposal.

Program spending for this quarter within Cummins is a total of $62.1K, as of September 2015, including a federal share of $28.5K and recipient share of $33.6K. The highlights of progress made in the third quarter are listed in Table 11.

Table 11. 2015 technology development progress highlight.

Task 1 Low-Temperature SCR	Quantified the sensitivity of developed model Fe-beta catalyst to NO_2/NO_x ratio and space velocity. Hybrid catalyst design proposed to minimize sensitivity and improve $deNO_x$ performance at 150°C with broader NO_2/NO_x ration 0.4 to 0.6. Future improvement can be achieved by optimization of ration and size of Fe/Cu. The sensitivity to HC is under evaluation.
Task 2 Integrated High NO_2	Received DOC prototype parts based on model-based DOC designs. Tested on engine and greater than 0.4 can be achievable when temperature is above 230°C. HC DOC performance to be improved. Pre-turbo location might be necessary to facilitate NO_2 generation. HC DOC part tested might be undersized. Additional testing with larger HC DC is in process.
	Two architecture working concepts are defined: pre-turbo HC-DOC with post-turbo NO_2-DOC and large HC DOC with NO_2 DOC at post-turbo. GT powder simulation conducted in parallel with engine test to understand design space pre-turbo. Will initialize engine exhaust manifold redesign work as necessary.
Task 3 Reductant Delivery System	Completed water droplet characterization of commercial vaporizer and droplet size is much smaller than current product. Testing with DEF is planned in the first quarter of next year due to availability of resources. DEF vaporizer is in process of design, including integration consideration such as mixer design, electronic control design, air flow design, and valve design.
Task 4 Commercial Viability	Revised commercial viability assessment criteria, defined risk factors and assessment will be given as percent of confidence against years of development based on technology maturity and application feasibility.

Based on the design/testing/analysis results of the developed low-temperature SCR, the integrated DOC system, DEF vaporizer testing, and the current architecture working concepts are listed below. The first concept is a

hybrid DOC at post-turbo followed by CSF, after mixer, a Fe/Beta SCR followed by a Cu/CHA SCR catalyst; the second concept is HC-DOC at pre-turbo and NO_2-DOC at post-turbo, followed by CSF, mixer, and a Fe/Beta SCR and a Cu/CHA SCR. In both concepts, the DEF vaporizer is taking compressed air from the turbo and connected to mixer to provide NH_3 mist to the system.

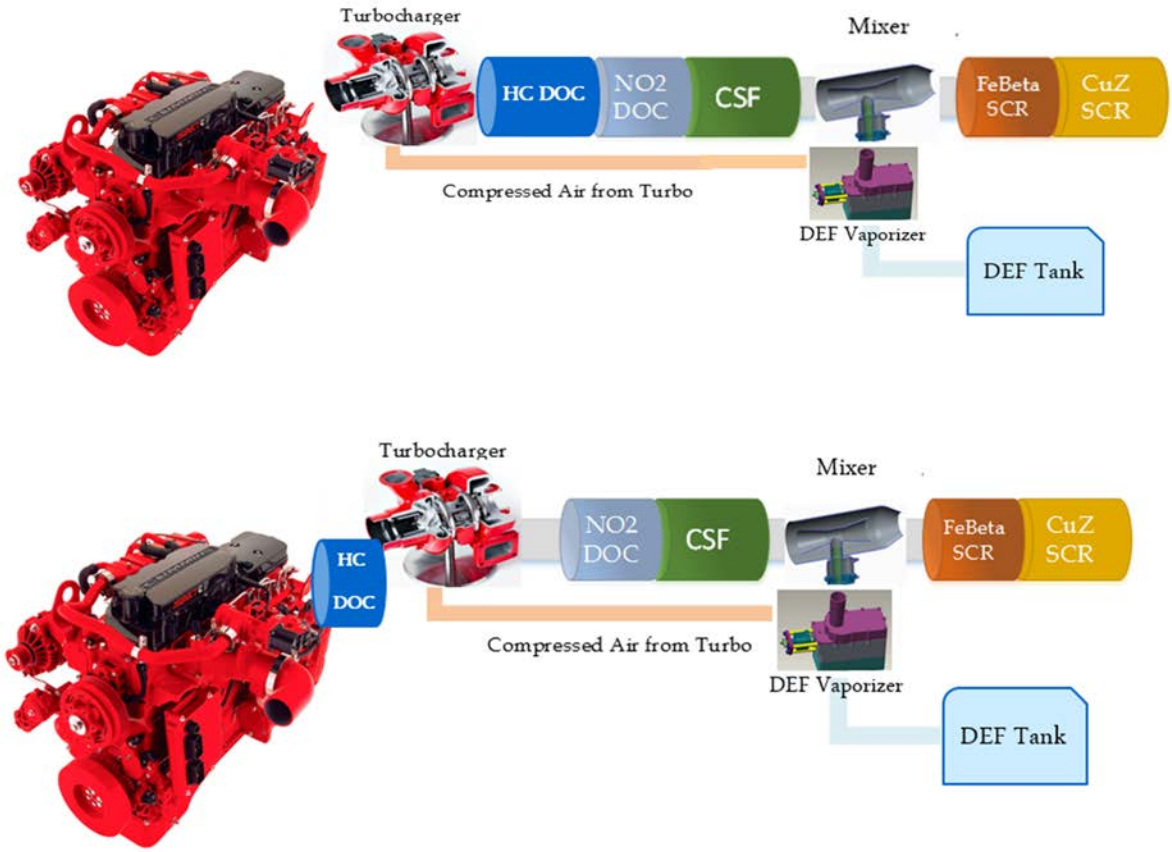

Figure 1: Architecture working concepts.

Important future activities for the fourth quarter of 2015 and 2016 include the following:

- Finish low-temperature SCR HC sensitivity study
- Initialize discussion and sample trial to prepare catalyst on monolith from powder formulated by PNNL
- Complete first generation hybrid DOC set engine test and further narrowing of architecture working concept
- Continue GT power simulation and define design space for pre-turbo catalyst
- Initialize discussion on exhaust manifold redesign
- Continue DEF vaporizer device design and integration design.

U.S. DEPARTMENT OF
ENERGY
Energy Efficiency &
Renewable Energy

For more information, visit: energy.gov/eere/vehicles/vehicle-technologies-office

EE-1507 • December 2016